

UNIVERSITÀ DEGLI STUDI DI TRIESTE

XXIII ciclo del
dottorato di ricerca in
FISICA

**Measurement at COMPASS of transverse spin
effects on identified hadrons on a transversely
polarised proton target**

Settore scientifico disciplinare FIS/04 FISICA NUCLEARE E SUBNUCLEARE

Responsabile del dottorato di ricerca:
prof. Paolo Camerini



Relatore/supervisore:
prof. Paolo Schiavon
Università degli Studi di Trieste



Dottoranda:
Giulia Pesaro



Correlatrice:
prof. Anna Martin
Università degli Studi di Trieste



Anno Accademico 2009-2010

Riassunto

La sezione d'urto che descrive la diffusione profondamente inelastica di un leptone carico (μ^+) su di un nucleone (protone) polarizzato trasversalmente rispetto alla direzione del moto con identificazione di almeno un adrone nello stato finale ($l p^\uparrow \rightarrow l' h X$) presenta otto modulazioni azimutali, rispetto al piano definito dallo spin del nucleone bersaglio e dal momento del leptone incidente. Tra queste le meglio conosciute sono dovute all'effetto Collins e all'effetto Sivers. Il primo effetto è la frammentazione di un quark polarizzato trasversalmente in un adrone e l'ampiezza della modulazione è data dalla convoluzione della "trasversità" (ovvero la funzione di distribuzione che descrive i partoni polarizzati parallelamente o antiparallelamente allo spin del nucleone, per nucleoni polarizzati trasversalmente) con la funzione di frammentazione di Collins. L'effetto Sivers è dovuto alla distribuzione di momento trasverso dei partoni all'interno del nucleone. Le rimanenti sei modulazioni sono dovute ad altre correlazioni tra la polarizzazione o il momento trasverso del partone e lo spin del nucleone.

Il lavoro presentato in questa tesi è la misura dell'ampiezza delle modulazioni azimutali (asimmetrie) per i dati raccolti nel 2007 dall'esperimento COMPASS, usando un bersaglio di NH_3 per accedere al protone polarizzato, focalizzando l'attenzione sulle asimmetrie di Collins e Sivers. Le asimmetrie sono state misurate sia su un campione di adroni carichi che su adroni identificati con il rivelatore di luce Cerenkov RICH-1. Ampia parte del lavoro è stata dedicata alla determinazione dell'errore sistematico della misura.

La tesi è scritta in lingua inglese.

Summary

The Semi-Inclusive Deep Inelastic Scattering (SIDIS) cross section, that describes the scattering of a charged lepton (μ^+) off a nucleon (proton) transversely polarised with respect to its momentum, and with the detection of a hadron in the final state ($l p^\uparrow \rightarrow l' h X$), has 8 independent azimuthal modulations, that depends on the spin of the target nucleon and on the lepton momentum. Among these modulations, the most famous are due to the Collins and Sivers effects. The Collins effect is the asymmetric fragmentation of a polarised quark into a hadron, and the amplitude of the modulation is proportional to the Collins fragmentation function with the transversity parton distribution function, that gives the probability difference to find a quark with the polarisation parallel or anti-parallel to the nucleon spin in a transversely polarised nucleon. The Sivers effect is due to the coupling of the quark transverse momentum and the spin in a transversely polarised nucleon. The other six modulations are due to other correlations between the quark polarisation or the quark transverse momentum and the nucleon spin.

The work presented in this Thesis is the measurement of the amplitude of the azimuthal modulations (asymmetries) on the data of the COMPASS experiment, collected in 2007 using a NH_3 target to access the polarised proton, focusing on the Collins and Sivers asymmetries. The asymmetries have been measured both the charged hadrons and on hadrons identified making use of the ring-imaging Cherenkov detector RICH-1 . Large part of the work presented here is devoted to the determination of the systematic error of the measurement.

Contents

| | | |
|----------|---|-----------|
| 1 | The transverse spin and TMD structure of the nucleon | 5 |
| 1.1 | The Deep Inelastic Scattering | 5 |
| 1.1.1 | The DIS cross-section | 8 |
| 1.1.2 | Transversity PDF | 9 |
| 1.1.3 | The non collinear approach | 11 |
| 1.2 | The Semi-inclusive DIS cross-section | 12 |
| 1.3 | Transversity | 15 |
| 1.3.1 | The Collins fragmentation function | 17 |
| 1.3.2 | Experimental results | 17 |
| 1.3.3 | The extraction of $h_1(x)$ | 18 |
| 1.4 | The Sivers effect | 20 |
| 1.4.1 | Experimental results | 21 |
| 1.4.2 | The extraction of the Sivers PDF | 22 |
| 1.5 | Other single spin asymmetries | 22 |
| 2 | The COMPASS experiment at CERN | 29 |
| 2.1 | The muon beam | 29 |
| 2.1.1 | The Beam Momentum Station | 31 |
| 2.2 | The polarized target | 31 |
| 2.3 | The large and small angle spectrometers | 32 |
| 2.4 | The tracking detectors | 34 |
| 2.4.1 | Very small area trackers | 34 |
| 2.4.2 | Small area trackers | 35 |
| 2.4.3 | The large angle trackers | 36 |
| 2.5 | Particle identification | 38 |
| 2.5.1 | The muon identification | 38 |
| 2.5.2 | The electromagnetic and hadronic calorimeters | 39 |
| 2.6 | The RICH-1 detector | 40 |
| 2.6.1 | The radiator gas system | 41 |
| 2.6.2 | The mirror system | 42 |
| 2.6.3 | The photon detectors | 42 |
| 2.6.4 | The Identification algorithms | 43 |
| 2.6.5 | The detector properties | 45 |
| 2.7 | The trigger system | 46 |
| 2.8 | The Data Acquisition | 48 |
| 2.9 | The Event Reconstruction | 49 |
| 3 | The extraction of the cross section asymmetries | 53 |
| 3.1 | Data sample | 54 |
| 3.2 | Data quality tests | 54 |

| | | |
|----------|--|------------|
| 3.3 | SIDIS Event selection | 56 |
| 3.4 | The cleaning procedure | 58 |
| 3.5 | Principle of the measurement and the Reasonable Assumption | 58 |
| 3.6 | Quality tests | 61 |
| 3.6.1 | The measurement of $R(\phi)$ | 61 |
| 3.6.2 | The test of the "Reasonable Assumption" | 63 |
| 3.6.3 | The selection of the <i>periods</i> used for the final analysis | 64 |
| 3.7 | The extraction of the raw asymmetries | 64 |
| 3.7.1 | 1D binned method | 68 |
| 3.7.2 | The COMPASS angular acceptance | 68 |
| 3.7.3 | 2D binned method | 72 |
| 3.7.4 | Unbinned maximum likelihood | 72 |
| 4 | The cross section asymmetries | 75 |
| 4.1 | Extraction of the physical asymmetries | 75 |
| 4.1.1 | Collins asymmetries | 75 |
| 4.1.2 | Sivers asymmetries | 76 |
| 4.2 | The determination of the systematic error | 79 |
| 4.2.1 | Systematic error due to the variation of the acceptance | 81 |
| 4.2.2 | Systematic effect due to the estimator of the asymmetry | 82 |
| 4.2.3 | Systematic error on the target polarization | 82 |
| 4.2.4 | Systematic error from the <i>period</i> compatibility | 83 |
| 4.2.5 | Other studies on systematic effects | 83 |
| 4.2.6 | Final tables of the systematic error | 84 |
| 4.3 | Final results on the Collins and the Sivers asymmetries | 85 |
| 4.3.1 | The measurement of the asymmetries as a function of W | 86 |
| 4.3.2 | Final results for The Collins and Sivers asymmetries as a function of W | 89 |
| 4.4 | The measurement of the further 6 asymmetries | 94 |
| 4.5 | Final results on the further 6 asymmetries | 100 |
| 5 | The Collins and Sivers asymmetries for identified π and K | 105 |
| 5.1 | The detector stability in 2007 | 105 |
| 5.2 | The PID efficiency and purity | 107 |
| 5.2.1 | Tuning of the likelihood | 110 |
| 5.3 | Extraction of the Collins and Sivers asymmetries for identified particles | 114 |
| 5.4 | Determination of the systematic error | 120 |
| 5.4.1 | Compatibility among different periods | 120 |
| 5.4.2 | Other contributions | 120 |
| 5.4.3 | Contamination of the kaon sample | 124 |
| 5.5 | Conclusions | 125 |
| 6 | The extraction of the Sivers and transversity PDF | 129 |
| 6.1 | The fit of the Sivers asymmetries | 130 |
| 6.2 | The Gaussian factorisation of the quark transverse momentum | 134 |
| 6.3 | Conclusions and comparison with the theoretical models | 135 |
| 6.4 | The extraction of the transversity PDF | 137 |
| | Appendices | 145 |
| A | The light-cone reference frame | 145 |

| | | |
|----------|--|------------|
| B | Fourier analysis of the COMPASS acceptance | 147 |
| B.1 | Example | 147 |
| C | The determination of the convolution integrals | 151 |
| C.1 | The evaluation of F_{UU} | 151 |
| C.2 | The evaluation of $F_{UT}^{\sin(\phi_h - \phi_s)}$ | 152 |
| C.3 | The evaluation of $F_{UT}^{\sin(\phi_h + \phi_s)}$ | 153 |

Introduction

"Spin is an essential and fascinating complication in the physics of elementary particles"

E.Leader, Spin in Particle Physics.

The measurement of the spin-dependent parton distribution functions started in the early 70's, with the Yale-SLAC E-80 experiment, the first DIS experiment with both longitudinally polarized beam and target. The experiment measured the spin-dependent structure function $g_1(x)$ from the spin-dependent asymmetries in the differential scattering cross section. In the quark-parton model the DIS reaction is interpreted as an incoherent scattering of the virtual photon off the components quarks and $g_1(x)$ is [1]:

$$g_1(x) = \sum_q e_q^2 (q_q^\uparrow(x) - q_q^\downarrow(x)) ,$$

the sum over the quark flavours of the difference of the distribution functions of the quarks with spin parallel (\uparrow) or anti-parallel (\downarrow) to the nucleon spin.

To compare the theoretical models with the experimental results, there are two important sum rules: the Bjorken sum rule

$$\int_0^1 dx (g_1^p(x) - g_1^n(x)) = \frac{1}{6} \left| \frac{g_A}{g_V} \right| \simeq 0.209(1)$$

that connects the structure functions of the proton (p) and of the neutron (n) to the axial and vector charge describing the β -decay [2] and the Ellis-Jaffe sum rule [3]:

$$\Gamma_1^p = \frac{1}{12} |g_A| \left[1 + \frac{5}{3} \frac{F}{D} \frac{-1}{+1} \right] = 0.189(5)$$

where F and D are coefficients defined in hyperon semileptonic decay ($F/D = 0.573(20)$). The Ellis-Jaffe sum rule is derived using SU(3) current algebra and under the "reasonable" assumption that the strange sea quark is unpolarized.

The experimental issue in the measurement of Γ_1 is the difficulty to measure the cross section asymmetries at small values of x , which could not be accessed in SLAC experiments. As a consequence, the violation of the Ellis-Jaffe sum rule was unnoticed until 1987, when, using a high-energy muon beam, the EMC collaboration measured $\Gamma_1^p = 0.126 \pm 0.018$, indicating that very little of the nucleon spin is carried by the quarks, a result later confirmed by many polarized DIS experiments.

Today the decomposition of the nucleon spin in terms of its constituents reads as:

$$\frac{1}{2} = \frac{1}{2} \Delta\Sigma + \Delta G + L_q + L_g$$

where $\Delta\Sigma$ is the number of quark with the spin parallel to the nucleon spin minus the number of quark with the spin anti-parallel to the nucleon spin, ΔG is the similar contribution from

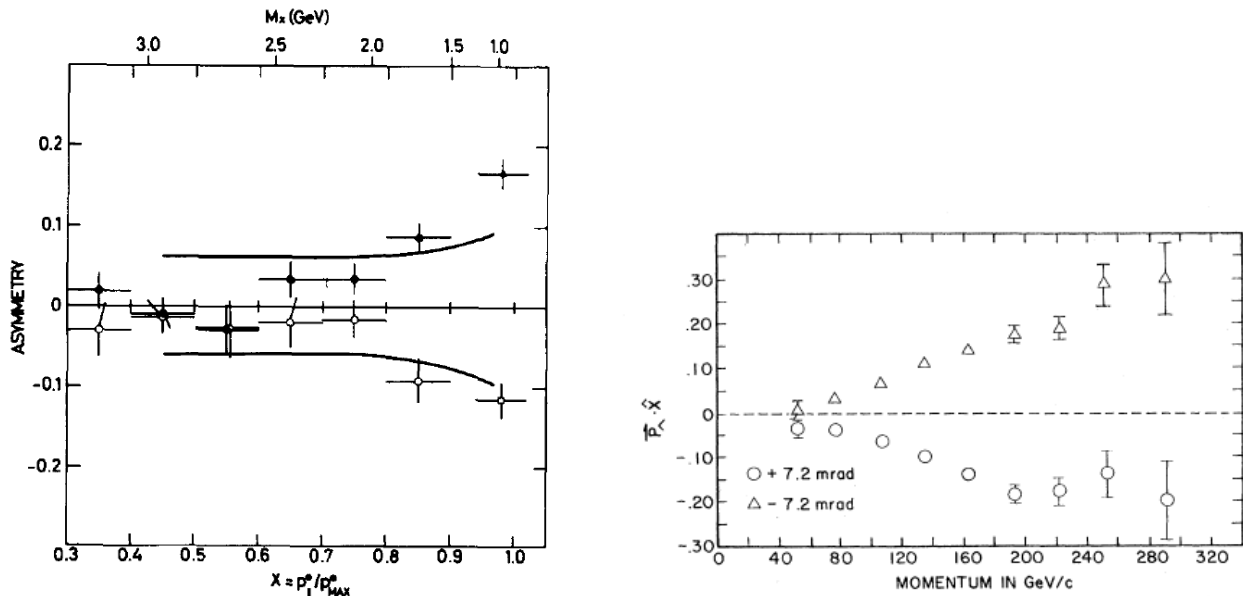


Figure 1: Left: The single spin asymmetry for the reaction $\pi^+ p^\uparrow \rightarrow \pi + \text{anything}$ (closed points) and $\pi^- p^\uparrow \rightarrow \pi + \text{anything}$ (open points) measured at the CERN PS in 1975 [4]. Right: the Λ^0 polarization as a function of its momentum as measured at Fermilab with the scattering of a 400 GeV/c proton beam off a beryllium target [5].

the gluons and L_q and L_g are the contributions from the orbital angular momentum of the quarks and of the gluons. The DIS experiments measure $\Delta\Sigma \approx 0.25$, in contrast with the value predicted by the quark-parton model of $\Delta\Sigma \approx 0.75$. A large contribution of ΔG was long believed to account for the difference, but recent measurements, by the COMPASS and HERMES experiments, show that the gluon contribution is small, giving importance to the orbital angular momentum of the partons, that is presently not experimentally accessible.

The history of the transverse spin is much more recent. In fact, the structure function $g_2(x)$, that is related to the transverse spin effects, is expected to be zero in the quark-parton model, the deviations from this result being due to higher-order QCD corrections.

Nonetheless, the first observation of a large transverse spin effects in hadronic interactions dates back to 1976, when large single-spin asymmetries were measured in the $\pi p^\uparrow \rightarrow \pi + X$ reaction ($\sqrt{S} \sim \text{GeV}$) [4] and the polarization of the Λ hyperons produced in the unpolarized pN scattering ($\sqrt{S} \simeq 24 \text{ GeV}$) [5] (Fig. 1). The first theoretical works interpreted these asymmetries as non perturbative QCD effects, expected to vanish at higher energies.

Since then, many experiments have measured pp and $p\bar{p}$ reactions at an increasing center of mass energy, as the E704 collaboration ($\sqrt{S} = 19.4 \text{ GeV}$), the STAR, BRAMS and PHOENIX collaborations at RHIC ($\sqrt{S} = 200 \text{ GeV}$), and they showed that the transverse spin effects are not suppressed at high energies.

In the 1990, soon after the discovery of the breaking of the Ellis-Jaffe sum rule, a new generation of semi-inclusive DIS (SIDIS) experiments was proposed, and the interest in the determination of the transverse spin-structure of the nucleon was revived. The "transversity" parton distribution function (PDF), introduced in 1979 by Ralston and Soffer [6] was rediscovered. Transversity is a leading order PDF, giving the probability difference to find the quark with the spin parallel or anti-parallel to the nucleon spin in a transversely polarized nucleon. Contrary to the number density and the helicity PDFs, transversity is chiral-odd and has to be coupled to another chiral-odd quantity in order to be measured. In SIDIS experiments,

there are three channels to access the transversity PDF: the Collins effect, where transversity is coupled with the Collins fragmentation function (FF), that describes the fragmentation of a transversely polarized quark into a hadron, the pair production, where transversity is coupled with the interference FF, that describes the fragmentation of a polarized quark into a hadron pair, and the polarization of the Λ hyperon. The extraction of the transversity PDF is subordinated to the knowledge of such chiral-odd FFs. Another possibility to measure transversity is given by the Drell-Yan reaction $p^\uparrow p^\uparrow \rightarrow ll$ or $p^\uparrow \bar{p}^\uparrow \rightarrow ll$, where the transversity of the quark and the antiquark couple to each other. Proposals for a new generation of polarised Drell-Yan experiments are being put forward and the feasibility of a polarized antiproton beam is under study.

The COMPASS (CERN) and HERMES (DESY) SIDIS experiments were proposed in the 90's, and started their operations about 10 years ago. Both experiments have a two-folded program, measuring both the longitudinal and the transverse spin effects. The transverse spin effects are not only related to the transversity PDF, but also to other transverse momentum dependent PDFs, that arise from the intrinsic transverse momentum of the quark inside the nucleon, like the Sivers PDF. These PDFs are responsible for azimuthal modulations in the SIDIS cross section.

The COMPASS experiment took data from 2002 to 2006 with a polarized deuteron target and it has been and still is the first and only experiment to measure the transverse spin and transverse momentum modulations of the SIDIS cross section on the deuteron [7, 8, 9]. In 2007 COMPASS took data with a polarized proton target, and the work presented in this Thesis is the analysis of those data. Since the Collins and the Sivers asymmetries are, by the time being, the most important, the algorithms presented are focused to the extraction of these asymmetries and then extended to the other modulations studied.

The work is organized as follows: in Chap. 1 a theoretical introduction to the SIDIS cross section is given, both in the collinear and in the non collinear approach, and the results achieved so far in this field are reviewed. This Thesis concerns only the single-hadron production modulations. The results on the two hadron asymmetries and the Λ polarization are described elsewhere [10, 11].

In Chap. 2 the COMPASS experiment is presented, and more details are given for the Ring Imaging Cherenkov (RICH) detector, that will be used in the following analysis for particle identification. The description of the RICH reconstruction algorithms, as well as its characterization are described in the article "Particle identification with COMPASS RICH-1" (P. Abbon et al., NIM A 631 (2011)), of which I am the corresponding author.

The original part of this Thesis is presented in Chap.s 3, 4 and 5. In Chap.s 3 and 4 the algorithms used to select the data, extract the asymmetries and determine the systematic error are described. The statistics used to estimate the asymmetries and the systematic errors are original and specific to the COMPASS geometry, and have been invented within the "Transversity group", about 20 physicists from Bonn, Erlangen, Freiburg, Torino and Trieste. Also, all the results have been cross-checked by at least two people in the group. The results of this work have been published in the article "Measurement of the Collins and Sivers asymmetries on transversely polarized protons" (Alekseev et al. [COMPASS Collaboration], PLB 692 2010).

In Chap.5 the tuning of the RICH detector response and the extraction of the Collins and Sivers asymmetries on the identified pion and kaon samples is reported. This results were first shown at the SPIN 2010 conference ("Single Spin asymmetries for identified hadrons at COMPASS" G. Pesaro on behalf of the COMPASS collaboration). In Chap.6 the Collins and Sivers asymmetries extracted in Chap.s 4 and 5 are used to extract the transversity and Sivers and the transversity PDFs from the data.

Chapter 1

The transverse spin and transverse momentum structure of the nucleon

In this Chapter the theoretical and phenomenological features of transverse spin effects in semi-inclusive deep inelastic scattering (SIDIS) are reviewed.

The SIDIS cross-section is first extracted at leading order and in the frame of the quark-parton model in the collinear approach, where the three structure functions (unpolarized, longitudinally polarized and transversely polarized) are defined. Afterwards the generalization of the cross-section including the transverse momentum of the partons is presented, and the full leading order SIDIS cross-section is introduced.

A description of the effects measurable on a transversely polarized target is given, focusing on those that are nowadays considered the most important and are the most studied: the Collins and the Sivers asymmetries. A review of the status of the experiments and of the phenomenological analysis is also given, while the COMPASS results on proton will be discussed in Chap.s 4 and 5.

1.1 The Deep Inelastic Scattering

The deep inelastic scattering (DIS) of a charged lepton off a nucleon (proton or neutron) is the simplest channel to study the nucleon inner structure. The reaction is illustrated by the Feynman diagram Fig. 1.1: a lepton with 4-momentum l exchanges a virtual photon of 4-momentum q with the nucleon of 4-momentum P and mass M , represented by the full circle. The spin of the nucleon is described by the 4-vector S , such as $S^2 = -1$ and $P \cdot S = 0$. The

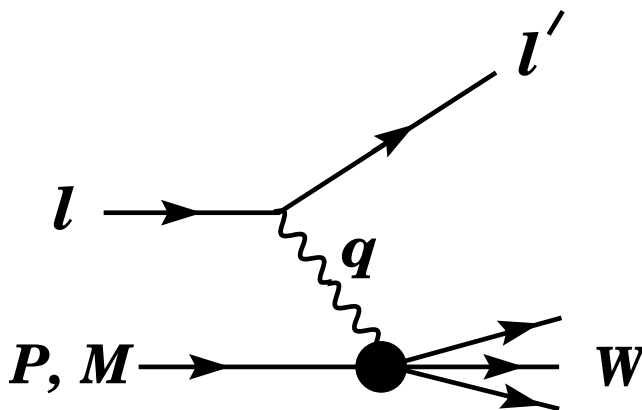


Figure 1.1: Relevant kinematic quantities in deep inelastic scattering processes. The diagram is taken from [12].

| | definition | Nucleon rest frame | |
|-------|-------------------------------|------------------------------------|--|
| ν | $\frac{q \cdot P}{M}$ | $E - E'$ | lepton's energy loss |
| Q^2 | $-q^2$ | $2(E E' - \vec{l} \cdot \vec{l}')$ | Squared momentum transfer |
| x_B | $\frac{Q^2}{2P \cdot q}$ | $\frac{Q^2}{2M\nu}$ | Bjorken scaling variable |
| y | $\frac{q \cdot P}{l \cdot P}$ | $\frac{\nu}{E}$ | Fraction of the lepton's energy |
| W^2 | $(P + q)^2$ | $M^2 + 2M\nu - Q^2$ | Squared mass of the system X |
| s | $(l + P)^2$ | $\frac{Q^2}{xy} + M^2$ | C.M. energy of the lepton-nucleon system |

Table 1.1: Definition of the invariants of the DIS reaction, neglecting the lepton mass and in the single photon exchange approximation.

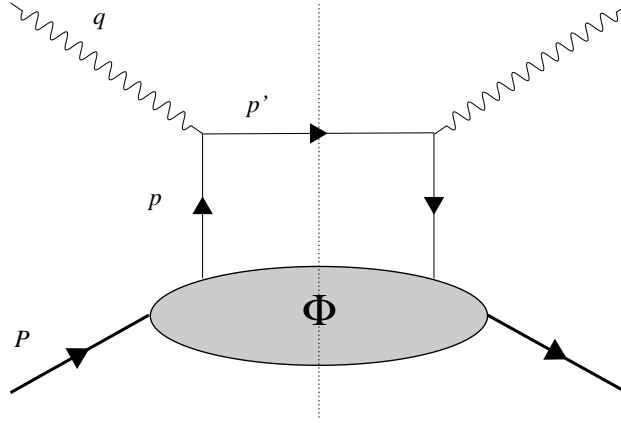


Figure 1.2: The so-called handbag diagram, representing the parton model in QCD.

momentum of the lepton in the final state is l' and W is the invariant mass of the undetected system, called X , recoiling against the scattered lepton. To measure the *inclusive* cross-section of the reaction, the integration over X is done.

The DIS reaction, in the single-photon-exchange approximation and neglecting the lepton mass, is conveniently described making use of the invariant quantities listed in Tab.1.1. In the QCD-parton model, the DIS reaction is represented by the so-called handbag diagram, shown in Fig. 1.2. The lepton scattering is described by QED, and the leptonic tensor is written as:

$$L_{\mu\nu} = \frac{1}{2} \bar{u}(l') \gamma_\mu u(l) \bar{u}(l') \gamma_\nu u(l) = 2\{l_\mu l'_\nu + l'_\mu l_\nu - g_{\mu\nu}(l \cdot l')\} \mp i2\{\epsilon_{\mu\nu\lambda\sigma} l^\lambda l'^\sigma\} = L_{\mu\nu}^{(S)} \mp L_{\mu\nu}^{(A)} \quad (1.1)$$

and has a symmetric ($L_{\mu\nu}^{(S)}$) and an antisymmetric ($L_{\mu\nu}^{(A)}$) part. The hadronic field is described by Φ , the correlation matrix, p is the momentum of the struck quark. The hadronic tensor is written in terms of the correlation matrix $\Phi(p, P; S)$:

$$W^{\mu\nu} = \sum_{quark} e_i^2 \int \frac{d^2p}{(2\pi)^4} \delta[(p+q)^2] Tr \left(\Phi \gamma^\mu (p + \not{q}) \gamma^\nu \right) \quad (1.2)$$

where the momentum is integrated over the loop. The sum over the quarks has to be intended as a sum over quarks and anti-quarks.

For simplicity the DIS cross-section in QCD is derived in the light-cone gauge ¹ (App.A), where the generic four vector is written as $a^\mu = (a^+, a^-, a_T^\vec{a})$ with $a^\pm = (a^0 \pm a^3)/\sqrt{2}$ and $a_T^\vec{a} = (a^1, a^2)$.

¹see f.i. [13] and references therein

In the presence of an hard scale, as it is in DIS the photon momentum [14, 15], the nucleon momentum fixes the direction of the base vector n_+ . Up to the order of $1/Q^2$, and in the collinear approach we have:

$$\begin{aligned} p^\mu &\simeq xP^+n_+^\mu \\ P_\mu &\simeq P^+n_+^\mu \\ q_\mu &\simeq \frac{M\nu}{P^+}n_-^\mu \end{aligned} \quad (1.3)$$

and

$$\delta[(p+q)^2] = \delta(-Q^2 + 2xP \cdot q) = \frac{1}{2P \cdot q} \delta(x - x_B). \quad (1.4)$$

In this situation the variable x can be interpreted as a fraction of the longitudinal nucleon momentum carried by the quark: $x = p^+/P^+$. Note that this interpretation is not valid at higher orders.

If we integrate the correlation matrix $\Phi(p, P, S)$ over the quark momentum p :

$$\Phi(x) = \int d^4p \Phi(p, P; S) \delta(p^+ - xP^+) = \int \frac{d\xi^-}{2\pi} e^{ixP^+ \cdot \xi^-} \langle P, S | \bar{\psi}(0) w(0, \xi) \psi(\xi) | P, S \rangle \Big|_{\xi^+=0, \vec{\xi}_T=0} \quad (1.5)$$

where the gauge link (or Wilson line) $w(0, \xi)$ for the DIS reaction has been introduced between the quark bilocal operator to restore the gauge invariance. Note that the quark index has been omitted.

At twist two² and in the collinear approach, the correlation matrix depends on three PDFs only [15] called, according to the Amsterdam notation, $f_1(x)$, $g_1(x)$ and $h_1(x)$ (the subscript 1 indicates that these are twist two):

$$\Phi(x) = \frac{1}{2} \left\{ f_1(x) \not{n}_+ + S_L g_1(x) \gamma_5 \not{n}_+ + h_1(x) \gamma_5 \frac{\not{S}_T \not{n}_+}{2} \right\} \quad (1.6)$$

where we have introduced the longitudinal ($(S_L/M)P^\mu$) and the transverse component (S_T^μ) of the polarization vector of the nucleon. The three flavour dependent PDFs can be projected out from $\Phi(x)$ by tracing Φ with the proper Dirac matrices:

$$f_1(x) = \frac{1}{2} Tr(\Phi \gamma^+) \quad (1.7)$$

$$g_1(x) = \frac{1}{2} Tr(\Phi \gamma^+ \gamma^5) \quad (1.8)$$

$$h_1(x) = \frac{1}{2} Tr(\Phi \gamma^+ \gamma_T \gamma^5) \quad (1.9)$$

In the light-cone gauge, where $w(0, \xi) = I$, the identity matrix, we have that

$$f_1(x) \sim \int d\xi^- e^{ixP^+ \xi^-} \langle pS | \psi_{(+)}^\dagger(0) I \psi_{(+)}(0) | pS \rangle. \quad (1.10)$$

$\psi_{(+)}$ is the so-called "good" component of the quark field ψ : $\psi_{(\pm)} = \frac{1}{2} \gamma^\mp \gamma^\pm \psi$. Replacing I with a full set of intermediate states $|n\rangle \langle n|$ it results that:

$$f_1(x) \sim \sum_n \delta(P^+ - xP - P_n^+) | \langle P, S | \psi_{(+)}^n(0) | n \rangle |^2 \quad (1.11)$$

²According to the operational definition given in [16], the *twist* is defined as the order in M/Q to which an effect is seen in a particular experiment: if it behaves as $(1/Q^2)^p$, the object is said to be of twist $t = 2 + 2p$. Twist 2 is also called *leading twist*

i.e. $f_1(x)$ is the probability of finding a quark with a fraction x of the nucleon momentum, historically indicated as $q(x)$.

Analogously, using the projector of the spin on its longitudinal components \mathcal{P}_{\pm} and the projector of the spin on its transverse components $\mathcal{P}_{\uparrow\downarrow}$ we have:

$$g_1(x) \sim \sum_n \delta(P^+ - xP - P_n^+) \{ | \langle P, S | \mathcal{P}_{\rightarrow} \psi_{(+)}^n(0) | n \rangle |^2 - | \langle P, S | \mathcal{P}_{\leftarrow} \psi_{(+)}^n(0) | n \rangle |^2 \} \quad (1.12)$$

$$h_1(x) \sim \sum_n \delta(P^+ - xP - P_n^+) \{ | \langle P, S | \mathcal{P}_{\uparrow} \psi_{(+)}^n(0) | n \rangle |^2 - | \langle P, S | \mathcal{P}_{\downarrow} \psi_{(+)}^n(0) | n \rangle |^2 \} \quad (1.13)$$

$g_1(x)$, called *helicity* PDF, is the difference of the probabilities to find a quark with a fraction x of the longitudinal momentum with the spin parallel or anti-parallel to the nucleon spin in a longitudinally polarized nucleon. In another commonly used notation $g_1(x) = \Delta q(x)$. $h_1(x)$, called *transversity* PDF, is the difference of the probabilities to find a quark with a fraction x of the longitudinal momentum with the polarization parallel or anti-parallel to the nucleon spin in a transversely polarized nucleon. It is also represented by the symbol $\Delta_T q(x)$.

1.1.1 The DIS cross-section

The DIS differential cross-section is [17]:

$$\frac{d^2\sigma}{dxdy} \propto [L_{\mu\nu}^{(S)} W^{\mu\nu(S)} - L_{\mu\nu}^{(A)} W^{\mu\nu(A)}] \quad (1.14)$$

where only the antisymmetric part of the tensors depends on the nucleon spin. The cross-section can then be decomposed in an unpolarized part:

$$\frac{d^2\sigma_{unpol}}{dxdy} \propto \sum_{quark} e_q^2 f_1^q(x) \frac{d^2\sigma^{lq \rightarrow lq}}{dxdy} \quad (1.15)$$

and the polarized one:

$$\frac{d^2\sigma_{pol}}{dxdy} \propto P_L P_{beam} \sum_{quark} e_q^2 g_1^q(x) \frac{d^2\sigma^{lq \rightarrow lq}}{dxdy} \quad (1.16)$$

that depends on the longitudinal polarization of the nucleon (P_L) and on the longitudinal polarization of the beam (P_{beam}). In a DIS experiment, the structure functions $F_2(x)$ and $g_1^N(x)$ are measured, that are related to the PDFs as:

$$\begin{aligned} F_2(x) &= x \sum_{quark} e_q^2 f_1^q(x) \\ g_1^N(x) &= \frac{1}{2} \sum_{quark} e_q^2 g_1^q(x). \end{aligned} \quad (1.17)$$

A collection of recent results, without meaning of completeness, is shown in Fig. 1.3 for measurements of $F_2(x)$ done on proton and on deuteron targets and in Fig. 1.4 for the measurements of g_1^N on proton, deuteron and neutron targets. From the measurement of the structure function on different targets it is possible to extract the flavour-separated PDFs from the experimental data.

The measured values of the structure function show a logarithmic dependence on Q^2 . At a given Q^2 the photon resolves only a given number of partons, but, at a higher value of Q^2

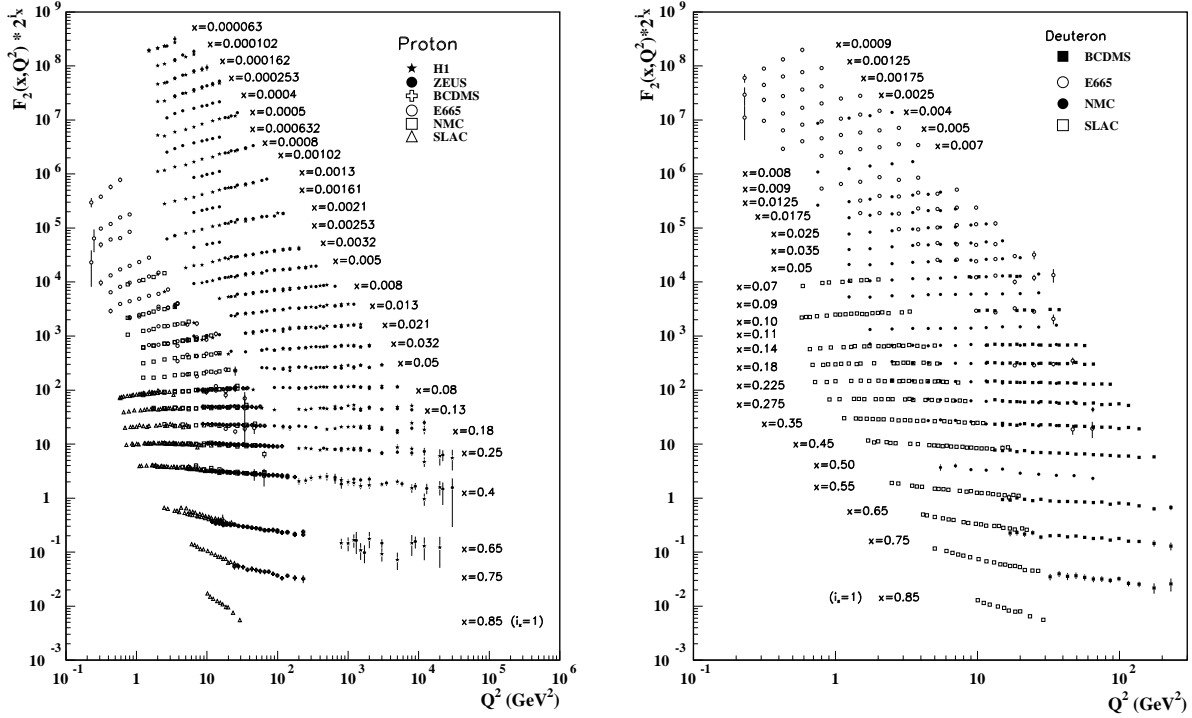


Figure 1.3: The proton structure function F_2^p and the deuteron structure function F_2^d [12].

it sees the quark surrounded by a cloud of partons. This quark, with a momentum fraction x comes from the parent quark with a momentum fraction y that has radiated a gluon, with a probability proportional to $\alpha_s P_{qq}\left(\frac{x}{y}\right)$. This effects can be calculated in QCD and gives rise to the "Altarelli-Parisi" evolution equation:

$$\frac{d}{d \log Q^2} q(x, Q^2) = \frac{\alpha_s}{2\pi} \int_0^1 \frac{dy}{y} q(y, Q^2) P_{qq}\left(\frac{x}{y}\right) \quad (1.18)$$

1.1.2 Transversity PDF

In a DIS reaction it is not possible to measure transversity. By definition, transversity corresponds to a process involving a quark and nucleon helicity flip: a transverse state ($|\uparrow\rangle$ or $|\downarrow\rangle$) can be written in the helicity basis ($|\rightarrow\rangle$ and $|\leftarrow\rangle$) as $|\uparrow\rangle = \frac{1}{\sqrt{2}}(|\rightarrow\rangle \pm |\leftarrow\rangle)$. The cross-section difference, from which transversity is extracted is $\sigma_{\uparrow} - \sigma_{\downarrow} = \langle \uparrow | \dots | \uparrow \rangle - \langle \downarrow | \dots | \downarrow \rangle$. With some simple algebra one gets that: $\sigma_{\uparrow} - \sigma_{\downarrow} \propto \langle \rightarrow | \dots | \leftarrow \rangle + \langle \leftarrow | \dots | \rightarrow \rangle$: the cross-section difference between the two states of polarization is proportional to the helicity flip. At leading order helicity and chirality are the same and all QCD and electroweak vertices conserve chirality: a single transverse spin flip is chirally odd and thus to measure transversity it has to be coupled with some soft process that flips the quark chirality a second time. As it is illustrated in Fig. 1.5, transversity can be measured in Drell-Yan processes or in semi-inclusive DIS reactions. In the helicity basis, transversity corresponds to both a quark and a nucleon helicity flip: this leads to the determination of the so-called Soffer bound [19]:

$$|h_1(x)| < \frac{1}{2}[f_1(x) + g_1(x)]. \quad (1.19)$$

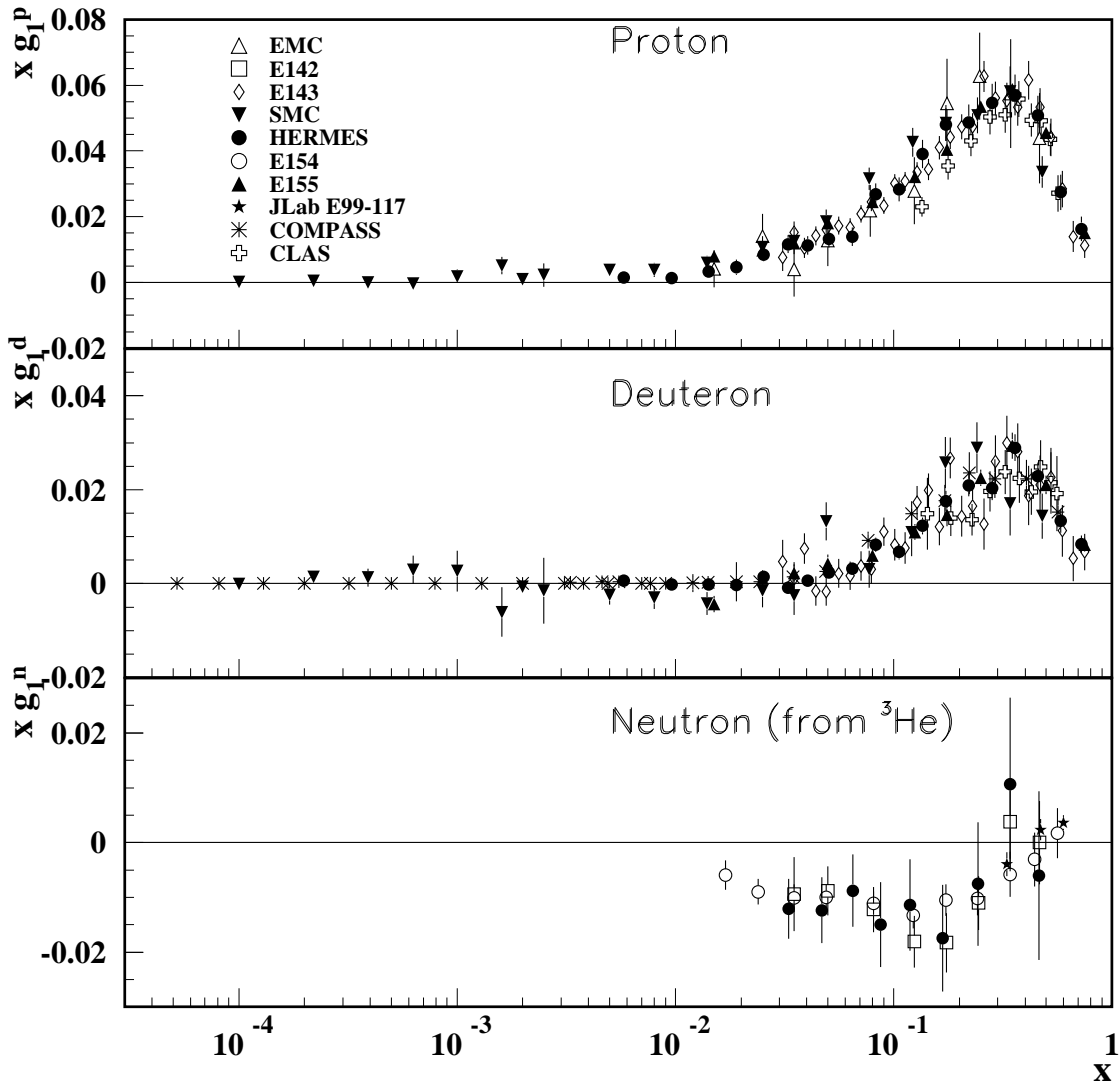


Figure 1.4: The spin-dependent structure function for the proton, g_1^p , the deuteron, g_1^d , and the neutron, g_1^n (^3He targets) [12]. Q^2 ranges from 0.001 to 100 GeV^2 .

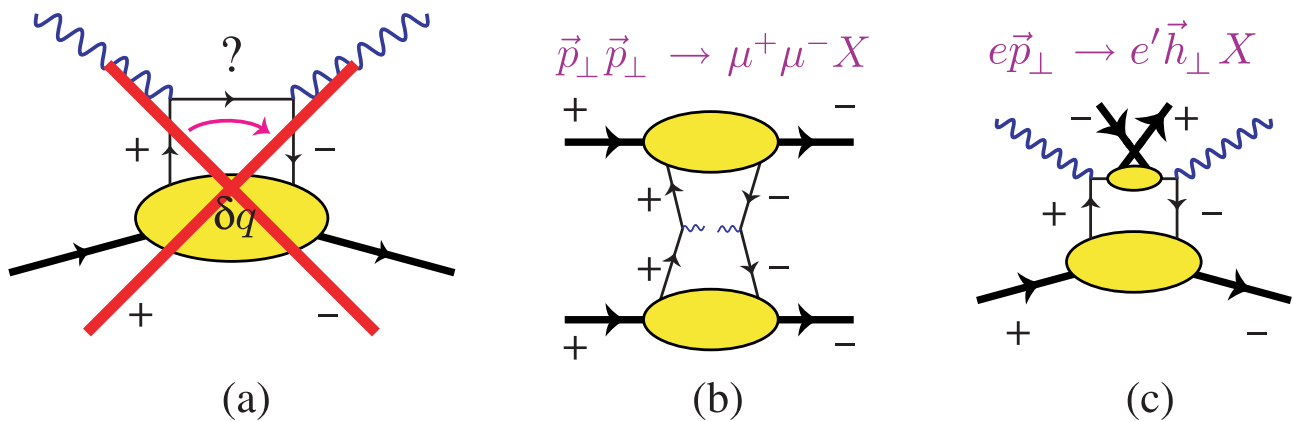


Figure 1.5: Deep inelastic processes relevant to transversity [18]. QCD and electroweak processes preserve chirality: in order to access transversity some soft process must flip the quark chirality a second time. Transversity can be accessed in Drell-Yan reaction (b), with two transversely polarised protons (\vec{p}_\perp) or in SIDIS (c).

Another property of transversity is that there is no gluon transversity distribution [13]; this is because the gluons have helicity ± 1 and in a gluon-nucleon helicity-flip, the nucleon should go to a two-units helicity flip, that is impossible: the $h_1(x)$ evolution equation is different from the $g_1(x)$ one, since there is no gluon transversity and thus no mixing of the two is possible. As a consequence, at low x , $h_1(x)$ is suppressed in the evolution with respect to $g_1(x)$. Despite the fact that helicity and transversity are the same in the non-relativistic limit, in the general case it has to be noted that transversity is a measure of the quark polarization inside a transversely polarized nucleon, and not of the transverse spin. The transverse spin has no partonic interpretation as is associated to the twist-3 structure function g_2 that vanishes at high Q^2 [20]. The tensor charge, that is obtained from the forward matrix element of the operator $\psi_f^\dagger \sigma^{\mu\nu} \psi_f$ is given by:

$$\delta q = \int_0^1 dx (h_{q1}(x) - h_{\bar{q}1}(x)) \quad (1.20)$$

and it can be identified with the transversity of the valence quarks only [19].

1.1.3 The non collinear approach

If the transverse momentum of the quark \vec{p}_T is considered, than $\Phi^q(x, p_T^2)$, the integral of the correlation matrix Φ over p^+ and p^- [15] is:

$$\Phi(x, p_T^2) \propto \int d\xi^- \int d^2\xi_T^+ e^{ixp^+\xi^- - i\vec{p}_T \cdot \vec{\xi}_T} \langle PS | \bar{\psi}(0) w(0, \xi) \psi(\xi) | PS \rangle |_{\xi^+=0} \quad (1.21)$$

It can be parametrized using as a base the combinations of the vectors P , q , S and p_T . The independent combinations of these vectors are 8 and each of them is associated with one transverse momentum dependent (TMD) PDF:

$$f_1, f_{1T}^\perp, g_1, g_{1T}, h_1, h_{1L}^\perp, h_{1T}^\perp, h_1^\perp.$$

The names of the PDFs are chosen according to the Amsterdam notation: f refers to unpolarized quarks, g refers to quarks polarized longitudinally and h refers to quarks polarized transversely. Tracing the propagator with the proper Dirac matrix, one can extract the probabilities to find a quark unpolarized ($\Phi^{[\gamma^+]}$), longitudinally polarized ($\Phi^{[\gamma^+\gamma^5]}$) or transversely

polarized ($\Phi^{[i\sigma^i+\gamma^5]}$):

$$\Phi^{[\gamma^+]} = f_1(x, p_T^2) - \frac{\epsilon_T^{ij} p_{Ti} S_{Tj}}{M} f_{1T}^\perp(x, p_T^2) \quad (1.22)$$

$$\Phi^{[\gamma^+\gamma^5]} = S_L g_1(x, p_T^2) + \frac{\vec{p}_T \cdot \vec{S}_T}{M} g_{1T}(x, p_T^2) \quad (1.23)$$

$$\Phi^{[i\sigma^i+\gamma^5]} = S_T^i h_1(x, p_T^2) + S_L \frac{p_T^i}{M} h_{1L}^\perp(x, p_T^2) - \frac{p_T^i p_T^j + \frac{1}{2} p_T^2 g_T^{ij}}{M^2} S_{Tj} h_{1T}^\perp(x, p_T^2) - \frac{\epsilon_T^{ij} p_{Tj}}{M} h_1^\perp(x, p_T^2) \quad (1.24)$$

The subscripts L, T describe the polarization of the parent nucleon spin. Upon integration over p_T^2 , only three TMD PDFs survive: f_1 , g_1 and h_1 , the previously introduced number density, helicity and transversity PDFs. The PDFs are ordered according to their physical meaning in the following table:

| | | quark | | |
|---------|---|----------------------------------|---------------------------------|---|
| | | U | L | T |
| nucleon | U | $f_1(x, p_T)$ | | $h_1^\perp(x, p_T)$ Boer-Mulders |
| | L | | $g_1(x, p_T)$ | $h_{1L}^\perp(x, p_T)$ Worm-gear 1 |
| | T | $f_{1T}^\perp(x, p_T)$ Sivers | $g_{1T}(x, p_T)$ Worm-gear 2 | $h_1(x, p_T)$ Transversity $h_{1T}^\perp(x, p_T)$ Pretzelosity |

The PDFs that depends on the transverse polarization of the quark are all chiral-odd. Both Boer-Mulders and Sivers PDFs are T-odd, which means that they change sign under "naive time reversal", which is defined as usual time reversal but without interchange between the initial and final state. An appropriate application of time reversal changes the shape of the gauge link: the gauge link depends on the specific process, thus the time reversal changes a reaction in a different one. As an example, time reversal applied to the SIDIS Sivers PDF transforms it into minus the PDF of the Drell-Yan process [15].

1.2 The Semi-inclusive DIS cross-section

In a semi-inclusive DIS (SIDIS) reaction, at least one of the hadrons produced from the fragmentation of the nucleon is detected in the final state. The hadron carries a momentum P_h and its mass is M_h . The relativistic invariant

$$z = \frac{P \cdot P_h}{P \cdot q} \quad (1.25)$$

represents the fraction of energy of the quark that is carried by the detected hadron after the fragmentation. In the following we will assume that the detected hadron comes from the fragmentation of the struck quark. Experimentally this condition can be achieved with a cut on the minimum value of the variable z , that selects the hadrons coming from the struck quark from those coming from the fragmentation of the target remnants. The SIDIS reaction is described in the target rest frame (that, in a fixed target experiment, corresponds to the laboratory frame) and the definitions of the angles are shown in Fig.1.6, according to the "Trento convention" [21]. The QCD diagram that represents the SIDIS reaction at leading order is shown in Fig.1.7. From the nucleon hadronic field Φ emerges a quark with momentum p . The fragmentation correlator Δ represents the fragmentation of the quark into a hadron with momentum P_h . The lightcone directions n_+ and n_- in SIDIS are defined (up to mass corrections of the order of

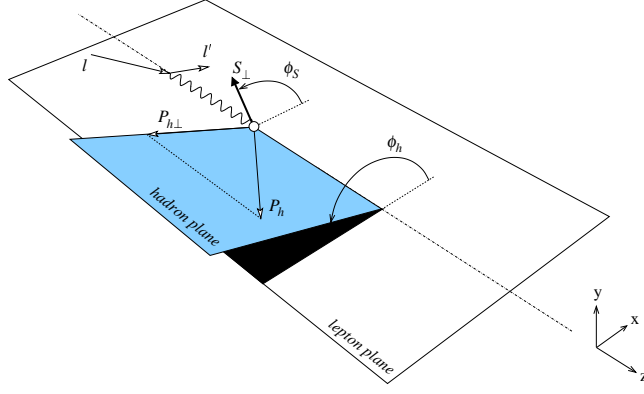


Figure 1.6: Definition of azimuthal angles for semi-inclusive deep inelastic scattering in the target rest frame [22], according to the Trento convention [21]. The z axis is given by the photon direction and the lepton-scattering plane defines the $x - z$ plane.

$1/Q^2$ [14]) as:

$$\begin{aligned}
 P^\mu &= \frac{xM^2}{Q^2\sqrt{2}}n_-^\mu + \frac{Q^2}{xM^2\sqrt{2}}n_+^\mu \\
 P_h^\mu &= \frac{zQ^2}{\sqrt{2}}n_-^\mu + \frac{M_h^2}{zQ^2\sqrt{2}}n_+^\mu \\
 q^\mu &= \frac{Q^2}{\sqrt{2}}n_-^\mu - \frac{Q^2}{\sqrt{2}}n_+^\mu + q_T^\mu
 \end{aligned} \tag{1.26}$$

The vector $q_T^\mu \simeq q^\mu + xP^\mu - P_h^\mu/z$ determines the off-collinearity of the process; in the frame where the nucleon and the photon are collinear, $\vec{q}_T \simeq -\vec{P}_T^h/z$. The momentum fractions $x = \frac{p^+}{P^+}$ and $z = \frac{P_h^-}{k^-}$ are identified with the scaling variable and the energy fraction. The hadronic tensor is:

$$2MW^{\mu\nu} = \frac{1}{(2\pi)^3} \sum_X \int \frac{d^3P_X}{2P_X^0} \delta^{(4)}(q + P - P_X - P_h) \langle P | J^\mu(0) | h, X \rangle \langle h, X | J^\nu(0) | P \rangle, \tag{1.27}$$

where X is the undetected hadronic state. The p and k vectors of Fig.1.7 are written as:

$$\begin{aligned}
 p^\mu &= p^- n_-^\mu + xP^+ n_+^\mu + p_T^\mu \\
 k^\mu &= \frac{P_h^-}{z} n_-^\mu + k^+ n_+^\mu + k_T^\mu
 \end{aligned} \tag{1.28}$$

In the leading order approximation:

$$2MW^{\mu\nu} = 2z \sum_{quarks} e_i^2 \mathcal{C} \left[\text{Tr}[\Phi^q(x, p_T) \gamma^\mu \Delta^q(x, k_T) \gamma^\nu] \right] \tag{1.29}$$

where the symbol \mathcal{C} indicates that the trace is integrated over the transverse components \vec{p}_T and \vec{k}_T with the constraint $\vec{k}_T = \vec{p}_T + \vec{q}_T = \vec{p}_T - \frac{P_T^h}{z}$.

The fragmentation correlator $\Delta^q(x, k_T)$ can be parametrized [22, 23] with the same technique that is used to parametrize the field correlator $\Phi(x, p_T)$. It has to be noted that the fragmentation function (FF) is a probability density w.r.t. the transverse momentum $k_T' = -zk_T$ of the final state hadron relative to the fragmenting quark. For a spinless hadron and at leading twist, it is function of two fragmentation FF:

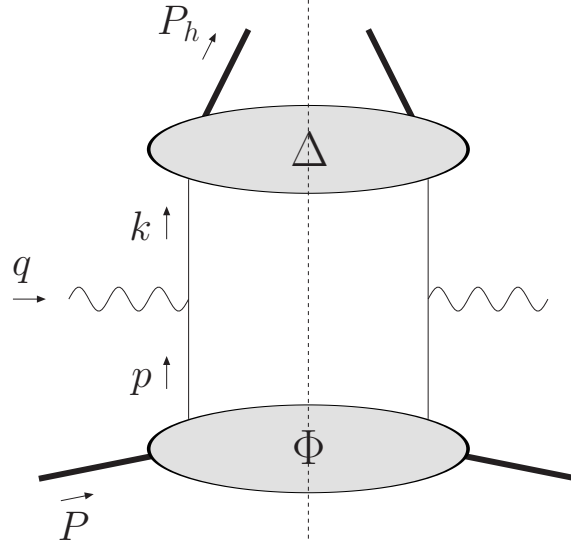


Figure 1.7: Leading order contribution to SIDIS [22]. Φ is the correlator for the quark distribution, Δ for the quark fragmentation.

$$D_1^q(z, k_T^2), H_1^{\perp q}(z, k_T^2)$$

$D_1^q(z, k_T^2)$ is the fragmentation function of an unpolarized quark into an unpolarized hadron, while $H_1^{\perp q}(z, k_T^2)$, called the Collins FF is the difference of the FF of a quark with transverse polarization upwards and the FF of a quark with polarization downwards into an unpolarized hadron.

Both Φ and Δ have been parametrized up to twist-3 level [22], using 16 more PDFs and 4 more FF. The SIDIS cross-section, up to twist-3 level, in the laboratory frame is:

$$\begin{aligned} \frac{d\sigma}{dx dy dz d\phi_h dP_{h\perp}^2} = & \frac{\alpha^2}{xyQ^2} \frac{y^2}{2(1-\epsilon)} \left(1 + \frac{\gamma^2}{2x}\right) \left\{ \right. \\ & F_{UU,T} + \epsilon F_{UU,L} + \sqrt{2\epsilon(1+\epsilon)} \cos\phi_h F_{UU}^{\cos\phi_h} \\ & + \epsilon \cos(2\phi_h) F_{UU}^{\cos 2\phi_h} + P_{\text{beam}} \sqrt{2\epsilon(1-\epsilon)} \sin\phi_h F_{LU}^{\sin\phi_h} \\ & + P_L \left[\sqrt{2\epsilon(1+\epsilon)} \sin\phi_h F_{UL}^{\sin\phi_h} + \epsilon \sin(2\phi_h) F_{UL}^{\sin(2\phi_h)} \right] \\ & + P_L P_{\text{beam}} \left[\sqrt{1-\epsilon^2} F_{LL} + \sqrt{2\epsilon(1-\epsilon)} \cos\phi_h F_{LL}^{\cos\phi_h} \right] \\ & + |P_T| \left[\sin(\phi_h - \phi_S) (F_{UT,T}^{\sin(\phi_h - \phi_S)} + \epsilon F_{UT,L}^{\sin(\phi_h - \phi_S)}) \right. \\ & + \epsilon \sin(\phi_h + \phi_S) F_{UT}^{\sin(\phi_h + \phi_S)} + \epsilon \sin(3\phi_h - \phi_S) F_{UT}^{\sin(3\phi_h - \phi_S)} \\ & + \sqrt{2\epsilon(1+\epsilon)} \sin\phi_S F_{UT}^{\sin\phi_S} \\ & \left. + \sqrt{2\epsilon(1+\epsilon)} \sin(2\phi_h - \phi_S) F_{UT}^{\sin(2\phi_h - \phi_S)} \right] \\ & + |P_T| P_{\text{beam}} \left[\sqrt{1-\epsilon^2} \cos(\phi_h - \phi_S) F_{LT}^{\cos(\phi_h - \phi_S)} \right. \\ & + \sqrt{2\epsilon(1-\epsilon)} \cos\phi_S F_{LT}^{\cos\phi_S} \\ & \left. + \sqrt{2\epsilon(1-\epsilon)} \cos(2\phi_h - \phi_S) F_{LT}^{\cos(2\phi_h - \phi_S)} \right] \left. \right\} \end{aligned} \quad (1.30)$$

where α is the fine structure constant. 18 structure functions are thus needed to parametrize the cross-section, that is composed by three main parts: the unpolarized cross-section, which structure functions have the sub-script UU , the longitudinal part in which the structure functions depends on the longitudinal polarization of the beam (LU), of the target (UL), or of both (LL) and the part that depends on the transverse polarization of the target, measurable with unpolarized beam (UT), or with the beam longitudinally polarized (LT). Each structure function corresponds to a different modulation, function of a combination of the azimuthal angles ϕ_h and ϕ_s . ϵ is the ratio between the longitudinal and the transverse photon flux:

$$\epsilon = \frac{1 - y - \frac{1}{4}\gamma^2 y^2}{1 - y + \frac{1}{2}y^2 + \frac{1}{4}\gamma^2 y^2} \quad (1.31)$$

The kinematical depolarization factors corresponding to the different modulations are reported in the following table, neglecting the contribution suppressed by the γ factor:

| | |
|---|---|
| $F_{UU,T}, F_{UU,T}^{\sin \phi_h, \phi_s}$ | $\frac{y^2}{2(1-\epsilon)} \approx (1 - y + \frac{1}{2}y^2)$ |
| $F_{UU,L}, F_{UU}^{\cos 2\phi_h}, F_{UU}^{\sin 2\phi_h}, F_{UT,L}^{\sin(\phi_h - \phi_s)}, F_{UT}^{\sin(\phi_h + \phi_s)}, F_{UT}^{\sin(3\phi_h - \phi_s)}$ | $\frac{y^2}{2(1-\epsilon)} \epsilon \approx (1 - y)$ |
| $F_{UU}^{\cos \phi_h}, F_{UL}^{\sin \phi_h}, F_{UT}^{\sin \phi_s}, F_{UT}^{\sin(2\phi_h - \phi_s)}$ | $\frac{y^2}{2(1-\epsilon)} \sqrt{2\epsilon(1+\epsilon)} \approx (2 - y) \sqrt{1 - y}$ |
| $F_{LU}^{\sin \phi_h}, F_{LL}^{\cos \phi_h}, F_{LT}^{\cos \phi_s}, F_{LT}^{\cos(2\phi_h - \phi_s)}$ | $\frac{y^2}{2(1-\epsilon)} \sqrt{2\epsilon(1-\epsilon)} \approx y \sqrt{1 - y}$ |
| $F_{LL}, F_{LT}^{\cos(\phi_h - \phi_s)}$ | $\frac{y^2}{2(1-\epsilon)} \sqrt{1 - \epsilon^2} \approx y (1 - \frac{1}{2}y)$ |

Each structure function is the convolution of some PDF with some fragmentation function, and their complete expression is reported in Tab.1.2 [22], where the quark flavour index has been omitted.

1.3 Transversity

One possible channel to access $h_1(x)$ is to measure the amplitude of the $\sin(\phi_h + \phi_s)$ modulation (the Collins asymmetry) from the SIDIS cross-section (Eq.1.30). All the terms that does not depend on the transverse polarization of the target are cancelled when making the cross-section difference of the states with opposite orientation of the polarization. It is possible to define the cross-section asymmetry:

$$\begin{aligned} \frac{\sigma^\uparrow - \sigma^\downarrow}{\sigma^\uparrow + \sigma^\downarrow} = & A^{\sin(\phi_h - \phi_s)} \sin(\phi_h - \phi_s) + A^{\sin(\phi_h + \phi_s)} \sin(\phi_h + \phi_s) \\ & + A^{\sin(2\phi_h - \phi_s)} \sin(2\phi_h - \phi_s) + A^{\sin(3\phi_h - \phi_s)} \sin(3\phi_h - \phi_s) \\ & + A^{\sin(\phi_s)} \sin(\phi_s) + A^{\cos(\phi_h - \phi_s)} \cos(\phi_h - \phi_s) \\ & + A^{\cos(2\phi_h - \phi_s)} \cos(2\phi_h - \phi_s) + A^{\cos(\phi_s)} \cos(\phi_s). \end{aligned} \quad (1.32)$$

The modulations are orthogonal, thus can be extracted independently from the same data set. For the Collins modulation, integrating over the other angles, we have that:

$$A^{\sin(\phi_h + \phi_s)} = \frac{1 - y}{1 - y - \frac{1}{2}y^2} P_T A_{Coll}. \quad (1.33)$$

where the Collins asymmetry is:

$$A_{Coll} = \frac{F_{UT}^{\sin(\phi_h + \phi_s)}}{F_{UU}} = \frac{\sum_q e_q^2 h_{1q}(x, p_T) \otimes H_1^{\perp q}(z, k_T)}{\sum_q e_q^2 f_q(x, p_T) \otimes D_1^q(z, k_T)} \quad (1.34)$$

| twist-2 structure functions | |
|--|--|
| unpolarized beam and target | $F_{UU,T} = \mathcal{C}[f_1 D_1]$ $F_{UU}^{\cos 2\phi} = \mathcal{C} \left[-\frac{2(\hat{h}\cdot k_T)(\hat{h}\cdot p_T) - k_T\cdot p_T}{MM_h} h_1^\perp H_1^\perp \right]$ |
| longitudinally polarized beam and/or target | $F_{UL}^{\sin 2\phi_h} = \mathcal{C} \left[-\frac{2(\hat{h}\cdot k_T)(\hat{h}\cdot p_T) - k_T\cdot p_T}{MM_h} h_{1L}^\perp H_1^\perp \right]$ $F_{LL} = \mathcal{C}[g_{1LD_1}]$ |
| transversely polarized target | $F_{UT,T}^{\sin(\phi_h - \phi_s)} = \mathcal{C} \left[-\frac{\hat{h}\cdot p_T}{M} f_{1T}^\perp D_1 \right]$ $F_{UT}^{\sin(\phi_h + \phi_s)} = \mathcal{C} \left[-\frac{\hat{h}\cdot k_T}{M_h} h_1 H_1^\perp \right]$ $F_{UT}^{\sin(3\phi_h - \phi_s)} = \mathcal{C} \left[\frac{2(\hat{h}\cdot p_T)(p_T\cdot k_T) + p_T^2(\hat{h}\cdot k_T) - 4(\hat{h}\cdot p_T)^2(\hat{h}\cdot k_T)}{2M^2 M_h} h_{1T}^\perp H_1^\perp \right]$ $F_{LT}^{\cos(\phi_h - \phi_s)} = \mathcal{C} \left[\frac{\hat{h}\cdot p_T}{M} g_{1T} D_1 \right]$ |
| twist-3 structure functions | |
| unpolarized beam and target | $F_{UU,L} = 0$ $F_{UU}^{\cos \phi} = \frac{2M}{Q} \mathcal{C} \left[-\frac{\hat{h}\cdot k_T}{M_h} \left(x h H_1^\perp + \frac{M_h}{M} f_1 \frac{\tilde{D}^\perp}{z} \right) - \frac{\hat{h}\cdot p_T}{M} \left(x f^\perp D_1 + \frac{M_h}{M} h_1^\perp \frac{\tilde{H}}{z} \right) \right]$ |
| longitudinally polarized beam and/or target | $F_{LU}^{\sin \phi_h} = \frac{2M}{Q} \mathcal{C} \left[-\frac{\hat{h}\cdot k_T}{M_h} \left(x e H_1^\perp + \frac{M_h}{M} f_1 \frac{\tilde{G}^\perp}{z} \right) + \frac{\hat{h}\cdot p_T}{M} \left(x g^\perp D_1 + \frac{M_h}{M} h_1^\perp \frac{\tilde{E}}{z} \right) \right]$ $F_{UL}^{\sin \phi_h} = \frac{2M}{Q} \mathcal{C} \left[-\frac{\hat{h}\cdot k_T}{M_h} \left(x h_L H_1^\perp + \frac{M_h}{M} g_{1L} \frac{\tilde{G}^\perp}{z} \right) + \frac{\hat{h}\cdot p_T}{M} \left(x f_L^\perp D_1 - \frac{M_h}{M} h_{1L}^\perp \frac{\tilde{H}}{z} \right) \right]$ $F_{LL}^{\cos \phi_h} = \frac{2M}{Q} \mathcal{C} \left[\frac{\hat{h}\cdot k_T}{M_h} \left(x e_L H_1^\perp - \frac{M_h}{M} g_{1L} \frac{\tilde{D}^\perp}{z} \right) - \frac{\hat{h}\cdot p_T}{M} \left(x g_L^\perp D_1 + \frac{M_h}{M} h_{1L}^\perp \frac{\tilde{E}}{z} \right) \right]$ |
| transversely polarized target | $F_{UT,L}^{\sin(\phi_h - \phi_s)} = 0$ $F_{UT}^{\sin \phi_s} = \frac{2M}{Q} \mathcal{C} \left\{ \left(x f_T D_1 - \frac{M_h}{M} h_1 \frac{\tilde{H}}{z} \right) - \frac{k_T\cdot p_T}{2MM_h} \left[\left(x h_T H_1^\perp + \frac{M_h}{M} g_{1T} \frac{\tilde{G}^\perp}{z} \right) - \left(x h_T^\perp H_1^\perp - \frac{M_h}{M} f_{1T}^\perp \frac{\tilde{D}^\perp}{z} \right) \right] \right\}$ $F_{UT}^{\sin(2\phi_h - \phi_s)} = \frac{2M}{Q} \mathcal{C} \left\{ \frac{2(\hat{h}\cdot p_T)^2 - p_T^2}{2M^2} \left(x f_T^\perp D_1 - \frac{M_h}{M} h_{1T}^\perp \frac{\tilde{H}}{z} \right) - \frac{2(\hat{h}\cdot k_T)(\hat{h}\cdot p_T) - k_T\cdot p_T}{2MM_h} \left[\left(x h_T H_1^\perp + \frac{M_h}{M} g_{1T} \frac{\tilde{G}^\perp}{z} \right) + \left(x h_T^\perp H_1^\perp - \frac{M_h}{M} f_{1T}^\perp \frac{\tilde{D}^\perp}{z} \right) \right] \right\}$ $F_{LT}^{\cos \phi_s} = \frac{2M}{Q} \mathcal{C} \left\{ -\left(x g_T D_1 + \frac{M_h}{M} h_1 \frac{\tilde{E}}{z} \right) + \frac{k_T\cdot p_T}{2MM_h} \left[\left(x e_T H_1^\perp - \frac{M_h}{M} g_{1T} \frac{\tilde{D}^\perp}{z} \right) + \left(x e_T^\perp H_1^\perp + \frac{M_h}{M} f_{1T}^\perp \frac{\tilde{G}^\perp}{z} \right) \right] \right\}$ $F_{LT}^{\cos(2\phi_h - \phi_s)} = \frac{2M}{Q} \mathcal{C} \left\{ -\frac{2(\hat{h}\cdot p_T)^2 - p_T^2}{2M^2} \left(x g_T^\perp D_1 + \frac{M_h}{M} h_{1T}^\perp \frac{\tilde{E}}{z} \right) + \frac{2(\hat{h}\cdot k_T)(\hat{h}\cdot p_T) - k_T\cdot p_T}{2MM_h} \left[\left(x e_T H_1^\perp - \frac{M_h}{M} g_{1T} \frac{\tilde{D}^\perp}{z} \right) - \left(x e_T^\perp H_1^\perp + \frac{M_h}{M} f_{1T}^\perp \frac{\tilde{G}^\perp}{z} \right) \right] \right\}$ |

Table 1.2: Structure function appearing in the SIDIS cross-section at twist-2 and twist-3 level.

The versor $\hat{h} = \frac{\vec{P}_T^h}{|\vec{P}_T^h|}$ [22]. The quark flavour index has been omitted.

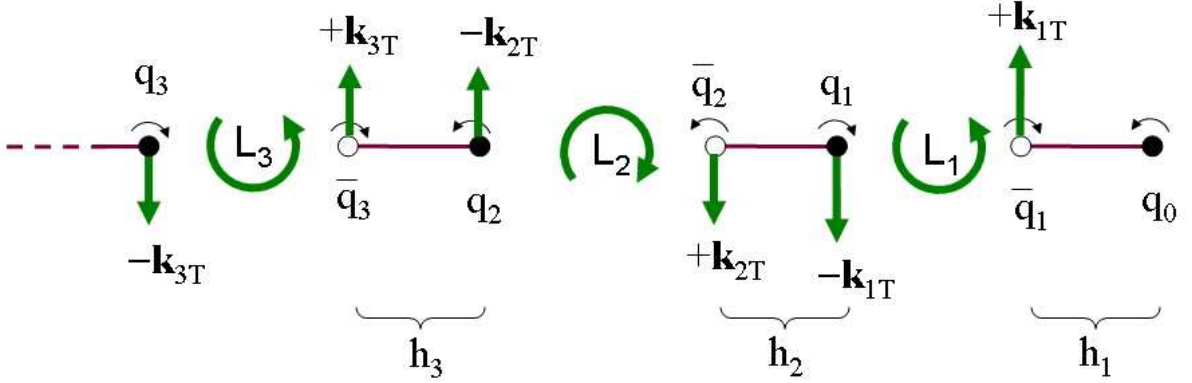


Figure 1.8: A string decaying into a pseudoscalar meson [24]. q_0 is polarized towards the reader, as indicated by the circular arrow.

1.3.1 The Collins fragmentation function

The fragmentation of a transversely polarized quark into an unpolarized hadron is described by the so-called Collins FF, denoted as $H_1^\perp(z, k_T^2)$.

The fragmentation of the polarized quarks is asymmetric: the difference between the fragmentation of the quarks polarized upwards with transverse momentum k_T and that of the quarks polarized downwards with transverse momentum $-k_T$ depends on the spin vector of the fragmenting quark:

$$D_1^{q\uparrow}(z, k_T) - D_1^{q\downarrow}(z, -k_T) = 2 \frac{(\hat{p} \times \vec{k}_T) \cdot \vec{S}'_{qT}}{zM_h} H_1^\perp(z, k_T). \quad (1.35)$$

Assume that the parton spin is polarized "upwards": then the hadron is emitted preferentially to the left side with respect to the quark.

The Lund string model

An interpretation of the Collins effect is given by Artru [24] in the framework of the string model. A massive string decays and a $q\bar{q}$ pair is created: in first approximation, the transverse hadron momentum comes from the internal angular momentum of the pair inside the string. In this model it is assumed that the pair comes on-shell in the 3P_0 state, which has the vacuum quantum number: the relative position of the $q\bar{q}$ pair is $\vec{r} \equiv \vec{r}(q) - \vec{r}(\bar{q})$, along $-\hat{z}$ (Fig. 1.8), the relative momentum is $\vec{k}(q) = -\vec{k}(\bar{q})$ and the orbital angular momentum is such as $\hat{z} \cdot [\vec{k}_T \times \vec{L}] < 0$. In a 3P_0 state $s(q) = s(\bar{q}) = -L/2$, thus the transverse spin of q and \bar{q} are correlated to their transverse momenta: $\hat{z} \cdot [\vec{k}_T \times \vec{s}(q)] > 0$ and $\hat{z} \cdot [\vec{k}_T \times \vec{s}(\bar{q})] < 0$.

When a pseudoscalar meson is produced ($s(q_0) = -s(\bar{q}_1)$), the transverse momentum of the hadron, p_T^h , is equal to the transverse momentum of the fragmenting quark, k_T : $\vec{k}_T(\bar{q}_1) = \vec{p}_T^h(h_1)$ (Fig. 1.8). Assuming that q_0 is polarized towards the reader, then the leading hadron is emitted to the left side.

1.3.2 Experimental results

The measurement of the transversity PDF coupled with the Collins FF (the Collins asymmetry) has been performed by the HERMES (DESY) [25], COMPASS (CERN) [9, 26], and HallA

(JLab) [27] experiments, in different kinematical ranges and on different targets, and the results will be presented in the following in a chronological order. The COMPASS results on proton, topic of this Thesis, will be discussed in Chap.s 4 and 5.

The HERMES experiment run in transverse configuration in the years 2002-2005, and scattered 27.6 GeV positrons off a gaseous polarized proton target. The measured Collins asymmetry is shown in Fig 1.9 for identified π and K [25]. The Collins amplitudes for pions are different from zero and increase in magnitude with x . The Collins amplitude for π^+ is positive, while it is negative for π^- . The Collins asymmetry for positive kaons is positive and larger than the corresponding asymmetry for pions, while the K^- asymmetry is compatible with zero. This is the first evidence that both the transversity PDF and the Collins FF are different from zero.

The COMPASS experiment run in transverse target configuration in the years 2002-2004 with a deuteron target and in year 2007 with a proton target, using a 160 GeV muon beam. The Collins asymmetries on deuteron [7, 8, 9] have been found to be compatible with zero both for pions and for kaons, while the Collins asymmetries on proton for charged hadrons (mainly pions) [28, 26], have been found to be different from zero and of opposite sign for positive and negative hadrons, as it will be discussed in Chap. 4. It has to be stressed here that the COMPASS and HERMES experiment uses a different definition of the Collins angle: in HERMES the so-called Trento-convention is used, $\phi_{Coll} = \phi_h + \phi_s$, while COMPASS uses the original definition $\phi_{Coll} = \phi_h + \phi_s - \pi$, thus the resulting sign of the measured asymmetries is opposite. The COMPASS and HERMES results on proton are compatible, despite the different average Q^2 at which the two experiments measure. The asymmetry measured on the deuteron target, together with the asymmetry different from zero measured on the proton target indicates that the transversity of the u and the d quark are of the same size and opposite sign.

The JLab-HallA experiment E06-010 has measured single spin asymmetries with a 6 GeV electron beam over a polarized Helium target [27]. The preliminary Collins asymmetries on Helium are compatible with zero.

The Collins FF decoupled from $h_1(x)$ is measured at the e^+e^- collider experiment BELLE. The azimuthal modulation in the hadron distribution due to the Collins effect is measurable if referred to an axis, as the polarization vector in SIDIS. Since in BELLE there is no such a reference axis, the effect averages to zero. The Collins effect can be observed combining the fragmentation of the quark and the anti-quark of the pair: the two FF give rise to a modulation that depends on the sum of the two azimuthal angles of the produced hadrons with respect to the scattering plane. The size of the measured amplitude is proportional to the convolution of the two Collins FF. The measured asymmetries (Fig. 1.10) show that the Collins FF is different from zero.

1.3.3 The extraction of $h_1(x)$

Given the experimental results presented in the previous Section, it is possible to perform a global fit of all the data to simultaneously extract the transversity PDF and the Collins FF. The global fit of the Torino-group [30] is presented in the following; the analysis used the preliminary HERMES proton data, the COMPASS deuteron data and the BELLE data. The COMPASS proton data were not published at the time of the analysis.

The fit assumes the universality of the Collins function entering SIDIS and e^+e^- processes, and rescales the results of the different experiment to a common value of Q^2 , assuming for

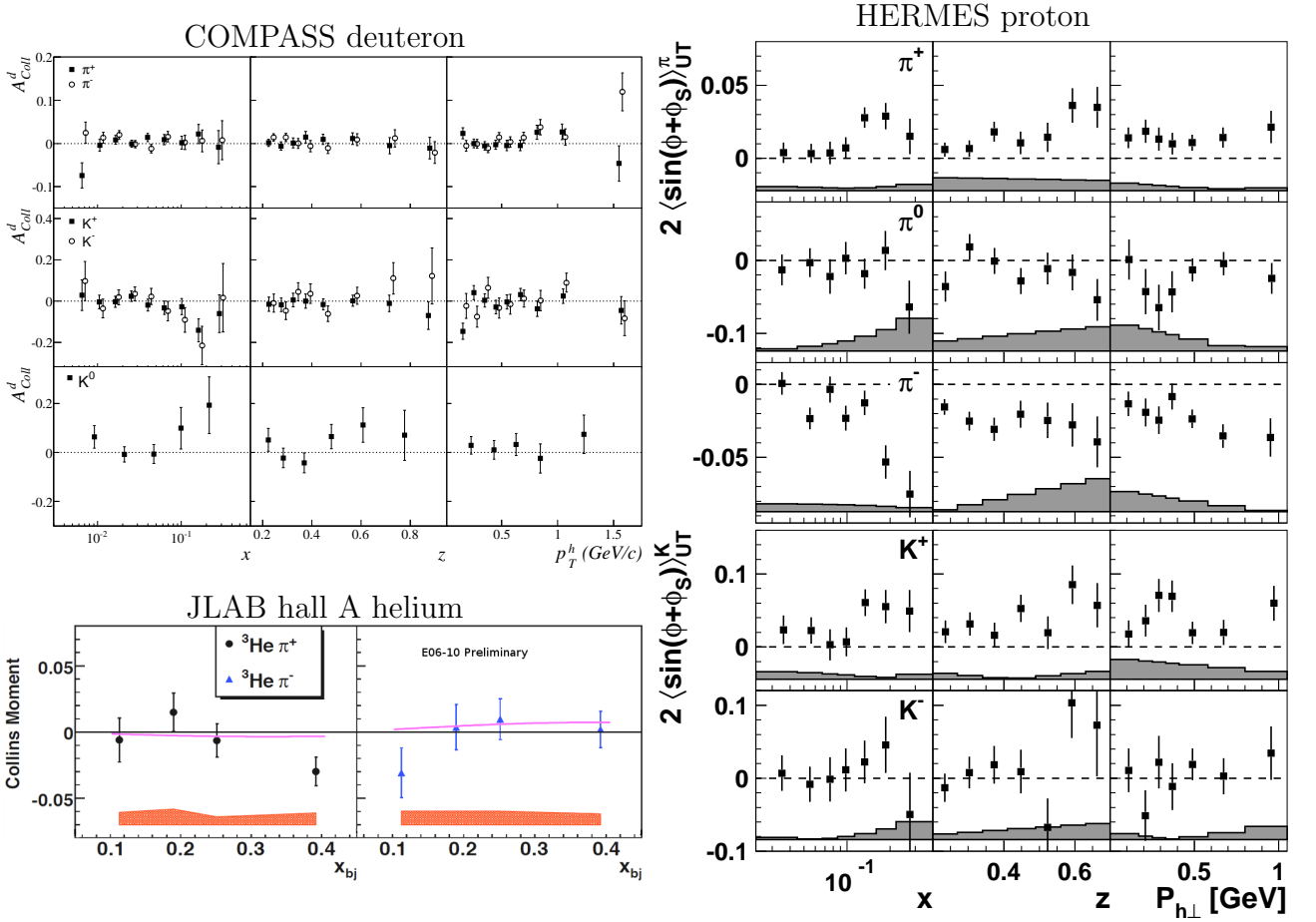


Figure 1.9: The Collins asymmetry measured at COMPASS (top left) on a polarized deuteron [9] target, at HERMES (right) on a polarized proton target [25] and JLab-Halla (bottom left) on a polarized Helium target [27]

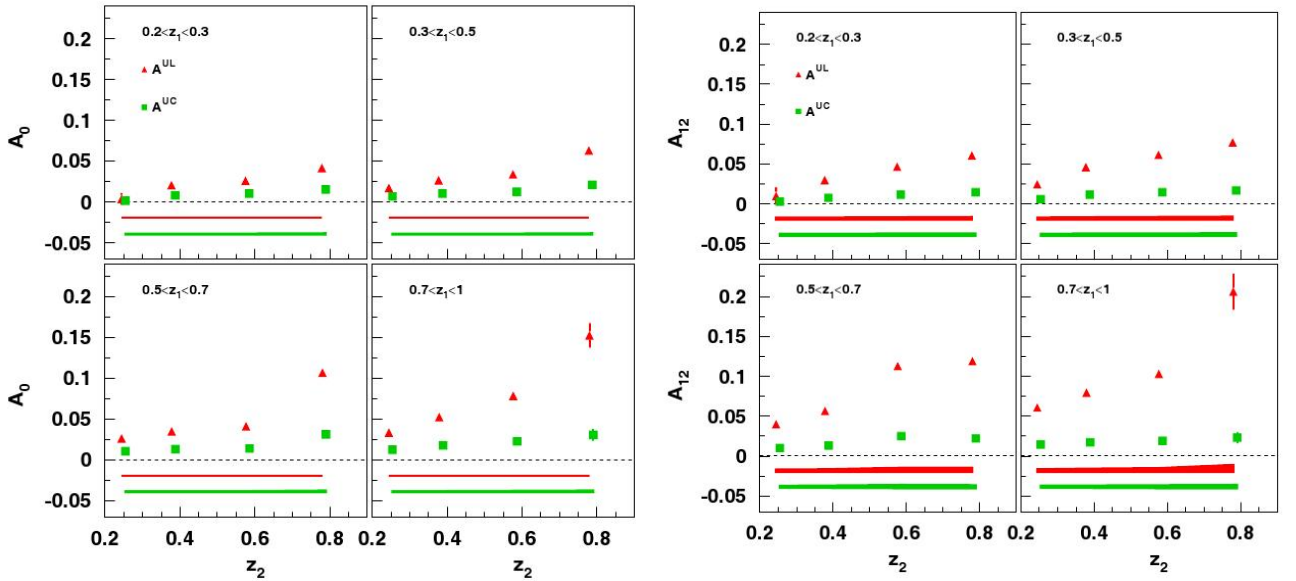


Figure 1.10: The azimuthal asymmetry of the inclusive di-hadron production in $e^+ e^-$ annihilation, extracted with two different analyses of the same data by the Belle collaboration [29].

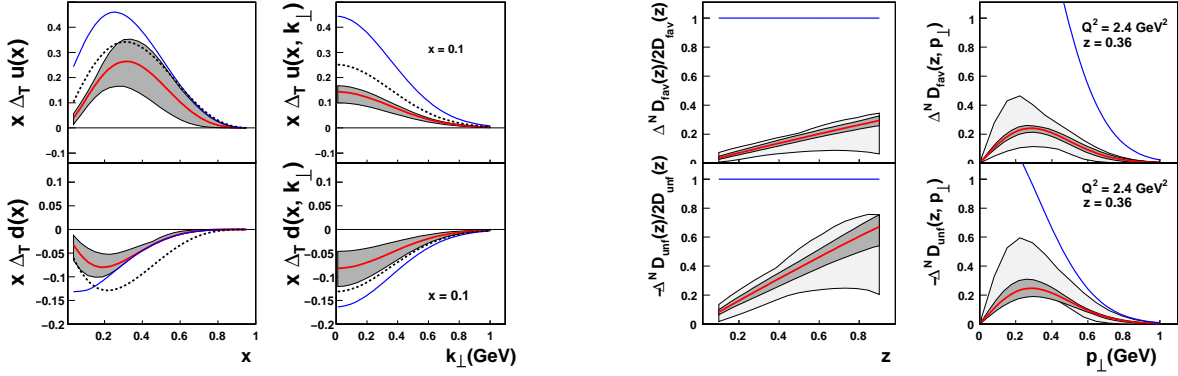


Figure 1.11: Left: $h_1(x)$ (solid line) at $Q^2 = 2.4\text{GeV}^2$. The blue line is the Soffer bound and the dashed line is the helicity PDF. Right: the Collins FF at $Q^2 = 2.4\text{GeV}^2$. The blue line is the positivity bound [30]

the Collins FF the same evolution properties as for the unpolarized FF. The measured SIDIS quantities are the Collins asymmetries (Eq. 1.34) while the BELLE collaboration measures a two hadrons asymmetry proportional to:

$$A_{12} \propto \frac{\sum_q e_q^2 H_{1h_1}^{\perp q}(z_1) H_{1h_2}^{\perp q}(z_2)}{\sum_q e_q^2 D_{h_1}^q(z_1) D_{h_2}^q(z_2)}$$

The PDF and the FF are parametrized assuming the Gaussian factorization of the transverse momentum, i.e., for the generic function $f(x, p_T) = f(x) \frac{e^{-p_T^2/\langle p_T \rangle}}{\pi \langle p_T \rangle}$. The transversity of the sea quarks is assumed to be zero in the analysis, and the relation between the favoured (the fragmenting quark is one of the valence quarks of the hadron) and unfavoured Collins FF (the fragmenting quark is one of the sea quarks of the hadron) is assumed to have the same functional form. The extracted transversity PDF and the Collins FF are shown in Fig. 1.11: the transversity distribution for the up and the down quark are of opposite sign and both are smaller than the corresponding helicity distribution (in a non relativistic theory helicity and transversity should be equal). The u quark distribution is driven by the proton data, while the d quark distribution is constrained by the deuteron asymmetries. h_{1d} is smaller in size than h_{1u} . The favoured and unfavoured Collins FF are almost of the same size, as suggested by the proton data, and of opposite sign.

1.4 The Sivers effect as a probe of the quark angular momentum

The Sivers effect is a kinematic effect that arises from the transverse momentum of the partons in a transversely polarized nucleon and leads to a single spin asymmetry in the production of the final state hadrons. A simple model is based on the work [31, and references therein] in the parameter space. The unpolarized spatial quark distribution in a transversely polarized nucleon $q_X(x, \vec{b}_\perp)$, where \vec{b}_\perp is the impact parameter, is not axially symmetric. This distortion arises from the electromagnetic coupling of the leptonic probe with a moving quark: if the quark moves towards the lepton, the electric and magnetic forces (that are of the same footing in the relativistic case) add up, while in the opposite situation they act in different directions.

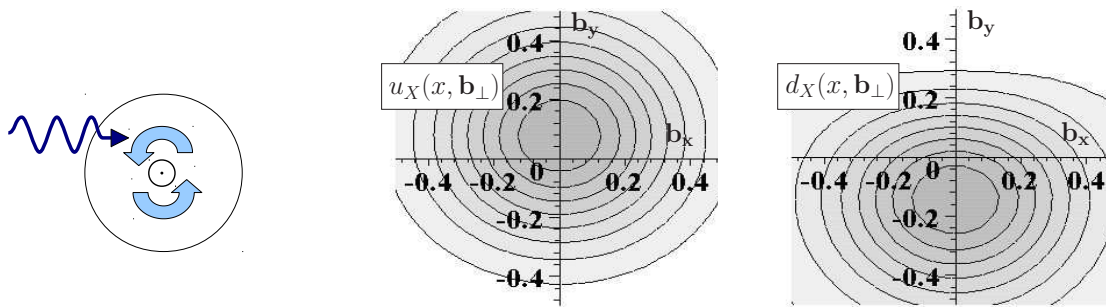


Figure 1.12: The Sivers effect: pictorial view of a photon (blue) impinging on a quark with orbital angular momentum (cyan circular arrow) inside a polarized nucleon (polarization vector towards the reader). The expected impact parameter dependent PDF for u (center) and d (right) quarks [31].

The connection between the distortion in the impact parameter space and the quark angular momentum is shown in [32], and a simplified visual interpretation is shown in Fig.1.12. The SIDIS Sivers asymmetry arises in the final state interaction; since the struck quark is coloured, for instance blue, the target remnants are collectively anti-blue (the bound state in colour-neutral) and thus attract the struck quark. Having the quark an asymmetric distribution, this attractive force creates an asymmetric distribution of the produced hadrons. The left-right asymmetry is parametrized by the Sivers function $f_{1T}^{\perp q}$:

$$f_{q/p\uparrow}(x, \vec{p}_{\perp}) = f_1^q(x, \vec{p}_{\perp}^2) - f_{1T}^{\perp q}(x, \vec{p}_{\perp}^2) \frac{(\hat{P} \times \vec{p}_{\perp}) \cdot \vec{S}}{M} \quad (1.36)$$

where $f_{q/p\uparrow}(x, \vec{k}_{\perp})$ represents the unintegrated parton density for quarks ejected from a transversely polarized target.

The Sivers asymmetry is extracted from the SIDIS cross-section asymmetry, integrating 1.32 over all the angles but the Sivers one. The amplitude of the Sivers modulation is

$$A^{\sin(\phi_h - \phi_s)} = P_T A_{Siv}. \quad (1.37)$$

and thus the Sivers asymmetry is:

$$A_{Siv} = \frac{F_{UT}^{\sin(\phi_h - \phi_s)}}{F_{UU}} = \frac{\sum_q e_q^2 f_{1T}^{\perp q}(x, p_T) \otimes D_h^q(z, k_T)}{\sum_q e_q^2 f_q(x, p_T) \otimes D_h^q(z, k_T)} \quad (1.38)$$

1.4.1 Experimental results

The Sivers asymmetry has been measured by the HERMES and the COMPASS experiments, using the same data and analysis used to extract the Collins asymmetry. A collection of the results is shown in Fig.1.13. As for Collins, the latest COMPASS results are not included in this Section.

HERMES measured the Sivers asymmetry on a proton target [33]. The asymmetry for positive π is large, almost constant as a function of x with a tendency to increase as a function of z and P_T^h , while the π^- and the π^0 asymmetries are compatible with zero, giving the first hint that $f_{1T}^{\perp u} \simeq f_{1T}^{\perp d}$. The Sivers asymmetry for positive K is larger than the corresponding asymmetry for pions, and shows the same trends as a function of x , z and p_T .

The COMPASS collaboration has first measured the Sivers asymmetry on the deuteron target [7, 8, 9]. The asymmetry, measured for identified charged pions and kaons, as well as for

the neutral kaons, was found to be compatible with zero, and this result was interpreted as the cancellation of the u and d quark contributions on an isoscalar target. In 2007 the asymmetry was measured also on a proton target [26]: the asymmetry on charged hadrons was found to be different from zero, smaller than that measured at HERMES, but still compatible within the large error bars. Note that COMPASS and HERMES use the same convention to define the Sivers angle.

Recently the Sivers asymmetry has been also measured at JLab-HallA on a Helium target [27]; the asymmetry has found to be small, compatible with zero.

1.4.2 The extraction of the Slivers PDF

The flavour separated Sivers PDFs can be extracted from the SIDIS data with a global analysis of the available results. The first global analysis was presented in 2005 [34], and since then many results have been produced. The analysis that is here presented [35], is that of the Torino-group, that uses the HERMES preliminary proton data and the COMPASS deuteron data.

The data used to extract the Sivers function are the HERMES π and K asymmetries on the proton target and the COMPASS asymmetries for charged π and K on the deuteron target. The Sivers PDF has been extracted for the u , d and s flavours (Fig. 1.14), assuming the Gaussian p_T factorization of the unpolarized fragmentation and distribution functions. The u and d Sivers PDF are of opposite sign, the u -quark distribution being positive. The relatively large contribution of the sea-quark ($f_{1T}^{\perp s}(x, p_{\perp}^2)$ is positive and $f_{1T}^{\perp \bar{d}}(x, p_{\perp}^2)$ is negative) is driven by the large K^+ asymmetry measured by the HERMES experiment. The other sea-flavours are not well determined. The extracted values of the Sivers PDF for u and d quarks are almost independent on the parametrization chosen for the FF, and it is possible to well reproduce the measured asymmetries. The Sivers PDF for the sea quarks instead is very sensitive to the choice of the FF.

1.5 Other single spin asymmetries

The eight modulations of the cross-section that depend only on the transverse polarization of the target, depend, at L.O. on four PDF: the already discussed transversity and Sivers PDF and pretzelocity and worm-gear 2. At the moment, transversity and Sivers PDF are more deeply studied than pretzelocity and worm-gear 2.

Pretzelocity PDF (h_{1T}^{\perp}) has a probabilistic interpretation [36, and ref. therein] and describes the quark transverse polarization along the quark intrinsic transverse momentum in a transversely polarized nucleon. h_{1T}^{\perp} is related to a relativistic effects that deviates the nucleon shape from that of a sphere. There are several model calculation for it and, in most of them, pretzelocity is the difference between helicity and transversity PDFs: $h_{1T}^{\perp}(x) = g_1(x) - h_1(x)$. This relation is not strictly valid in QCD, where all the TMDs are independent.

The $A_{UT}^{\sin(3\phi_h - \phi_s)}$ asymmetry measures pretzelocity PDF convoluted with the Collins FF. This asymmetry is measured at the SIDIS experiment COMPASS (deuteron)[37] and HERMES (proton) [38]: in both cases the measured asymmetry is compatible with zero (Fig. 1.15). There are also calculations of the expected SIDIS asymmetry based on several models [36, 39]: the calculated asymmetry in the COMPASS kinematics is much smaller than the present statistical accuracy of the data.

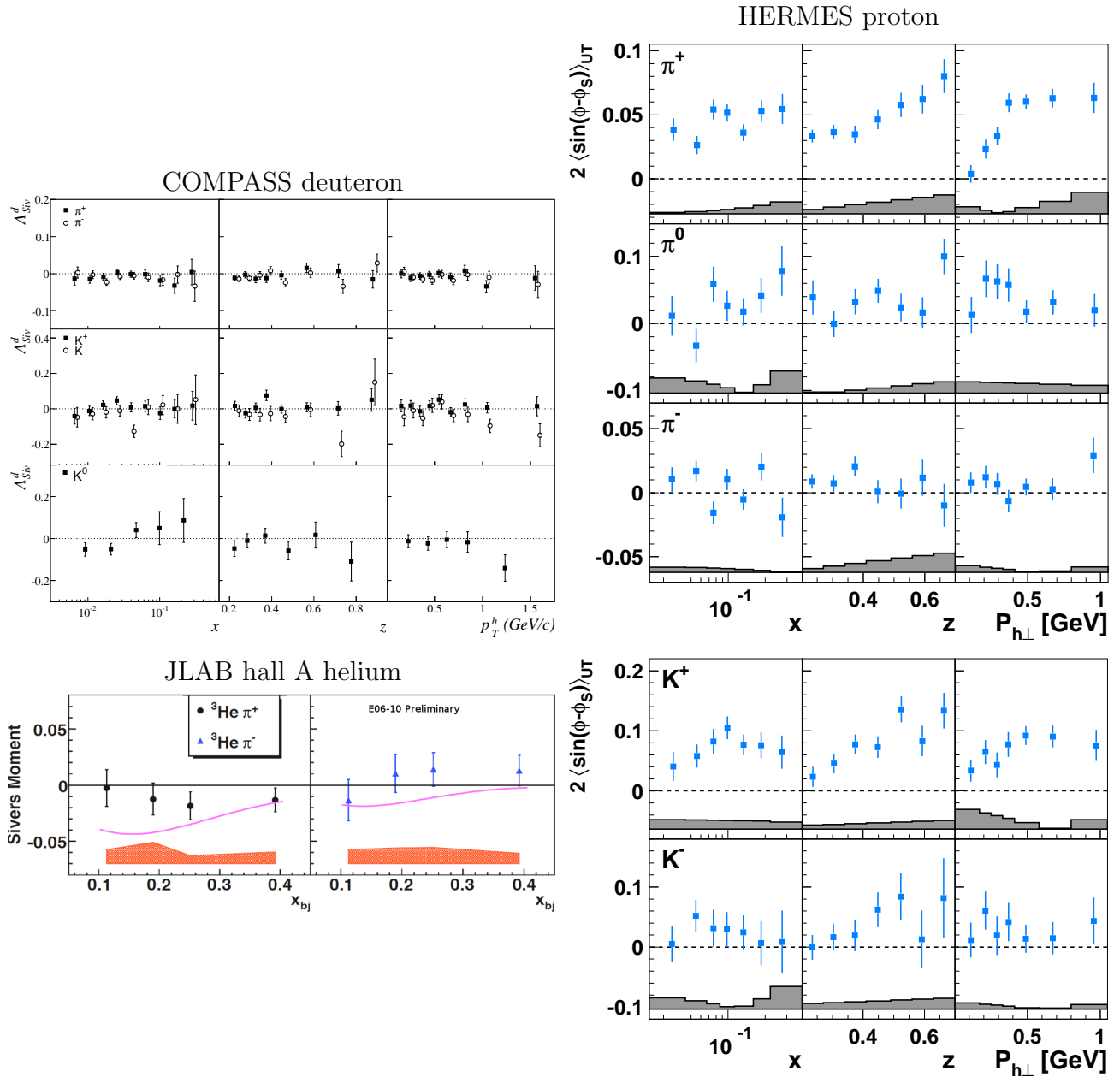


Figure 1.13: The Siverson asymmetry measured at COMPASS (top left) on a polarized deuteron target [9], at HERMES (right) on a polarized proton target [33] and JLab-Halla (bottom left) on a polarized Helium target [27]

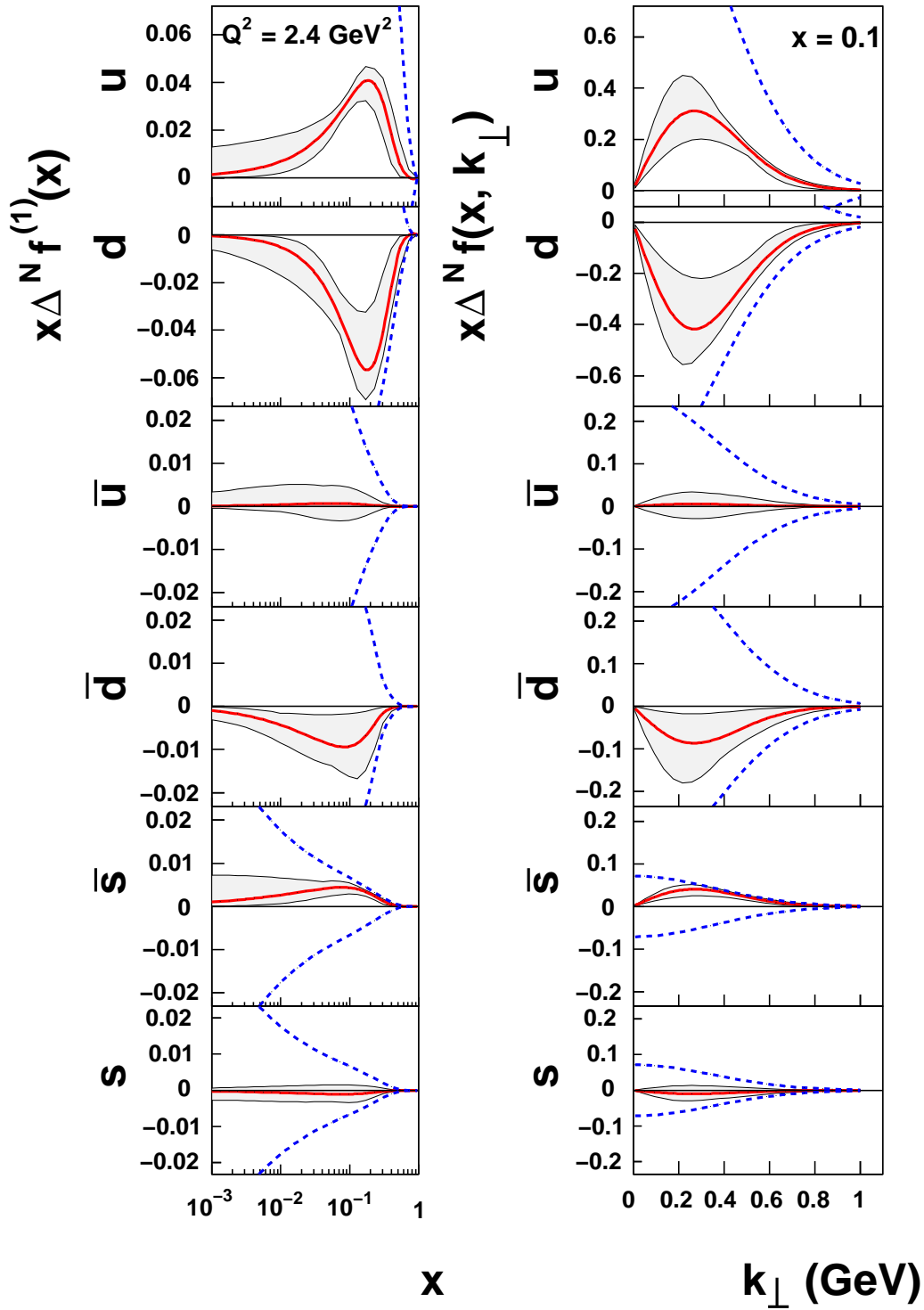


Figure 1.14: The first moment of the Sivers distribution functions for u, d, s flavours at the scale of $Q^2 = 2.4 \text{ GeV}^2$ [35] as a function of x and k_T . The blue dashed line is the positivity bound.

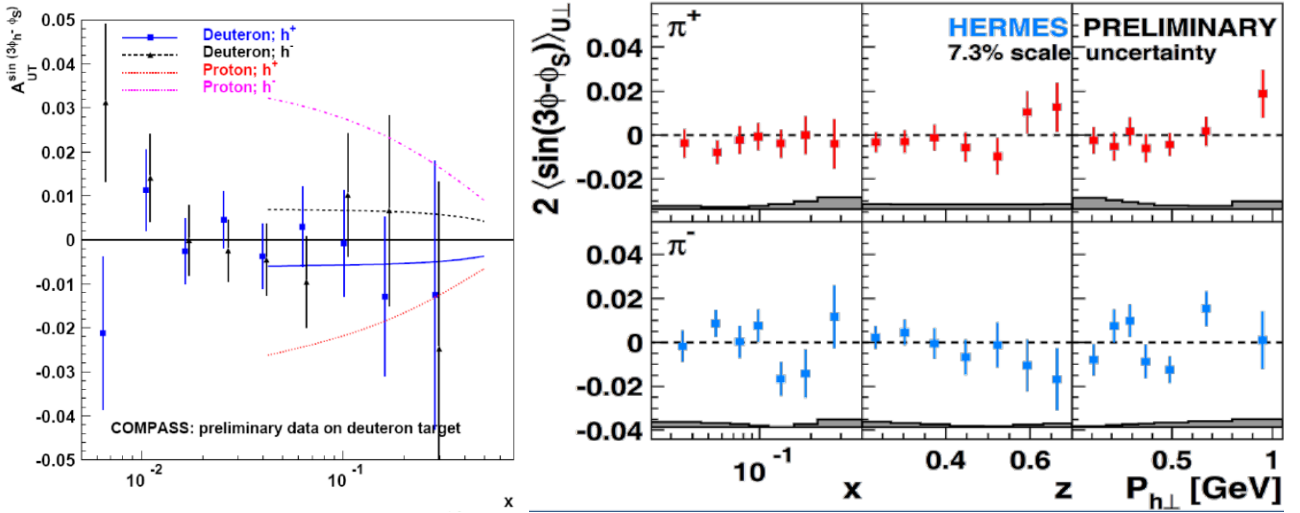


Figure 1.15: The $A_{UT}^{\sin(3\phi_h - \phi_s)}$ asymmetry as measured at COMPASS (left) [37] on a deuteron target and at Hermes(right) on a proton target [38]. The lines in the COMPASS plot are the results of the calculations in the quark-diquark model[39].

Worm-gear 2 PDF is the helicity distribution of the longitudinal polarized quarks in a transversely polarized nucleon.

The $A_{LT}^{\cos(\phi_h - \phi_s)}$ asymmetry measures worm-gear 2 convoluted with the unpolarized FF. This asymmetry is measured at the SIDIS experiments COMPASS (deuteron)[37] and JLab-hallA (helium) [27] (Fig. 1.16). The deuteron asymmetry has found to be compatible with zero, while the helium asymmetry for negative pions has found to be slightly positive. The quark-diquark model calculations in the COMPASS range predicts that the asymmetry is small, smaller than the present statistical accuracy.

The amplitudes of the other modulations, $A_{UT}^{\sin(2\phi_h - \phi_s)}$, $A_{UT}^{\sin(\phi_s)}$, $A_{LT}^{\cos(2\phi_h - \phi_s)}$ and $A_{LT}^{\cos(\phi_s)}$, are related to higher order effects, and thus are expected to be small. The available experimental results and model calculations (Fig. 1.17, 1.18 and 1.19) show that all these amplitudes are very small on the deuteron target. The HERMES results for proton target show a negative $A_{UT}^{\sin(\phi_s)}$ for negative pions.

All these modulations have been measured at COMPASS on the proton target. The results are presented in Chap.4.

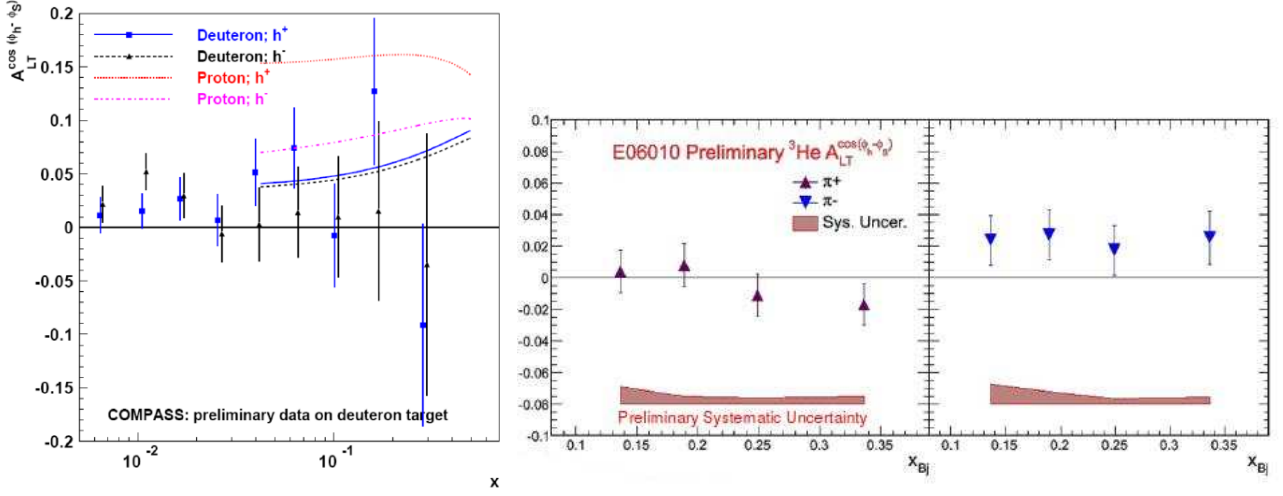


Figure 1.16: The $A_{LT}^{\cos(\phi_h - \phi_s)}$ asymmetry as measured at COMPASS (left)[37] on a deuteron target and at JLab-halla E06-010 (right) on a helium target[27]. The lines in the COMPASS plot are the results of the calculations in the quark-diquark model[39].

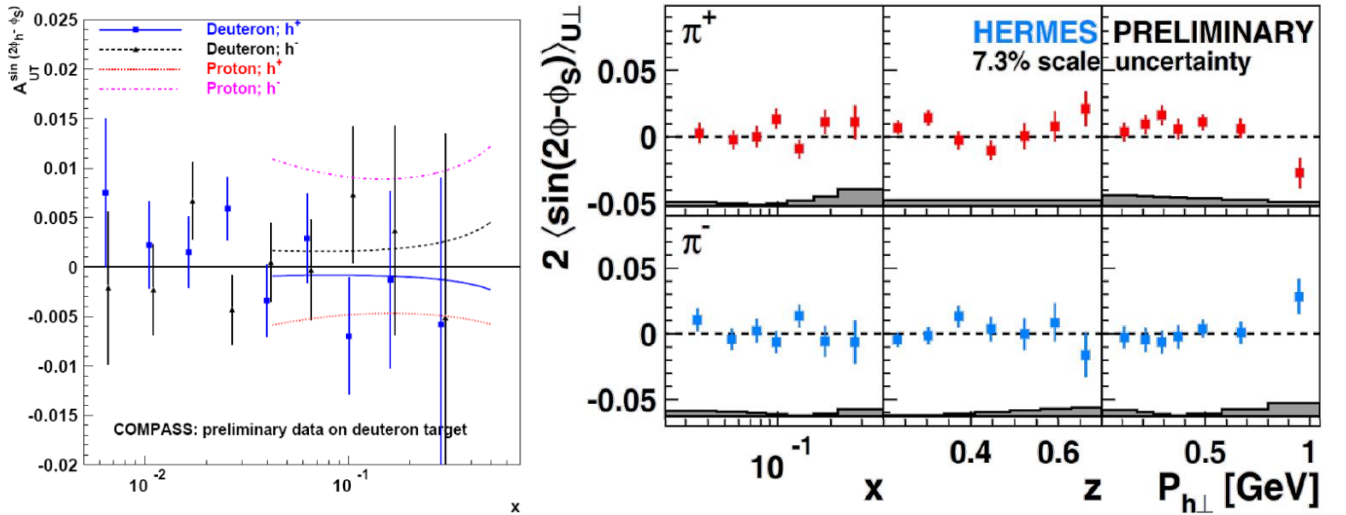


Figure 1.17: The $A_{UT}^{\sin 2\phi_h - \phi_s}$ asymmetry as measured at COMPASS (left)[37] on a deuteron target and at HERMES(right) on a proton target. The lines in the COMPASS plot are the results of the calculations in the quark-diquark model[39].

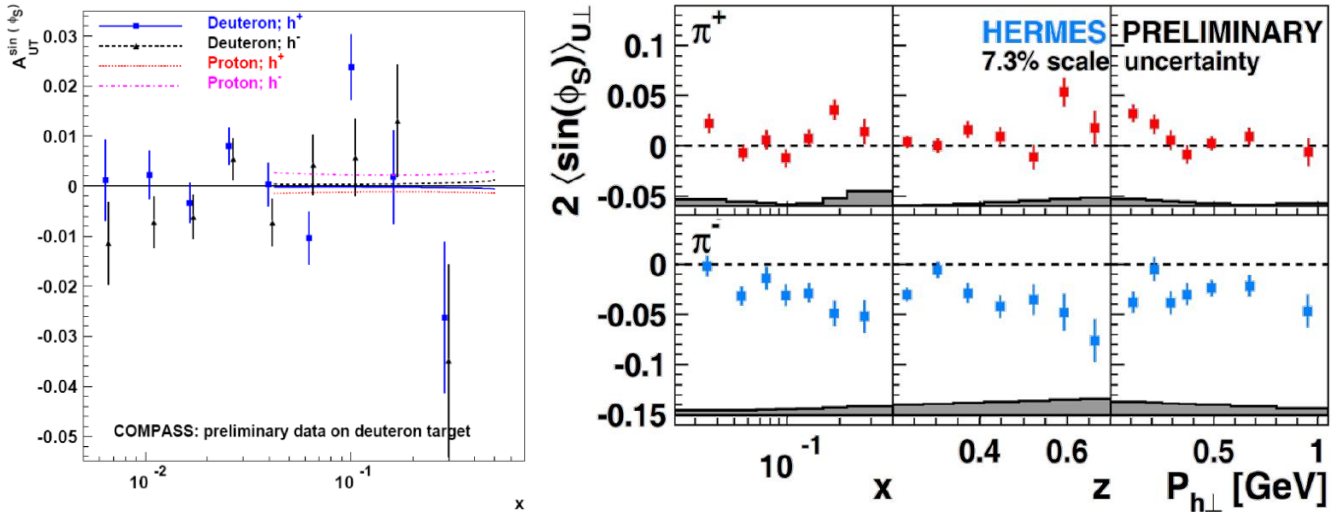


Figure 1.18: The $A_{UT}^{\sin\phi_s}$ asymmetry as measured at COMPASS (left)[37] on a deuteron target and at Hermes(right) on a proton target. The lines in the COMPASS plot are the results of the calculations in the quark-diquark model[39].

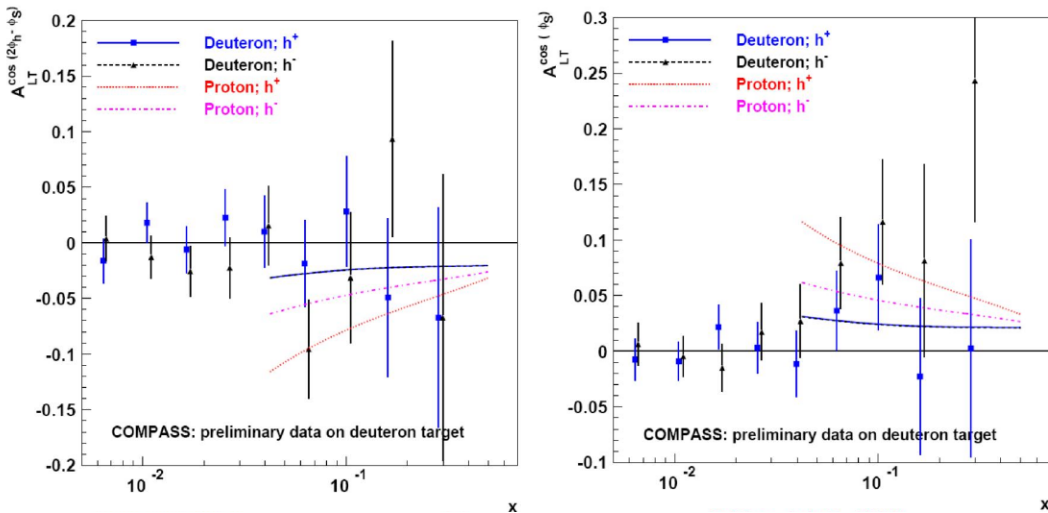


Figure 1.19: The $A_{UT}^{\cos 2\phi_h - \phi_s}$ (left) and $A_{UT}^{\cos\phi_s}$ (right) asymmetries as measured at COMPASS on deuteron target[37]. The lines are the results of the calculations in the quark-diquark model[39].

Chapter 2

The COMPASS experiment at CERN

COMPASS is a fixed target experiment at the M2 beam line of the CERN SPS. The detector consists of three main parts (Fig. 2.1): the part before the target, to measure the beam, the first spectrometer, built around the analysing magnet SM1, that measures the particles produced at large angles and the second spectrometer, built around the analysing magnet SM2, that measures the particles produced at small angles, making use of the longer lever arm. The two spectrometers are both capable of momentum measurement and particle identification, thanks to the electromagnetic and hadronic calorimeters. The small angle spectrometer has a RICH detector, capable of π/K identification over a large momentum range.

To cope with the different requirements of its broad physics program [40], all the detectors are mounted on rails, thus their position along the beam axis can easily be changed. Also the target can be changed according to the physics program, as well as the beam: the M2 beam line can deliver hadron (pions), muon and electron beams.

In this Chapter the COMPASS spectrometer will be described in the configuration used during the 2007 data-taking. In 2007 a SIDIS measurement was done, using a 160 GeV/ c polarized muon beam impinging on a transversely polarized proton target.

More room is given to the RICH-1 detector description, which plays an essential role to extract the identified hadrons asymmetries. A complete review of the RICH-1 detector image reconstruction and performances, comprehensive of the details on its calibration can be found on [41], article of which who writes is the corresponding author.

2.1 The muon beam

The compass muon beam is a tertiary beam. The primary beam is a proton beam extracted from the SPS at 400 GeV/ c , with a nominal flux of 1.2×10^{13} protons in an extraction interval of 4.8 s, called *spill*, with a 16.8 s SPS cycle. The proton beam impinges on a 500 mm thick Beryllium target, producing a secondary hadron beam; at the production target the pion flux has a kaon contamination of $\sim 3.6\%$. The produced pions are transported along a 600 m channel, consisting in a series of focusing and defocussing (FODO) quadrupoles, with a phase advance of 60° each. Along this channel, the pion decays in a muon and a neutrino. Due to the parity violating nature of the decay, the muons are 100% polarized in the centre of mass reference system. The polarization in the laboratory system depends on the particle momentum (Fig. 2.2).

The residual pions present in the muon beam are filtered out thanks to a hadron absorber, made of 9 motorized modules of Beryllium, each 1.1 m long. The momentum selection of the muon beam is made using a series of four dipole magnets that provide a total deflection of 24 mrad. After that, a series of acceptance quadrupoles and two horizontal and three vertical magnetic collimators is found. The muons are transported to the surface level by a 250 m

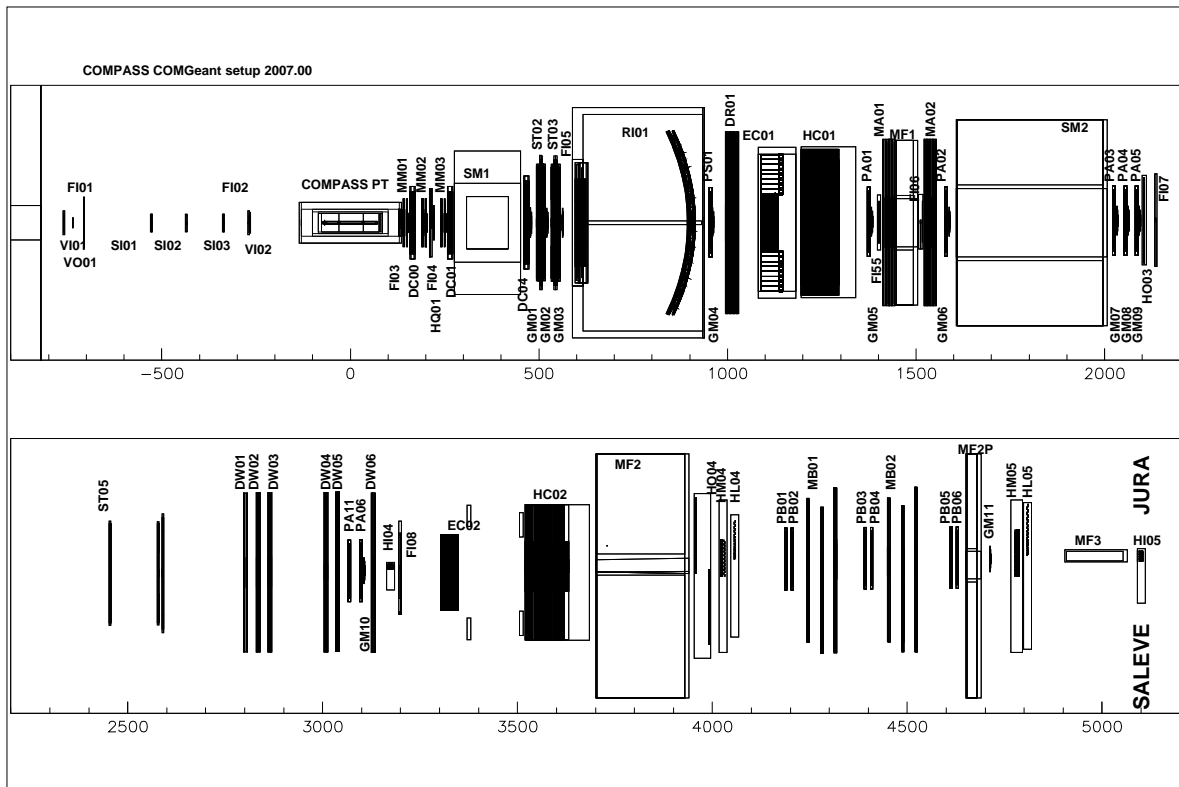
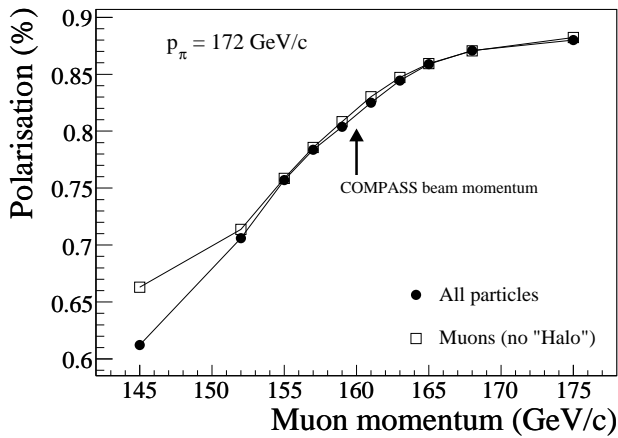


Figure 2.1: The COMPASS spectrometer in 2007 configuration, top view



| Beam parameters | Measured |
|---|---------------------------------------|
| $(p_\mu)/(p_\pi)$ | $(160\text{GeV}/c)/(172\text{GeV}/c)$ |
| p on T6 / SPS cycle | $1.2 \cdot 10^{13}$ |
| μ flux / SPS cycle | $2 \cdot 10^8$ |
| Beam polarization | $(-80 \pm 4)\%$ |
| Spot size ($\sigma_x \times \sigma_y$) | $8 \times 8 \text{ mm}^2$ |
| Divergence ($\sigma_x \times \sigma_y$) | $0.4 \times 0.8 \text{ mrad}$ |
| Muon halo $ x, y < 15 \text{ cm}$ | 16% |
| Muon halo $ x, y > 15 \text{ cm}$ | 7% |

Figure 2.2: The muon beam polarization as a function of the central muon momentum, assuming a central hadron momentum of 172 GeV/c (left) and the muon beam parameters (right).

FODO channel, and finally bent to the horizontal axis by three 5 meters long dipole magnets, which are also used to measure the beam momentum (Sec. 2.1.1). In the final section of the beam line, several dipoles and quadrupoles are used to fine-steer the beam and to compensate for the horizontal deflection induced by the 0.42 T transverse dipole field of the polarized target (Sec. 2.2).

The beam momentum selected for the muon program is 160 GeV/c, to which corresponds a polarization of $(-80 \pm 4)\%$. The beam momentum spread given by the beam line is $\sim 5\%$. The beam intensity corresponding to an incident proton flux of 1.2×10^{13} protons per *spill* is 2×10^8 muons. The spot size of the beam at the COMPASS target is $8 \times 8 \text{ mm}^2$, with a divergence of $0.4 \times 0.8 \text{ mrad}$. The beam arrives in the hall with a large muon halo, which intensity is higher closer to the nominal beam trajectory. The high intensity halo near the beam line is measured by a dedicated veto counter (size $30 \times 30 \text{ cm}^2$, with a 4 cm diameter central hole), and it amounts to $\sim 16\%$ of the muon beam. The large halo, which intensity is lower, is measured by a large veto counter, with a central hole of $30 \times 30 \text{ cm}^2$, where it amounts to the 7% of the nominal muon beam.

2.1.1 The Beam Momentum Station

The beam momentum is measured by a dedicated detector, to better constrain the kinematics of the event. The Beam Momentum Station (BMS, Fig. 2.3) is composed by six hodoscopes (four scintillating strips and two scintillating fibres), placed before and after the last vertical bending magnet of the beam line (B6). The design of these hodoscopes is such that the maximum rate is $1 \times 10^7 \text{ s}^{-1}$ in the scintillating strips and $3 \times 10^6 \text{ s}^{-1}$ in the scintillating fibres. Thanks to these design parameters and the plane redundancy, the momentum of each track can be measured with a precision $< 1\%$ with a track reconstruction efficiency of $\sim 93\%$.

2.2 The polarized target

To measure spin dependent asymmetries, COMPASS makes use of a solid state polarized target that allows a higher luminosity if compared to the commonly used gaseous targets. The target material used for 2007 data-taking was Ammonia (NH_3), that allows to measure the spin asymmetries on the polarized proton. Ammonia can be polarized up to 90%, and this compensates for the low dilution factor $f \sim 0.15$, where f is the fraction of polarizable material inside the target. From 2002 to 2004 COMPASS used as target material ^6LiD , to access the

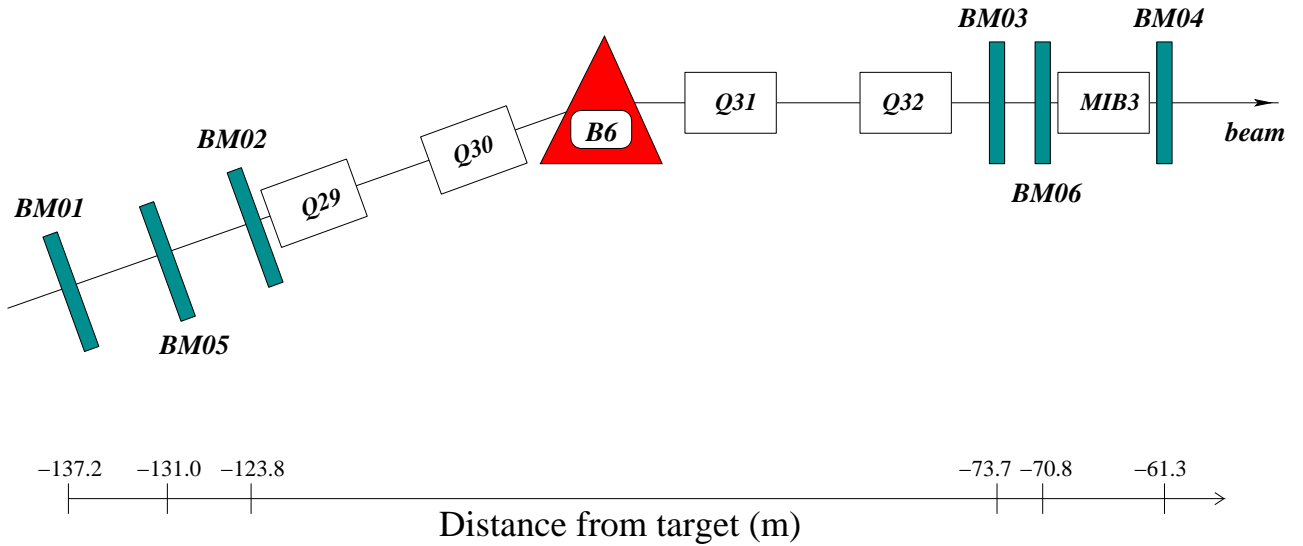


Figure 2.3: The beam momentum station

polarized deuteron. The deuteron polarization was above 40%, and its dilution factor was more favourable: $f \sim 0.35$.

While electrons can be easily polarized in a high magnetic field, the polarization of the protons is only minimal. Thus, to reach a high polarization level, the technique of the Dynamic Nuclear Polarization (DNP) is used. With this technique the electrons of the paramagnetic centres contained in the target material are polarized at low temperature (below 1K) in a strong and homogeneous magnetic field. The electron polarisation is then transferred to the nucleons by means of a microwave field. The target is polarized in the longitudinal (i.e. parallel to the beam) direction, using a 2.5 T solenoid field. When the target is in longitudinal configuration, the polarisation is hold by the solenoid field. When the target is operated in transverse mode, after the polarisation, the spin direction is rotated and the polarisation is hold by a dedicated 0.42 T transverse dipole field.

The target structure is described in Fig 2.4: a 130 cm long target holder , with a diameter of 3 cm and divided in three cells, is included in a large angle solenoid magnet (± 180 mrad acceptance for the most downstream edge). The uniformity of the solenoid field is within $\pm 3 \times 10^{-5}$ over the useful volume of the target cells. A cryogenic system is used to keep the temperature of the target at 90 mK during the frozen spin mode, by evaporating ^4He in ^3He .

The two external target cells are 30 cm long, while the internal cell is 60 cm long, with a 5 cm spacing among them. The two external cells are polarized in the opposite direction with respect to the central one: it is thus possible to make measurements at the same time with the two different orientation of the target spin, and this reduced the false asymmetries of the experiment. Moreover, to allow a better control of the systematic effects of the measurement, the overall polarization of the target is reversed every 5 days, destroying and rebuilding the polarization.

2.3 The large and small angle spectrometers

The COMPASS spectrometer is divided in two parts: the large angle spectrometer (LAS), that is built around the dipole magnet SM1 and the small angle spectrometer (SAS), built around the dipole magnet SM2. A large variety of detectors is used to allow tracking as well as momentum measurement.

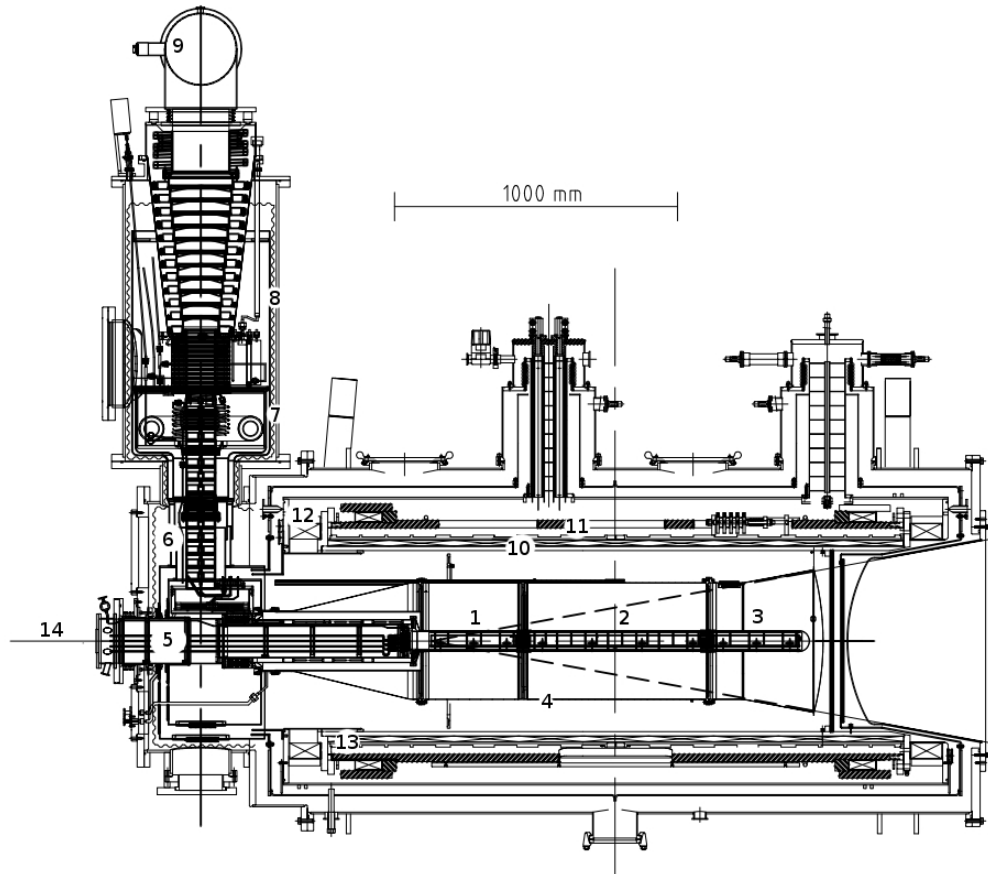


Figure 2.4: Side view of the COMPASS polarized target: upstream (1), central (2) and downstream (3) target cells inside mixing chamber, microwave cavity (4), target holder (5), ^3He evaporator (6), ^4He evaporator (7), ^4He liquid/gas phase separator (8), ^3He pumping port (9), solenoid coil (10), correction coils (11), end compensation coil (12), dipole coil (13), muon beam entrance (14). The two halves of the microwave cavity are separated by a thin microwave stopper.

SM1 is located 4 m downstream the target centre, it is 110 cm long and provides an integrated field of 1 Tm; the field is in the vertical direction, thus the particles are bent in the horizontal plane. Its vertical opening size matches the desired acceptance of ± 180 mrad. Due to the bending effect, the detectors downstream SM1 need to have a ± 250 mrad acceptance in the horizontal plane. SM1 is followed by a RICH detector, an Electromagnetic calorimeter and an Hadronic calorimeter. At the end of the LAS a muon filter is set.

SM2 is located 18 m downstream the target, it is 4 m long and has a 4.4 Tm bending power with the main field component in the vertical direction. The SAS is built to detect particles produced at small angles and higher momenta ($p > 5$ GeV/ c). Downstream the magnet there are an Electromagnetic and an Hadronic calorimeter, and also a second muon filter.

The Cartesian reference system of the spectrometer is such as the z axis is along the undeflected beam direction and the y axis points upwards.

2.4 The tracking detectors

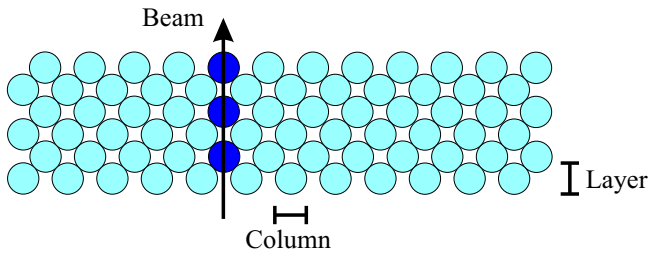
The particle flux varies by more than five order of magnitude in the overall spectrometer acceptance. For this reason, detectors with different characteristics are used to equip the different regions of the spectrometer. All the detectors have a central hole corresponding to the trajectory of the non-interacting beam. The detectors are divided in three categories: the very small area trackers, that cover the transverse beam size up to distances of the order of 3 cm, the small area trackers, that covers the region up to 40 cm, and the large area trackers. Since the particle flux depends strongly on the distance from the beam axis, the central region of the small area trackers and the large area trackers is deactivated, to avoid the detector saturation.

2.4.1 Very small area trackers

For a distance up to ~ 3 cm from the beam axis, the particle rate is very high (10^5 s $^{-1}$ mm $^{-2}$ in the centre of the muon beam), thus the detector require excellent time or position resolutions. The chosen detectors are scintillating fibres and silicon microstrip detectors.

The scintillating fibres (SciFi) provide an excellent time resolution, that is used to correlate the track time informations of the incoming and of the scattered muon tracks. In total 8 SciFi stations are used: two upstream and two downstream the target, and two upstream and two downstream SM2. Each station consists of at least two planes, one that measures the vertical direction (Y) and one the horizontal (X) one; three of them have an additional plane (U) rotated 45° clockwise with respect to the x axis. Each plane is built by several layers of scintillating fibres (Fig. 2.5); the readout groups several fibres along the beam direction (a column) to the same photomultiplier channel, to achieve the required time resolution while minimizing the amount of material in the beam. The spatial resolution of the SciFi detectors depends on the fibre diameter, and varies from $130 \mu\text{m}$ to $210 \mu\text{m}$. The time resolution, almost constant across the plane, has an R.m.s. value between 350 ps and 450 ps.

Silicon microstrip detectors are also used to detect the incoming muon beam tracks. The silicon wafer of type n is $300 \mu\text{m}$ thick and has 1280 readout strips with a pitch of $56.6 \mu\text{m}$. The p-side is divided in 1024 readout strips (pitch $51.7 \mu\text{m}$), perpendicular to the n-side strips: each wafer measures two coordinates. Each silicon station is composed by two wafers, one orientated in the $X - Y$ plane, the following tilted around the beam axis of 5° (U-V direction). The detector spatial resolution is $8 \mu\text{m}$ for the p-side (Y and V planes) and $11 \mu\text{m}$ for the n-side (X and U planes), with a time resolution < 2.5 ns.



| No. | Proj. | # of layers | Size (cm ²) | Fibre ϕ (mm) | Pitch (mm) |
|-----|---------|-------------|---|-------------------|------------|
| 1,2 | X, Y | 14 | 3.9 ² , 3.9 ² | 0.5 | 0.41 |
| 3,4 | X, Y, U | 14 | 5.3 ² , 5.3 ² , 5.3 ² | 0.5 | 0.41 |
| 5 | X, Y | 12 | 8.4 ² , 8.4 ² | 0.75 | 0.52 |
| 6 | X, Y, U | 8 | 10.0 ² , 10.0 ² , 12.3 ² | 1.0 | 0.70 |
| 7 | X, Y | 8 | 10.0 ² , 10.0 ² | 1.0 | 0.70 |
| 8 | X, Y | 8 | 12.3 ² , 12.3 ² | 1.0 | 0.70 |
| 9 | U, V | 8 | 12.3 \times 6.3, 12.3 \times 6.3 | 1.0 | 0.70 |

Figure 2.5: Typical fibre configuration in a SciFi plane

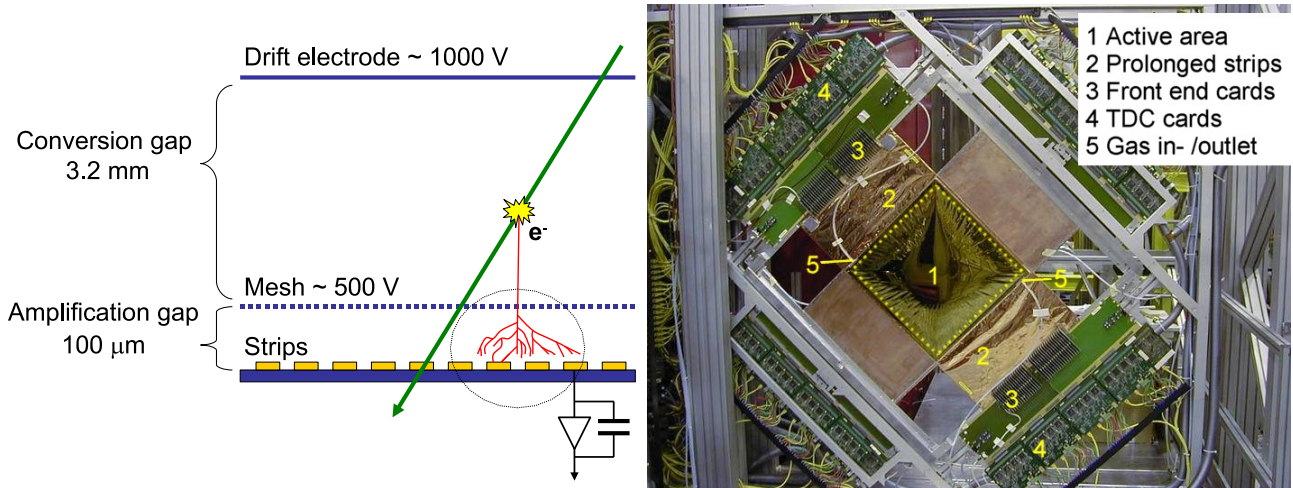


Figure 2.6: Principle of a Micromegas detector (left) and a Micromegas doublet (U and V projections) in the COMPASS experiment (right). The active zone is the 40×40 cm² internal square (1). Strips are extended (2) in order to keep the front-end electronics (3) outside the acceptance of the spectrometer.

2.4.2 Small area trackers

These detectors cover distances from the beam axis larger than 2.5 cm. These medium size detectors must have high spatial resolution and minimal material budget: MicroMegas and GEMs are used. Both these gaseous detector types were used for the first time in the COMPASS experiment.

The Micromegas (Micromesh Gaseous Structure) detectors are used to track the particles in the region between the target solenoid and the SM1 dipole magnet. In total there are 3 stations, each composed by 4 planes (X, Y, U, V directions) of 1024 strips. A scheme of principle of the detector is shown in Fig. 2.6: in the conversion gap the ionization takes place and the resulting primary electrons drift in a moderate field; a mesh separates the conversion gap from the amplification gap, where the avalanche is formed, and captures the produced ions. The drift time of the ions, given the 50 kV/cm field over a distance of $100 \mu\text{m}$, is about 100 ns. The fast drift time of the ions combined with the reduced transverse diffusion of the electrons and the high granularity of the detector, results in a high rate capability. The detector size is 40×40 cm², with a central dead zone of 5 cm diameter. The inner part of the detector consist in 512 strips with a pitch of $360 \mu\text{m}$, the two outer part consist in 256 strips each with a pitch of $410 \mu\text{m}$. The mean time resolution of the detector is 9.3 ns and the average spatial resolution is of the order of $90 \mu\text{m}$. The efficiency is up to 97% at the nominal beam intensity.

The COMPASS GEM (Gas Electron Multipliers) gaseous detectors (Fig. 2.7) consist in

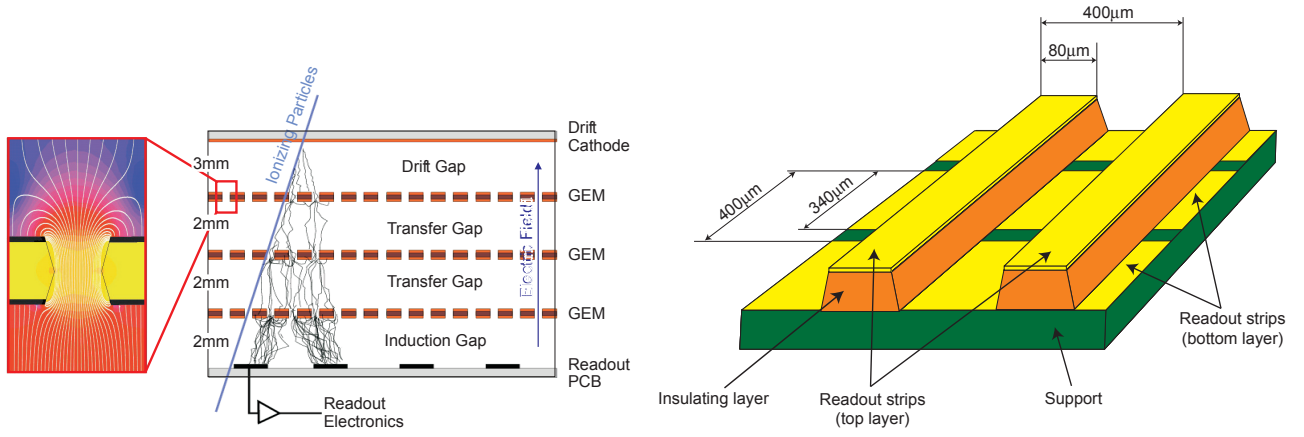


Figure 2.7: Principle of a triple GEM detector (left) and schematic view of the two dimensional readout (right)

three amplification stages, separated by thin spacer grids of 2 mm height. A GEM is a thin ($50\mu\text{m}$) polyamide foil, with Cu cladding on both sides, into which a large number of micro holes ($\sim 10^4/\text{cm}^2$, with a diameter of $70\mu\text{m}$) has been chemically etched using lithographic techniques. Across the foil a high voltage (several 100V) is applied to generate the avalanche multiplication of the electron through the holes. The fast signal is induced by the electron cloud emerging from the last GEM foil on an anode segmented into two sets of 768 orthogonal strips (pitch $400\mu\text{m}$).

The detector size is $31 \times 31\text{ cm}^2$ and the central region (5 cm diameter) is deactivated during normal data taking. It can be activated to align the detector with low intensity beams. The time resolution is about 12.3 ns and the spatial resolution $66.4\mu\text{m}$, with an average efficiency of 97.2%.

2.4.3 The large angle trackers

The large angle trackers have to provide a good spatial resolution while efficiently covering all the spectrometer acceptance. In the LAS, there are three Drift Chambers before the magnet SM1, two after, followed by three stations of Straw Drift Tubes. In the SAS 14 multiwire proportional chambers are used, and downstream the SM2 two additional straw stations and six large area drift chambers are found.

The Drift Chambers (DC) are designed to operate between the target dipole and the SM1 magnet, where the particle flux through the chambers is a factor three higher than after SM1 due to the low-energy background event which are bent away by the magnet. Each DC station consists of eight layers of wires with different orientation (vertical Y, horizontal X, tilted by $+20^\circ$ U and by -20° V with respect to the vertical). Two consecutive planes with the same inclination are staggered by 3.5 mm to solve the left-right ambiguities, and the ordering of the plane with different orientations is such to minimize the fake track combinations. Each layer of wires consists of 176 sensitive wires of $20\mu\text{m}$ diameter, alternated with a total of 177 potential wires with $100\mu\text{m}$ diameter and enclosed in two Mylar cathode foils, coated with graphite (Fig. 2.8).

The active area of the chambers is $180 \times 127\text{ cm}^2$, with a central dead zone of 30 cm. The central dead zone can be activated for alignment purposes with a low intensity beam. The average spatial resolution of a single DC layer is $270\mu\text{m}$ and the the efficiency is above 95%.

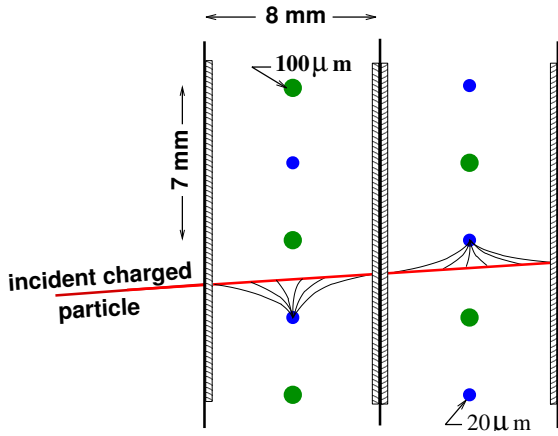


Figure 2.8: Drift cell geometry

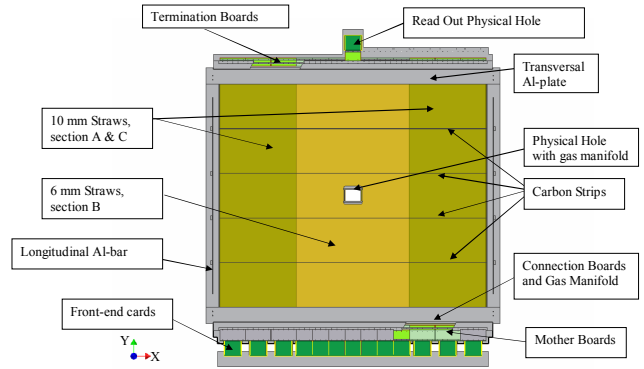


Figure 2.9: Schematic view of a COMPASS straw detector (type X)

The Straw tube drift chambers are used for the tracking of particles produced at large scattering angles. The straw tubes consists in two layers of thin plastic film, one is coated with carbon loaded Kapton, the other one is an aluminised Kapton foil. The anode wires are made of gold-plated tungsten with $30\mu\text{m}$ diameter, centred in the tube by means of small plastic spacers. There are 15 straw detectors, for a total of 12440 tubes. Each detector consists in two layers of straw tubes with the same orientation, staggered to resolve the left-right ambiguities, and a station is formed by three detectors with different orientation (X,Y and rotated 10° with respect to the vertical).

The detector (Fig.2.9) has an active area on 9 m^2 divided in three sections. In the central one, which is the closest to the beam axis and thus is exposed to a higher counting rate, the straw tubes have an outer diameter of 6.14 mm, forming a central dead zone of about $20 \times 20\text{ cm}$. In the outer parts the diameter of the tube is 9.65 mm. The average resolution is $190\mu\text{m}$, and does not depend on the diameter of the straw.

The Multiwire Proportional Chambers (MWPC) are used to measure large angle particles in SAS. There are three types of chambers installed (Tab. 2.1): type-A, that consists of three layers, one vertical (X) and two tilted with respect to the vertical axis ($+10.14^\circ$ U and -10.14° V), with an active area of $170 \times 120\text{ cm}^2$; type-A*, with an additional horizontal layer (Y), and type-B composed of two double-layers detectors with opposite orientation fixed together, of which only the X U and V planes are read out.

The layers have a wire length of about 1 m, a wire diameter of $20\mu\text{m}$ and a pitch of 2 mm, and are enclosed on both sides by graphite-coated Mylar foils. A central dead zone with a diameter ranging from 16 to 22 cm is present. The ionizing particles induces a signal on several neighbouring wires, and the centre of gravity of the signal is used in the tracking algorithm. The average spatial resolution of the chamber is 1.6 mm.

Six large area drift chambers are also used, with an active surface of $5 \times 2.5\text{ m}^2$. Each plate consists of 4 layers of sensitive anode wires (diameter $20\mu\text{m}$), with a wire pitch of 4 cm, separated by cathode wires (diameter $100\mu\text{m}$) with a pitch of 2 cm and tilted by 5° with respect to the vertical direction to provide a better field homogeneity. Each chamber is composed by two plates, each consisting in two layers of wires shifted by half of a pitch. The two plates have different orientations and the following combinations are possible (Tab. 2.2): XY, XV, XU, YV and YU, where X,Y,U and V have the standard meaning.

The chambers have a central dead zone with a diameter of 0.5 m and 1 m. The average layer efficiency is 93% and an average spatial resolution of 0.5 mm is achieved.

| | A-type | A*-type | B-type |
|---------------------|--------------------------------|--------------------------------|--------------------------------|
| # of chambers | 7 | 1 | 6 |
| Active area | $178 \times 120 \text{ cm}^2$ | $178 \times 120 \text{ cm}^2$ | $178 \times 80 \text{ cm}^2$ |
| # of layers/chamber | 3 | 4 | 2 |
| Planes | X, U, V | X, U, V, Y | $X, U/V$ |
| Dead zone \odot | 16 – 20mm | 16 mm | 22mm |
| Wire pitch | 2mm | 2mm | 2mm |
| Anode/cathode gap | 8mm | 8mm | 8mm |
| # of wires/plane | 752 (X, U, V), 512 (Y) | 752 (X, U, V), 512 (Y) | 752 (X, U, V), 512 (Y) |

Table 2.1: Characteristics of the COMPASS MWPC detectors.

| | XY-type | XV-type | XU-type | YV-type | YU-type |
|---------------------|-------------------------------|-------------------------------|-------------------------------|-------------------------------|-------------------------------|
| # of chambers | 2 | 1 | 1 | 1 | 1 |
| Active area | $500 \times 250 \text{ cm}^2$ |
| # of layers/chamber | 4 | 4 | 4 | 4 | 4 |
| Planes | X, Y | X, V | X, U | Y, V | Y, U |
| Dead zone \odot | 500mm | 1000mm | 1000mm | 1000mm | 1000mm |
| Anode wire pitch | 4cm | 4cm | 4cm | 4cm | 4cm |
| Anode/cathode gap | 10mm | 10mm | 10mm | 10mm | 10mm |
| # of wires/plane | 260 (X), 130 (Y) | 260 (X), 288 (V) | 260 (X), 288 (U) | 130 (Y), 288 (V) | 130 (Y), 288 (U) |

Table 2.2: Basic characteristics of the COMPASS large area drift chambers.

The RichWall (RW) detector is positioned downstream of the RICH-1 detector, and covers its exit window ($4.86 \times 4.22 \text{ m}^2$). The detector consists of Mini Drift Tubes (MDT), mounted to measure the X and Y projections of the track trajectory. The MDT module design (Fig. 2.10, right) is the same used for the previously in use muon detectors MW1 (Sec. 2.5.1). The aim of the RichWall detector is to better constraint the track parameters at the RICH exit, to improve the ring resolution of the RICH detector (Sec. 2.6.5) and to act as a preshower for the Ecal1 calorimeter (Sec. 2.5.2). For this reason a converter made of three plates (steel/lead/steel) is inserted in front of each of the four pairs of layers.

2.5 Particle identification

Several detectors are used to provide particle identification: in the LAS a RICH detector allows to identify the hadrons in pions, kaons and protons up to momenta of 60 GeV/c. Two hadron calorimeters (HCAL1 and HCAL2) are used to measure the energy of the hadrons and two electromagnetic calorimeters (ECAL1 and ECAL2) determine the energy of the photons and the electrons. To identified the scattered as well as the produced muons, two muon wall system (MW1 and MW2) are used, both consisting of tracking detectors combined with an hadron absorber. The identification detectors are described in the following Subsections, except the RICH detector, that will be described in Sec. 2.6.

2.5.1 The muon identification

The Muon Wall 1 (MW1) (Fig. 2.10, left) detector is composed of two hodoscopes of wire detectors, called Mini Drift Tubes (MDT), around a 60 cm thick iron absorber. Each MDT module (Fig. 2.10, right) consist of an eight cell aluminium comb extrusion, covered by a stainless steel foil. The pitch of the wires is of 10 mm. Four MDT modules are combined in a station. The active area of the station is $484.5 \times 405 \text{ cm}^2$, with a central hole of $144.5 \times 80 \text{ cm}^2$ for the X planes and an active area of $473 \times 416.5 \text{ cm}^2$ with a central hole of $147.5 \times 76.5 \text{ cm}^2$

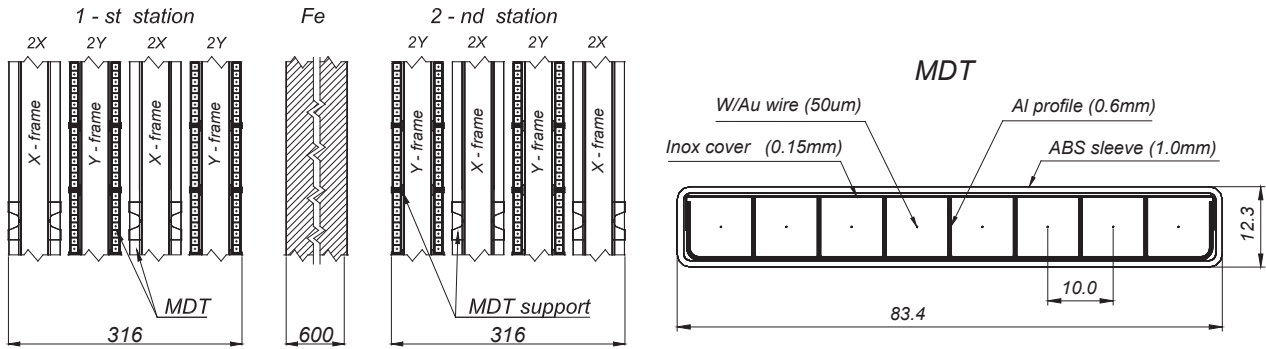


Figure 2.10: Schematic cross section of the MW1 detector (left) and cross section of a MDT module (right).

for the Y plane, the hole matching the acceptance of SM2.

Muon Wall 2 (MW2) is placed at the very end of the spectrometer. The hadron absorber is a 2.4 m thick concrete wall, the tracking upstream the absorber is provided by the SAS trackers, while downstream a dedicated straw drift tubes detector is used. Each of the two straw detector stations is composed by three double layers of tubes, in the X, Y directions and inclined -15° with respect to the vertical. The active area is $447 \times 201 \text{ cm}^2$, with a hole of $100 \times 80 \text{ cm}^2$ in the centre of the detector, around the beam area. The tracking efficiency of these planes is between 81% and 84%.

2.5.2 The electromagnetic and hadronic calorimeters

Each of the two spectrometers is equipped with a pair of calorimeters, an electromagnetic one and a hadronic one.

ECAL1 and ECAL2

The size of the ECAL1 calorimeter is $400 \times 291 \text{ cm}^2$. The calorimeter is formed by blocks of three different sizes: in the central region 576 blocks of $38.2 \times 38.2 \text{ mm}^2$ are used ($\sigma(E)/E = 5.4\%/\sqrt{E} \oplus 1.9\%$), in the intermediate regions 580 blocks of $75 \times 75 \text{ mm}^2$ are used ($\sigma(E)/E = 7.0\%/\sqrt{E}$) and in the outer region the size of the 320 blocks is $143 \times 143 \text{ mm}^2$ ($\sigma(E)/E = 4.3\%/\sqrt{E} \oplus 3.2\%$).

The ECAL1 information is used to trigger on the events (Sec. 2.7), and during the data analysis this trigger component was found to be unstable (Sec.3.2). During a study of the calorimeter performance [42], it was found that the use of the RichWall detector as a preshower caused a degradation of the performance of the ECAL1 in 2007 data-taking run. On a π^0 calibration sample it was found that the energy reconstruction was smeared by the presence of the preshower and that there was a significant loss of information for low energy ($E < 5 \text{ GeV}/c$) particles.

The ECAL2 calorimeter consists in a matrix of 64×48 lead glass modules with $38 \times 38 \times 450 \text{ cm}^3$ dimensions amounting to 16 radiation lengths. The incident electron or gamma forms a shower that emits Cherenkov light proportionally to the deposited energy. Each cell is read out by a phototube. The calorimeter had an hole of 10×10 modules in the centre to allow the passage of the beam particles. The energy resolution in the GeV region is $\sigma(E)/E = 5.5\%/\sqrt{E} \oplus 1.5\%$.

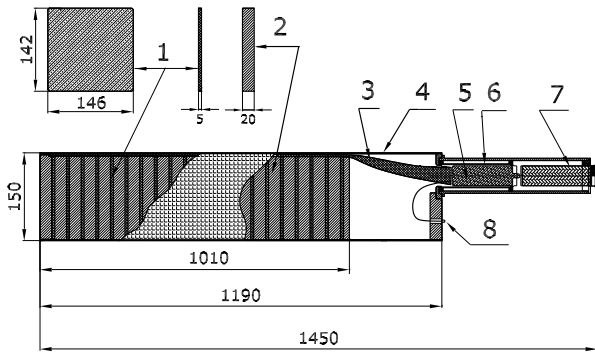


Figure 2.11: Structure of the HCAL1 module: 1-scintillators, 2-iron plates, 3-light guide, 4-container, 5-PMT, 6-PMT magnetic shielding, 7-Cockcroft-Walton divider, 8-optical connector for LED control. Dimensions are in mm.

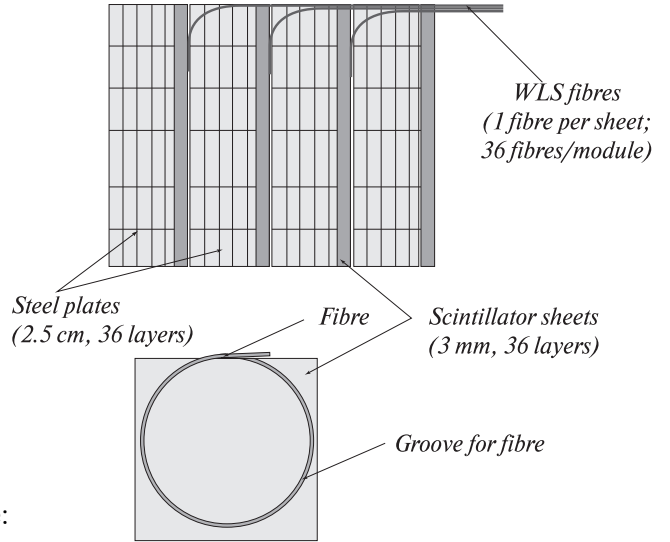


Figure 2.12: Principle of the fibre light readout of HCAL2, top: side view of part of a module, bottom: front view of a scintillator plate with the fibre readout.

HCAL1 and HCAL2

HCAL1 is a sampling hadronic calorimeter, with a modular structure. Each module (Fig. 2.11) consist of 40 layers of iron and scintillating plates, 20 mm and 5 mm thick, amounting to 4.8 nuclear radiation lengths. The modules are assembled in a matrix of 28×20 elements, with 12 modules removed from each corner. In the centre of the matrix a hole of 8×4 modules allows the passage of the beam particles and of the scattered muons that are to be detected in the SAS. The light emitted by the shower is collected by a light-guide positioned on the open side of the scintillator. The energy resolution in the GeV region is $\sigma(E)/E = (59.4 \pm 2.9)\%/\sqrt{E} \oplus (7.6 \pm 0.4)\%$ and the space resolution is $\sigma(x, y) = 14 \pm 2$ mm.

The stability of the response is monitored during the data-taking with a LED system.

HCAL2 hadronic calorimeter is composed by an array of 22×10 modules, with a central hole of 2×2 modules. Each module is a sandwich with 20×20 cm² transverse dimensions. Most of the modules used are 25 mm thick plates intervalled with 5mm thick scintillator sheets. The central 8×6 modules are thicker and consists of 40 layers. The light is collected by a circular wavelength shifting fibre that grooves around the scintillator sheet (Fig. 2.12). The calorimeter has a LED based on-line monitoring system. In the range from 10 to 100 GeV, the energy resolution is $\sigma(E)/E = 66\%/\sqrt{E} \oplus 5\%$

2.6 The RICH-1 detector

The RICH-1 detector [43] is designed to separate kaons from pions in a high-intensity environment, in a momentum range that goes from the Cherenkov threshold to ~ 60 GeV/ c . The detector covers the full spectrometer acceptance (horizontal ± 250 mrad, vertical ± 200 mrad), with the minimum possible material budget, to preserve the resolution of the downstream de-

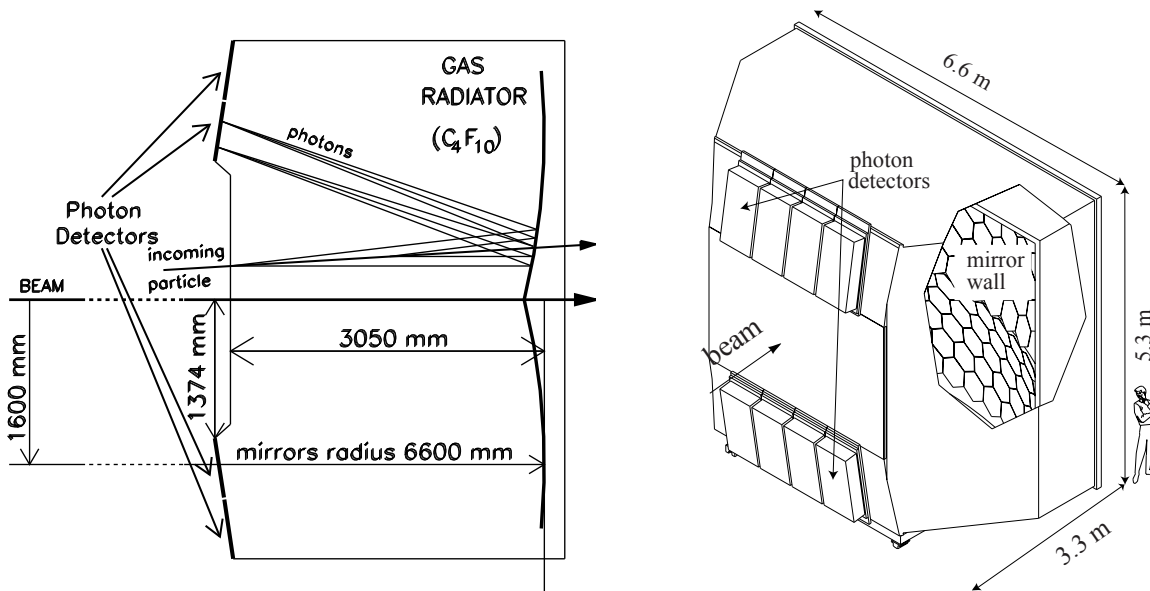


Figure 2.13: A scheme of principle and an artistic view of the COMPASS RICH-1 detector.

tectors (trackers (Sec. 2.4) and calorimeters (Sec. 2.5.2)). RICH-1 is of large size ($\sim 3 \times 5 \times 6 \text{ m}^3$, Fig. 2.13) and is filled with a gaseous radiator (C_4F_{10}) kept at atmospheric pressure. The photon detectors, sensitive to a large wavelength range, from visible to far UV, are placed outside the spectrometer acceptance, one above and the other below the beam line, and the Cherenkov rings are there focalized by two spherical mirrors. The whole structure of the detector vessel is built mainly in thin aluminium. The overall radiation length is only 22.5% of X_0 in the acceptance region.

2.6.1 The radiator gas system

The gas system [44] purifies the radiator gas from water vapour and oxygen contamination and keeps its pressure inside the vessel at the proper value. It is also used to fill the vessel and for the C_4F_{10} recovery.

The gas is constantly circulated to allow its cleaning. Two compressors extract the gas from the bottom of the vessel at a constant rate and a pneumatic valve regulates the incoming gas flux to keep the vessel pressure 1 mbar higher than the atmospheric pressure. The overpressure of the vessel is needed to prevent the air contamination, and the overpressure value is little above to the atmospheric pressure to avoid mechanical stress to the detector, given its large size. A second closed loop circuit (called "fast circulation") allows a reshuffling of the gas inside the vessel, to avoid stratification, that may cause a gradient in the value of the refractive index from top to bottom.

The gas extracted from the vessel is filtered, to remove polluting contaminants, like water vapour and oxygen, that makes the detector blind. The quality of the gas is monitored periodically (Fig.2.14): an external setup allows the measurement of the transparency of the gas in a wavelength range from 160 nm to 210 nm, that covers the full UV domain of the photon detectors.

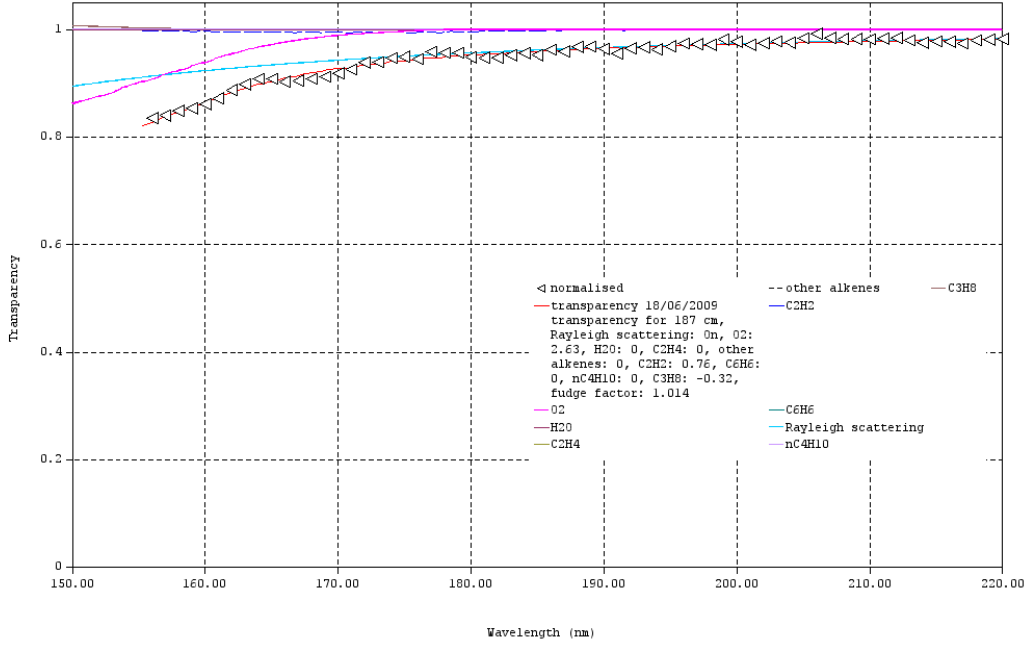


Figure 2.14: Measurement of the transparency of the C4F10. The triangles are the measured points. In red the fit to the data, to extract the percentage of polluting contaminants.

2.6.2 The mirror system

The RICH-1 optical system [45] is composed by two spherical mirror surfaces, with their centres vertically displaced by ± 1600 mm with respect to the beam axis; they localize the image in the two photon detectors (Fig. 2.13.left). The total surface of the mirror system is ~ 22 m² and is a mosaic of hexagonal spherical mirrors (Fig. 2.15, left), pentagons at the borders to avoid saw-teeth patterns. All the mirrors have a reflectance above 80% in the UV region, and their radius of curvature is $R = 6606 \pm 20$ mm in average.

To minimize the possible distortions of the image, the central region of the mirror wall (that with highest occupancy) is equipped with the hexagons with the angle of curvature closest to the nominal value, and going farther, sequences of mirrors minimizing R-variation are chosen. The mirrors are mounted on a net-like mirror wall (Fig.2.15, right), making use of joints that allow the adjustment of the mirror position by rotations on two orthogonal axis. This allowed the mirrors alignment.

The image formed may suffer small distortions, if the mirror radius is different from the nominal one. This effect, that is more pronounced in the outer region, is taken into account in the reconstruction of the photon trajectory inside the detector. The focal plane of the mirrors is a spherical surface and the photon detector plane is its best approximation. This causes a geometrical aberration of 0.32 mrad for images produced by particles incident at small angles and larger for particles produced at larger angles.

2.6.3 The photon detectors

The geometry of a spherical mirror is such as to focalise parallel incident rays in the same point of the focal plane: thus, the distance of the detected photon from the centre of the photon detector depends only on the polar angle of the track at the RICH-1 entrance (θ_{RICH}). Since COMPASS is a fixed target experiment, there is a strong correlation between the particle mo-

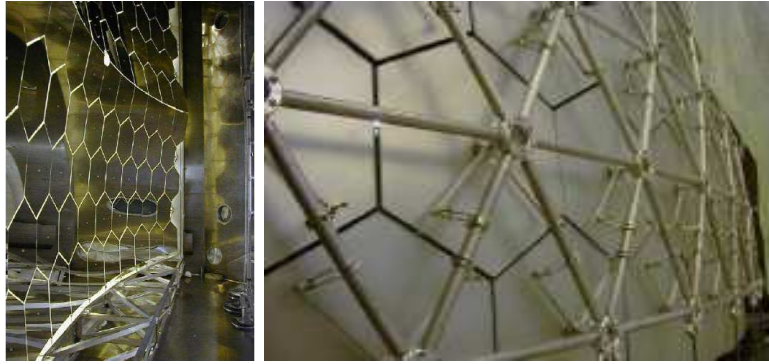


Figure 2.15: Details of the mirror system: the mirror wall, composed by a mosaic of hexagonal units (left) and the net-like support (right).

mentum and the polar angle of its track: low momentum particles are mainly detected in the outer part of the detector. The Cherenkov effect saturates with the momentum: the Cherenkov angles produced by different particles become closer as momentum increases, and thus the resolution needed for PID at high momentum is higher than the one needed at low momentum.

The photon detector system is split into two symmetric parts (Fig. 2.13), one above and one below the beam line. Each part is divided in 8 units (Fig. 2.16, left): 6 equipped with Multiwire Proportional chambers (MWPC) and the two central ones equipped with multianode photomultipliers tubes (MAPMT).

The photoconversion in the MWPCs is provided by a CsI photocathode, that is a printed circuit board, segmented into $8 \times 8 \text{ mm}^2$ pads coated with a CsI film. The CsI photoconverts photons in the UV domain, below 200 nm. The MWPC are operated in methane at atmospheric pressure, at low gain ($< 5 \times 10^4$) to preserve the CsI. The read-out system is based on the APV chip, which measures three amplitude samples on the rising edge of the signal and has a negligible dead-time.

The units equipped with MAPMTs are arrays of 12×12 multianode photomultipliers, segmented into 16 pixels $4 \times 4 \text{ mm}^2$ each. Each MAPMT is coupled with a fused silica lens telescope (a field lens followed by a concentrator lens), that allows to enlarge the pixel size to a final equivalent dimension of $12 \times 12 \text{ mm}^2$. The wavelength sensitivity goes from the near UV to the visible region, namely from 200 to 650 nm and the gain is high ($> 10^6$). The fast signal rise time ($< 1 \text{ ns}$), makes this kind of detector suitable for high background occupancy regions, like the central part of the detector, where the image of the beam halo (Sec.2.1) is formed. The lens telescope introduces a distortion in the image, that is larger for photons with large incidence angle, mainly due the chromatic dispersion of the photons. With a ray-tracking exercise, the distortion have been estimated to be up to 4 mm.

2.6.4 The Identification algorithms

The photon trajectory inside the detector is reconstructed making use of the Ypsilantis-Seguino algorithm [46]: the trajectory of each photon is calculated, relative to each particle in the event, making use of the guessed emission point and the measured photon impact point, and two polar angles are reconstructed: the Cherenkov angle θ and the azimuthal angle ϕ with respect to the particle plane, i.e. the plane that contains the particle track and its virtual reflection in the mirror. The photons emitted by the considered particle are expected to have the same Cherenkov angle θ and a uniformly distributed ϕ , while the uncorrelated photons (photons emitted by the other particles, or electronic noise, or out of time hits), are expected to have

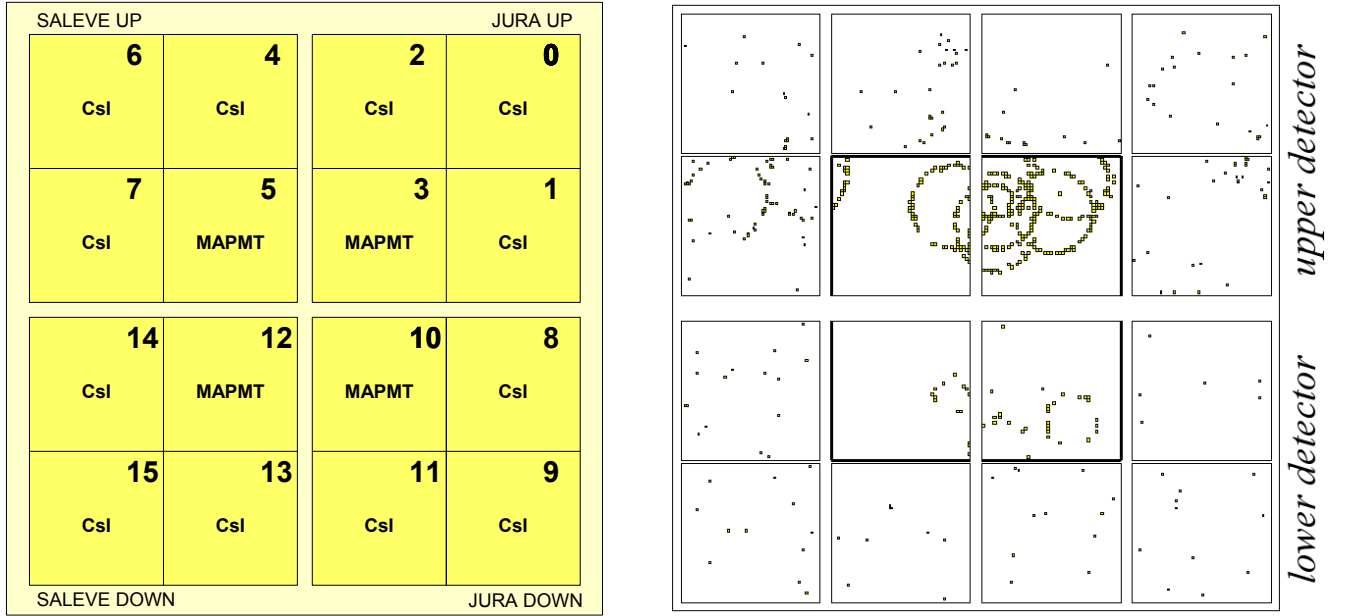


Figure 2.16: Scheme of the photon detector position and an example of event display. The distance between the upper and the lower detector sets is not represented in the plot.

a flat θ distribution. The detector occupancy is not constant and thus also the distribution of uncorrelated photons depends on the position on the photon detector. The background is parametrized as a function of the position coordinates on the detector, and is given as the average cluster distribution in the photon detector, normalized to one event.

The identification algorithm is based on the maximum likelihood estimator [47, 41]: the measured Cherenkov angle of each photon found in a fiducial region F ($\theta < 70$ mrad) is compared with the expected one (θ_M), given, for the mass hypothesis M , by the Cherenkov equation $\cos\theta_M = \frac{1}{n\beta}$. The refractive index value n is measured on the data (Sec. 2.6.5). For each particle the Likelihood function is computed for five different mass hypothesis (e , μ , π , K and p) and for the hypothesis of no signal (the *background*). The expression of the likelihood function is:

$$\mathcal{L}_M = \mathbf{exp}[-(S_M + B)] \prod_{j=1}^N s_M(\theta_j, \varphi_j) + b \quad (2.1)$$

where s_M and b are the signal and the background probabilities, respectively, and S_M and B their integral over the fiducial region. The signal probability depends on the mass hypothesis M :

$$s_M(\theta_j, \varphi_j) = \frac{S_0}{\sigma_{\theta_j} \sqrt{2\pi}} \mathbf{exp}\left[-\frac{1}{2} \frac{(\theta_j - \Theta_M)^2}{\sigma_{\theta_j}^2}\right] \epsilon_D(\theta_j, \varphi_j) \quad (2.2)$$

where $S_0 = N_0 \sin^2 \theta_M$ is the number of expected photons from the Frank-Tamm law and σ_{θ_j} is the single photon resolution of the corresponding detector type. $\epsilon_D(\theta_j, \varphi_j)$ is the photon probability to reach the detector, that takes into account the possible photon losses.

Given the expression of the likelihood, it is possible to use at the same time the contributions from the photons coming from the MWPC and the MAPMT detectors, even if they have a different resolution and are sensitive to different refractive indexes.

The likelihood value is used for the test of the hypothesis: the maximum of the six likelihood values is assumed to correspond to the good hypothesis. It is possible to refine the identifi-

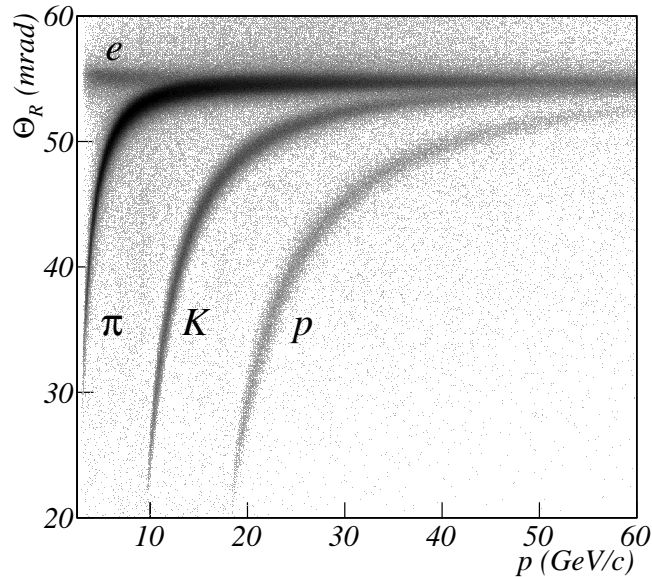


Figure 2.17: The measured Cherenkov angle versus the particle momentum p .

cation algorithm, requiring that the maximum likelihood value over the second maximum is larger than some threshold. This cut is used to reject events in which the separation between two hypotheses is not clear, thus reducing the number of misidentified particles. The cut of the ratio of the maximum likelihood over the background one is not needed: the central region is almost background-free, thanks to the pushed time resolution of the MAPMTs and in the outer region, still equipped with MWPC the number of events that can contribute to the background is low.

The positive particle identification is possible only above the Cherenkov momentum threshold of the particle (Fig. 2.17). In the COMPASS case, the threshold for pions is $p_{thr}^{\pi} = 2.8$ GeV/ c , for kaons is $p_{thr}^K = 9.5$ GeV/ c and for protons $p_{thr}^p = 18.9$ GeV/ c .

Thanks to the likelihood algorithm, it is possible to perform also "below threshold" identification: the particle below threshold does not emit photons and is identified if the *background* hypothesis has the highest likelihood. This is possible only if the "real" background contribution is negligible, as it is for the MAPMT detectors. The efficiency for identification below threshold, in the MAPMT region is above 90%, and has been tested on a sample of K coming from the decay channel $\phi \rightarrow KK$. Below p_{thr}^K both the protons and kaons does not emit photons, and are identified as *background*, thus below threshold identification of the kaons is only possible in samples that does not contain protons. On the contrary, it is always possible to identify protons in the momentum range $p_{thr}^K < p < p_{thr}^p$.

2.6.5 The detector properties

The particle identification relies on the comparison of the measured Cherenkov angle with the expected one, that is calculated from the particle momentum and the refractive index. The refractive index of a gaseous radiator depends on many parameters, as the gas temperature and pressure, and its purity: it is thus time dependent. The refractive index is measured from the data: all the photons associated to one particle of given momentum are used to compute the refractive index, from the Cherenkov relation, assuming the pion mass. Practically, two refractive indexes are measured, one for the photons detected in the MAPMTs and one for the

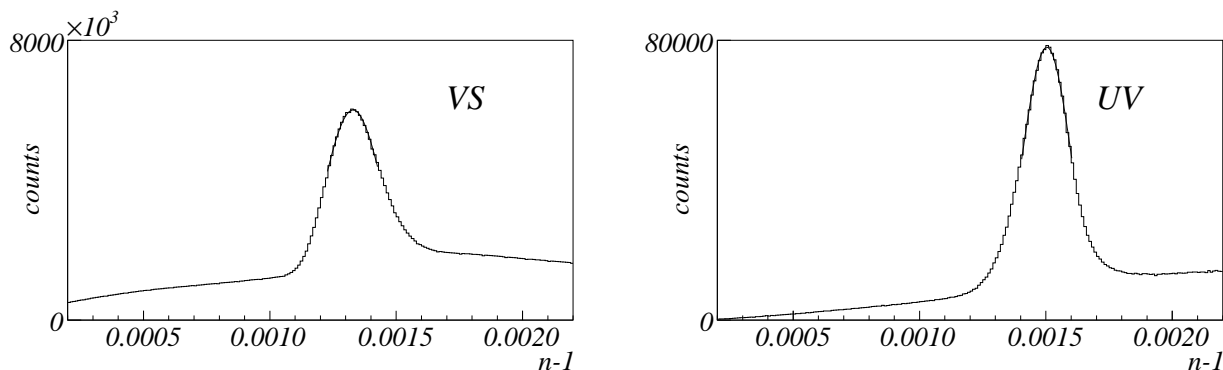


Figure 2.18: The typical refractive index measured from the data, in the visible region (left) and in the UV region (right)

photons detected in the MWPC (Fig. 2.18), since the two detectors are sensitive to photons with different wavelength. The refractive index is measured at fixed time intervals, and the evolution is calculated as a function of the pressure and temperature of the gas, that are continuously monitored (Fig. 2.19), with a precision at the 0.1% level.

For calibration purposes, the Cherenkov *ring* is defined. The *ring* is defined from the expected Gaussian distribution of the Cherenkov angle θ , that corresponds to the experimentally smeared Cherenkov line. The mean value of the distribution is the *ring* angle θ_R and all the photons within the 3σ confidence level are considered photons of the *ring*.

The single photon resolution σ_θ is the error associated to the reconstruction of the Cherenkov angle. It is measured as the Gaussian RMS of the distribution $\theta - \theta_M$, assuming the pion mass hypothesis. The different contributions to the error are the geometrical contribution from the pad size, the chromatic dispersion of the photon, the aberrations due to the spherical mirror system and the chromaticity of the lens telescope for the MAPMT detectors only. The overall single photon resolution is ~ 2.0 mrad for MAPMTs and ~ 2.5 mrad for MWPC (Fig. 2.20).

The *ring* resolution σ_{θ_R} is the width of the distribution of $\theta_R - \theta_M$. In absence of background $\sigma_{\theta_R} = \sigma_\theta / \sqrt{N}$, where N is the number of photons of the ring. σ_{θ_R} is estimated from the data: it is ~ 0.3 mrad for MAPMTs and ~ 1.6 mrad for MWPCs.

2.7 The trigger system

The COMPASS trigger system for the muon program has the task to select DIS and SIDIS events in a high rate environment. The trigger system covers a wide range in y and Q^2 (Fig. 2.22), each region being covered by a different subsystem, each composed by two hodoscope stations: the inner, middle, ladder and outer triggers. The basic idea is to select the events if the muon track points to the target. Due to the large halo of non-interacting muons, a veto system, composed of three stations, is installed before the target and the muons detected in coincidence in the trigger hodoscopes and in the veto hodoscopes are not selected. Despite its efficiency in detecting the halo muons, due to its high occupancy, the veto system introduces

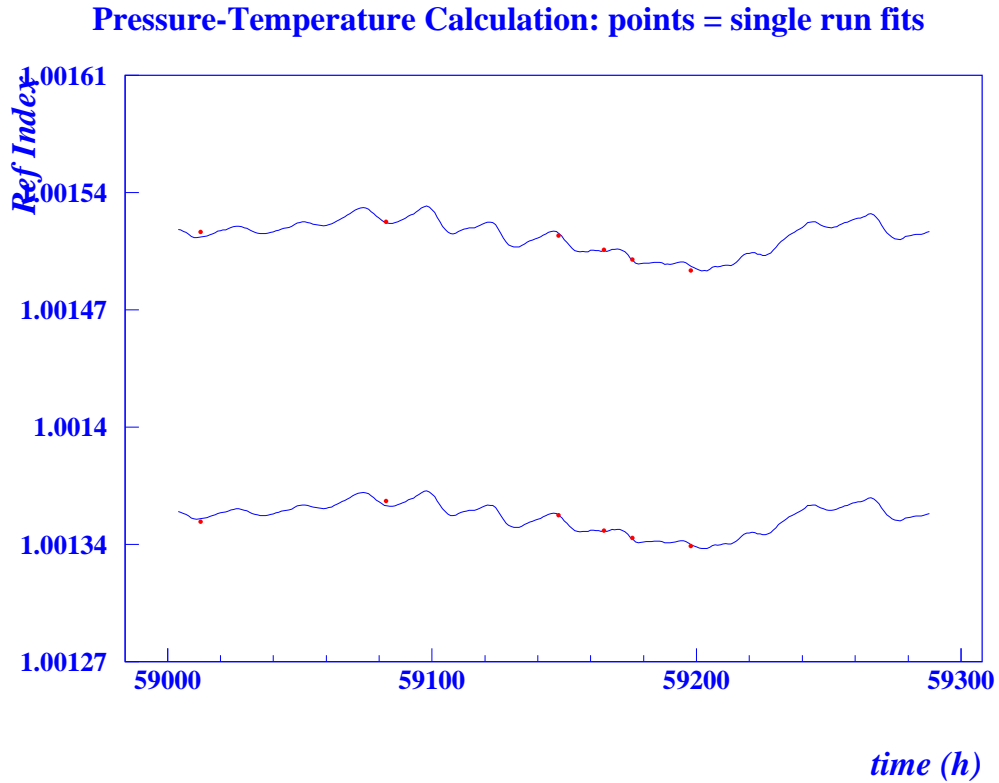


Figure 2.19: An example of the evolution of the refractive index as a function of the time. The solid line is the estimated index from the pressure and temperature variations, the red points are the fit to the data. There is a good agreement between the predicted and the measured value.

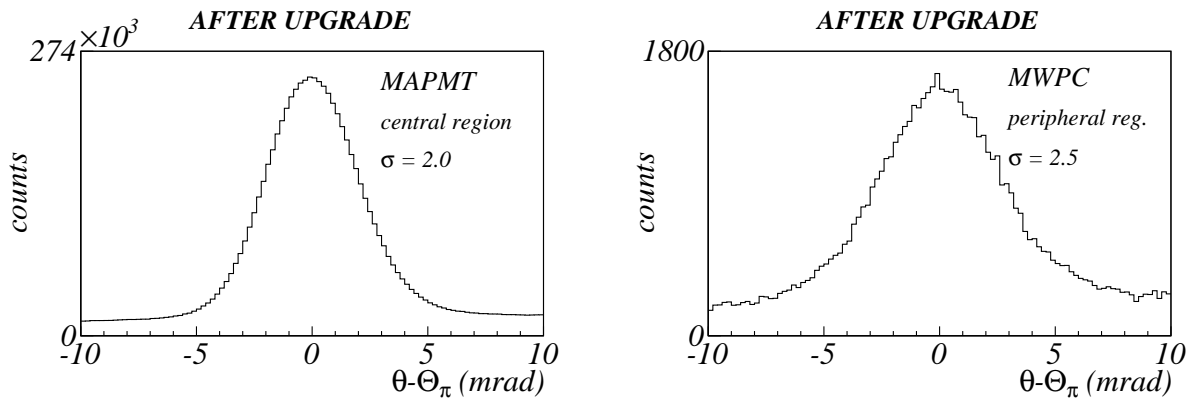


Figure 2.20: The typical single photon resolution for MAPMTs(left) and MWPCs (right).

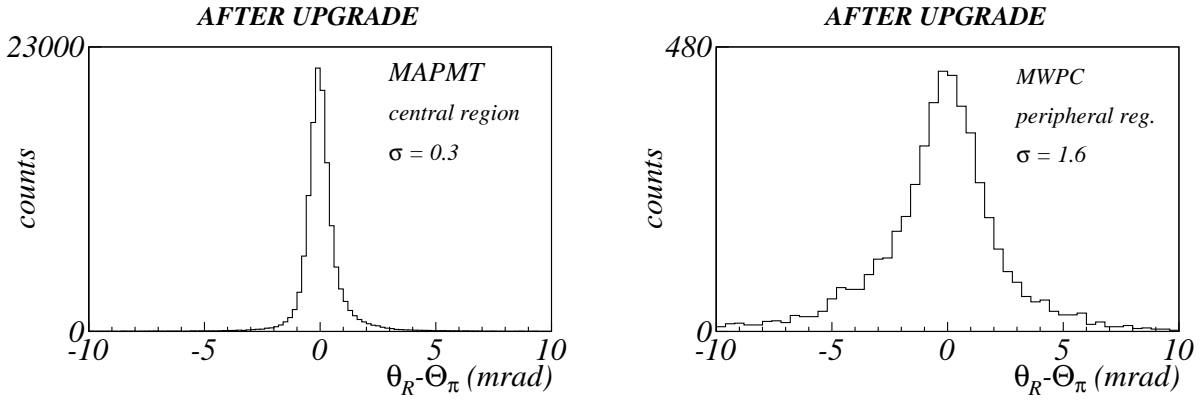


Figure 2.21: The typical ring resolution for MAPMTs(left) and MWPCs (right).

a dead-time of about 20% in the nominal beam conditions.

The inner, ladder and outer trigger signals are built using the target pointing algorithm and cover different spectrometer regions (the position of the trigger hodoscopes is shown in Fig.2.23). The principle of operation of these sub-trigger is to reconstruct the muon trajectory in the ZY plane, where it is not bent by the dipole magnet. The middle trigger, that triggers on the quasi-real photon regime in which the muons scattering angle is close to zero, uses two vertical scintillators to measure the bending of the muon track in the spectrometer magnet.

To select SIDIS events over the large background that have the same signature (elastic electron scattering, elastic and quasi-elastic radiative scattering off target nuclei) the presence of a hadron in the event is required. This is possible thanks to the inclusion of the calorimetric information in the trigger logic: it is required that, in coincidence with the hodoscope trigger, an energy deposit in the calorimeter well beyond the value expected for a single muon is found.

During 2007 data taking the trigger logic was as follows:

| | | | | |
|------------------------|--------------|----------|--------------------------|--|
| Outer Trigger (OT) | OT hodoscope | \wedge | $\overline{\text{veto}}$ | |
| Inner Trigger (IT) | IT hodoscope | \wedge | $\overline{\text{veto}}$ | \wedge (HCAL1 \vee HCAL2 \vee ECAL1) |
| Ladder Trigger (LT) | LT hodoscope | \wedge | $\overline{\text{veto}}$ | \wedge (HCAL1 \vee HCAL2 \vee ECAL1) |
| Middle Trigger (MT) | MT hodoscope | \wedge | $\overline{\text{veto}}$ | \wedge (HCAL1 \vee HCAL2 \vee ECAL1) |
| Pure Calo Trigger (CT) | | | $\overline{\text{veto}}$ | \wedge (HCAL1 \vee HCAL2 \vee ECAL1) |

2.8 The Data Acquisition

The general layout of the data acquisition system (Fig. 2.24) is as follows: the analogue signals of the detector are pre-amplified, discriminated, digitized and buffered at the front-end electronics, by custom made TDC or ADC modules, reducing the cable length and thus the signal degradation. Upon the arrival of a trigger signal, provided by the Trigger Control System (TCS), the data are transferred via fast links to the read-out modules named CATCH or GeSiCA, that combine the data from up to 16 cards and transmit them via an optical S-Link to the readout buffer (maximum through output 160 MB/s), where they are stored in 512 MB spill buffer cards. The event building takes place on- and off-spill, with an average data rate of 70 MB/s and the data are transferred to the CERN data recording facility (CASTOR).

The TCS distributes the trigger, time reference and event identification information to the readout modules. The controller synchronizes the data taking with the accelerator duty cycle

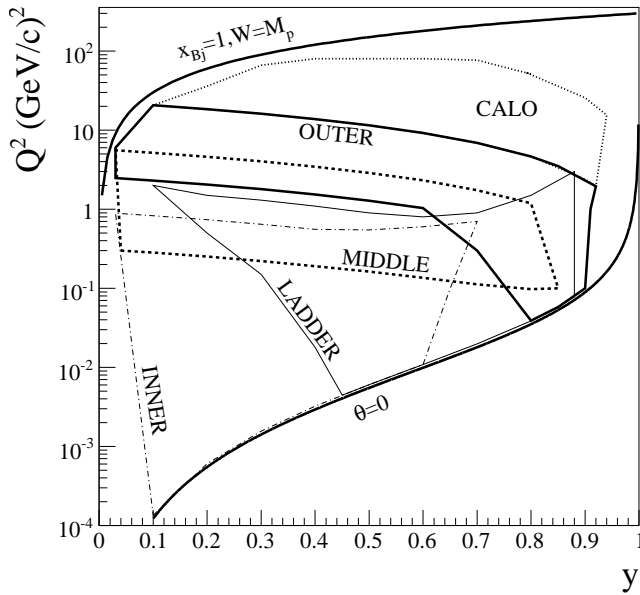


Figure 2.22: The kinematical coverage in y and Q^2 for the four hodoscope trigger subsystems and the standalone calorimetric trigger. The two lines, $x_{Bj} = 1, W = M_p$ and $\theta = 0$ show the kinematic limits of elastic scattering and forward scattering, respectively.

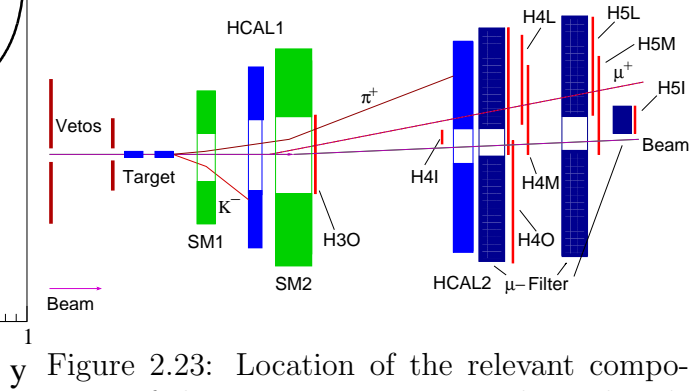


Figure 2.23: Location of the relevant components of the trigger system. For the real scale see Fig.2.1

and generates the dead-time interval between two consecutive triggers.

To improve the purity of the trigger and reduce the number of recorded events, an on-line filter is implemented. For the muon program, the filter algorithm provides a simplified reconstruction of the scattered muon track, based on the time coincidence between the trigger time and the BMS time.

2.9 The Event Reconstruction

The off-line analysis of the events is performed by CORAL, the COmpass Reconstruction ALgorithm, an object-oriented modular program written in C++ (Fig.2.25). The input to the reconstruction are the raw data collected by the experiment, or the MonteCarlo data provided by the dedicated software. The flow of the program is as follows: the digitized data provided by the front-end electronics are decoded, i.e. the information on the fired detector channels is extracted. In a second step, the information is clustered: the detector channels that were fired by the same particle are grouped together, and the coordinate of the cluster in the experiment reference system is extracted. In this phase the calibration constants of the detectors are used and also the informations on the detector position. The position of the detectors as measured by the surveyors are the starting point of alignment of the apparatus: using the halo muons of a low intensity beam, the position of the detector is fine-tuned minimizing the χ^2 of all the reconstructed tracks simultaneously.

The tracking and momentum reconstruction takes place after the clusterisation. First the detector is divided in five zones: upstream the target, from the target to SM1, from SM1 to SM2, from SM2 to muon filter and after the muon filter. In each of these zones the linear tracks

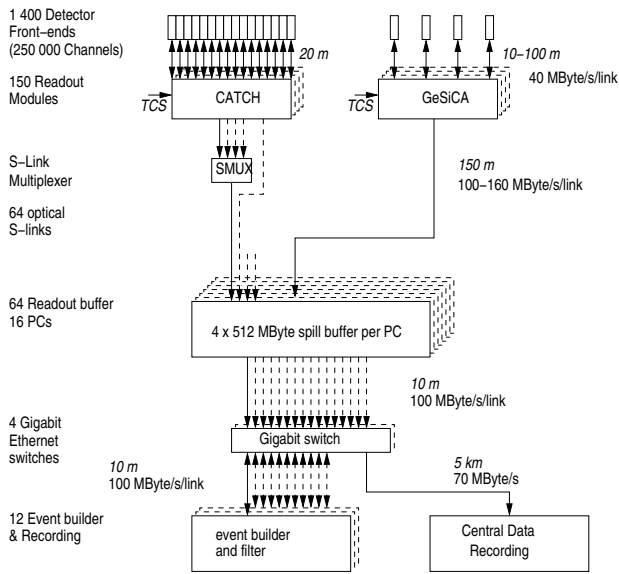


Figure 2.24: General architecture of the DAQ system. Digitized data from the detector front-ends are combined on the readout modules named CATCH and GeSiCA close to the detectors. The storage of the data during the spill and the event building is performed locally. The data are recorded at the CERN computer centre.

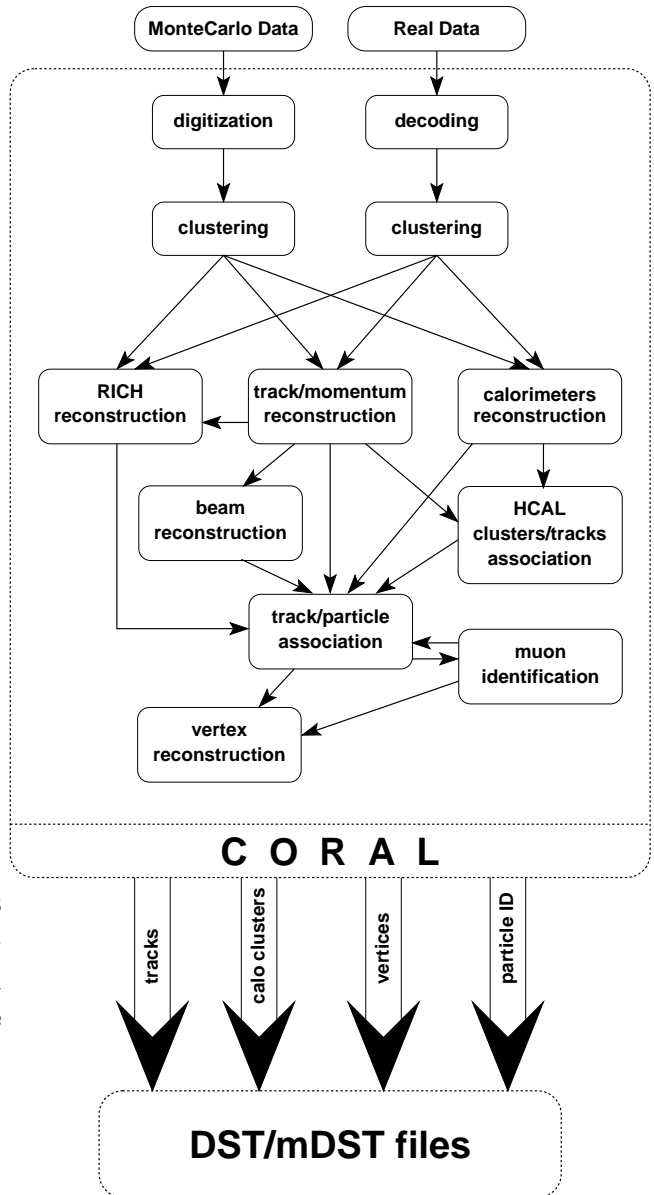


Figure 2.25: Schematic representation of the COMPASS reconstruction software.

segments are reconstructed. The connection of the track segments (bridging) of two adjacent zones is made by using a lookup table of all the possible tracks, and selecting as track candidates the combinations with the best χ^2 . As a last phase, the parameter of the track candidate are estimated with the method of the Kalman fit, that starts from the first cluster position and adds iteratively the following clusters, taking into account the magnetic field and the material budget crossed by the particle.

Once all the tracks in one event are reconstructed, the scattered muons are found, as those particles which track is compatible with the hits registered in the trigger hodoscope and that also have a minimum number of hits downstream one of the hadron absorbers. A vertex finding algorithm is applied. The position of the primary interaction point, i.e. the position of the DIS vertex (*primary vertex*) is found using the beam and the scattered muon tracks, as well as the other particle tracks, if their distance of closest approach to the vertex position is not too large. The vertex position is then refined by an inverse Kalman fit algorithm. In a second phase the decay vertices of neutral particles (*secondary vertex*) are found.

For each track the particle identification is carried on, both for charged particles (RICH and calorimeters) and neutral ones (calorimeters only).

The informations, grouped on an event-basis, are stored in a ROOT structure called MDST (Mini Data Summary Tape), that is distributed among the local computing farms. These MDSTs are analysed using Phast (PHysics Analysis Software Tools), a customizable C++ collection of libraries for physics analysis.

Chapter 3

The extraction of the cross section asymmetries

The transverse spin and transverse momentum effects reflect in asymmetries in the azimuthal distributions of the produced hadrons that depends on the direction of the nucleon spin: the measurement of the asymmetries is done comparing the distributions obtained with the two opposite polarizations of the target.

To detect these asymmetries, that are expected to be at the percent level, great care is reserved to the reduction of the possible systematic effects. The approach used in COMPASS consists in measuring at the same time the two opposite state of polarization, making use of the three cells polarized target (described in Sec. 2.2). Moreover, two consecutive weeks of data taking in which the polarization of the target is reversed are coupled to cancel all the contributions to the asymmetries coming from the spectrometer acceptance.

A DIS event is tagged by the presence of the scattered muon: any instability in its detection, due to some change in the trigger conditions or to detector failures that affect the reconstruction of the produced hadrons, is a source of false asymmetries: the stability of the spectrometer is a main issue for the measurements.

In this Chapter all the steps needed to define the final sample of data will be discussed: first the removal of the short time instabilities, then the selection of good SIDIS events and the removal of bad runs on a statistical basis and, at the end, some quality test based on physical observables. At the present time the Collins and Sivers asymmetries play an important role in the description of the nucleon structure, while the interest in the other asymmetries is not so pronounced. For this reason, all the studies done are developed to measure the Collins and Sivers asymmetries, and then applied to the other 6 asymmetries.

The extraction of the asymmetries will be described. Three methods are used to extract the asymmetries from the data: a one dimensional binned algorithm, a bi-dimensional binned algorithm and an unbinned approach that makes use of the extended maximum likelihood formalism. The method described here will be used for the asymmetries extraction described in Chap. 4 and Chap. 5.

The original work presented in this Chapter consist in the setup of the quality tests based on the physical observables, the study of the acceptance effects with the binned algorithms and the extraction of the asymmetries with the methods described.

| Period name | Week | U(%) | C (%) | D (%) | Polarization | integrated muon flux (10^{12}) |
|-------------|------|-------|-------|-------|--------------|------------------------------------|
| W25 | W25 | 89.87 | 90.35 | 85.38 | ↓↑↓ | 5.2 |
| | W26 | 85.07 | 86.82 | 78.44 | ↑↓↑ | 4.0 |
| W28 | W27 | 83.58 | 83.94 | 79.76 | ↓↑↓ | 3.8 |
| | W28 | 90.56 | 89.58 | 86.11 | ↑↓↑ | 4.2 |
| W30 | W30 | 88.31 | 86.83 | 81.84 | ↓↑↓ | 2.6 |
| | W31 | 84.57 | 87.53 | 76.09 | ↑↓↑ | 3.9 |
| W39 | W39 | 95.68 | 92.65 | 94.26 | ↑↓↑ | 3.9 |
| | W40 | 85.58 | 89.96 | 84.89 | ↓↑↓ | 2.6 |
| W41 | W41 | 90.09 | 91.84 | 86.93 | ↓↑↓ | 3.1 |
| | W42 | 91.11 | 89.89 | 89.39 | ↑↓↑ | 4.6 |
| W42 | W43 | 73.54 | 87.88 | 76.63 | ↓↑↓ | 1.8 |

Table 3.1: Summary of the 2007 data taking. The conventional *period* name, the average target polarization (the upstream target cell-U-, the central cell-C-, the downstream cell-D are shown separately) and spin direction (w.r.t. the lepton beam) are shown, as well as the corresponding integrated muon flux.

3.1 Data sample

In 2007 COMPASS took data with a polarized proton target. The full data-taking period was shared almost equally between the longitudinal polarization program and the transverse polarization program. The configuration of the spectrometer for the two programs differs by the polarization of the target and the position of the trackers before the target, that lay in the fringing field of the target magnets, needed to account for the different trajectories of the incoming muons, and for the settings of the last dipole magnets of the beam line (Sec.2.1). The integrated flux of $\sim 42 \times 10^{12}$ muons recorded in transverse mode is divided into 11 *weeks*, slots of time dedicated to data taking in which ordinary detector maintenance is not allowed. The full transverse data taking was not continuous: the first six *weeks* were at the beginning of the data-taking period and the last five at the end. In between longitudinal data taking took place. Two consecutive *weeks* with opposite polarization are coupled in a *period*; by convention the first *week* of the *period* is that with the first target cell polarized upwards. In Tab. 3.1 the average target polarization, the *period* name and the recorded muon flux are shown. For practical reasons, *week* W42 is split in two parts for data analysis, the first is coupled with W41 and the second is coupled with W43.

3.2 Data quality tests

The first step in data selection consists in the search of beam or spectrometer instabilities. This task is performed monitoring some "macro variables" of the event reconstruction, namely: the number of reconstructed beam tracks per vertex, the number of outgoing tracks per vertex and the number of primary vertexes per event. The primary vertexes are the vertexes of the μ proton interaction, and are the only used in the present data analysis. The time-unit used is the *spill*, that corresponds to a bunch of delivered muons (see Sec. 2.1). The stability of the calorimeters, that are used for hadron tagging, is monitored using the mean energy deposit associated to a single particle (*cluster*) and the number of recorded *clusters* per event. The stability of the trigger system is also monitored. A detailed list of the variables used is given in Tab. 3.2. An example of the time evolution of a typical variable is shown in Fig. 3.1, where each point represents the mean value of the variable in the spill. A fiducial region of $\pm 3\sigma$ around

| macro variables | trigger informations (inclusive/exclusive) | calorimetry (hadronic/electromagnetic) |
|---|--|--|
| beam particle per vertex tracks per primary vertex primary vertexes per event | number of "middle" triggers number of "ladder" triggers number of "outer" triggers number of "calorimetric" triggers number of "inclusive middle" triggers | charged cluster energy per event charged clusters per event neutral cluster energy per event (Hcals only) neutral clusters per event (Hcals only) |

Table 3.2: Quantities monitored on a spill-by-spill basis

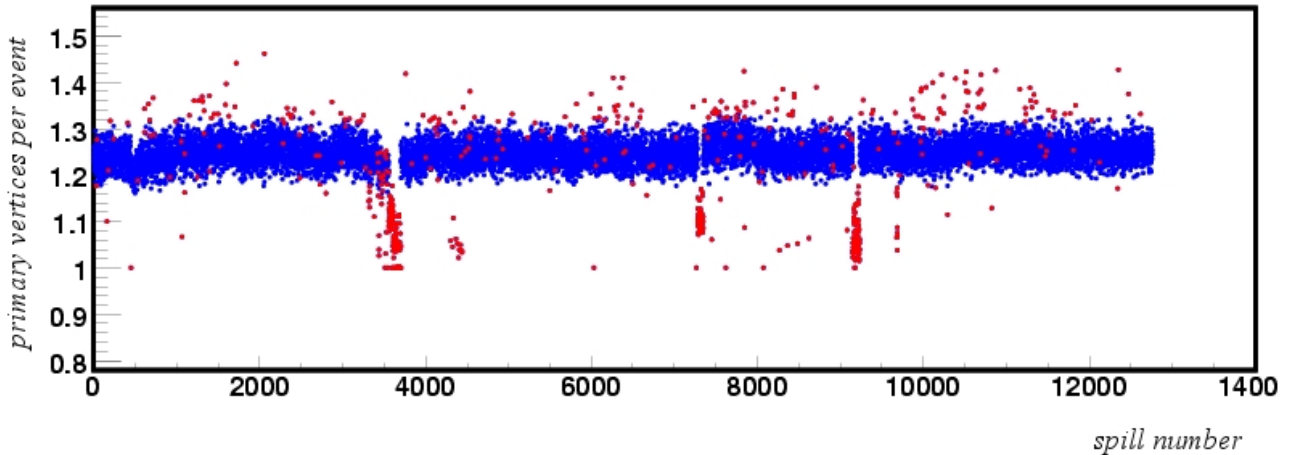


Figure 3.1: Number of primary vertexes per event as a function of the spill number. The spills tagged as bad are plotted in red.

the mean value (probability 99.7%) is defined and all spills out of the fiducial region are tagged for rejection (red points in figure).

A particular care is used in the study of the stability of the trigger system. Each trigger type covers a different kinematical region, thus a variation in the efficiency of one of the triggers between two *weeks* may mimic a physical asymmetry depending on the target polarization. For this reason the number of triggers per event is monitored, for each trigger type, both in the *inclusive* case, i.e. when the specific trigger fired in coincidence with another one and in the *exclusive* case, i.e. when only the considered trigger fired.

Although rejecting a trigger means reducing the kinematical acceptance of the apparatus and then reducing the statistics, in case of instabilities, a trigger has to be excluded from the data analysis to avoid the introduction of false asymmetries. In the present analysis, the pure calorimetric trigger due to ECAL1 (Sec. 2.5.2) was not used.

A more significant tool that is used to monitor the data-taking stability, is the reconstruction of the K_s^0 mass spectrum. The K_s^0 s are identified from their decay in $\pi^+ \pi^-$ using the invariant mass technique. The number of K_s^0 found is used as a stability monitor. Due to the small production cross section, the number of K_s^0 per *spill* suffers from statistical fluctuations, thus another time units is used: the *run*. A *run* is the storage unit of the data and in principle is composed by 200 *spills*.

If the mean number of reconstructed K_s^0 per primary vertex differs for more than 3σ from the *period* mean value, the run is rejected. This procedure leads to the rejection of about 3% of the *runs*. The measured K_s^0 mass, compared with the value known from literature (PDG), as

well as the mass resolution, are used as estimators of the quality of the reconstruction.

Further tests have been done on distributions obtained from the selected SIDIS events, as will be described in Sec. 3.4.

3.3 SIDIS Event selection

In COMPASS standard analysis, an event is defined by its primary vertex, i.e. a vertex with at least one incoming beam muon and one outgoing scattered muon (μ'). The incoming muon must have the track defined by the scintillators upstream the target and the momentum defined by the beam momentum station (Sec. 2.1.1). The trigger of the experiment is based on the detection of a muon, compatible with the kinematics of a scattered muons in a DIS event, in one of the trigger hodoscopes. In this case it is checked that the μ' identified in the event reconstruction is also responsible for the trigger of that event. There is also the possibility to trigger on an energetic hadron, using the energy deposit in the calorimeters. In this case it is required that the reconstructed μ' of the event is identified by one of the muon filters (Sec. 2.5.1).

The vertexing procedure may identify more than one primary vertex in the same event, the different vertexes coming from independent fits of the possible combinations of the μ' tracks with different beam tracks. In the analysis the *best primary vertex* is used: it is defined as that with the highest number of outgoing tracks. In the case that more primary vertexes have the same number of outgoing tracks, that with the best χ^2 is chosen.

Since the kinematics of the event is defined by the track of the scattered muon, a search of alternative μ' candidates is done on all the outgoing tracks of the events. To define a particle as a muon, its trajectory along the spectrometer is examined. The number of radiation lengths that are crossed, due to the presence of the detectors, the magnet yokes and the muon filters, is taken into account and the particle is defined a muon if more than 30 radiation lengths are crossed. Tracks that have hits in the muon filters automatically fulfil this condition. In the case that more than one muon which originates from the primary vertex is found in the event, the event is rejected because the μ' is not distinguishable from the other muons found. Moreover, all the events in which the μ' track crosses the SM2 magnet yoke are rejected, since a description of the magnetic field inside the yoke is not available: thus the reconstruction of the particle momentum is not reliable.

The target is described in Sec. 2.2. The interaction of interest for this analysis occurs only inside the target active volume, i.e. in one of the three cells. The interactions that occur on the target structure between as well as around the cells are rejected with a cut on the position of the vertex. The muon flux across the target is equalized, i.e. only the events for which the extrapolated beam track crosses all the three target cells are used.

From all the good events, those belonging to the DIS kinematical region are selected applying some standard cuts: the minimum photon virtuality Q^2 is required to be larger than $1(\text{GeV}/c)^2$, the fractional energy y of the virtual photon between 0.1 and 0.9 to reduce the radiative effects and the invariant mass of the hadronic final state W above $5 \text{ GeV}/c^2$ to cut off the resonance region.

The definition of a hadron is the following. At first, the outgoing tracks other than the μ' are analysed and muons and electrons present in the sample are rejected. This is done by looking at the energy deposit in the hadronic calorimeters: the energy deposit, due to electromagnetic interaction only is smaller than that expected from hadrons. To reject these particles a cut on the minimum energy deposit is applied at 4 and 5 GeV on Hcal1 and Hcal2, respectively. The reconstruction quality of the other particles is then checked: the reduced χ^2 of the track

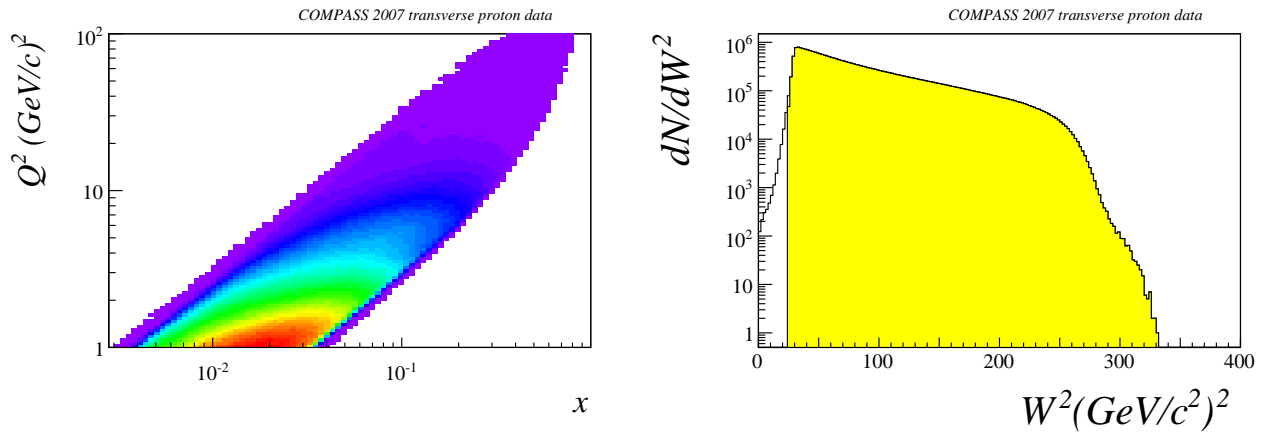


Figure 3.2: Q^2 versus x distribution of the events accepted for this analysis (left) and W^2 distribution.

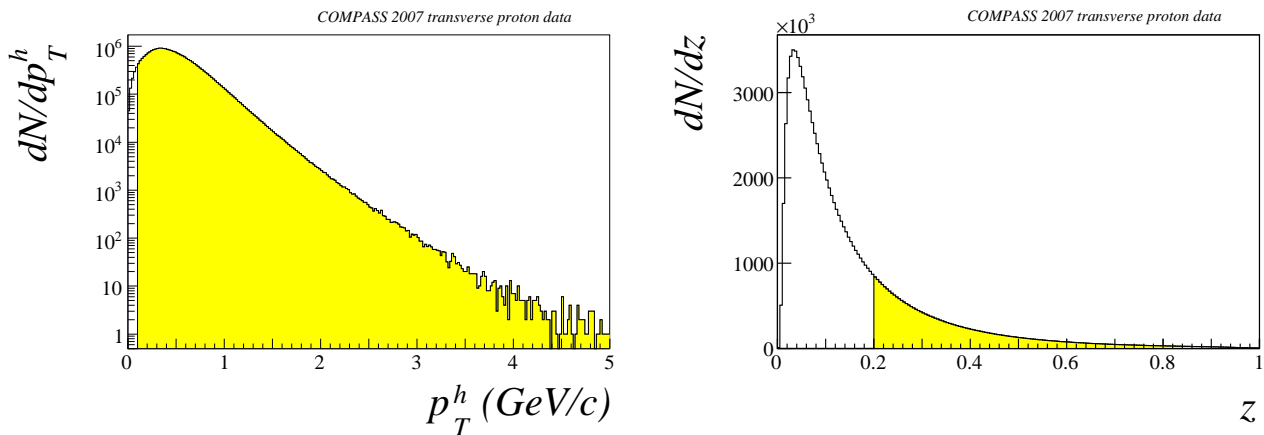


Figure 3.3: Distribution of the transverse momentum p_T^h of the hadrons accepted for this analysis (left) and of z (right)

has to be smaller than 10 and the tracks reconstructed in the fringe field of the magnets (i.e. tracks which last measured point is before the SM1 magnet, Sec. 2.3) are rejected. Further requirements are applied: the transverse momentum p_T^h of the hadron has to be larger than 0.1 for a good angular resolution and the hadron relative energy $z > 0.2$, to discard events coming from the target fragmentation region (Sec. 1.2).

The final event distribution depends partly on the COMPASS acceptance (both due to the geometry and to the trigger system) and partly from the cuts applied.

The x vs. Q^2 distribution is presented in Fig. 3.2 (left), where the strict correlation between the two variables is visible, due to the spectrometer acceptance. Most of the statistics is concentrated at small values of x and consequently small values of Q^2 , but nevertheless the whole x range is covered, from 0.003 to 1. At high x , Q^2 values up to 100 (GeV/c)² are reached.

The distribution of the invariant mass W of the hadronic state produced in the reaction is shown in Fig. 3.2 (right), the distribution of the hadron transverse momentum p_T^h and of the hadron relative energy z are shown in Fig. 3.3 left and right, respectively. The yellow plot represents the selected events, while the white plot represents the events found after all the cuts of the analysis are applied but that of interest.

| | all spills | good spills | good spills after run selection | fraction of good spills |
|------|------------|-------------|---------------------------------|-------------------------|
| W25 | 3 424 273 | 2 657 850 | 2 166 696 | 0.63 |
| W26 | 3 077 285 | 2 599 108 | 2 398 197 | 0.78 |
| W27 | 4 688 217 | 2 162 521 | 1 634 817 | 0.35 |
| W28 | 5 671 100 | 3 243 816 | 2 876 400 | 0.51 |
| W30 | 3 675 715 | 3 434 067 | 2 971 904 | 0.81 |
| W31 | 5 499 483 | 5 197 775 | 4 139 874 | 0.75 |
| W39 | 4 681 875 | 3 821 185 | 3 147 164 | 0.67 |
| W40 | 2 631 480 | 2 191 519 | 2 131 710 | 0.81 |
| W41 | 3 598 786 | 3 185 375 | 2 867 328 | 0.80 |
| W42a | 3 556 175 | 2 545 595 | 2 085 990 | 0.59 |
| W42b | 1 433 629 | 1 314 075 | 1 209 303 | 0.84 |
| W43 | 1 966 820 | 1 422 473 | 1 317 508 | 0.67 |

Table 3.3: Summary of the number of good spills recorded in each *week* after the cleaning procedures.

3.4 The cleaning procedure

On the final hadron sample the shape of the distribution of the main kinematical variables, Z_{prim} , $E_{\mu'}$, $\Theta_{\mu'}$, $\phi_{\mu'}$, x_{bj} , Q^2 , y , W , E_{had} , Θ_{had} , Φ_{had} , p_t , z , ϕ_h and ϕ_s , is monitored on a run-by-run basis. It is expected that the distribution, normalized to the number of events, of each different run is statistically compatible with that of the *period*. A $\chi^2_{ij} = \sum_{bins} \frac{(N_{bin}^i - N_{bin}^j)^2}{N_{bin}^i + N_{bin}^j}$ is then computed on the difference of the normalized distribution of one *run* (labelled i) with respect to all the other *runs* (j) and a χ^2_i distribution is built. This distribution has as many entries as the number of *runs* in the *period*. The resulting average χ^2 is compared with the expected one and, if it differs by more than 3.5σ (confidence level 99.9%) for at least one variable, the *run* is marked as bad and excluded from any further analysis. This exercise is done for all the runs in the *period*.

Since the number of spills contained in a *run* is not fixed, the quantity of events that survive the selection is given in term of spills, and it is shown in Tab. 3.3. It has to be said that neither the event content of each spill is constant, depending on the spill length and intensity. The fraction of good spills ranges from a minimum of 35% to a maximum of 84% depending on the *week*. It is clear from the table that the data taking during 2007 was rather problematic.

3.5 Principle of the measurement and the Reasonable Assumption

The SIDIS cross section Eq.(1.30), in case of transversely polarized target, can be written as the sum of 8 independent transverse spin dependent modulations plus an unpolarized part, function of the azimuthal angle of the spin of the target nucleon ϕ_s and of the azimuthal angle of the produced hadron ϕ_h . The expected number of produced hadrons, depending on the length of the target cell l and on the beam flux B is then

$$N(\phi_h, \phi_s) = B l \alpha(\phi_h, \phi_s)(\sigma^0 + \sigma^\pm(\phi_h, \phi_s)) = B l \alpha(\phi_h, \phi_s) \sigma^0(1 \pm \epsilon(\phi_h, \phi_s)) \quad (3.1)$$

where σ^0 is the unpolarized cross section and σ^\pm is the polarized part, the sign \pm depending on the sign of the polarization. $\alpha(\phi_h, \phi_s)$ is the term that represents the COMPASS angular

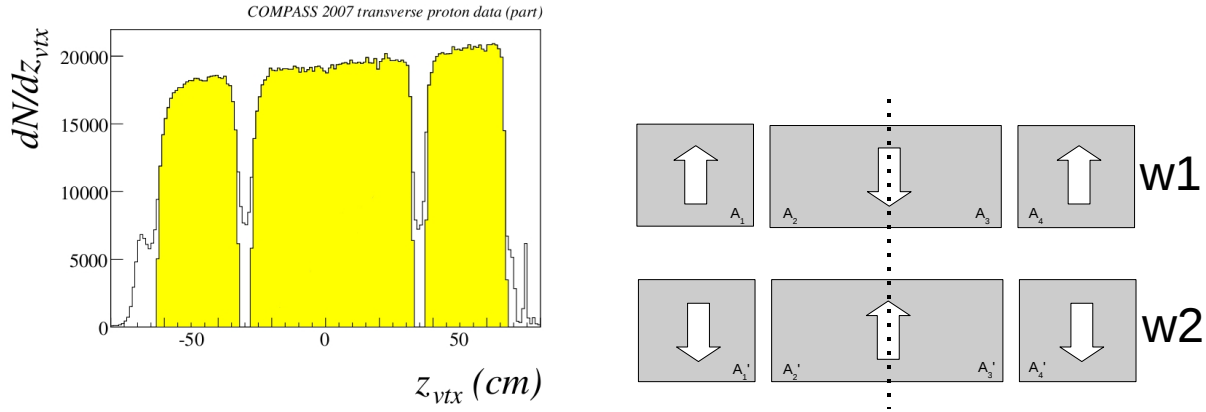


Figure 3.4: Left: the distribution of the interaction vertexes inside the target. The yellow distribution corresponds to the events used in the analysis. The interactions on the target holders are also visible (white). The resolution on the z position of the vertex increases from about 5 mm at the downstream end of the target to about 25 mm in average at the upstream end. Right: the numbering and polarization of the target cells used in the analysis is shown.

acceptance and efficiency, later called only acceptance for brevity.

The COMPASS polarized target (described in Sec. 2.2 and Fig. 3.4) is composed by 3 target cells, the central one being long twice the external ones and oppositely polarized. In the analysis the central cell is virtually split into two halves, to deal with a target composed by four cells of about the same length. To disentangle the polarized part of the cross section from the unpolarized one and from the acceptance modulations, we compare the number of events found in the two opposite state of polarization, building the ratio:

$$F^{QR} = \frac{N_1 N'_2 N'_3 N_4}{N'_1 N_2 N_3 N'_4} \quad (3.2)$$

where N_i is the number of event found in the i^{th} cell of the target in the first *week* of the *period* and N'_i is the number of event found in the coupled *week*, that has the opposite polarization. The unpolarized cross section σ^0 is simplified in the ratio, as well as the target length l . The beam flux across the target cells is equalized (Sec. 3.3), thus, in the ratio of the number of events in the different cells of the same *period*, it cancels out. At first order, assuming that $\epsilon \ll 1$, one obtains that:

$$F^{QR}(\phi_h, \phi_s) = \frac{\alpha_1(\phi_h, \phi_s) \alpha'_2(\phi_h, \phi_s) \alpha'_3(\phi_h, \phi_s) \alpha_4(\phi_h, \phi_s)}{\alpha'_1(\phi_h, \phi_s) \alpha_2(\phi_h, \phi_s) \alpha_3(\phi_h, \phi_s) \alpha'_4(\phi_h, \phi_s)} \left(1 + 8\epsilon(\phi_h, \phi_s) \right) \quad (3.3)$$

and the amplitude of ϵ can be extracted with a fit of F^{QR} with some modulation in ϕ_h and ϕ_s . The extraction of the asymmetry is unbiased if:

$$\frac{\alpha_1(\phi_h, \phi_s) \alpha'_2(\phi_h, \phi_s) \alpha'_3(\phi_h, \phi_s) \alpha_4(\phi_h, \phi_s)}{\alpha'_1(\phi_h, \phi_s) \alpha_2(\phi_h, \phi_s) \alpha_3(\phi_h, \phi_s) \alpha'_4(\phi_h, \phi_s)} = const \quad (3.4)$$

Eq.(3.4) is satisfied if the ratio between the acceptance term of the first and that of the second *week* has the same azimuthal modulation for all the target cells, and it is referred to as the "reasonable assumption" (RA).

It is not possible to test (3.4) from data, but it is possible to build the quantity

$$R(\phi_h, \phi_s) = \frac{N_1 N_2 N_3 N_4}{N'_1 N'_2 N'_3 N'_4} = \frac{B \alpha_1(\phi_h, \phi_s) \alpha_2(\phi_h, \phi_s) \alpha_3(\phi_h, \phi_s) \alpha_4(\phi_h, \phi_s)}{B' \alpha'_1(\phi_h, \phi_s) \alpha'_2(\phi_h, \phi_s) \alpha'_3(\phi_h, \phi_s) \alpha'_4(\phi_h, \phi_s)} \quad (3.5)$$

$R(\phi_h, \phi_s)$ gives the global variation of the acceptance between the two weeks. It is constant if the ratio between the acceptance term of the first and of the second *week* is constant, which is in general a condition stricter than the RA. If $R(\phi_h, \phi_s) = \text{const}$, then the RA holds but, if the modulations are the same between the cells with opposite polarization, the RA can still hold even though $R(\phi_h, \phi_s)$ is not constant. Note that there is an exception: in case the modulation of cells 1 and 4 is opposite to that of cells 2 and 3, the RA does not hold even if R is constant. The azimuthal modulations of $R(\phi_h, \phi_s)$, as well as those of the cross section, are orthogonal one another, as can be seen in Appendix B. It is therefore possible to study one modulation at a time integrating over the others. In the following we will refer to $R(\phi)$ as the integral on all the azimuthal modulations, except that of interest.

To break the reasonable assumption, the acceptance ratio should have the same dependence from the azimuthal angle as the asymmetry. Let us assume that the acceptance (integrated on all the modulations but that on $\sin \phi$) is $\alpha(\phi) = c(1 + a \sin \phi)$ where c is constant and a is the amplitude of the modulation, with the condition that $a \ll 1$. The ratio of the acceptance terms of the cell i between the two *weeks* is $\frac{\alpha_i}{\alpha'_i} \simeq 1 + (a_i - a'_i) \sin \phi = 1 + e_i \sin \phi$, where the multiplicative constant has been neglected since it gives no contribution to the amplitude of the modulation that is under investigation. With this definitions Eq. (3.5) becomes:

$$R(\phi) \simeq 1 + (e_1 + e_2 + e_3 + e_4) \sin \phi \quad (3.6)$$

and Eq. (3.3) :

$$F^{QR} = \frac{N_1 N'_2 N'_3 N_4}{N'_1 N_2 N_3 N'_4} \simeq \left(1 + (8\epsilon + e_1 - e_2 - e_3 + e_4) \sin \phi \right) \quad (3.7)$$

If all the e_i terms are equal, then the reasonable assumption holds. Obviously, it is very unlikely that, if e_i are large, they compensate in F^{QR} .

The statistical error associated to the F^{QR} (and R) is:

$$\sigma_{F^{QR}} = F^{QR} \sqrt{\frac{1}{N_1} + \frac{1}{N_2} + \frac{1}{N_3} + \frac{1}{N_4} + \frac{1}{N'_1} + \frac{1}{N'_2} + \frac{1}{N'_3} + \frac{1}{N'_4}} \quad (3.8)$$

Since $F^{QR} - 1 \sim 0$, F^{QR} is considered as 1 in the previous definition.

It is possible to define other combinations of the measured number of events to extract the asymmetries. They are mainly used for systematic studies.

The Double Ratio method (DR) makes use of only two cells at a time, thus it is possible to extract two independent measurements of the asymmetry in the same *period*:

$$F^{DR,0} = \frac{N_1 N'_2}{N'_1 N_2} = \frac{\alpha_1(\phi_h, \phi_s) \alpha'_2(\phi_h, \phi_s)}{\alpha'_1(\phi_h, \phi_s) \alpha_2(\phi_h, \phi_s)} \left(1 + 4\epsilon(\phi_h, \phi_s) \right) \quad (3.9)$$

$$F^{DR,1} = \frac{N'_3 N_4}{N_3 N'_4} = \frac{\alpha'_3(\phi_h, \phi_s) \alpha_4(\phi_h, \phi_s)}{\alpha_3(\phi_h, \phi_s) \alpha'_4(\phi_h, \phi_s)} \left(1 + 4\epsilon(\phi_h, \phi_s) \right) \quad (3.10)$$

It has been proven that the weighted average of the two asymmetries extracted with the DR corresponds to the asymmetry extracted with the QR approach within 0.1σ in average.

It is also possible to extract one measurement of the asymmetry from each target cell, with the Single Ratio (SR):

$$F_i^{SR} = \frac{N_i}{N'_i} = \frac{B}{B'} \frac{a_i(\phi_h, \phi_s)}{a'_i(\phi_h, \phi_s)} \left(1 \pm 2\epsilon(\phi_h, \phi_s) \right) \quad (3.11)$$

$$\sigma_i^{SR} = F_i^{SR} \sqrt{\frac{1}{N_i} + \frac{1}{N'_i}} \quad (3.12)$$

where \pm depends on the sign of the polarization of the cell i in the first *week*. This method is much weaker than the DR and the QR: it gives unbiased results only if there is no variation of the acceptance between the two *weeks*. Moreover the beam flux is not washed out in the ratio and no hypothesis can be made on the size of F^{SR} . This method is used for systematical studies only.

3.6 Quality tests

In all *periods* it is checked whether the reasonable assumption holds. Two different tests are done: the first consists in measuring the amplitude of the azimuthal modulations of $R(\phi_h, \phi_s)$, and will be described in Sec. 3.6.1. The second probes possible large variations of the acceptance ratios between the target cells and will be described in Sec. 3.6.2. The two pieces of information are used to define a χ^2 value, which is used to select the data taking *periods* that will be used for the final analysis.

3.6.1 The measurement of $R(\phi)$

The first check is to test if $R(\phi)$ is constant. If this is the case, the R.A. holds.

The χ^2 distribution of the fit of $R(\phi)$ to a constant function is built (later called "R-test") for all the *periods* of the 2007-transverse data taking, with the same binning used to extract the asymmetries, both for the ϕ angle and for the kinematical variables. The latter point is very important: the shape of the angular acceptance is different in the different kinematic bins, due to the different coverage of the various triggers types. Thus there may be bins which are more sensitive than others to possible acceptance variations.

For each *period* the χ^2 distribution has 52 entries, one for each kinematical bin, for positive and negative hadrons. The distributions obtained for the 6 *periods* are shown in Fig. 3.5 for the test of $R(\phi_c) = const.$ as a function of the Collins angle and, in Fig. 3.6, for the test of $R(\phi_s) = const.$ as a function of the Sivers angle. The continuous line in the plots represents the expected χ^2 distribution for the given number of degrees of freedom. The distribution clearly differs from the expected one in *period* W41, both for the Collins and for the Sivers modulations, and for the Sivers modulation in *period* W28.

A more quantitative test is the fit of $R(\phi)$ with some modulation. The amplitude of the modulation, called T , is computed as a function of the angle ϕ in each of the 9 independent x bins, as if it were a physical asymmetry: $R(\phi) = 1 + T \sin(\phi)$. From Eq.(3.6) T results to be the mean variation of the acceptance $\langle e \rangle$ between the two coupled *weeks*, the average being done over the target cells. If $R(\phi)$ is constant, T is compatible with zero.

Two examples of T as a function of x are shown in Fig. 3.7. On the left side of the figure, an example of T compatible with zero, on the right side a case in which T is different from zero and T has a strong dependence on the x variable.

The weighted average over the x bins of T in the 6 *periods* for the Collins and Sivers asymmetries is shown in Tab. 3.4. The mean T for the Collins modulation is not compatible with zero for *period* W39 (positive hadrons) and *period* W41, where the deviation is of the order of three sigmas. T for the Sivers modulation is more than three sigmas away from zero both for *period* W28 and W41. In *period* W25 and W42 the deviation of T from zero for positive hadrons is of the order of three sigmas.

The tests of $R(\phi)$ and of T give access to the same information: all the *periods* that fail the R-test have T different from zero. On the contrary the measurement of T is more sensitive

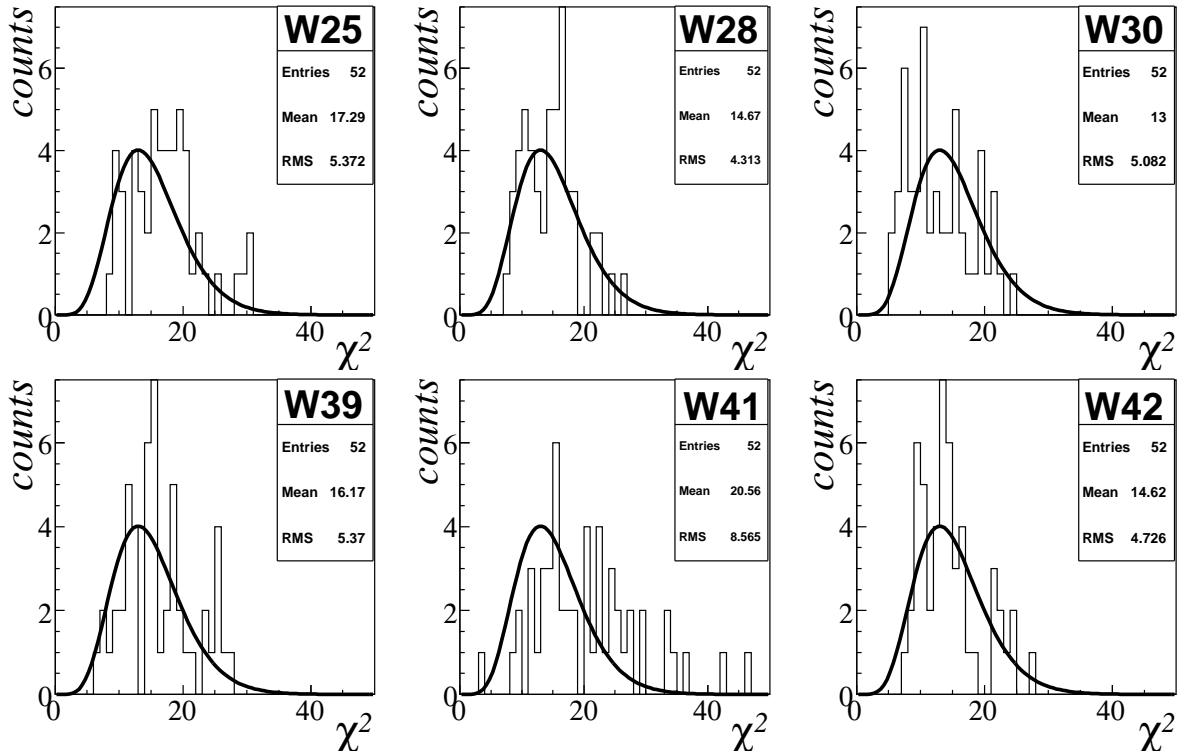


Figure 3.5: χ^2 distributions of the test of $R(\phi_c) = const.$, modulation as a function of the Collins angle . The black curve represents the expected χ^2 distribution for the given number of degrees of freedom. Each plot represents one of the 2007 data taking *periods*.

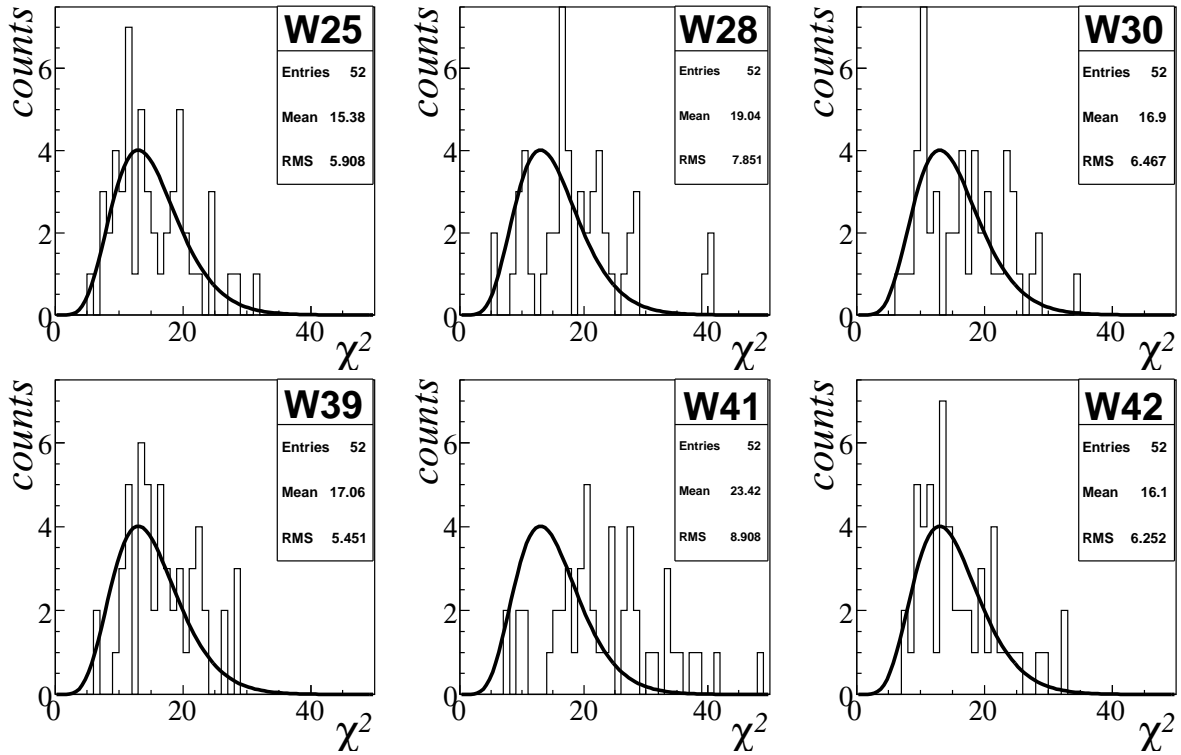


Figure 3.6: χ^2 distributions of the test of $R(\phi_s) = const.$, modulation as a function of the Siverson angle . The black curve represents the expected χ^2 distribution for the given number of degrees of freedom. Each plot represents one of the 2007 data taking *periods*.

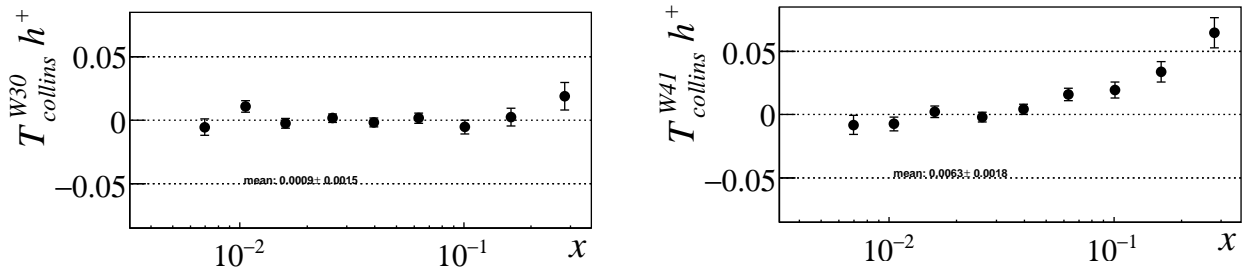


Figure 3.7: Examples of the mean value of the variation of the amplitude T of the acceptance modulation $\sin \phi_{collins}$ as a function of x in a case in which T is compatible with zero (left) and in a case in which T is not compatible with zero (right).

| Collins | | | | | | |
|---------|--------------|--------------|---------------|--------------|--------------|--------------|
| | W25 | | W28 | | W30 | |
| | $h+$ | $h-$ | $h+$ | $h-$ | $h+$ | $h-$ |
| T | -29 ± 18 | -14 ± 20 | -13 ± 19 | 15 ± 22 | 11 ± 15 | -12 ± 17 |
| | W39 | | W41 | | W42 | |
| | $h+$ | $h-$ | $h+$ | $h-$ | $h+$ | $h-$ |
| T | 54 ± 17 | 32 ± 20 | 63 ± 18 | 61 ± 20 | -20 ± 25 | -29 ± 28 |
| Sivers | | | | | | |
| | W25 | | W28 | | W30 | |
| | $h+$ | $h-$ | $h+$ | $h-$ | $h+$ | $h-$ |
| T | -68 ± 18 | 9 ± 21 | -118 ± 19 | -68 ± 22 | -10 ± 15 | 48 ± 17 |
| | W39 | | W41 | | W42 | |
| | $h+$ | $h-$ | $h+$ | $h-$ | $h+$ | $h-$ |
| T | 37 ± 17 | 2 ± 20 | 86 ± 18 | -68 ± 20 | 68 ± 25 | 29 ± 28 |

Table 3.4: Mean value of the variation of the amplitude of the acceptance modulation as a function of $\sin \phi_{Collins}$ and $\sin \phi_{Sivers}$ for the six *periods* of data taking.

than the R-test and reveals instabilities in other *periods*.

3.6.2 The test of the "Reasonable Assumption"

It is possible to extract four independent measurements of the physical asymmetry making use of the four target cells. The asymmetry extracted in each cell is given by the physical asymmetry ϵ plus a contribution depending on the change of acceptance, e_i :

$$\begin{cases} A_1 = \epsilon + \frac{e_1}{2} \\ A_2 = \epsilon - \frac{e_2}{2} \\ A_3 = \epsilon - \frac{e_3}{2} \\ A_4 = \epsilon + \frac{e_4}{2} \end{cases}$$

The sign of the e_i contributions comes from the sign of the cell polarization in the first *week*.

The mean asymmetry and the mean variation of the acceptance are then $\langle \epsilon \rangle = \frac{\sum A_i}{\sum \frac{1}{\sigma_i^2}}$ and

$$\langle e \rangle = \frac{\sum \frac{\pm A_i}{\sigma_i^2}}{\sum \frac{1}{\sigma_i^2}}, \text{ where } \sigma_i \text{ is the error associated to } A_i.$$

If the reasonable assumption holds, all e_i are compatible with their mean value and the following χ^2 with two degrees of freedom can be defined:

$$\chi^2 = \sum_{i=1}^4 \left(\frac{A_i - (\epsilon_{\pm} < e >)}{\sigma_i} \right)^2 \quad (3.13)$$

This χ^2 can be used as a test statistics.

3.6.3 The selection of the *periods* used for the final analysis

To determine the quality of a data-taking *period*, an overall χ^2 is used, that combines the information of the measurement of T and of the test of the RA.

The χ^2 on T compares the measured value with the hypothesis $T = 0$. It is very unlikely that the RA holds for big variation of the acceptance between the two coupled *weeks*, but it was already explained that this request is stronger than the RA. For this reason the measured T is normalized with twice its statistical error. The χ^2 is defined as $\chi_T^2 = \sum \left(\frac{T}{2\sigma} \right)^2$.

The χ^2 of the RA was described in the previous subsection. A final χ_{TOT}^2 value for the *period* is given, using the sum of the two χ^2 defined, for positive and negative hadrons.

Both T and the RA can be tested using the nine independent kinematical bins or the averaged value. The two approaches give a coherent picture, even if the larger statistical error dilutes the effects in the bin-by-bin approach. For this reason only the results based on the integrated values will be considered. The χ_{TOT}^2 values for the Collins and Sivers modulations are shown in Tab. 3.5. All the *periods* are suitable to extract the Collins asymmetries, while the situation for the Sivers asymmetries is more critical: the confidence level well below 1% suggests that *periods* W28 and W41 have to be discarded, and the confidence level of the remaining *weeks* is only marginal. Please note that when a period is discarded, this means that the asymmetry extracted is not used in the final average value. The systematics effects arising from the possible break of the reasonable assumption will be investigated and estimated in Sec. 4.2.2.

The test has been performed also for the other transverse-target cross section modulations: $\sin(3\phi_h - \phi_s)$, $\sin(2\phi_h - \phi_s)$, $\cos(2\phi_h - \phi_s)$, $\cos(\phi_h - \phi_s)$, $\sin(\phi_s)$ and $\cos(\phi_s)$. The confidence level of the test for the first three modulations (Tab.3.6) suggests that all periods are suitable to extract them. For the latter, the confidence level well below 1% (Tab. 3.7) suggests that W28, W39 and W41 should be discarded. To limit the number of data selection used in the analysis it is decided that for the extraction of the $\cos(\phi_h - \phi_s)$, $\sin(\phi_s)$ and $\cos(\phi_s)$ modulations the same periods used to extract the Sivers asymmetry will be used. The contribution to the final result of the asymmetries extracted for period W39 will be investigated in Sec. 4.4.

3.7 The extraction of the raw asymmetries

The asymmetries are extracted as a function of x , W , z and p_T^h , each time integrating over the other variables. The bins used to extract the asymmetries are reported in Tab. 3.8.

There are two main approaches to the extraction of the asymmetries: it is possible to divide the ϕ_h, ϕ_s space in bins or to fit with an unbinned likelihood. The binned approach itself is implemented in two different ways: a one dimensional fit algorithm, that considers only one of the modulations at a time and a two dimensional fit algorithm, in which all the eight modulations of the angles ϕ_h, ϕ_s are considered simultaneously. The differences among the asymmetries extracted with the three methods will be considered as contribution to the systematic error.

The three different methods used will be described in this Section. The extracted asymmetries are the so-called "raw asymmetries". They are the asymmetries in the number of produced hadrons in a SIDIS interaction, as defined in Eq. 1.33 and Eq. 1.37. The raw asymmetries are

| | Collins | | | | | |
|-------------|----------------|-------|---------------|-------|--------------|-------|
| | W25 | | W28 | | W30 | |
| | h^+ | h^- | h^+ | h^- | h^+ | h^- |
| R.A.(NdF=2) | 0.99 | 2.52 | 1.18 | 1.86 | 2.37 | 1.75 |
| T (NdF=1) | 0.64 | 0.12 | 0.12 | 0.12 | 0.13 | 0.12 |
| TOT | 1.63 | 2.64 | 1.30 | 1.98 | 2.50 | 1.87 |
| | 4.27 (64%) | | 3.28 (77%) | | 4.37 (63%) | |
| | W39 | | W41 | | W42 | |
| | h^+ | h^- | h^+ | h^- | h^+ | h^- |
| R.A.(NdF=2) | 4.04 | 0.08 | 3.77 | 0.84 | 4.29 | 1.58 |
| T (NdF=1) | 2.52 | 0.64 | 3.06 | 2.32 | 0.16 | 0.27 |
| TOT | 6.56 | 0.72 | 6.83 | 3.16 | 4.45 | 1.85 |
| | 7.28 (30%) | | 9.99 (12%) | | 6.30 (39%) | |
| | Sivers | | | | | |
| | W25 | | W28 | | W30 | |
| | h^+ | h^- | h^+ | h^- | h^+ | h^- |
| R.A.(NdF=2) | 2.00 | 6.42 | 2.11 | 6.00 | 6.89 | 3.40 |
| T (NdF=1) | 3.75 | 0.05 | 9.69 | 2.38 | 0.11 | 1.99 |
| TOT | 5.57 | 6.47 | 11.75 | 8.39 | 7.00 | 5.39 |
| | 12.04 (6.1%) | | 20.13 (0.26%) | | 12.4 (5.4%) | |
| | W39 | | W41 | | W42 | |
| | h^+ | h^- | h^+ | h^- | h^+ | h^- |
| R.A.(NdF=2) | 5.83 | 0.05 | 5.40 | 4.99 | 10.67 | 0.94 |
| T (NdF=1) | 1.18 | 0.01 | 5.70 | 2.89 | 1.85 | 0.27 |
| TOT | 7.01 | 0.06 | 11.10 | 7.88 | 12.52 | 1.21 |
| | 7.07 (31%) | | 18.90 (0.4%) | | 13.73 (3.3%) | |

Table 3.5: Quality test for the 6 available *periods* with respect to the Collins and Sivers modulations. χ^2 values and overall confidence level.

| $\sin(3\phi_h - \phi_s)$ | | | | | | |
|--------------------------|---------|-------|--------|-------|--------|-------|
| | W25 | | W28 | | W30 | |
| | h^+ | h^- | h^+ | h^- | h^+ | h^- |
| R.A.(NdF=2) | 2.61 | 1.78 | 7.55 | 2.27 | 0.48 | 0.11 |
| T (NdF=1) | 0.46 | 0.14 | 0.00 | 0.50 | 7.56 | 2.77 |
| TOT | 3.08 | 1.92 | 7.56 | 2.77 | 1.14 | 0.28 |
| | 54.39 % | | 11.16% | | 96.4% | |
| | W39 | | W41 | | W42 | |
| | h^+ | h^- | h^+ | h^- | h^+ | h^- |
| R.A.(NdF=2) | 1.37 | 4.64 | 2.20 | 0.14 | 0.64 | 2.06 |
| T (NdF=1) | 0.09 | 0.07 | 0.20 | 0.00 | 0.09 | 0.06 |
| TOT | 1.45 | 4.71 | 2.40 | 0.14 | 0.73 | 2.12 |
| | 40.48 % | | 86.37% | | 82.75% | |
| $\sin(2\phi_h - \phi_s)$ | | | | | | |
| | W25 | | W28 | | W30 | |
| | h^+ | h^- | h^+ | h^- | h^+ | h^- |
| R.A.(NdF=2) | 2.56 | 0.12 | 1.55 | 9.11 | 2.24 | 1.48 |
| T (NdF=1) | 0.12 | 0.17 | 0.71 | 0.04 | 2.35 | 1.90 |
| TOT | 2.69 | 0.29 | 2.26 | 9.15 | 2.35 | 1.90 |
| | 81.22% | | 7.67% | | 64.39% | |
| | W39 | | W41 | | W42 | |
| | h^+ | h^- | h^+ | h^- | h^+ | h^- |
| R.A.(NdF=2) | 0.32 | 1.22 | 2.39 | 0.86 | 5.33 | 2.01 |
| T (NdF=1) | 0.22 | 0.01 | 0.48 | 0.29 | 0.73 | 0.01 |
| TOT | 0.55 | 1.23 | 2.87 | 1.15 | 6.06 | 2.02 |
| | 93.88% | | 67.38% | | 23.23% | |
| $\cos(2\phi_h - \phi_s)$ | | | | | | |
| | W25 | | W28 | | W30 | |
| | h^+ | h^- | h^+ | h^- | h^+ | h^- |
| R.A.(NdF=2) | 2.61 | 0.25 | 0.09 | 1.15 | 0.40 | 0.45 |
| T (NdF=1) | 0.01 | 0.00 | 0.65 | 0.17 | 0.22 | 0.75 |
| TOT | 2.62 | 0.25 | 0.74 | 1.32 | 0.73 | 2.71 |
| | 82.49% | | 91.40% | | 93.61% | |
| | W39 | | W41 | | W42 | |
| | h^+ | h^- | h^+ | h^- | h^+ | h^- |
| R.A.(NdF=2) | 0.48 | 2.55 | 2.51 | 1.94 | 1.10 | 0.47 |
| T (NdF=1) | 0.25 | 0.16 | 0.15 | 0.06 | 0.09 | 0.51 |
| TOT | 0.73 | 2.71 | 2.65 | 2.00 | 1.19 | 0.98 |
| | 82.75% | | 23.23% | | 90.33% | |

Table 3.6: Data quality of the different periods for the $\sin(3\phi_h - \phi_s)$, $\sin(2\phi_h - \phi_s)$, $\cos(2\phi_h - \phi_s)$ asymmetries.

| | $\cos(\phi_h - \phi_s)$ | | | | | |
|-------------|-------------------------|-------|-------|-------|--------|-------|
| | W25 | | W28 | | W30 | |
| | h^+ | h^- | h^+ | h^- | h^+ | h^- |
| R.A.(NdF=2) | 6.16 | 1.99 | 19.44 | 23.44 | 0.25 | 0.47 |
| T (NdF=1) | 0.12 | 0.01 | 2.33 | 1.20 | 0.56 | 0.10 |
| TOT | 6.28 | 2.01 | 21.77 | 24.64 | 0.81 | 0.57 |
| | 21.76% | | 0.00% | | 96.71% | |
| | W39 | | W41 | | W42 | |
| | h^+ | h^- | h^+ | h^- | h^+ | h^- |
| R.A.(NdF=2) | 11.26 | 26.35 | 0.02 | 4.51 | 0.36 | 0.49 |
| T (NdF=1) | 5.26 | 3.12 | 16.52 | 5.74 | 0.34 | 0.64 |
| TOT | 16.51 | 29.46 | 16.54 | 10.25 | 0.70 | 1.13 |
| | 0.00% | | 0.02% | | 93.44% | |
| | $\sin(\phi_s)$ | | | | | |
| | W25 | | W28 | | W30 | |
| | h^+ | h^- | h^+ | h^- | h^+ | h^- |
| R.A.(NdF=2) | 3.75 | 4.16 | 2.94 | 5.60 | 13.81 | 0.86 |
| T (NdF=1) | 1.03 | 0.89 | 0.28 | 8.05 | 2.54 | 0.83 |
| TOT | 4.78 | 5.05 | 3.22 | 13.64 | 16.35 | 1.68 |
| | 13.19% | | 0.98% | | 0.61% | |
| | W39 | | W41 | | W42 | |
| | h^+ | h^- | h^+ | h^- | h^+ | h^- |
| R.A.(NdF=2) | 5.29 | 0.87 | 2.13 | 6.22 | 1.10 | 1.15 |
| T (NdF=1) | 6.07 | 7.96 | 0.18 | 3.74 | 2.46 | 0.83 |
| TOT | 11.37 | 8.84 | 2.30 | 9.97 | 3.56 | 1.97 |
| | 0.25% | | 5.63% | | 47.72% | |
| | $\cos(\phi_s)$ | | | | | |
| | W25 | | W28 | | W30 | |
| | h^+ | h^- | h^+ | h^- | h^+ | h^- |
| R.A.(NdF=2) | 1.90 | 0.79 | 11.25 | 41.46 | 0.42 | 2.06 |
| T (NdF=1) | 7.65 | 5.18 | 5.23 | 4.03 | 0.01 | 3.52 |
| TOT | 9.56 | 5.97 | 16.48 | 45.49 | 0.43 | 3.52 |
| | 1.65% | | 0.00% | | 68.40% | |
| | W39 | | W41 | | W42 | |
| | h^+ | h^- | h^+ | h^- | h^+ | h^- |
| R.A.(NdF=2) | 7.88 | 12.02 | 6.36 | 4.14 | 0.11 | 6.04 |
| T (NdF=1) | 0.07 | 0.11 | 1.31 | 9.48 | 0.11 | 1.01 |
| TOT | 7.94 | 12.31 | 7.67 | 13.62 | 0.21 | 7.05 |
| | 0.27% | | 0.16% | | 29.67% | |

Table 3.7: Data quality of the different periods for the $\cos(\phi_h - \phi_s)$, $\sin(\phi_s)$ and $\cos(\phi_s)$ asymmetries.

| bin | x | | W (Gev/ c^2) | | p_T^h (Gev/ c) | | z | |
|-----|-------|-------|-------------------|------|---------------------|------|------|------|
| | from | to | from | to | from | to | from | to |
| 1 | 0.003 | 0.008 | 5 | 5.7 | 0.10 | 0.20 | 0.20 | 0.25 |
| 2 | 0.008 | 0.013 | 5.7 | 6.7 | 0.20 | 0.30 | 0.25 | 0.30 |
| 3 | 0.013 | 0.020 | 6.7 | 7.5 | 0.30 | 0.40 | 0.30 | 0.35 |
| 4 | 0.020 | 0.032 | 7.5 | 8.5 | 0.40 | 0.50 | 0.35 | 0.40 |
| 5 | 0.03 | 0.050 | 8.5 | 9.5 | 0.50 | 0.60 | 0.40 | 0.50 |
| 6 | 0.050 | 0.080 | 9.5 | 10.5 | 0.60 | 0.75 | 0.50 | 0.65 |
| 7 | 0.080 | 0.130 | 10.5 | 12 | 0.75 | 0.90 | 0.65 | 0.80 |
| 8 | 0.130 | 0.210 | 12 | - | 0.90 | 1.30 | 0.80 | 1 |
| 9 | 0.210 | 1 | - | - | 1.30 | - | - | - |

Table 3.8: The bins used to extract the asymmetries.

smaller than the physical ones because of the diluting effects due to the target polarization, the target dilution factor and the kinematical depolarization factor (Sec.1.2).

3.7.1 1D binned method

Assume that the modulation of interest is $\sin(\Phi)$. with amplitude $\epsilon^{\sin \Phi}$, where Φ is one of the combinations of ϕ_h and ϕ_s that enters in the SIDIS cross-section. Then $F^{QR}(\Phi)$ is defined as :

$$F^{QR}(\Phi) = \frac{\prod_{i=1}^4 \int_{-\pi}^{\pi} N_i^{\uparrow}(\phi_h, \Phi) d\phi_h}{\prod_{i=1}^4 \int_{-\pi}^{\pi} N_i^{\downarrow}(\phi_h, \Phi) d\phi_h} \quad (3.14)$$

Making use of the formulae reported in Appendix B and assuming that the acceptance term $a(\phi_h, \phi_s)$ in Eq.(3.1) is flat, it is possible to demonstrate that:

$$F^{QR}(\Phi) = 1 + (8\epsilon^{\sin \Phi}) \sin(\Phi).$$

The amplitude A of the modulation is extracted with a fit with the function $f^{QR}(\Phi) = 1 + 8A \sin(\Phi)$.

The Φ range is divided into bins of equal width Δ . The finite size of the bin is a possible source of bias for the measured asymmetry [37]. The number of events measured in each bin i :, corresponds to the mean value of the expected distribution: $\langle f^{QR}(\Phi) \rangle = \frac{1}{\Delta} \int_{\Phi_i}^{\Phi_i + \Delta} f^{QR}(\Phi) d\Phi$. In the analysis this number is associated to the Φ_i value at the centre of the bin ($\Phi_i + \frac{\Delta}{2}$) and the function used to evaluate the amplitude of the modulation is $f^{QR}(\Phi + \frac{\Delta}{2}) = 1 + 8A \sin(\Phi_i + \frac{\Delta}{2})$. It is easily demonstrated that the mean value of f^{QR} is not the value at the centre of the bin and the value of the extracted asymmetry A is then:

$$A = \epsilon^{\sin \Phi} \frac{2}{\Delta} \sin \frac{\Delta}{2} \quad (3.15)$$

For this analysis the Φ range is divided in 16 bins (Fig. 3.8). This division allows to have all bins highly populated also in the cases where the total statistics of the *period* is low, thus we can always assume that the number of events counted in each bin corresponds to $\langle f^{QR}(\Phi) \rangle$ and that the errors can be treated in Gaussian approximation. The bias due to the bin width is at the 0.6% level, and can be neglected.

3.7.2 The COMPASS angular acceptance

The COMPASS acceptance is not flat as a function of ϕ_h and ϕ_s . The distributions are shown in Fig. 3.9, for ϕ_h (left) and ϕ_s (right). We can consider in first approximation the modulations

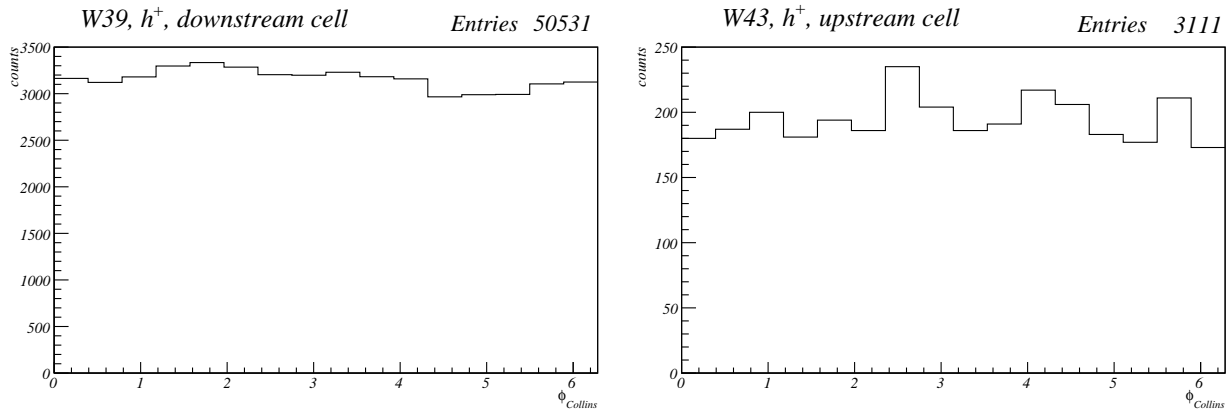


Figure 3.8: Example of the ϕ_C distribution divided in 16 bins, for one of the kinematical bins of the analysis. **Left** the second x bin for the downstream cell of W39, as an example of high statistics. **Right** the last x bin for the upstream cell of *week* W43, as an example of low statistics. In both cases the number of events in each bin is high enough to guarantee the Gaussian distribution of the counts.

as a function of ϕ_h independent from those as a function of ϕ_s and decompose each modulation in its Fourier amplitudes (this approach is described in [48]) :

$$\alpha(\phi) = c_0 \left(1 + 2 \sum_{n=1}^{n=\infty} [c_n \cos(n\phi) + s_n \sin(n\phi)] \right) \quad (3.16)$$

The amplitudes of the Fourier decomposition are extracted with a fit to the data, applying a cut off at $n=5$. The only amplitude that is relevant for the description of the ϕ_h modulations is $c_1 = 0.03$. In contrast, the modulations in ϕ_s are more evident and three amplitudes are significantly different from zero, s_1 , s_3 and c_2 which numerical values are reported in Tab. 3.9. The physical spin dependent modulations, that introduce modulations in ϕ_h , ϕ_s , are at first approximation cancelled by the integration over the different target cells that have opposite polarization, thus the fitted amplitudes are entirely due to the acceptance. In the following, only the ϕ_s modulations will be considered.

| n | c_n | s_n |
|---|-------|-------|
| 1 | -0.04 | 0.10 |
| 2 | 0.10 | 0.01 |
| 3 | 0.04 | -0.08 |
| 4 | -0.02 | 0.00 |
| 5 | 0.00 | 0.01 |

Table 3.9: Amplitudes of the Fourier decomposition of the COMPASS acceptance as a function of ϕ_s .

In Sec. 3.7.1 it was assumed that the acceptance term $a(\phi_s, \phi_s)$ in Eq.(3.1) is flat. We have shown that this is not the case: there are modulations of the acceptance that depends on the same angles as the cross section. These modulations can mix the contributions of different physical modulations to a single fitted value. The polarization dependent cross section can be written as:

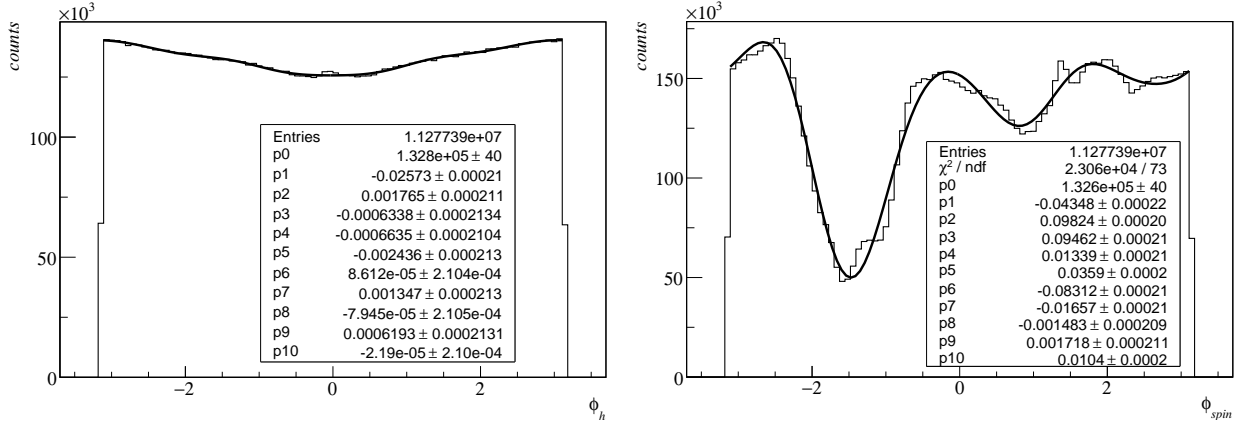


Figure 3.9: COMPASS acceptance in ϕ_h (left) and ϕ_s (right). The solid line is the fit of the data with the Fourier expansion (3.16) of the corresponding angle, up to $n = 5$.

$$\sigma_{\pm}(\phi_h, \phi_s) \propto 1 \pm \left[\epsilon_C \sin(\phi_h + \phi_s) + \epsilon_S \sin(\phi_h - \phi_s) + \epsilon_2 \sin(3\phi_h - \phi_s) + \epsilon_4 \cos(\phi_h - \phi_s) \right. \\ \left. + \epsilon_5 \sin(\phi_s) + \epsilon_6 \sin(2\phi_h - \phi_s) + \epsilon_7 \cos(\phi_s) + \epsilon_8 \cos(2\phi_h - \phi_s) \right]$$

Let's assume that Φ is the Siverson angle $\Phi_S = \phi_h - \phi_s$ (note that capital S stands for Siverson, lower-case s for spin). The number of measured events depends on the convolution of the cross section with the acceptance of the apparatus, and is, as a function of the angle Φ_S :

$$N_{\pm}(\Phi_S) \propto \int_{-\pi}^{\pi} d\phi_h \alpha(\phi_h, \Phi_S; c_i, s_i) \sigma_{\pm}(\phi_h, \Phi_S)$$

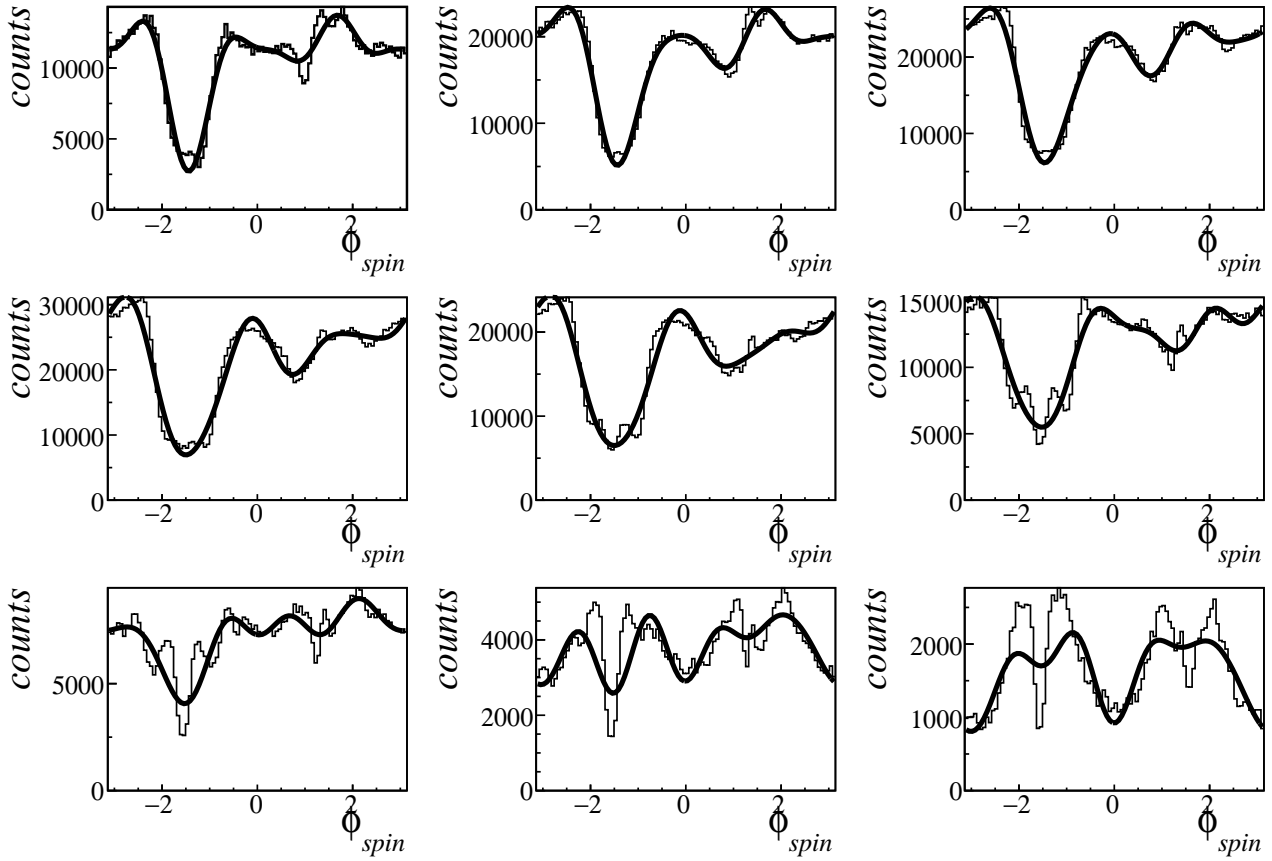
As it is described in detail in appendix B, we have that:

$$N_{\pm}(\Phi_S) \propto 1 \pm \left[(\epsilon_S + \epsilon_C \cdot c_2) \sin(\Phi_S) + \epsilon_4 \cos(\Phi_S) + \epsilon_2 \cdot c_2 \sin(3\Phi_S) + (\epsilon_6 \cdot s_1 + \epsilon_8 \cdot c_1) \cos(2\Phi_S) + (\epsilon_6 \cdot c_1 - \epsilon_8 \cdot s_1) \sin(2\Phi_S) \right]$$

thus the fitted amplitude of the Siverson asymmetry is a mixture of the "true" Siverson asymmetry ϵ_S and the "true" Collins ϵ_C asymmetry: $A_S^{Fit} = \epsilon_S + c_2 \epsilon_C$. Analogously $A_C^{Fit} = \epsilon_C + c_2 \epsilon_S$.

The modulation of the distribution in ϕ_h is mainly due to the contribution of the physical unpolarized asymmetries, thus even if the amplitude of the modulation is different in the different kinematical bins, the shape of the modulation is the same. The acceptance modulations as a function of ϕ_s are non-physical and depend on the trigger system: the size of the Fourier amplitudes is not constant in the different kinematical bins and moreover their relative size changes, thus the mixing of the different modulations changes from bin to bin. This is shown in Fig. 3.10 for the nine x bins, from which it is also clear that the fit description is rather poor in the last bins. The numerical values of the amplitudes are also shown. The main amplitudes of the decomposition are s_1 , c_2 and s_3 in the first seven bins, while the c_4 amplitude is important in last two x bins. Note that the c_2 amplitude changes sign in the last x bin: the correlation introduced by the acceptance between the measured values of ϵ_C and ϵ_S is then bin dependent.

One should correct the measured asymmetries for the acceptance correlations with an unfolding procedure. The measured asymmetries at COMPASS are smaller than 0.07, the measured c_2 amplitude is smaller than 0.2, thus the maximum correction is smaller than 0.014.



| bin1 | | | bin2 | | | bin3 | | |
|------|-------|-------|------|-------|-------|------|-------|-------|
| i | c | s | i | c | s | i | c | s |
| 1 | -0.03 | 0.10 | 1 | -0.05 | 0.10 | 1 | -0.07 | 0.12 |
| 2 | 0.07 | 0.03 | 2 | 0.09 | 0.03 | 2 | 0.11 | 0.03 |
| 3 | 0.05 | -0.10 | 3 | 0.06 | -0.10 | 3 | 0.05 | -0.10 |
| 4 | -0.03 | -0.02 | 4 | -0.01 | -0.01 | 4 | 0.00 | -0.01 |
| 5 | -0.02 | 0.03 | 5 | 0.00 | 0.02 | 5 | 0.02 | 0.01 |
| bin4 | | | bin5 | | | bin6 | | |
| i | c | s | i | c | s | i | c | s |
| 1 | -0.08 | 0.13 | 1 | -0.06 | 0.13 | 1 | -0.03 | 0.13 |
| 2 | 0.17 | 0.02 | 2 | 0.20 | 0.01 | 2 | 0.19 | -0.01 |
| 3 | 0.04 | -0.12 | 3 | 0.04 | -0.11 | 3 | 0.02 | -0.08 |
| 4 | 0.02 | 0.01 | 4 | 0.02 | 0.01 | 4 | 0.00 | 0.02 |
| 5 | 0.03 | -0.01 | 5 | 0.02 | -0.02 | 5 | -0.01 | -0.04 |
| bin7 | | | bin8 | | | bin9 | | |
| i | c | s | i | c | s | i | c | s |
| 1 | -0.01 | 0.13 | 1 | 0.01 | 0.09 | 1 | 0.06 | 0.05 |
| 2 | 0.13 | -0.02 | 2 | 0.02 | -0.02 | 2 | -0.13 | -0.03 |
| 3 | 0.02 | -0.05 | 3 | 0.02 | -0.05 | 3 | -0.01 | -0.02 |
| 4 | -0.02 | 0.02 | 4 | -0.09 | 0.0 | 4 | -0.12 | -0.02 |
| 5 | -0.02 | -0.01 | 5 | -0.02 | 0.04 | 5 | -0.04 | 0.04 |

Figure 3.10: COMPASS acceptance in ϕ_s in the nine x bins, numbered from left to right, from top to bottom. The solid line is the fit of the data with the Fourier decomposition (Eq.(3.16)), up to $n = 5$. In the tables the numerical values of the fit are reported.

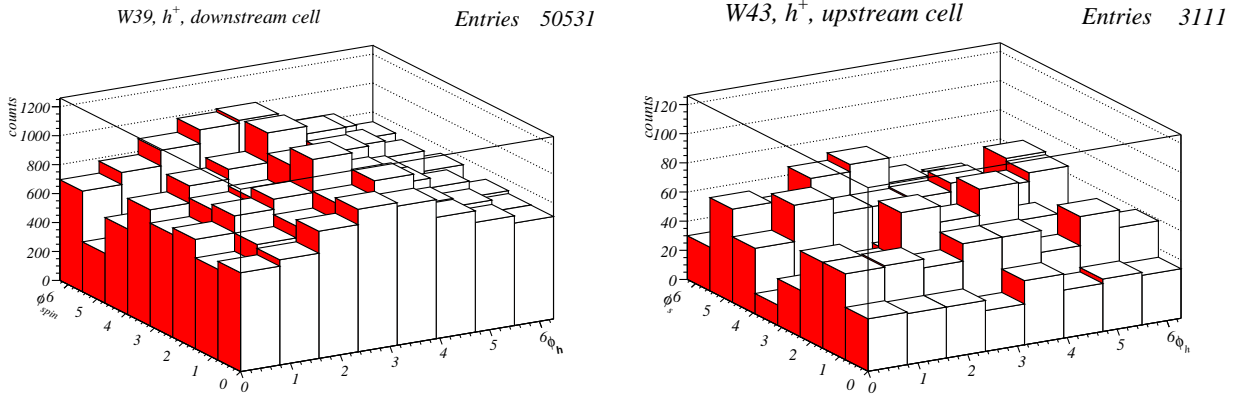


Figure 3.11: Example of the ϕ_C distribution divided in the 8×8 ϕ_h , ϕ_s grid, for one of the kinematical bins of the analysis. **Left** the second x bin for the downstream cell of W39, as an example of high statistics. **Right** the last x bin for the upstream cell of *week* W43, as an example of low statistics. The same *periods* and kinematical bins of Fig. 3.8 are used.

The average error size is of the order of 0.01. The bias introduced by the 1D fit algorithm is at most of the order of 1σ .

3.7.3 2D binned method

The two dimensional fit allows to overcome the problem of the correlations introduced by the non flat acceptance [7]. This method relies on the fit of $F^{QR}(\phi_h, \phi_s)$ on a (ϕ_h, ϕ_s) grid: avoiding the integration over the non-flat acceptance, the asymmetries are extracted unbiased.

In this analysis a grid of $8 \phi_h \times 8 \phi_s$ bins has been used, as shown in Fig. 3.11. Due to the width of the bin, the possible bias introduced by the binning is no longer negligible: the bin width correction (Sec. 3.7.1) for the Collins and the Sivers angles is $\frac{2}{\Delta} \sin \frac{\Delta}{2}$, where $\Delta = \frac{\pi}{4}$. The bias is of the order of 5%. The bin width correction is applied to rescale the amplitude extracted with the fit.

The total number of bins in which the full sample is divided depends quadratically in the number of bins in which the ϕ angle is divided. Even if the number of bins on each axis has been reduced from 16 to 8, this is not enough to have a good population in each bin, considering the big dip in the angle ϕ_s (Fig. 3.9, left) due to the asymmetric construction of the trigger system. An example of the population in the different ϕ_h, ϕ_s bins is shown in Fig. 3.11, in a case of high (left) and low (right) statistics. Note that the *periods* and bins considered are the same shown in Fig. 3.8 for the 1D method. There are bins in which the measured number of events is very low, thus the statistical fluctuations may not be under control. In the analysis, bins that contains less than 10 counts are not used for the fit.

With the two dimensional fit, it is possible to extract both the unbiased values of the asymmetries and the correlation coefficients. The correlation coefficients between the Collins and the Sivers asymmetries in the nine x bins are shown in Tab. 3.10 and result to be in very good agreement with the c_2 coefficients extracted from the decomposition of the acceptance in its Fourier amplitudes that are shown in Fig. 3.10.

3.7.4 Unbinned maximum likelihood

Both the 1D and the 2D binned methods have advantages and disadvantages. In the former, the extracted values of the asymmetries are correlated among them because of the integration over

| | | |
|-------|-------|-------|
| bin 1 | bin 2 | bin 3 |
| 0.06 | 0.07 | 0.11 |
| bin 4 | bin 5 | bin 6 |
| 0.16 | 0.20 | 0.20 |
| bin 7 | bin 8 | bin 9 |
| 0.13 | 0.01 | -0.20 |

Table 3.10: Correlation coefficients between the measured Collins and Sivers asymmetries given by the 2D fit.

the non flat acceptance, in the latter the increased number of bins and the dip in ϕ_s acceptance may cause statistical fluctuations that are not under control. To overcome these problems, a different approach is used, based on the unbinned maximum likelihood estimator [49]. Even if the principle of the measurement is unchanged, i.e. combining the number of events measured in the different target cells in the two *weeks* to cancel the acceptance and the constant terms, the likelihood method does not fit directly F^{QR} .

In this method a probability is associated to each event, $p(\phi_h, \phi_s; \epsilon_1, \dots, \epsilon_8)$. The procedure of the extended maximum likelihood is used [47], thus the probabilities $p(\phi_h, \phi_s; \epsilon_1, \dots, \epsilon_8)$ are not normalized to one. The probability, that is different for the different target cells and the two *weeks*, is proportional to the product of the acceptance and of the cross section. The cross section is parametrized as:

$$\begin{aligned} \sigma_{\pm}(\phi_h, \phi_s) \propto 1 + \epsilon_{u,1} \cos(\phi_h) + \epsilon_{u,2} \sin(2\phi_h) \pm \left[\epsilon_c \sin(\phi_h + \phi_s) + \epsilon_s \sin(\phi_h - \phi_s) + \right. \\ \left. + \epsilon_2 \sin(3\phi_h - \phi_s) + \epsilon_4 \cos(\phi_h - \phi_s) + \epsilon_5 \sin(\phi_s) + \epsilon_6 \sin(2\phi_h - \phi_s) + \right. \\ \left. + \epsilon_7 \cos(\phi_s) + \epsilon_8 \cos(2\phi_h - \phi_s) \right] \end{aligned} \quad (3.17)$$

where $\epsilon_{u,1}$ and $\epsilon_{u,2}$ are the amplitudes of the unpolarized modulations and ϵ_i are the spin dependent modulations. The acceptance was initially parametrized as a two dimensional Fourier decomposition of the real COMPASS acceptance, but it results that the extracted asymmetries does not depend on the description of the acceptance, thus it is parametrized as a flat function for simplicity. The description of the cross section is common to the events measured in the different target cells and in the two *weeks* of the *period* (apart from the sign of the spin dependent amplitudes), while individual descriptions of the acceptance are provided for the different cells and the different periods.

The probabilities of the events are used to build the likelihood function of the sample:

$$\mathcal{L} = \left(\exp^{-\mathcal{N}^{\uparrow}} \prod_{i=0}^{\mathcal{N}^{\uparrow}} p(\phi_h^i, \phi_s^i; \epsilon_1, \dots, \epsilon_8) \right)^{\frac{1}{\mathcal{N}^{\uparrow}}} \cdot \left(\exp^{-\mathcal{N}^{\downarrow}} \prod_{i=0}^{\mathcal{N}^{\downarrow}} p(\phi_h^i, \phi_s^i; \epsilon_1, \dots, \epsilon_8) \right)^{\frac{1}{\mathcal{N}^{\downarrow}}} \quad (3.18)$$

The contributions to the likelihood from the different orientation of the polarization are separated and the N -th roots are used to give the same importance to the different sets.

The likelihood function is built for the different kinematical bins used in the analysis, and its logarithm is minimized with the MINUIT package. The asymmetries extracted are the raw asymmetries, that are then corrected to extract the physical asymmetries as will be explained in Sec. 4.1. It is also possible to weight every event with the appropriate correction and directly extract the physical asymmetry, instead of the raw one. The difference between the two results is found to be negligible in the present experimental condition, thus the simplest method is used in the analysis.

Chapter 4

The cross section asymmetries

The analysis procedure described in Chap. 3 is here applied to extract the asymmetries of the transverse-target dependent cross section and the systematic error is carefully estimated. As in the previous Chapter, the algorithms are tuned on the Collins and the Sivers asymmetries and then extended to the remaining 6 asymmetries.

All the work presented in this Chapter is original, and the results for the Collins and Sivers asymmetries have been published in "Measurement of the Collins and Sivers asymmetries on transversely polarised protons" [26]. The results for the other six asymmetries have been presented at international conferences [50].

4.1 Extraction of the physical asymmetries

The physical asymmetries are derived from the raw ones with the algorithm:

$$A = \frac{A_{raw}}{D_{NN} P f}$$

where D_{NN} is the depolarization factor, P is the target polarization and f is the target dilution factor. D_{NN} is calculated according to the formulae given in Chap. 1. These factors are calculated on an even-by-event basis and their mean value in each kinematical bin is used for the correction.

The numerical values of D_{NN} and f in each bin are reported in Tab. 4.1. D_{NN} for the Sivers modulation is equal to 1. f shows a clear dependence on x , since it accounts for the radiative effects, while it is almost constant as a function of the other variables.

The target polarization P is the average of the target polarization in each of the considered cells of the two *weeks*, weighted with the number of events produced in each cell. The mean values of the polarization in each data taking *period* are reported in Tab. 4.2.

The standard analysis extracts the Collins and the Sivers asymmetries as a function of the DIS variable x as well as a function of the hadronic variables z and p_T^h for each data-taking *period* separately. The final results is the weighted average of the different *periods*.

4.1.1 Collins asymmetries

The Collins asymmetries for positive and negative hadrons extracted from the different *periods* are shown in Fig. 4.1 as a function of x . The different *periods* show a general good compatibility, that is also tested via the pull distribution (Fig. 4.2). The pull is defined as $p = \frac{A - \langle A \rangle}{\sqrt{\sigma_A^2 - \sigma_{\langle A \rangle}^2}}$ and its distribution is expected to be a Gaussian centred at zero with an RMS of 1. The pull distribution presented is built using the asymmetries measured in each bin of x , z and p_T^h in the six *periods*; the histogram has thus 156 entries. The pull distribution is centred at zero

| x range | D_{NN}^{Coll} | f | p_T^h range | D_{NN}^{Coll} | f |
|----------------|-----------------|------|---------------|-----------------|------|
| [0.003, 0.008] | 0.61 | 0.14 | [0.10, 0.20] | 0.91 | 0.15 |
| [0.008, 0.013] | 0.80 | 0.14 | [0.30, 0.40] | 0.91 | 0.15 |
| [0.013, 0.020] | 0.88 | 0.14 | [0.40, 0.50] | 0.91 | 0.15 |
| [0.020, 0.032] | 0.93 | 0.14 | [0.50, 0.60] | 0.90 | 0.15 |
| [0.032, 0.050] | 0.95 | 0.15 | [0.60, 0.75] | 0.90 | 0.15 |
| [0.050, 0.080] | 0.95 | 0.15 | [0.75, 0.90] | 0.90 | 0.15 |
| [0.080, 0.130] | 0.95 | 0.15 | [0.90, 1.30] | 0.89 | 0.15 |
| [0.130, 0.210] | 0.96 | 0.16 | [1.30, 3.00] | 0.88 | 0.14 |
| [0.210, 1.000] | 0.94 | 0.17 | > 3.00 | 0.83 | 0.14 |

| z range | D_{NN}^{Coll} | f | W range | D_{NN}^{Coll} | f |
|--------------|-----------------|------|----------------|-----------------|------|
| [0.20, 0.25] | 0.90 | 0.15 | [5.00, 5.70] | 0.99 | 0.15 |
| [0.25, 0.30] | 0.90 | 0.15 | [5.70, 6.70] | 0.99 | 0.15 |
| [0.30, 0.35] | 0.90 | 0.15 | [6.70, 7.50] | 0.98 | 0.15 |
| [0.35, 0.40] | 0.90 | 0.15 | [7.50, 8.50] | 0.97 | 0.15 |
| [0.40, 0.50] | 0.90 | 0.15 | [8.50, 9.50] | 0.95 | 0.15 |
| [0.50, 0.65] | 0.91 | 0.15 | [9.50, 10.50] | 0.92 | 0.14 |
| [0.65, 0.80] | 0.91 | 0.15 | [10.50, 12.00] | 0.86 | 0.14 |
| [0.80, 1.00] | 0.91 | 0.15 | > 12.00 | 0.63 | 0.14 |

Table 4.1: Mean values of f and D_{NN}^{Coll} in the different bins used in the analysis.

| <i>period</i> | $\langle P \rangle$ |
|---------------|---------------------|
| W25 | 0.81772 |
| W28 | 0.81725 |
| W30 | 0.80236 |
| W39 | 0.86135 |
| W41 | 0.85828 |
| W42 | 0.81049 |

Table 4.2: Mean value of the polarization used in the different *periods* of data taking. The polarization does not depend on the kinematical variables

with an RMS compatible with one both for positive and for negative hadrons.

The mean values of the asymmetries measured in the different *periods* are reported in Tab. 4.3.

The χ^2 probability of the compatibility among the six mean asymmetries, $\chi^2 = \sum_{periods} \frac{(A_p - \langle A \rangle)^2}{\sigma_{A_p} + \sigma_{\langle A \rangle}}$, is 34% for positive hadrons and 86% for negative hadrons respectively.

4.1.2 Sivers asymmetries

The Sivers asymmetries for positive and negative hadrons extracted from the different *periods* are shown in Fig. 4.3 as a function of x .

The different *periods* show a general good compatibility for negative hadrons, while a clear systematic effect is visible for positive hadrons: the *periods* belonging to the first half of the data taking, show a Sivers asymmetry different from zero, the mean value being 0.024 ± 0.05 , while the *periods* belonging to the second half of the data taking, show a Sivers asymmetry compatible with zero, the mean value being 0.004 ± 0.06 . The χ^2 probability of the compatibility between the two measurements is smaller than 1%. The χ^2 probability of all the measured *periods* is 4% for positive hadrons and 32% for negative hadrons respectively. The systematic effect found will be taken into account in the determination of the systematic error (Sec. 4.2.4). The mean values of the asymmetries are reported in Tab. 4.4.

The pull of the Sivers asymmetries for positive and negative hadrons are shown in Fig. 4.4.

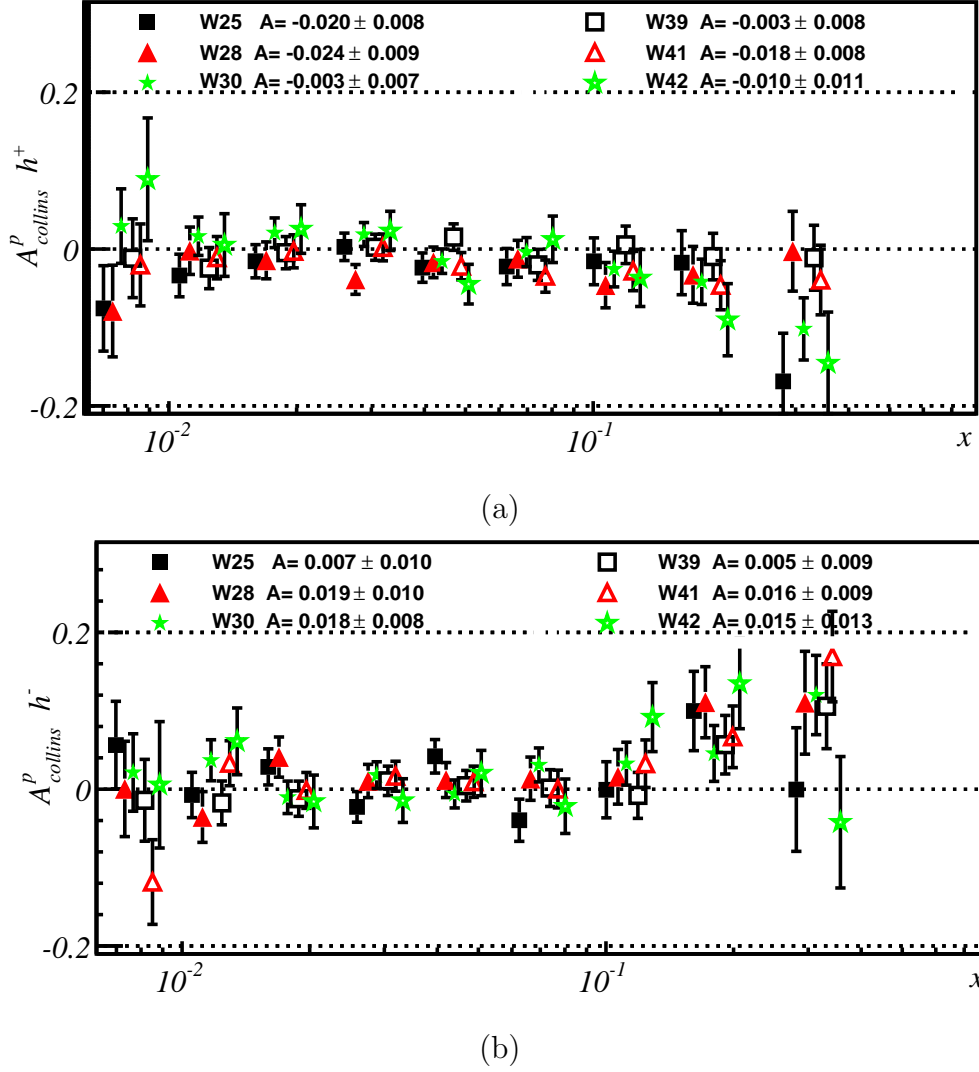


Figure 4.1: Collins asymmetries as a function of x for the six different *periods* selected for the analysis, for positive hadrons (a) and negative hadrons (b). The closed points represent the asymmetries extracted in the first part of the data taking, i.e. W25 (squares), W28 (triangles) and W30 (stars). The open points represent the asymmetries extracted in the second part of the data taking, i.e. W39 (squares), W41 (triangles) and W42 (stars).

| h^+ | A | σ_A | h^- | A | σ_A |
|-------|---------|------------|-------|--------|------------|
| W25 | -0.0201 | 0.0085 | W25 | 0.0072 | 0.0096 |
| W28 | -0.0241 | 0.0089 | W28 | 0.0189 | 0.0101 |
| W30 | -0.0030 | 0.0071 | W30 | 0.0177 | 0.0080 |
| W39 | -0.0028 | 0.0076 | W39 | 0.0046 | 0.0087 |
| W41 | -0.0178 | 0.0079 | W41 | 0.0157 | 0.0089 |
| W42 | -0.0104 | 0.0115 | W42 | 0.0155 | 0.0131 |
| mean | -0.0121 | 0.0034 | mean | 0.0131 | 0.0038 |

Table 4.3: Mean values of the Collins asymmetry in the different data taking *periods*. The χ^2 probability of the compatibility is 34% for positive hadrons and 86% for negative hadrons.

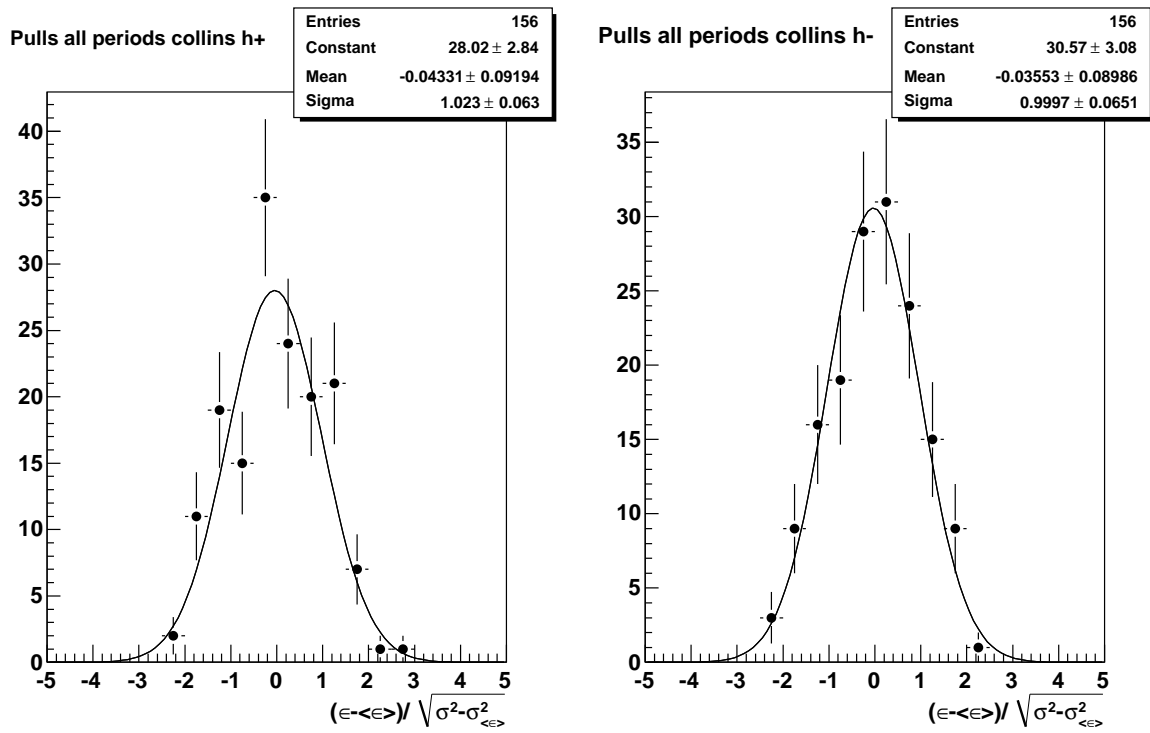


Figure 4.2: Pulls distribution of the Collins asymmetries for the six different *periods* selected for the analysis, for positive hadrons (left) and negative hadrons (right). There is one entry for each x , z and p_T^h bin of each *period*, corresponding to a total of 156 entries.

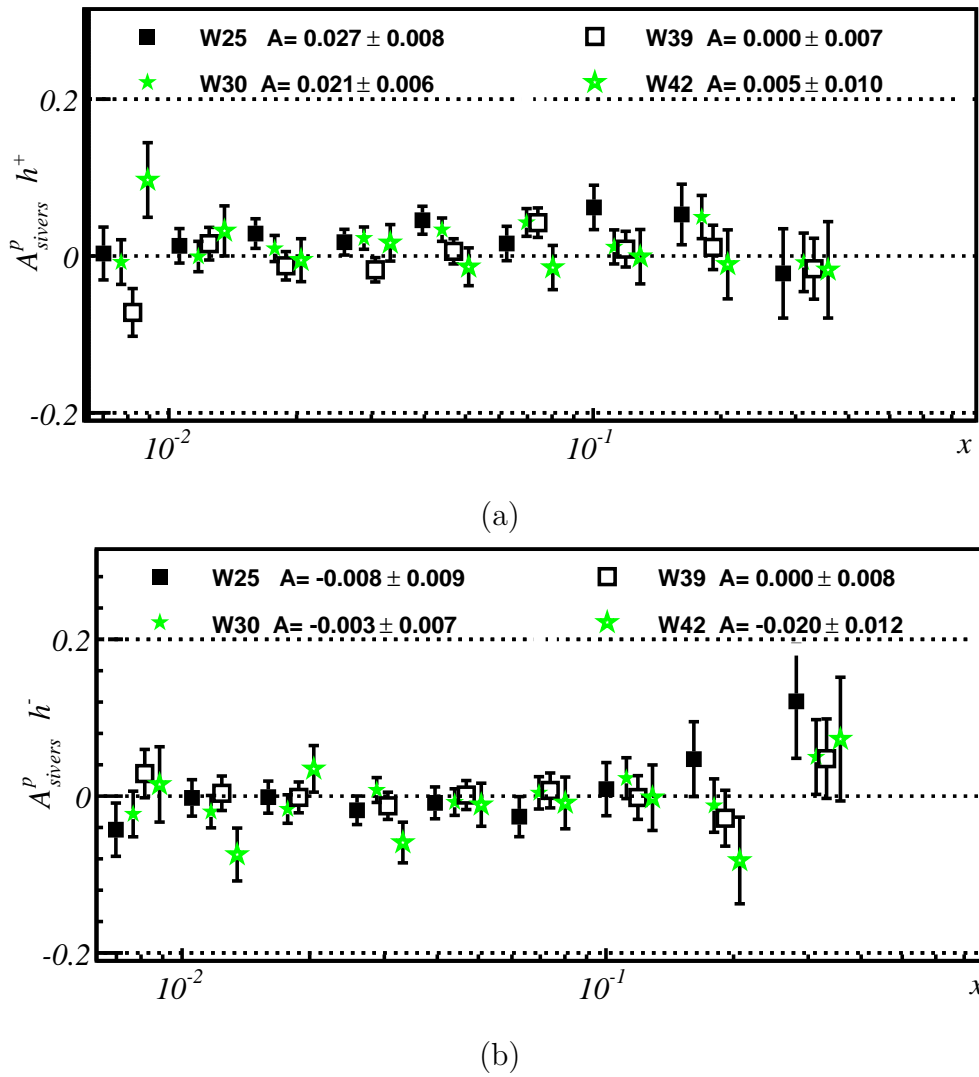


Figure 4.3: Siverts asymmetries as a function of x for the four different *periods* selected for the analysis, for positive hadrons (a) and negative hadrons (b). The closed points represent the asymmetries extracted in the first part of the data taking, i.e. W25 (squares) and W31 (stars). The open points represent the asymmetries extracted in the second part of the data taking, i.e. W39 (squares) and W42 (stars).

The pulls distribution is built using the asymmetries measured in the different bins of x , z and p_T^h in the four different *periods*, thus the entries of the histogram are 104. The pull distribution for positive hadrons has an RMS of 1.16 and it is not centred at zero; this is expected due to the marginal compatibility among *periods* described above. The RMS of the pulls distribution for negative hadrons is 1.2.

4.2 The determination of the systematic error

Several sources of possible systematic errors are investigated in the following. The main contribution comes from the estimation of the false asymmetries introduced by a possible breaking of the reasonable assumption (Sec. 3.5). There are other contributions that are taken into account, as the systematic effects due to the fit algorithm, the uncertainty of the target polarization and the compatibility of the asymmetries extracted dividing the data into sub-samples.

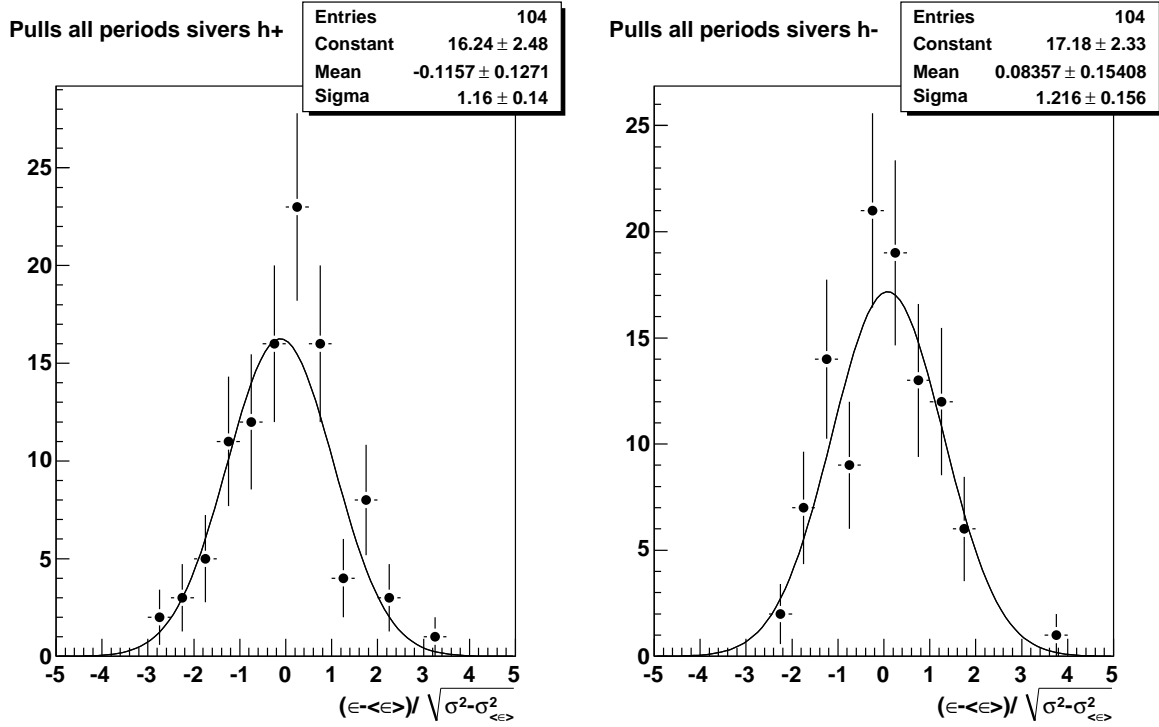


Figure 4.4: Pulls distribution of the Siverson asymmetries for the four different *periods* selected for the analysis, for positive hadrons (left) and negative hadrons (right). There is one entry for each x , z and p_T^h bins of each *period*, corresponding to a total of 104 entries.

| $h+$ | A | σ_A | $h-$ | A | σ_A |
|------|--------|------------|------|---------|------------|
| W25 | 0.0271 | 0.0077 | W25 | -0.0080 | 0.0086 |
| W31 | 0.0209 | 0.0064 | W31 | -0.0033 | 0.0072 |
| W39 | 0.0005 | 0.0069 | W39 | 0.0003 | 0.0078 |
| W42 | 0.0049 | 0.0104 | W42 | -0.0202 | 0.0118 |
| mean | 0.0143 | 0.0037 | mean | -0.0055 | 0.0042 |

Table 4.4: Mean values of the Siverson asymmetry in the different data taking *periods*. The χ^2 probability of the compatibility among the different *periods* is 4% for positive hadrons and 32% for negative hadrons respectively.

4.2.1 Systematic error due to the variation of the acceptance

It was mentioned in Sec. 3.5 that a variation of the acceptance between the two *weeks* such to break the reasonable assumption, introduces a bias in the measured asymmetry: Eq. 3.7 shows that the bias is $\frac{e_1 - e_2 - e_3 + e_4}{8}$. The two independent measurements of the asymmetry $A^{DR,0}$ and $A^{DR,1}$ (extracted from $F^{DR,0}$ and $F^{DR,1}$, Sec. 3.5) suffer from different biases: therefore the difference between them, that is expected to be zero, is an estimator of the possible systematic error of the measurement. Note that the difference is not a direct measurement of the bias: $A^{DR,0} - A^{DR,1} \propto e_1 - e_2 + e_3 - e_4$. The estimator of the systematic error coming from this difference is the difference properly normalized and referred to the statistical error of the measured asymmetry:

$$b^{0,1} = \frac{A^{DR,0} - A^{DR,1}}{2} \frac{1}{\sigma_{stat}^{asymmetry}} = \frac{e_1 - e_2 + e_3 - e_4}{8} \frac{1}{\sigma_{stat}^{asymmetry}}. \quad (4.1)$$

Another way to estimate the systematic error is the use of the false asymmetries. The false asymmetries are measured from the data combining the events in such a way that the spin-dependent effects cancel out. It is possible to define two different false asymmetries, building two different double ratios:

$$F^{FA0} = \frac{N_1^\uparrow N_4^\downarrow}{N_1^\downarrow N_4^\uparrow} \simeq 1 + (e_1 - e_4) \sin \Phi \quad (4.2)$$

$$F^{FA1} = \frac{N_2^\uparrow N_3^\downarrow}{N_2^\downarrow N_3^\uparrow} \simeq 1 + (e_2 - e_3) \sin \Phi \quad (4.3)$$

Both the false asymmetries extracted from the fit of the corresponding double ratios must be zero. The sum of the false asymmetries extracted is used as an estimator of the systematic error:

$$b^{FA} = \frac{A^{FA,0} + A^{FA,1}}{8} \frac{1}{\sigma_{stat}^{asymmetry}} = \frac{e_1 + e_2 - e_3 - e_4}{8} \frac{1}{\sigma_{stat}^{asymmetry}}. \quad (4.4)$$

Both the estimators have been studied as a function of the different variables. It has been found (Fig. 4.5) that there may be cases in which b shows large positive and negative variations, that averages out to zero. To be protected from this case, it has been decided that the absolute value will be used. The use of the absolute value may lead to the overestimation of the systematic error; assume that $A_{upstream}$ and $A_{downstream}$ are $N(\epsilon, \sqrt{2}\sigma_{asy})$, where ϵ is the *true* value of the measured asymmetry and σ_{asy} is the error on the asymmetry measured with the full target configuration. The difference $d = A_{upstream} - A_{downstream}$ is then $N(0, 2\sigma_{asy})$. The distribution of the absolute value $|d|$ is not a proper Gaussian but a distribution that goes from 0 to infinity with a half-Gaussian-like shape. The median of $|d|$ is $0.68 \cdot 2\sigma_{asy}$ ¹: this means that even if b is centred at zero, its absolute value is not and this fact has to be taken into account when $|b|$ is used to evaluate a distance from zero. In the specific case of $b_{0,1}$ and b_{FA} , which are normalized to the statistical error, the median is just 0.68. For this reason the term 0.68 is subtracted in quadrature to the absolute value of b .

The estimator of the bias that is used is the average of the two contributions coming from the different configurations and from the false asymmetries:

$$B(x) = \sqrt{\left(\frac{|b_{0,1}| + |b_{FA}|}{2}\right)^2 - 0.68^2}.$$

¹Being $x \sim N(\mu, \sigma)$ $P(\mu < x < (\mu + 0.68\sigma)) = P(x > (\mu + 0.68\sigma)) = 0.25$

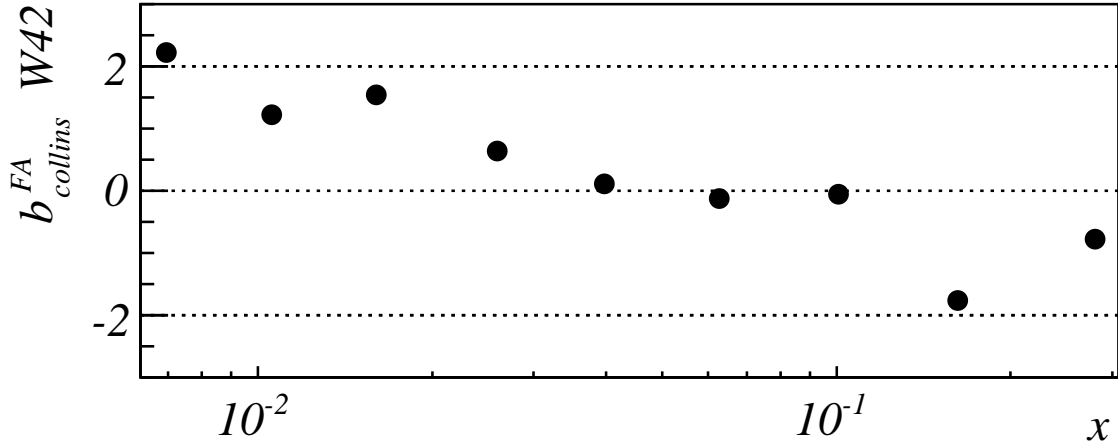


Figure 4.5: An example of the distribution of the estimator b^{FA} as a function of x . The Collins modulation of the false asymmetries for positive hadrons in W42b-W43 is used.

The final systematic error is given by the average over the x bins and over the *periods* of the bias estimator B .

4.2.2 Systematic effect due to the estimator of the asymmetry

The physical asymmetries are extracted with three different estimators, namely 1D, 2D and unbinned likelihood. These asymmetries show small differences among them, that are due to the systematic effects introduced by the estimator. The contribution to the statistical error is estimated as half of the RMS of the pulls distribution, where the pulls are defined as $\frac{A^{method1} - A^{method2}}{0.5(\sigma^{method1} + \sigma^{method2})}$. The pulls distribution are shown in Fig. 4.6, for the Collins and Sivers asymmetries separately for positive and negative hadrons.

The contribution of the difference between the 1D and the unbinned likelihood methods is $\sim 0.3\sigma_{stat}$, while the difference between the 2D and the unbinned likelihood methods contributes for $\sim 0.5\sigma_{stat}$. A systematic error for the fit of 15% of the statistical error is then assigned to the final systematic error, that is a half of the difference between 1D and the unbinned likelihood extractions, that are the two most reliable methods.

4.2.3 Systematic error on the target polarization

The target polarisation can be measured only in longitudinal configuration, with a precision of approx $\sim 2\%$. As it was described in Sec. 2.2, the polarisation of the target during the transverse data taking is measured at the very beginning and at the very end of the *week*, when the target is in longitudinal configuration. The average value of the polarisation during a *week* is calculated taking into account the two measured values and the relaxation time of the material.

A conservative value of 5% has been used as scale error on the asymmetry, due to the uncertainty on the measured target polarization. Moreover, a contribution of 2% from the determination of the dilution factor has to be added in quadrature.

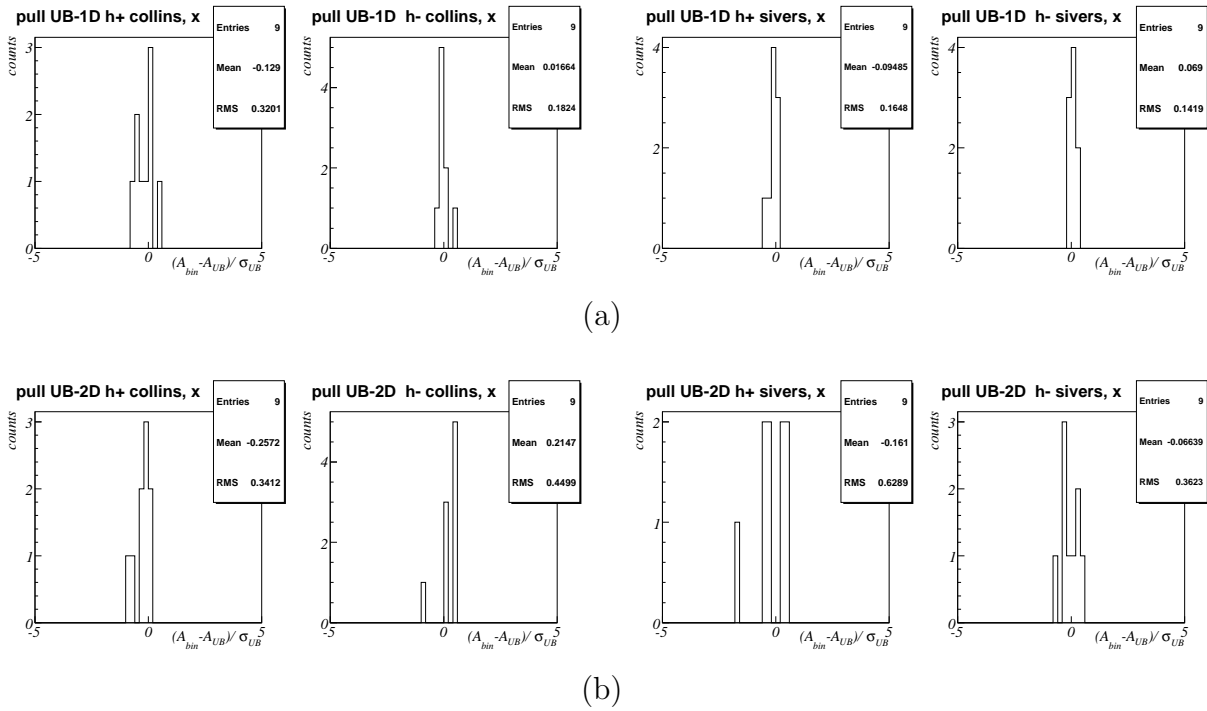


Figure 4.6: Pull distribution for the Collins and Sivers asymmetries, for positive and negative hadrons. The pull is defined as $\frac{A_{method1} - A_{method2}}{0.5(\sigma_{method1} + \sigma_{method2})}$. (a) Unbinned likelihood and 1D, (b) Unbinned likelihood and 2D.

4.2.4 Systematic error from the *period* compatibility

The Collins asymmetries extracted in the different *periods* are found to be compatible (Sec. 4.1.1). On the contrary a systematic effect has been found in the measurement of the Sivers asymmetry for positive hadrons (Sec. 4.1.2). The mean value of the Sivers asymmetry in the first part of the run is 0.024 ± 0.005 , while in the second part of the run is 0.004 ± 0.006 . The semi-difference of the two values (± 0.01) is taken as an absolute scale error on the asymmetry.

4.2.5 Other studies on systematic effects

Besides the estimates of the size of the possible bias on the asymmetries, other sources of systematics have been searched in the data. In the following two of them will be presented: the effect of dividing one of the two *weeks* into two parts and the effect of a cut on the geometrical acceptance.

The first test consists in splitting one of the two *weeks* of the *period* into two halves and extracting the asymmetries combining each half with the full coupled *week*. The two asymmetries measured are expected to be fully compatible.

This test has been done on all the *periods* selected for the analysis. The asymmetries extracted for all the *periods* resulted in good agreement, except for *period* W30 for the Sivers h^+ modulation, in which a considerable systematic effects has been found, as it is shown in Fig. 4.7. The contribution of this difference to the systematic error is evaluated as the average of the two different asymmetries measured divided by the statistical error of the difference; it results to be 0.8σ

The second test consists in applying a cut on the position of the hadron tracks on a fixed

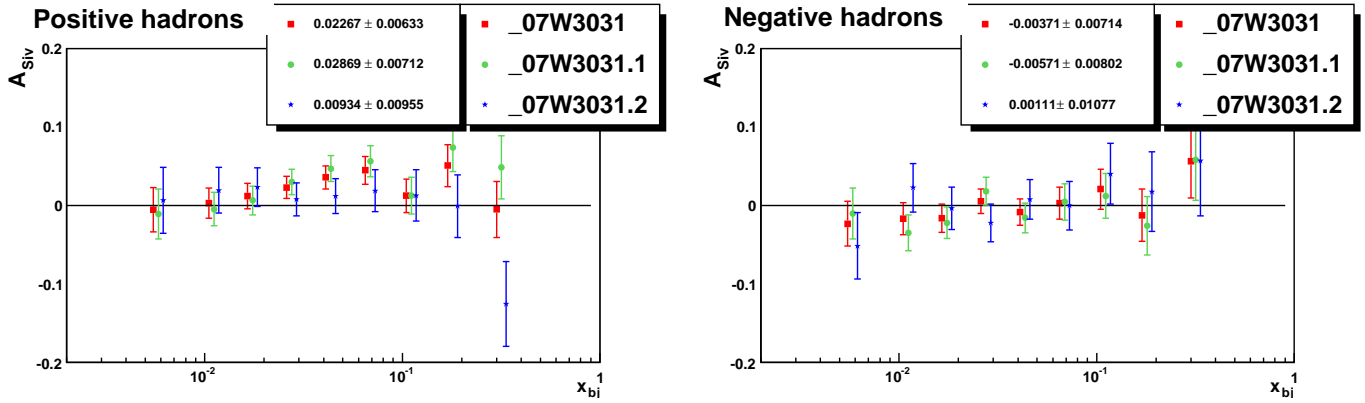


Figure 4.7: W30-31, Siverson asymmetries vs x ; left: positive hadrons; right: negative hadrons. The red squares are the asymmetries computed using all the data, the green dots and the blue stars are that obtained splitting *week* W30 in two parts and combining them with the full *week* W31

plane. This test was introduced to make the COMPASS acceptance close to that of the 2004 data-taking, in which the systematic effects were much smaller [8]. All hadron tracks are extrapolated to a plane at a distance of 600 cm from the target centre. The centre of the plane is defined as the centroid of all the extrapolated tracks, to compensate for the bending effect of the magnetic field. After that, a squared cut is applied on the tracks: if the horizontal or the vertical distance of the track intercept on that plane is larger than 40 cm, the track is rejected. The asymmetries extracted for all the *periods* resulted in good agreement, except for *period* W30 for the Siverson h^+ modulation, in which a considerable systematic effect has been found, as it is shown in Fig. 4.8. Also in this case, the contribution of this difference to the systematic error is evaluated as the average of the two different asymmetries measured divided by the statistical error of the difference; it results to be 0.7σ .

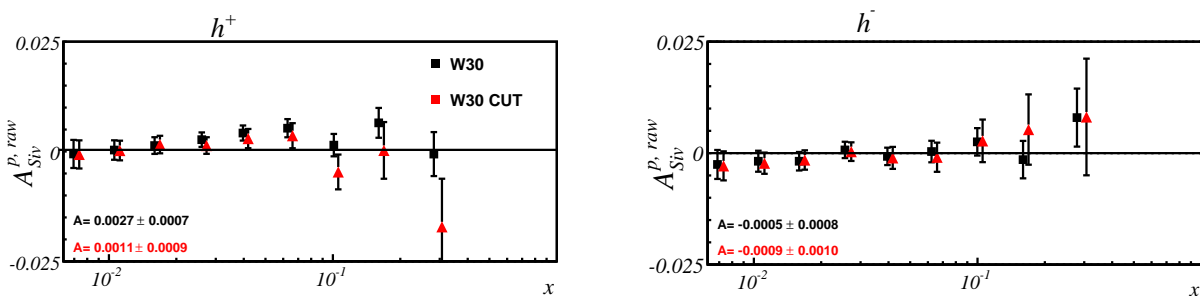


Figure 4.8: W30-31, Siverson raw asymmetries vs x without (black squares) and with (red triangles) the cut on the acceptance. Left: positive hadrons; right: negative hadrons.

The two contributions are summed up in quadrature and added to the systematic error of W30 for the Siverson asymmetry for positive hadrons.

4.2.6 Final tables of the systematic error

Tab. 4.5 gives the various contributions to the systematic error for the Collins asymmetries. The values for the Siverson asymmetries are reported in Tab. 4.6.

The systematic errors, in particular for the Sivers asymmetry, are larger than expected. Given the relevance of these measurements, the Collaboration decided to ask for a further year of data taking with the transversely polarised NH_3 target. The proposal has been accepted by the CERN scientific committees and the data were collected in 2010. A substantial reduction of the statistical and systematic errors is expected for these new measurements.

| Collins | h+ | h- |
|---|---------------------|---------------------|
| Point to point systematic error | | |
| estimator for extraction of asymmetries | $0.15\sigma_{stat}$ | $0.15\sigma_{stat}$ |
| acceptance variations | $0.5\sigma_{stat}$ | $0.6\sigma_{stat}$ |
| total | $0.52\sigma_{stat}$ | $0.62\sigma_{stat}$ |
| Scale factors | | |
| <i>period</i> compatibility (absolute) | 0 | 0 |
| target polarization | $0.05A$ | $0.05A$ |
| dilution factor | $0.02A$ | $0.02A$ |

Table 4.5: Contributions to the systematic error for Collins asymmetries for positive and negative hadrons.

| Sivers | h+ | h- |
|---|---------------------|---------------------|
| Point to point systematic error | | |
| estimator for extraction of asymmetries | $0.15\sigma_{stat}$ | $0.15\sigma_{stat}$ |
| acceptance variations | $0.8\sigma_{stat}$ | $0.4\sigma_{stat}$ |
| total | $0.81\sigma_{stat}$ | $0.43\sigma_{stat}$ |
| Scale factors | | |
| <i>period</i> compatibility (absolute) | 0.01 | 0 |
| target polarization | $0.05A$ | $0.05A$ |
| dilution factor | $0.02A$ | $0.02A$ |

Table 4.6: Contributions to the systematic error for Sivers asymmetries for positive and negative hadrons.

4.3 Final results on the Collins and the Sivers asymmetries

The Collins asymmetries for positive and negative hadrons are shown in Fig. 4.9 as a function of x , p_T^h , z . The asymmetries show a strong x dependence; at low x they are compatible with zero both for positive and negative hadrons, while in the valence region, i.e. at $x > 0.050$ the Collins asymmetry for positive hadron is negative and that for negative hadrons is positive,

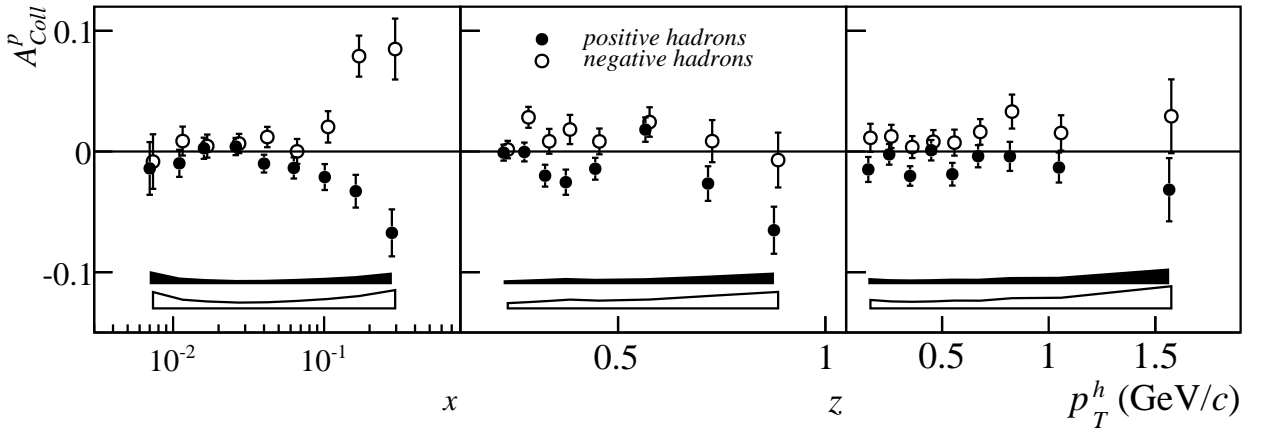


Figure 4.9: The Collins asymmetries for positive (closed points) and negative (open points) hadrons as a function of x , z and p_T^h . The bands represent the point to point systematic errors, that have been evaluated as $0.5\sigma_{stat}$ for positive hadrons and $0.6\sigma_{stat}$ for negative hadrons.

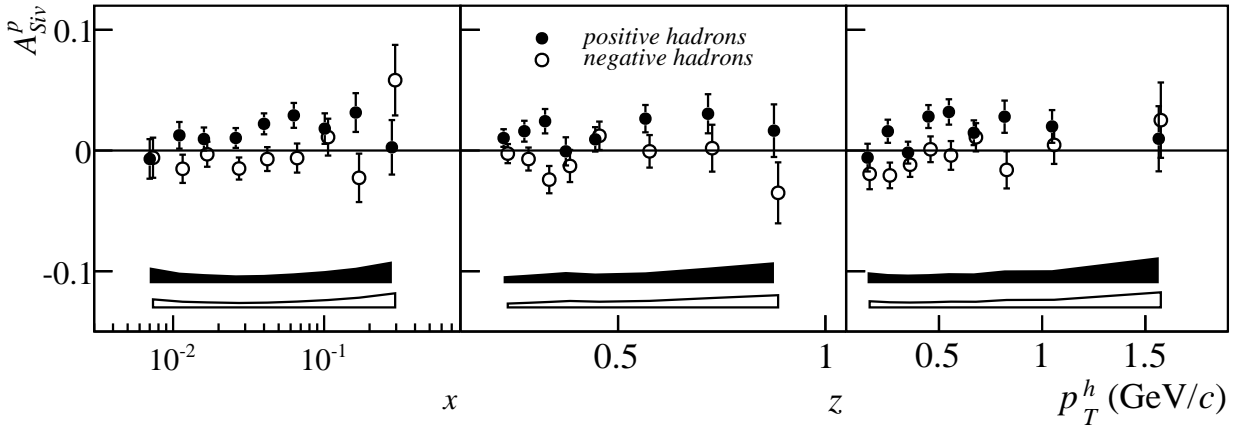


Figure 4.10: The Siverson asymmetries for positive (closed points) and negative (open points) hadrons as a function of x , z and p_T^h . The bands represent the point to point systematic errors, that have been evaluated as $0.8\sigma_{stat}$ for positive hadrons and $0.4\sigma_{stat}$ for negative hadrons. An absolute scale uncertainty of ± 0.01 has to be taken into account for positive hadrons only.

almost equal in size. The maximum value of the asymmetry is of the order of 10%. The asymmetries do not show any significant dependence as a function of z and p_T^h .

The Siverson asymmetries for positive and negative hadrons are shown in Fig. 4.10 as a function of x , p_T^h , z . The Siverson asymmetry for negative hadron is always compatible with zero. The Siverson asymmetry for positive hadrons shows a small positive signal (up to about 3%).

4.3.1 The measurement of the asymmetries as a function of W

The Collins and the Siverson asymmetries have been studied also as a function of W , the invariant mass of the final hadronic state. W and y are strongly correlated (Fig. 4.12) and the different trigger types are defined by the Q^2 and y values (Fig. 2.22): thus the events measured at different values of W are recorded thanks to different trigger combinations. In Fig. 4.13 the percentage of inclusive triggers as a function of W is shown. At high W the calorimetric trigger alone contributes with 15 to 35% of the events. The range in W is divided in two bins, i.e. $W < 7.5 \text{ GeV}/c^2$ and $W > 7.5 \text{ GeV}/c^2$. All the systematic studies presented in Sec. 3.6 have been done also in the two different W bins, and no new systematic effect has been found that

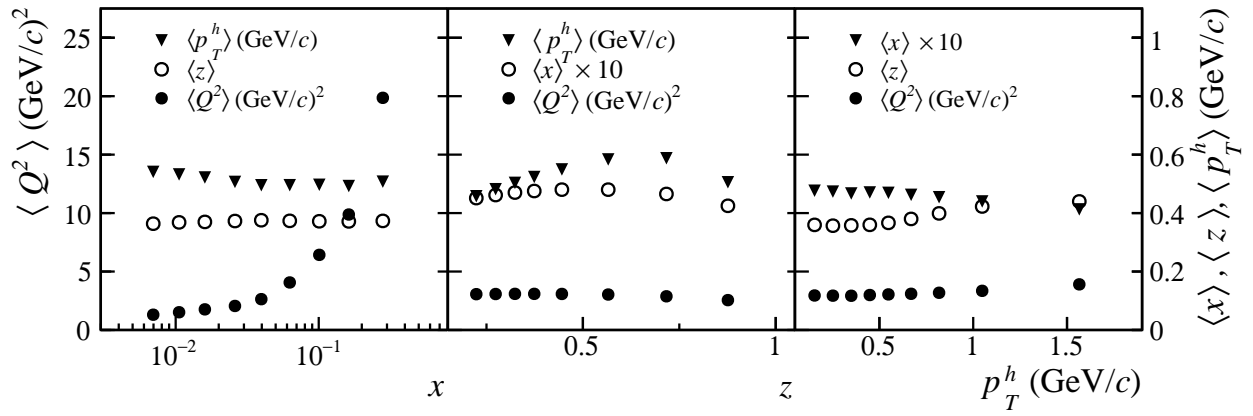


Figure 4.11: Mean values of some kinematical variables. Left: p_T^h , z and Q^2 as a function of x . p_T^h . Centre: x and Q^2 as a function of z ; the mean value of x has been multiplied by 10 for clarity. Right: x , z and Q^2 as a function of p_T^h .

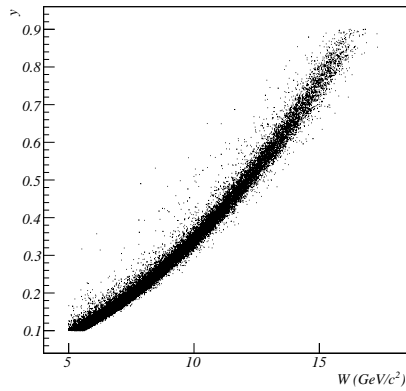


Figure 4.12: Distribution of y vs W .

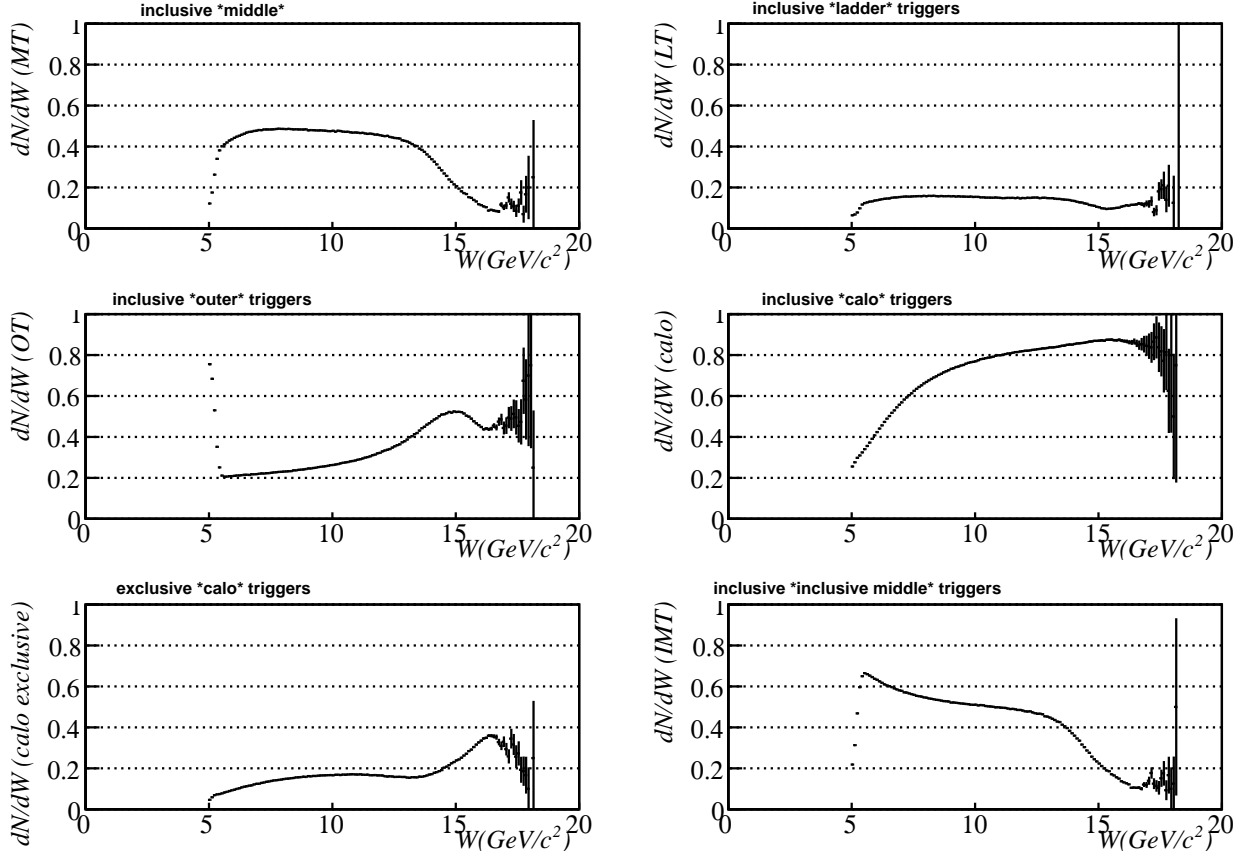


Figure 4.13: Inclusive trigger composition of the events as a function of W

can be ascribed to the specific trigger condition.

The mean values of the Collins asymmetry in the two different bins, measured in the six *periods*, are shown in Tab. 4.7. In the range $W < 7.5 \text{ GeV}/c^2$ the different measurements of the Collins asymmetry for positive hadrons are compatible, as well as those for negative hadrons. In the bin $W > 7.5 \text{ GeV}/c^2$ the asymmetries measured for negative hadrons are still compatible among them while, for positive hadrons, the χ^2 probability of the compatibility among the different *periods* is only marginal, of the order of 1%, but there is no systematic effect between the first three and the second three *periods*. The Collins asymmetry at small W is larger in size than that at higher values of W . As it will be shown in the next Section, this effect is the reflection of the sizeable Collins asymmetry at large x .

| | Collins, $W < 7.5 \text{ GeV}/c^2$ | | Collins, $W > 7.5 \text{ GeV}/c^2$ | | |
|-----------|------------------------------------|--------------------|------------------------------------|--------------------|-------------------|
| | h^+ | h^- | h^+ | h^- | |
| W25 | -0.026 ± 0.013 | -0.005 ± 0.015 | W25 | -0.013 ± 0.011 | 0.009 ± 0.012 |
| W28 | -0.029 ± 0.013 | 0.019 ± 0.015 | W28 | -0.020 ± 0.012 | 0.020 ± 0.013 |
| W30 | -0.020 ± 0.010 | 0.010 ± 0.012 | W30 | 0.013 ± 0.009 | 0.021 ± 0.011 |
| W39 | -0.017 ± 0.011 | 0.011 ± 0.013 | W39 | 0.007 ± 0.010 | 0.00 ± 0.011 |
| W41 | -0.007 ± 0.012 | 0.021 ± 0.014 | W41 | -0.025 ± 0.010 | 0.007 ± 0.012 |
| W42 | -0.038 ± 0.017 | 0.029 ± 0.020 | W42 | 0.019 ± 0.015 | 0.002 ± 0.017 |
| W25-28-30 | -0.025 ± 0.007 | 0.008 ± 0.008 | W25-28-30 | -0.005 ± 0.007 | 0.018 ± 0.008 |
| W39-41-42 | -0.017 ± 0.007 | 0.019 ± 0.008 | W39-41-42 | -0.004 ± 0.007 | 0.005 ± 0.008 |

Table 4.7: Mean values of the Collins asymmetries for the different *periods* of data taking and for the two different bins of W .

The mean values of the Sivers asymmetries for the different *periods* in the two W bins are reported in Tab. 4.8. The measurements of the Sivers asymmetry for negative hadrons are well compatible, in both W bins. At variance with what we showed in Tab. 4.4, in the range $W < 7.5 \text{ GeV}/c^2$ the asymmetries measured in the different *periods* are compatible: the confidence level of the χ^2 is 41%. This means that the Sivers signal measured is there at small W . The systematic effects between the two parts of the data taking are still visible in the range $W > 7.5 \text{ GeV}/c^2$ where the χ^2 probability for the compatibility of the two mean values is marginal, of the order of 1%. Moreover, for all the periods, the size of the asymmetry at small W is larger than that at higher W . This effect will be investigated in the next Section.

| | Sivers, $W < 7.5$ | | Sivers, $W > 7.5$ | | |
|--------|-------------------|--------------------|-------------------|--------------------|--------------------|
| | h^+ | h^- | h^+ | h^- | |
| W25 | 0.040 ± 0.013 | -0.009 ± 0.015 | W25 | 0.019 ± 0.009 | -0.010 ± 0.010 |
| W30 | 0.039 ± 0.010 | 0.004 ± 0.012 | W30 | 0.012 ± 0.008 | -0.008 ± 0.009 |
| W39 | 0.028 ± 0.011 | -0.007 ± 0.013 | W39 | -0.014 ± 0.009 | 0.004 ± 0.010 |
| W42 | 0.024 ± 0.017 | -0.012 ± 0.020 | W42 | -0.002 ± 0.013 | -0.026 ± 0.015 |
| W25-30 | 0.040 ± 0.008 | 0.011 ± 0.009 | W25-30 | 0.015 ± 0.006 | 0.008 ± 0.007 |
| W39-42 | 0.026 ± 0.009 | -0.009 ± 0.010 | W39-42 | -0.012 ± 0.007 | -0.006 ± 0.008 |

Table 4.8: Mean values of the Sivers asymmetries for the different *periods* of data taking and for the two different bins of W .

4.3.2 Final results for The Collins and Sivers asymmetries as a function of W

The asymmetries as a function of W are shown in Fig. 4.14. The Sivers asymmetry for positive hadrons show a dependence on W , having the signal concentrated in the small W region. The Sivers asymmetry for negative hadrons is compatible with zero and no clear indication is given for the Collins asymmetries.

In the interpretation of the results, the correlation between W and x (Fig. 4.15) has to be taken into account: bins at small W are populated with events with large values of x . To better investigate this effect, the W range is divided into two bins, $W < 7.5 \text{ GeV}/c^2$ and $W > 7.5 \text{ GeV}/c^2$ to separate the regions where a signal is shown and the region in which the asymmetries are compatible with zero. In the two W bins the asymmetries are studied as a function of x (Fig. 4.16). Also the complementary test is done: the x range is divided in two bins, $x < 0.032$ where the Collins and Sivers asymmetries are compatible with zero and $x > 0.032$, i.e. the signal region. The shape of the Collins and Sivers asymmetries is different: the Collins signal is concentrated in the valence region, i.e. for $x > 0.05$, while the Sivers signal does not show a strong x dependence and is in higher in average above $x = 0.032$. For simplicity it was decided to uniform the binning between the Collins and the Sivers asymmetries and in the two x bins the asymmetries are studied as a function of W (Fig. 4.17).

The Collins asymmetries for positive and negative hadrons have a clear dependence on x , in both W bins. The signals in the two bins have the same strength, and no dependence of the Collins asymmetries on W can be stated. From Fig. 4.16 it is clear that, integrating over x , the mean value of the asymmetry in the $W > 7.5 \text{ GeV}/c^2$ bin will be dominated by the events coming from the signal region, while the main contribution to the mean Collins asymmetry in the $W < 7.5 \text{ GeV}/c^2$ comes from the region of x in which the signal is compatible with zero. Figure 4.17 shows the Collins asymmetries as a function of W in the two x bins; no clear

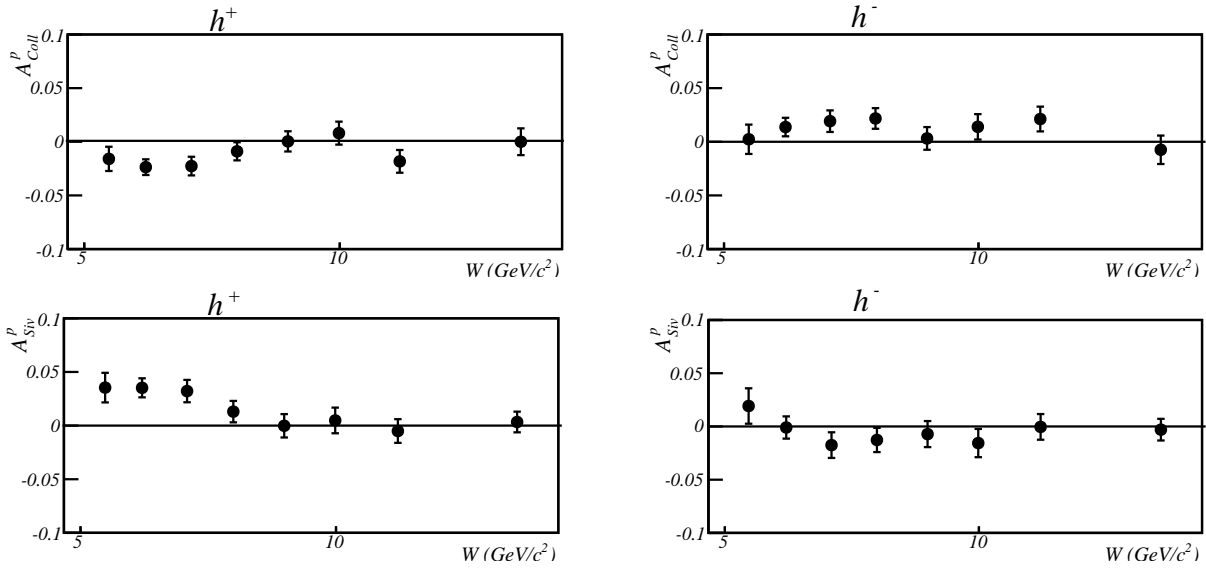


Figure 4.14: Collins (top) and Sivers (bottom) asymmetries as a function of W . The asymmetries for positive hadrons is shown on the left, the asymmetry for negative hadrons is shown on the right.

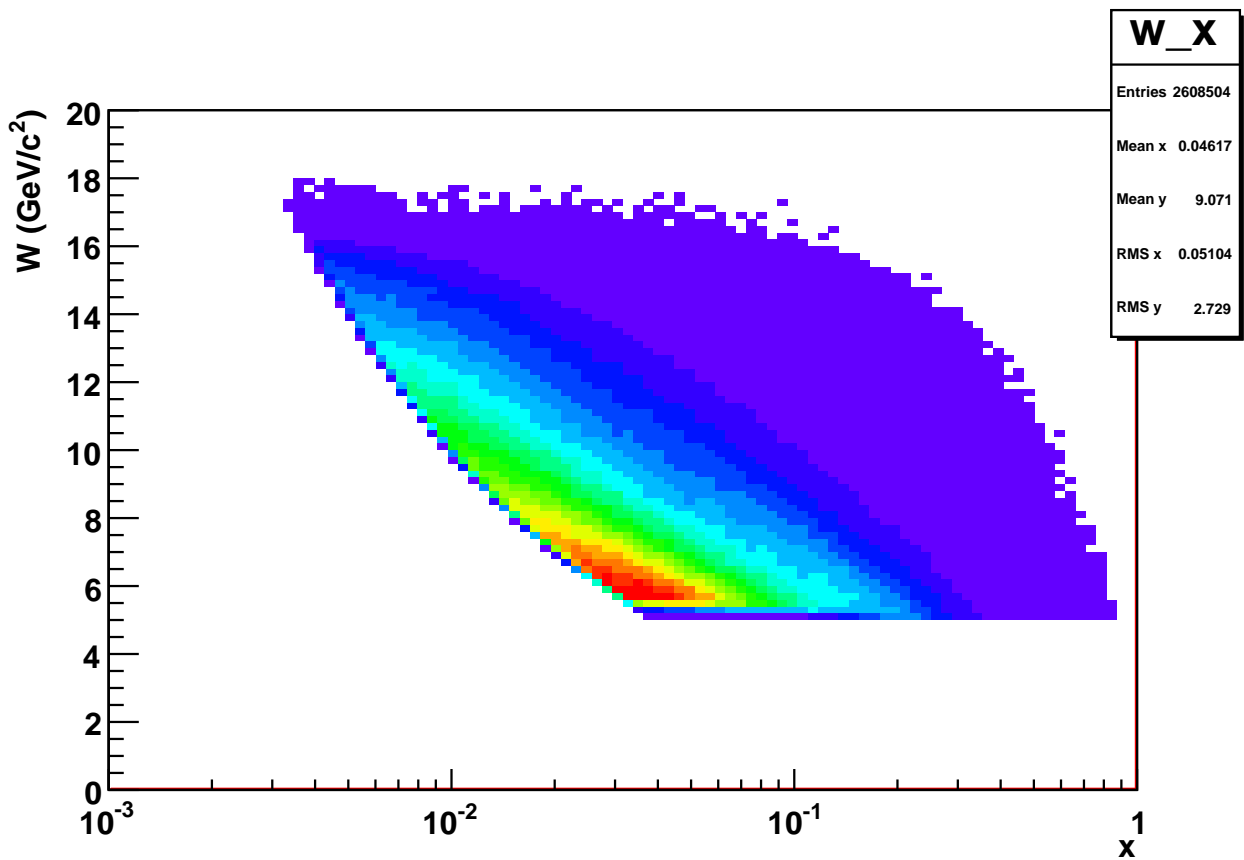


Figure 4.15: Scatter plot W vs x .

indication can be derived.

In Tab. 4.9 the mean values of the Collins asymmetries for positive and negative hadrons are shown in the two W bins for all the events and for the events with $x > 0.032$ and $x < 0.032$ respectively. The mean value of the asymmetries in the two different x bins changes by more than 2σ , while it is constant in the two W bins, if x is kept fixed. The almost 3σ effect between the mean values in the two W bins for the full x range is due to the different contribution to the final asymmetry of the $x > 0.032$ and $x < 0.032$ regions in the two bins.

The Collins asymmetries for positive and negative hadrons show a clear dependence on the signal from x , while no evidence is found that the asymmetries depend on any of the other variables that have been tested, i.e. p_T^h , z and W .

The Sivers asymmetry for positive hadrons is compatible with zero on the full x range in the $W > 7.5 \text{ GeV}/c^2$ bin, while a sizeable signal with no clear dependence on x is present in the $W < 7.5 \text{ GeV}/c^2$ bin. The Sivers asymmetry for positive hadrons as a function of W is shown in the two x bins in Fig. 4.17: at small W there is a signal, while the asymmetries are compatible with zero at large W , in both x ranges. At variance with the Collins asymmetry, the Sivers asymmetries for positive hadrons show a dependence on W . The Sivers asymmetry for negative hadrons is compatible with zero in all W and x bins.

The mean values of the Sivers asymmetries are shown in Tab. 4.9. The mean Sivers asymmetry at $W < 7.5 \text{ GeV}/c^2$ (full x range) is $5\sigma_{stat}$ from zero, while it is compatible with zero in the range $W > 7.5 \text{ GeV}/c^2$. Taking into account also the systematic contribution to the error, the mean values of the asymmetries in the two W ranges differ for more than 2σ . The mean values of the asymmetries measured in the two x bins are compatible between them, in both W ranges.

| Mean Collins asymmetry | | | | |
|------------------------|---------------------------|--------------------|---------------------------|--------------------|
| | $W < 7.5 \text{ GeV}/c^2$ | | $W > 7.5 \text{ GeV}/c^2$ | |
| | h^+ | h^- | h^+ | h^- |
| all x | -0.022 ± 0.005 | 0.013 ± 0.005 | -0.004 ± 0.004 | 0.012 ± 0.005 |
| $0.032 < x < 1$ | -0.024 ± 0.006 | 0.019 ± 0.007 | -0.015 ± 0.008 | 0.019 ± 0.009 |
| $x < 0.032$ | -0.000 ± 0.010 | 0.007 ± 0.012 | -0.001 ± 0.005 | 0.009 ± 0.006 |
| Mean Sivers asymmetry | | | | |
| | $W < 7.5 \text{ GeV}/c^2$ | | $W > 7.5 \text{ GeV}/c^2$ | |
| | h^+ | h^- | h^+ | h^- |
| all x | 0.033 ± 0.006 | -0.003 ± 0.007 | 0.003 ± 0.004 | -0.007 ± 0.005 |
| $0.032 < x < 1$ | 0.034 ± 0.007 | 0.000 ± 0.008 | 0.002 ± 0.009 | -0.003 ± 0.010 |
| $x < 0.032$ | 0.025 ± 0.012 | -0.019 ± 0.013 | 0.003 ± 0.005 | -0.007 ± 0.006 |

Table 4.9: Mean values of the Collins and Sivers asymmetries in the different bins of x and W

The Sivers asymmetry for positive hadrons shows a clear dependence of the signal from W . This dependence is unexpected and has been observed for the first time. The signal is large at small W , the range where the HERMES experiment has measured a clear Sivers effect, and goes to zero at large W , which, for large x , means large Q^2 (Fig. 4.18).

Despite the known problems of the measurement of the Sivers effect, that were described at length in this chapter, the W dependence of the Sivers asymmetry is a more than $2\sigma_{TOT}$ effect. Moreover, the measurements done in the first two and the second two periods give the same indication (Tab. 4.8): the difference of the mean asymmetry in the two W bins is larger than 2σ both for the average of the first two and the second two *periods*, the asymmetry being larger in the small W bin. To conclude, there is an indication for a possible W dependence of this asymmetry, but the present statistical and systematic uncertainties do not allow definite

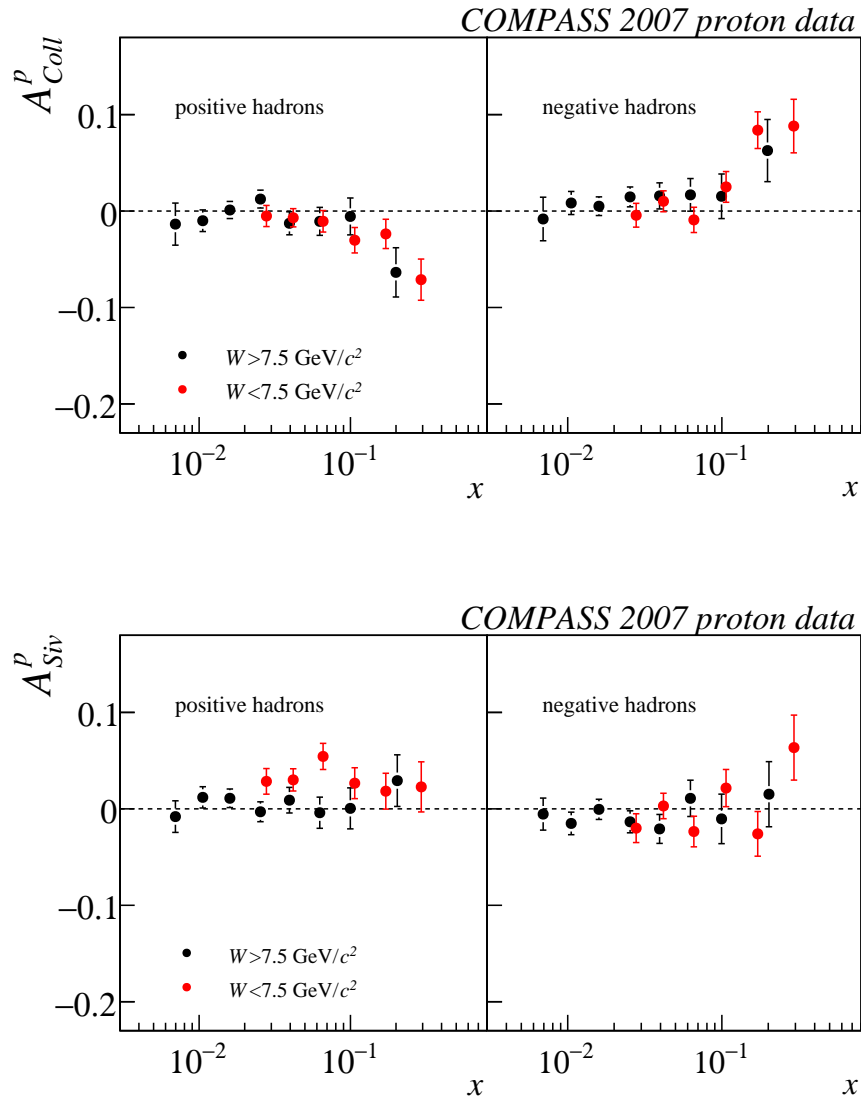


Figure 4.16: Collins (upper row) and Sivers (lower row) asymmetries as a function of x in two complementary ranges of W i.e. $W < 7.5 \text{ GeV}/c^2$ (red points) and $W > 7.5 \text{ GeV}/c^2$ (closed black points) for positive hadrons (left) and negative hadrons (right).

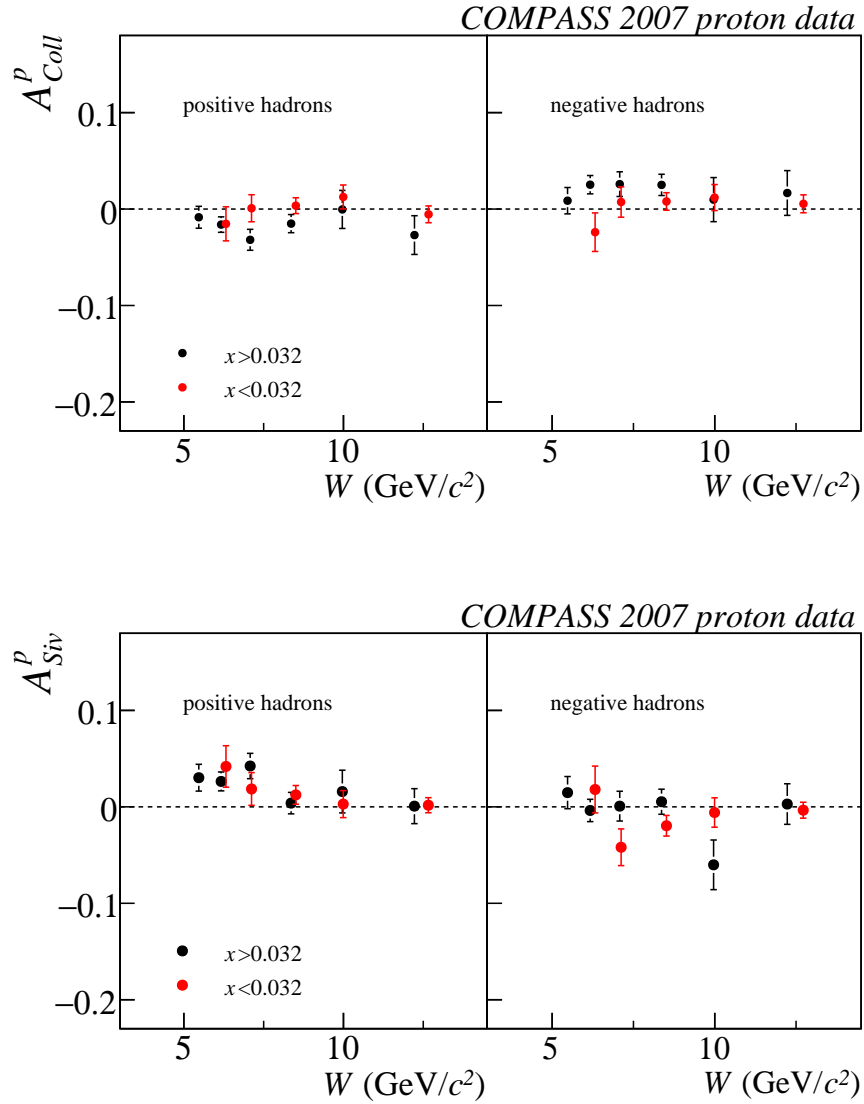


Figure 4.17: Collins (upper row) and Sivers (lower row) asymmetries as a function of W in two complementary ranges of x i.e. $x < 0.032$ (red points) and $W > 0.032$ (closed black points) for positive hadrons (left) and negative hadrons (right).

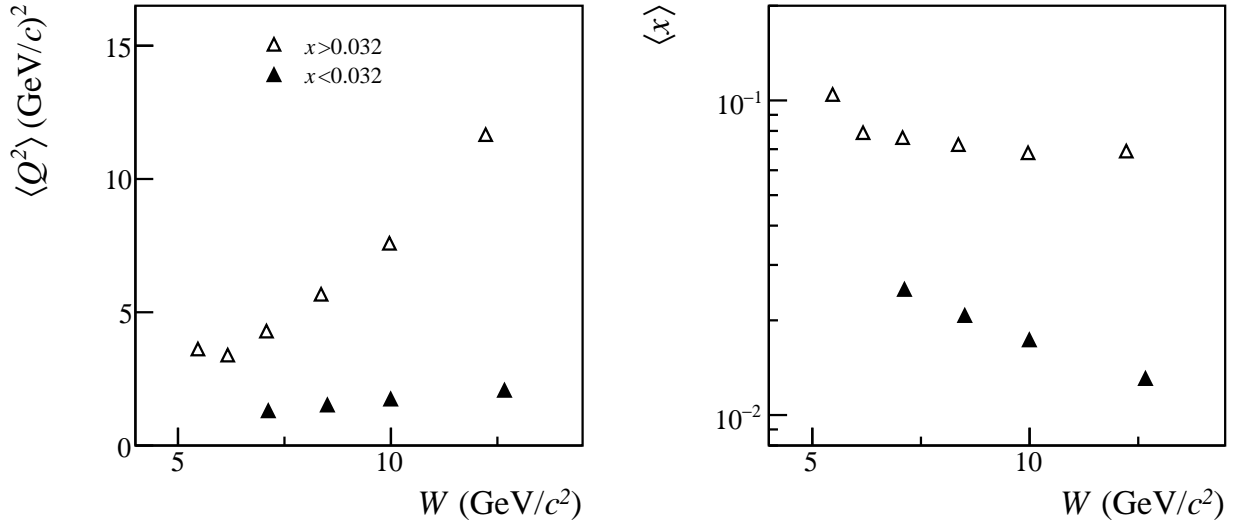


Figure 4.18: Mean values of Q^2 and x as a function of W in two complementary ranges of W i.e. $x < 0.032$ (open points) and $W > 0.032$ (closed points)

conclusions.

4.4 The measurement of the further 6 asymmetries

The amplitude of the other 6 modulations, i.e. $A^{\sin(3\phi_h - \phi_s)}$, $A^{\sin(2\phi_h - \phi_s)}$, $A^{\cos(2\phi_h - \phi_s)}$, $A^{\sin(3\phi_h - \phi_s)}$, $A^{\sin(2\phi_h - \phi_s)}$ and $A^{\cos(2\phi_h - \phi_s)}$ are extracted with the same procedure used to extract the Collins and the Sivers asymmetries. The $A^{\cos(2\phi_h - \phi_s)}$, $A^{\cos(\phi_h - \phi_s)}$ and $A^{\cos(\phi_s)}$ asymmetries are double-spin asymmetries (Sec.1.2), thus the raw asymmetry value has to be divided by the average value of the beam polarisation (Fig. 2.2), that, in 2007 is estimated to be 79%. The D_{NN} factors corresponding to these modulations are reported in Tab.4.10.

The $A^{\sin(3\phi_h - \phi_s)}$, $A^{\sin(2\phi_h - \phi_s)}$ and $A^{\cos(2\phi_h - \phi_s)}$ modulations have been extracted using all the periods available. In Fig. 4.19 the extracted asymmetries for the first and the second parts of the run are shown, as a function of x , as a check of the period compatibility. The mean value of the asymmetry extracted in every *period* and the average over the periods is shown in Tab. 4.11. The modulation $A^{\sin(3\phi_h - \phi_s)}$ shows a systematic difference between the first and the second part of the data-taking. For positive hadrons the difference is visible mainly at large x , while for negative hadrons it covers the whole range and the average difference between the two parts is 4.5σ . The modulation $A^{\sin(2\phi_h - \phi_s)}$ shows a good compatibility between all the measured periods. The modulation $A^{\cos(2\phi_h - \phi_s)}$ shows an average good compatibility between the measured periods for negative hadrons, while there is a difference between the two parts is 2.7σ . Both for positive and for negative hadrons some systematic effect is visible in the valence region.

The $\cos(\phi_h - \phi_s)$, $\sin(\phi_s)$ and $\cos(\phi_s)$ modulations have been measured on the same periods used to extract the Sivers asymmetry (i.e. $W25$, $W30$, $W39$ and $W42$). The mean value of the asymmetries extracted in the two parts of the run is shown in Fig. 4.20 as a function of x , and the mean values in the different periods are shown in Tab. 4.12. The modulation $\cos(\phi_h - \phi_s)$ shows an overall compatibility between the two halves of the data taking at the 2σ level, and no specific systematic effect is visible in the plot. The modulation $\sin(\phi_s)$ for positive hadrons has a mean difference of 2.7σ between the two parts of the run, visible on the plot on the full x range. For the negative hadrons a systematic effect of 2.4σ is also visible. The modulation

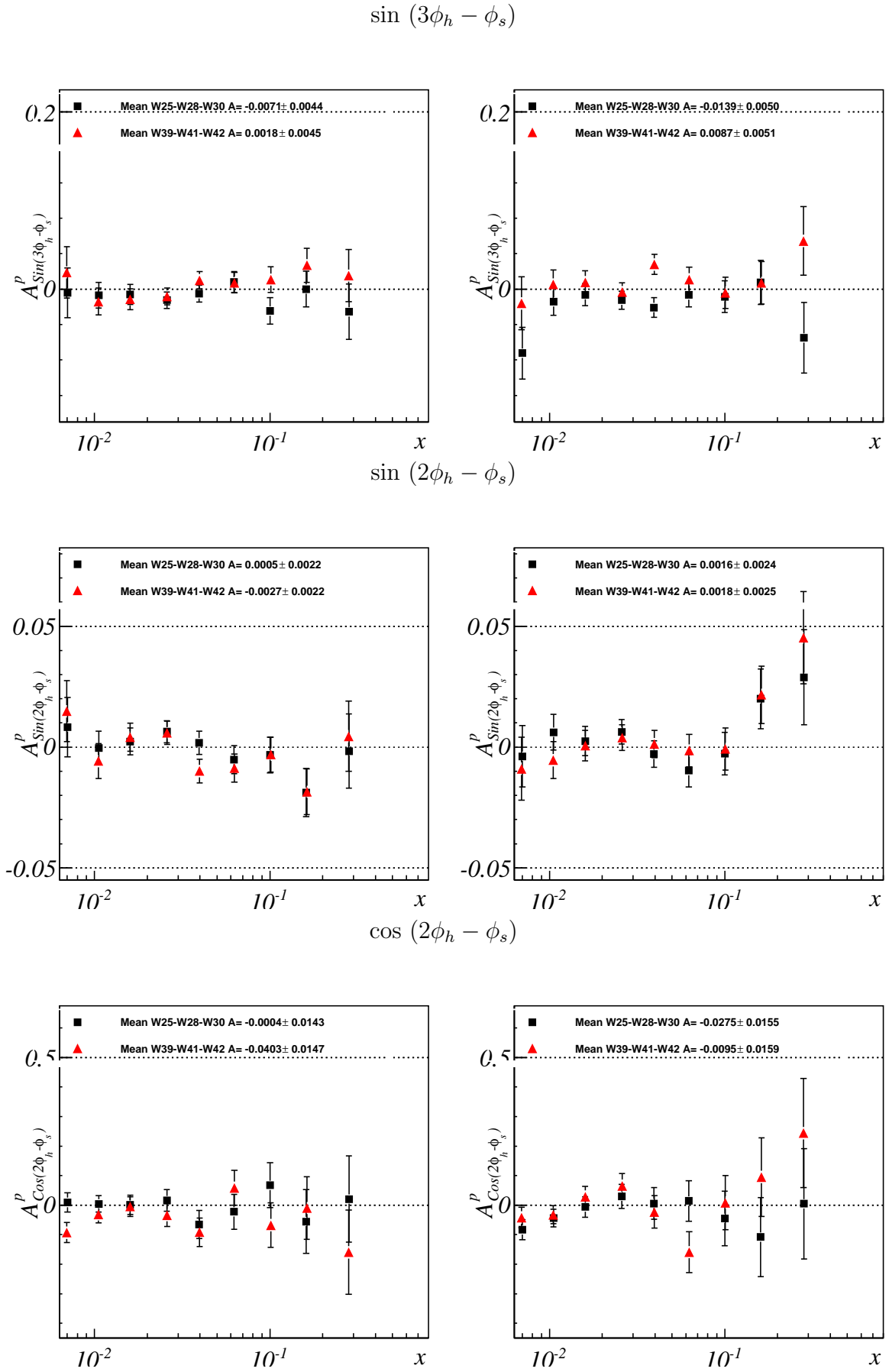


Figure 4.19: The "Collins-like" asymmetries for positive (left) and negative (right) hadrons as a function of x . Black squares are the first part of the run, the red triangles are the second part of the run.

| x range | $D_{NN}^{\sin(3\phi_h-\phi_s)}$ | $D_{NN}^{\cos(\phi_h-\phi_s)}$ | $D_{NN}^{\sin(2\phi_h-\phi_s)}, D_{NN}^{\sin(\phi_s)}$ | $D_{NN}^{\cos(2\phi_h-\phi_s)}, D_{NN}^{\phi_s}$ |
|----------------|---------------------------------|--------------------------------|--|--|
| [0.003, 0.008] | 0.61 | 0.77 | 1.39 | 0.65 |
| [0.008, 0.013] | 0.80 | 0.56 | 1.69 | 0.52 |
| [0.013, 0.020] | 0.88 | 0.42 | 1.82 | 0.39 |
| [0.020, 0.032] | 0.93 | 0.31 | 1.90 | 0.29 |
| [0.032, 0.050] | 0.95 | 0.25 | 1.92 | 0.24 |
| [0.050, 0.080] | 0.95 | 0.24 | 1.93 | 0.24 |
| [0.080, 0.130] | 0.95 | 0.24 | 1.93 | 0.23 |
| [0.130, 0.210] | 0.96 | 0.23 | 1.93 | 0.22 |
| [0.210, 1.000] | 0.94 | 0.26 | 1.91 | 0.25 |
| z range | $D_{NN}^{\sin(3\phi_h-\phi_s)}$ | $D_{NN}^{\cos(\phi_h-\phi_s)}$ | $D_{NN}^{\sin(2\phi_h-\phi_s)}, D_{NN}^{\sin(\phi_s)}$ | $D_{NN}^{\cos(2\phi_h-\phi_s)}, D_{NN}^{\phi_s}$ |
| [0.20, 0.25] | 0.90 | 0.36 | 1.84 | 0.34 |
| [0.25, 0.30] | 0.90 | 0.35 | 1.84 | 0.33 |
| [0.30, 0.35] | 0.90 | 0.35 | 1.85 | 0.33 |
| [0.35, 0.40] | 0.90 | 0.35 | 1.85 | 0.32 |
| [0.40, 0.50] | 0.90 | 0.34 | 1.85 | 0.32 |
| [0.50, 0.65] | 0.91 | 0.34 | 1.86 | 0.32 |
| [0.65, 0.80] | 0.91 | 0.33 | 1.86 | 0.31 |
| [0.80, 1.00] | 0.91 | 0.33 | 1.87 | 0.31 |
| p_T^h range | $D_{NN}^{\sin(3\phi_h-\phi_s)}$ | $D_{NN}^{\cos(\phi_h-\phi_s)}$ | $D_{NN}^{\sin(2\phi_h-\phi_s)}, D_{NN}^{\sin(\phi_s)}$ | $D_{NN}^{\cos(2\phi_h-\phi_s)}, D_{NN}^{\phi_s}$ |
| [0.10, 0.20] | 0.91 | 0.34 | 1.86 | 0.32 |
| [0.30, 0.40] | 0.91 | 0.33 | 1.86 | 0.31 |
| [0.40, 0.50] | 0.91 | 0.34 | 1.86 | 0.32 |
| [0.50, 0.60] | 0.91 | 0.34 | 1.86 | 0.32 |
| [0.60, 0.75] | 0.90 | 0.34 | 1.85 | 0.32 |
| [0.75, 0.90] | 0.90 | 0.35 | 1.85 | 0.33 |
| [0.90, 1.30] | 0.89 | 0.37 | 1.84 | 0.34 |
| [1.30, 3.00] | 0.88 | 0.39 | 1.81 | 0.37 |
| > 3.00 | 0.83 | 0.47 | 1.74 | 0.43 |
| W range | $D_{NN}^{\sin(3\phi_h-\phi_s)}$ | $D_{NN}^{\cos(\phi_h-\phi_s)}$ | $D_{NN}^{\sin(2\phi_h-\phi_s)}, D_{NN}^{\sin(\phi_s)}$ | $D_{NN}^{\cos(2\phi_h-\phi_s)}, D_{NN}^{\phi_s}$ |
| [5.00, 5.70] | 0.99 | 0.12 | 1.99 | 0.12 |
| [5.70, 6.70] | 0.99 | 0.15 | 1.98 | 0.15 |
| [6.70, 7.50] | 0.98 | 0.19 | 1.97 | 0.19 |
| [7.50, 8.50] | 0.97 | 0.25 | 1.95 | 0.24 |
| [8.50, 9.50] | 0.95 | 0.32 | 1.92 | 0.31 |
| [9.50, 10.50] | 0.92 | 0.40 | 1.87 | 0.39 |
| [10.50, 12.00] | 0.86 | 0.51 | 1.78 | 0.49 |
| > 12.00 | 0.63 | 0.75 | 1.44 | 0.65 |

Table 4.10: Mean values of D_{NN} for the different modulations in the kinematical bins used in the analysis.

$\cos(\phi_s)$ shows an overall good compatibility between the two parts of the data taking.

The compatibility of the asymmetries measured in $W39$ with that measured in the other *periods* is then checked, since the quality test for $W39$ gives a confidence level $< 1\%$, (Sec.3.6.3). The mean asymmetry is compatible for the modulations $A^{\cos(\phi_h-\phi_s)}$ and $A^{\sin(\phi_s)}$, both for positive and negative hadrons, while a 2σ effect is present for the $A^{\cos(\phi_s)}$ (negative hadrons).

The systematic error is calculated as for the Collins and Sivers asymmetries. The contribution from the variation of the acceptance is of the order of half σ_{stat} , for all the modulations. The contribution of each period is shown in Tab.4.13: notice that the contribution of $W39$ for the $A^{\cos(\phi_h-\phi_s)}$, $A^{\sin(\phi_s)}$ and $A^{\cos(\phi_s)}$ is larger than for the other weeks, reflecting the poor quality of the period.

The contribution from the different estimators is $0.16 \sigma_{stat}$, the scale uncertainty introduced by the measurement of the target polarisation is 5% , and that coming from the measurement of the beam polarisation (for the double-spin asymmetries only) is 4% (Tab. 2.2). The detailed

| | $\sin(3\phi_h - \phi_s)$ | |
|--------------------|--------------------------|----------------------|
| | h^+ | h^- |
| W25 | -0.0076 ± 0.0081 | -0.0073 ± 0.0092 |
| W28 | -0.0130 ± 0.0083 | -0.0200 ± 0.0094 |
| W30 | -0.0028 ± 0.0067 | -0.0144 ± 0.0076 |
| W39 | 0.0019 ± 0.0068 | 0.0001 ± 0.0078 |
| W41 | 0.0092 ± 0.0071 | 0.0084 ± 0.0081 |
| W42 | -0.0145 ± 0.0106 | 0.0292 ± 0.0120 |
| W25-28-30 | -0.0071 ± 0.0044 | -0.0139 ± 0.0050 |
| W39-41-42 | 0.0018 ± 0.0045 | 0.0087 ± 0.0051 |
| W25-28-30-39-41-42 | -0.0027 ± 0.0031 | -0.0029 ± 0.0036 |
| | $\sin(2\phi_h - \phi_s)$ | |
| | h^+ | h^- |
| W25 | 0.0010 ± 0.0040 | 0.0022 ± 0.0045 |
| W28 | -0.0004 ± 0.0041 | 0.0023 ± 0.0046 |
| W30 | 0.0007 ± 0.0033 | 0.0006 ± 0.0037 |
| W39 | -0.0015 ± 0.0034 | -0.0023 ± 0.0038 |
| W41 | -0.0043 ± 0.0035 | 0.0040 ± 0.0040 |
| W42 | -0.0020 ± 0.0052 | 0.0066 ± 0.0059 |
| W25-28-30 | 0.0005 ± 0.0022 | 0.0016 ± 0.0024 |
| W39-41-42 | -0.0027 ± 0.0022 | 0.0018 ± 0.0025 |
| W25-28-30-39-41-42 | -0.0011 ± 0.0015 | 0.0017 ± 0.0017 |
| | $\cos(2\phi_h - \phi_s)$ | |
| | h^+ | h^- |
| W25 | -0.0172 ± 0.0263 | -0.0555 ± 0.0283 |
| W28 | 0.0068 ± 0.0270 | 0.0031 ± 0.0292 |
| W30 | 0.0067 ± 0.0221 | -0.0281 ± 0.0239 |
| W39 | -0.0482 ± 0.0224 | -0.0147 ± 0.0242 |
| W41 | -0.0502 ± 0.0233 | -0.0155 ± 0.0252 |
| W42 | 0.0014 ± 0.0350 | 0.0168 ± 0.0378 |
| W25-28-30 | -0.0004 ± 0.0143 | -0.0275 ± 0.0155 |
| W39-41-42 | -0.0403 ± 0.0147 | -0.0095 ± 0.0159 |
| W25-28-30-39-41-42 | -0.0199 ± 0.0103 | -0.0187 ± 0.0111 |

Table 4.11: Mean values of the amplitudes of the $\sin(3\phi_h - \phi_s)$, $\sin(2\phi_h - \phi_s)$ and $\cos(2\phi_h - \phi_s)$ modulations in the different periods, in the first and the second part of the data-taking and the overall mean value.

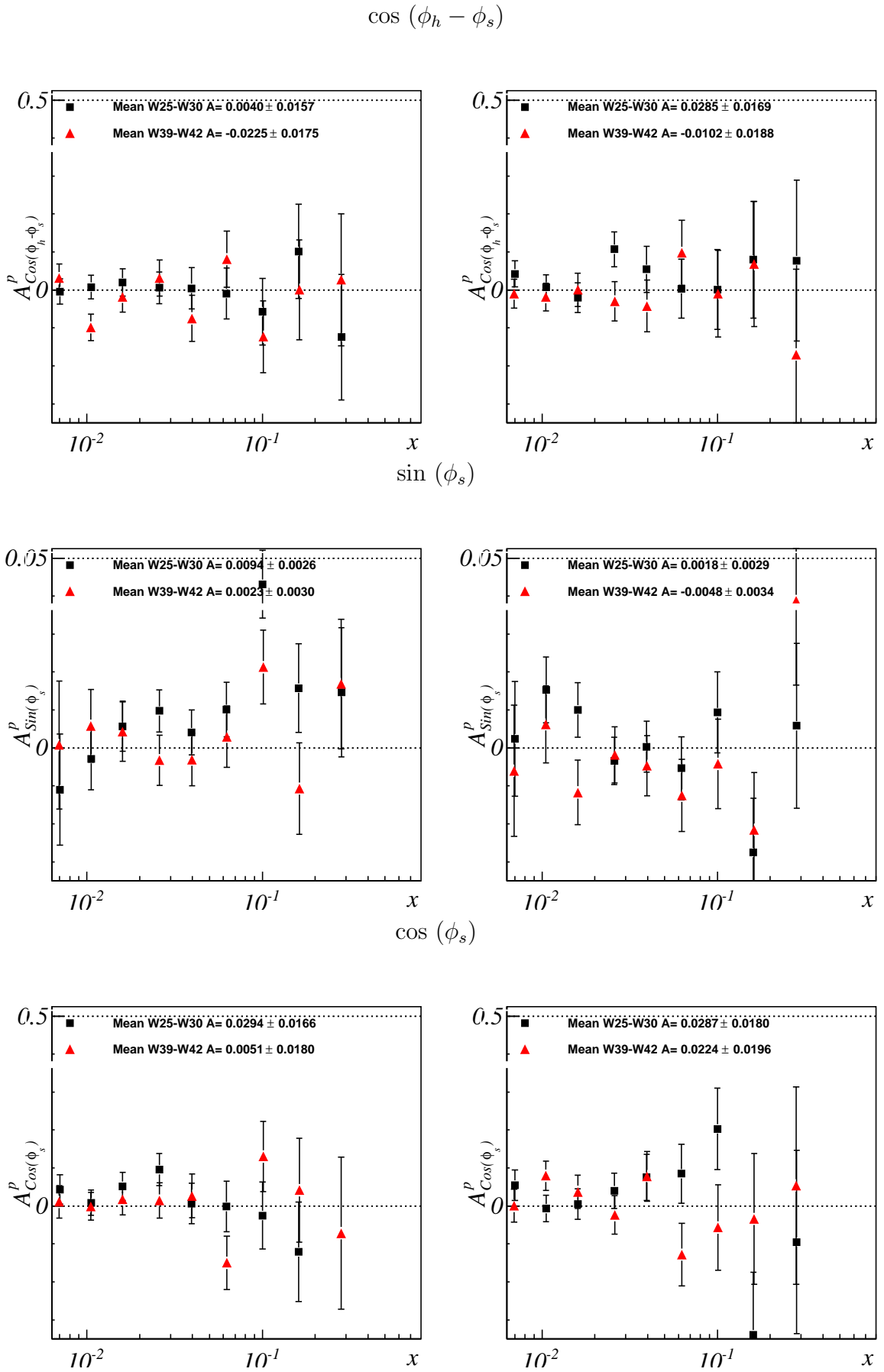


Figure 4.20: The "Sivers-like" asymmetries for positive (left) and negative (right) hadrons as a function of x . Black squares are the first part of the run, the red triangles are the second part of the run.

| $\cos(\phi_h - \phi_s)$ | | |
|-------------------------|----------------------|----------------------|
| | h^+ | h^- |
| W25 | 0.0102 ± 0.0244 | -0.0142 ± 0.0262 |
| W30 | -0.0003 ± 0.0205 | 0.0587 ± 0.0221 |
| W39 | -0.0090 ± 0.0208 | 0.0063 ± 0.0224 |
| W42 | -0.0557 ± 0.0326 | -0.0506 ± 0.0349 |
| W25-30 | 0.0040 ± 0.0157 | 0.0285 ± 0.0169 |
| W39-42 | -0.0225 ± 0.0175 | -0.0102 ± 0.0188 |
| W25-30-39-42 | -0.0078 ± 0.0117 | 0.0112 ± 0.0126 |
| $\sin(\phi_s)$ | | |
| | h^+ | h^- |
| W25 | 0.0052 ± 0.0041 | 0.0026 ± 0.0046 |
| W30 | 0.0123 ± 0.0034 | 0.0013 ± 0.0039 |
| W39 | 0.0041 ± 0.0036 | -0.0052 ± 0.0041 |
| W42 | -0.0017 ± 0.0054 | -0.0041 ± 0.0061 |
| W25-30 | 0.0094 ± 0.0026 | 0.0018 ± 0.0029 |
| W39-42 | 0.0023 ± 0.0030 | -0.0048 ± 0.0034 |
| W25-30-39-42 | 0.0063 ± 0.0020 | -0.0010 ± 0.0022 |
| $\cos(\phi_s)$ | | |
| | h^+ | h^- |
| W25 | 0.0329 ± 0.0261 | 0.0442 ± 0.0281 |
| W30 | 0.0271 ± 0.0216 | 0.0180 ± 0.0234 |
| W39 | 0.0035 ± 0.0213 | -0.0009 ± 0.0231 |
| W42 | 0.0093 ± 0.0341 | 0.0820 ± 0.0369 |
| W25-30 | 0.0294 ± 0.0166 | 0.0287 ± 0.0180 |
| W39-42 | 0.0051 ± 0.0180 | 0.0224 ± 0.0196 |
| W25-30-39-42 | 0.0183 ± 0.0122 | 0.0258 ± 0.0132 |

Table 4.12: Mean values of the amplitudes of the $\cos(\phi_h - \phi_s)$, $\sin(\phi_s)$ and $\cos(\phi_s)$ modulations in the different periods, in the first and the second part of the data-taking and the overall mean value.

| | $\sin(3\phi_h - \phi_s)$ | | $\sin(2\phi_h - \phi_s)$ | | $\cos(2\phi_h - \phi_s)$ | |
|---------|--------------------------|-------|--------------------------|-------|--------------------------|-------|
| | h^+ | h^- | h^+ | h^- | h^+ | h^- |
| W25 | 0.4 | 0.3 | 0.5 | 0.4 | 0.8 | 0.4 |
| W30 | 0.3 | 0.5 | 0.4 | 0.6 | 0.7 | 1.0 |
| W39 | 0.3 | 0.6 | 0.6 | 0.4 | 0.3 | 0.7 |
| W42 | 0.6 | 0.9 | 0.6 | 0.7 | 0.9 | 0.2 |
| W28 | 0.8 | 0.4 | 0.7 | 0.5 | 0.6 | 0.5 |
| W41 | 0.5 | 0.5 | 0.4 | 0.4 | 0.6 | 0.6 |
| Average | 0.5 | 0.5 | 0.5 | 0.5 | 0.6 | 0.5 |
| | $\cos(\phi_h - \phi_s)$ | | $\sin(\phi_s)$ | | $\cos(\phi_s)$ | |
| | h^+ | h^- | h^+ | h^- | h^+ | h^- |
| W25 | 0.5 | 0.7 | 0.3 | 0.5 | 0.6 | 0.6 |
| W30 | 0.4 | 0.4 | 0.7 | 0.3 | 0.5 | 0.5 |
| W39 | 0.7 | 1.1 | 1.0 | 0.5 | 0.6 | 0.8 |
| W42 | 0.2 | 0.5 | 0.6 | 0.5 | 0.3 | 0.4 |
| Average | 0.5 | 0.7 | 0.6 | 0.4 | 0.5 | 0.6 |

Table 4.13: Systematic error due to acceptance variation, in units of the statistical one.

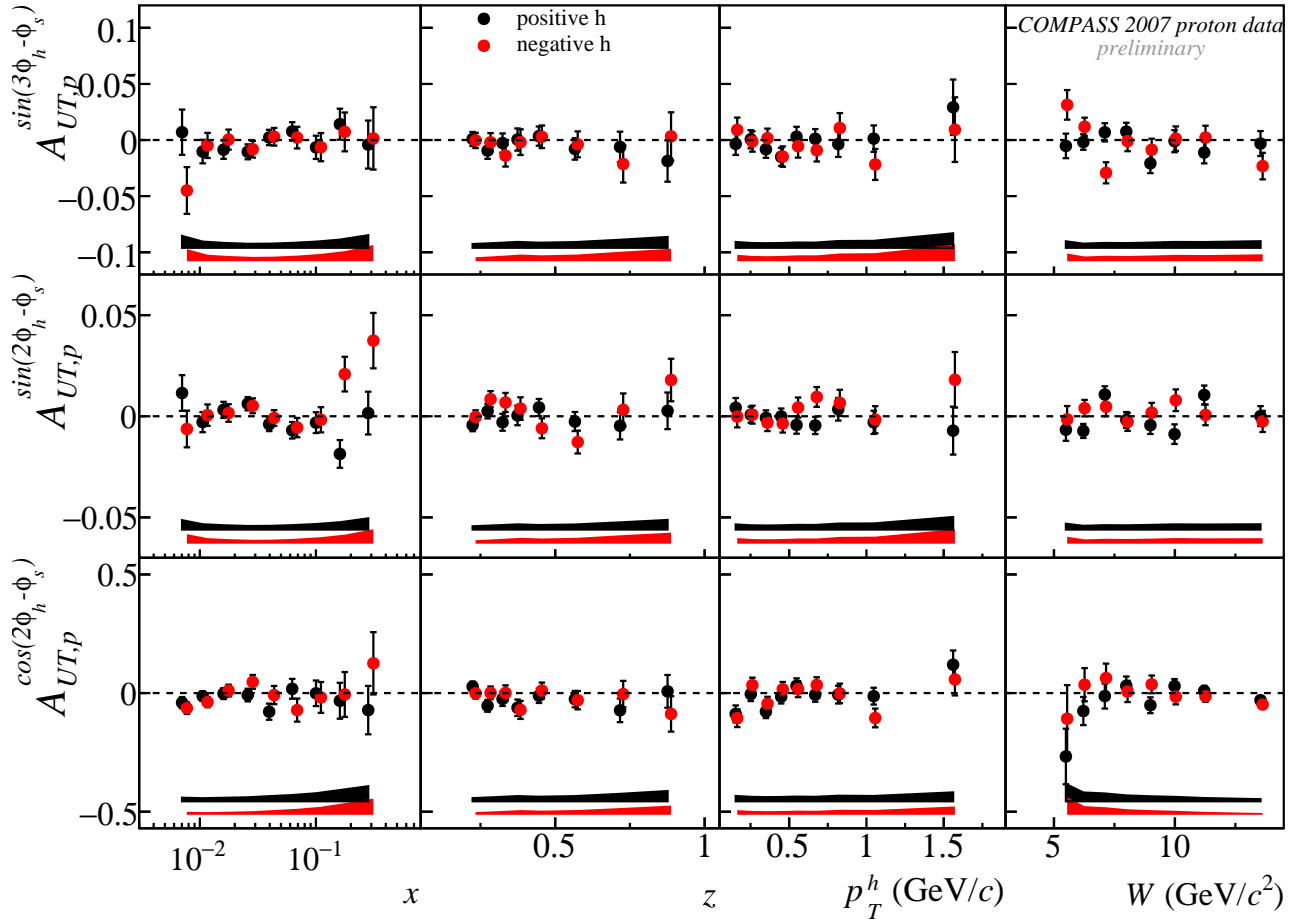


Figure 4.21: The single spin asymmetries $\sin(3\phi_h - \phi_s)$, $\sin(2\phi_h - \phi_s)$ and $\cos(2\phi_h - \phi_s)$ asymmetries for positive and negative hadrons as a function of x, z, p_T and W .

contribution list is shown in Tab. 4.14 and 4.15.

4.5 Final results on the further 6 asymmetries

The single spin asymmetries $A_{UT}^{\sin(3\phi_h)}$, $A_{UT}^{\sin(\phi_s)}$ and $A_{UT}^{\sin(2\phi_h - \phi_s)}$ are shown in Fig. 4.21, as a function of x and, z, p_T and W . The measured asymmetries are all compatible with zero, apart from $A_{UT}^{\sin(2\phi_h - \phi_s)}$, where there is an indication of a possible signal at high values of x . These asymmetries have also been measured by the HERMES collaboration [38], and they resulted to be compatible with zero, apart from the $A_{UT}^{\sin(\phi_s)}$ asymmetry for negative pions, which has found to be negative. Within the present statistical error, the $A_{UT}^{\sin(\phi_s)}$ measured at COMPASS is still compatible with that measured at HERMES.

The double spin asymmetries $A_{LT}^{\cos(\phi_h - \phi_s)}$, $A_{LT}^{(\phi_s)}$ and $A_{LT}^{\cos(2\phi_h - \phi_s)}$ are shown in Fig. 4.22, as a function of x and, z, p_T and W . The measured asymmetries are all compatible with zero.

| $\sin(3\phi_h - \phi_s)$ | h+ | h- |
|--|---------------------|---------------------|
| Point to point systematic error | | |
| estimator for extraction of asymmetries | $0.15\sigma_{stat}$ | $0.15\sigma_{stat}$ |
| acceptance variations | $0.5\sigma_{stat}$ | $0.5\sigma_{stat}$ |
| total | $0.52\sigma_{stat}$ | $0.52\sigma_{stat}$ |
| Scale factors | | |
| period compatibility (absolute) | 0 | 0.011 |
| target polarization | $0.05A$ | $0.05A$ |
| dilution factor | $0.02A$ | $0.02A$ |
| $\sin(2\phi_h - \phi_s)$ | | |
| Point to point systematic error | | |
| estimator for extraction of asymmetries | $0.15\sigma_{stat}$ | $0.15\sigma_{stat}$ |
| acceptance variations | $0.5\sigma_{stat}$ | $0.5\sigma_{stat}$ |
| total | $0.52\sigma_{stat}$ | $0.52\sigma_{stat}$ |
| Scale factors | | |
| target polarization | $0.05A$ | $0.05A$ |
| dilution factor | $0.02A$ | $0.02A$ |
| total | $0.05A$ | $0.05A$ |
| $\cos(2\phi_h - \phi_s)$ | | |
| Point to point systematic error | | |
| estimator for extraction of asymmetries | $0.15\sigma_{stat}$ | $0.15\sigma_{stat}$ |
| acceptance variations | $0.6\sigma_{stat}$ | $0.5\sigma_{stat}$ |
| total | $0.62\sigma_{stat}$ | $0.52\sigma_{stat}$ |
| Scale factors | | |
| target polarization | $0.05A$ | $0.05A$ |
| dilution factor | $0.02A$ | $0.02A$ |
| beam polarisation | $0.04A$ | $0.04A$ |
| total | $0.07A$ | $0.07A$ |

Table 4.14: Contributions to the systematic error for $\sin(3\phi_h - \phi_s)$, $\sin(2\phi_h - \phi_s)$, $\cos(2\phi_h - \phi_s)$ asymmetries, positive and negative hadrons

| $\cos(\phi_h - \phi_s)$ | h+ | h- |
|---|---------------------|---------------------|
| Point to point systematic error | | |
| estimator for extraction of asymmetries | $0.15\sigma_{stat}$ | $0.15\sigma_{stat}$ |
| acceptance variations | $0.5\sigma_{stat}$ | $0.7\sigma_{stat}$ |
| total | $0.52\sigma_{stat}$ | $0.72\sigma_{stat}$ |
| Scale factors | | |
| target polarization | $0.05A$ | $0.05A$ |
| dilution factor | $0.02A$ | $0.02A$ |
| beam polarisation | $0.04A$ | $0.04A$ |
| total | $0.07A$ | $0.07A$ |
| <hr/> | | |
| $\sin(\phi_s)$ | h+ | h- |
| Point to point systematic error | | |
| estimator for extraction of asymmetries | $0.15\sigma_{stat}$ | $0.15\sigma_{stat}$ |
| acceptance variations | $0.6\sigma_{stat}$ | $0.4\sigma_{stat}$ |
| total | $0.62\sigma_{stat}$ | $0.43\sigma_{stat}$ |
| Scale factors | | |
| target polarization | $0.05A$ | $0.05A$ |
| dilution factor | $0.02A$ | $0.02A$ |
| total | $0.05A$ | $0.05A$ |
| <hr/> | | |
| $\cos(\phi_s)$ | h+ | h- |
| Point to point systematic error | | |
| estimator for extraction of asymmetries | $0.15\sigma_{stat}$ | $0.15\sigma_{stat}$ |
| acceptance variations | $0.5\sigma_{stat}$ | $0.6\sigma_{stat}$ |
| total | $0.52\sigma_{stat}$ | $0.62\sigma_{stat}$ |
| Scale factors | | |
| target polarization | $0.05A$ | $0.05A$ |
| dilution factor | $0.02A$ | $0.02A$ |
| beam polarisation | $0.04A$ | $0.04A$ |
| total | $0.07A$ | $0.07A$ |

Table 4.15: Contributions to the systematic error for $\cos(\phi_h - \phi_s)$, $\sin(\phi_s)$, $\cos(\phi_s)$ asymmetries, positive and negative hadrons

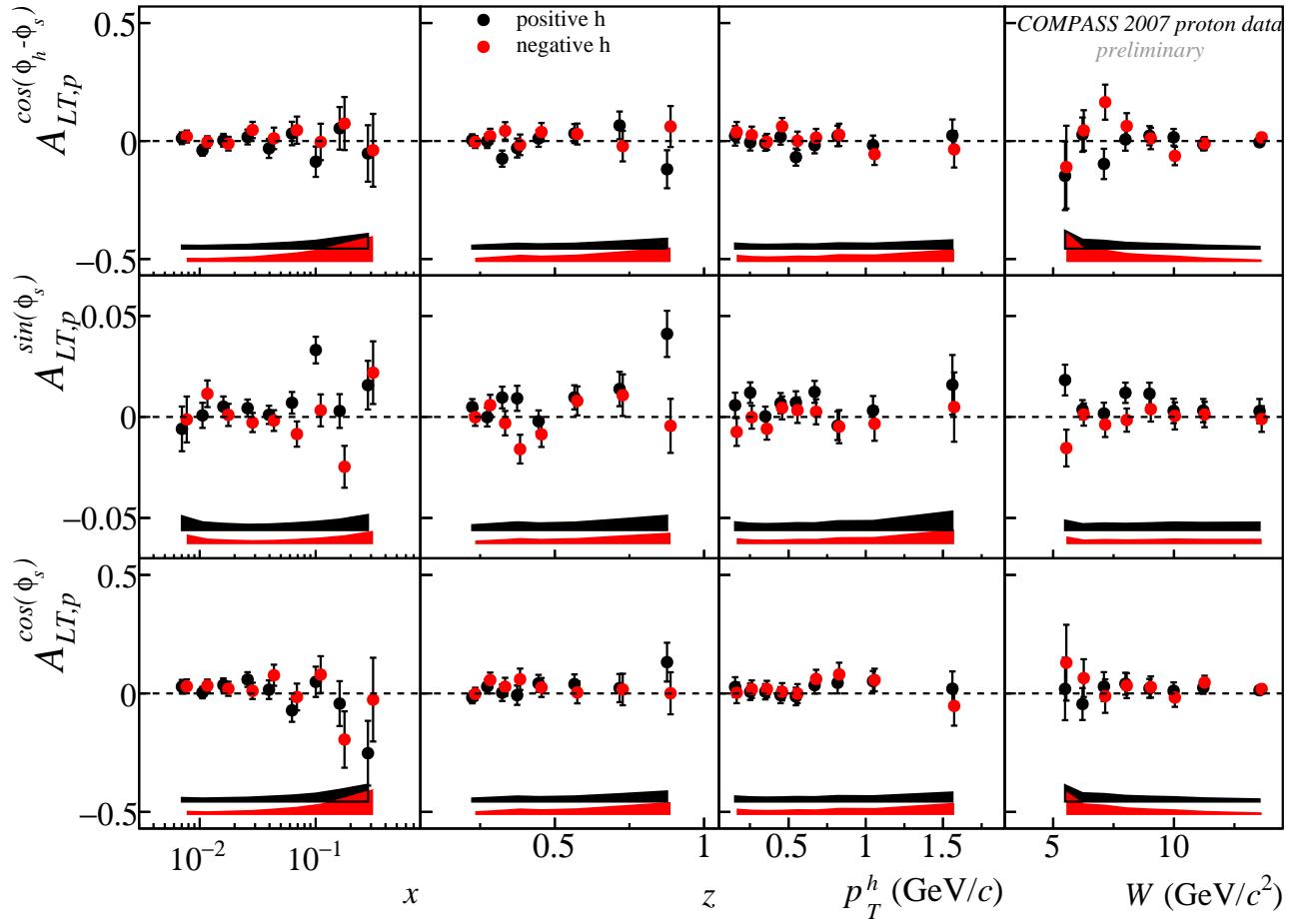


Figure 4.22: The double spin asymmetries $\cos(\phi_h - \phi_s)$, $\sin(\phi_s)$ and $\cos(\phi_s)$ asymmetries for positive and negative hadrons as a function of x, z, p_T and W .

Chapter 5

The Collins and Sivers asymmetries for identified π and K

To extract the flavour-separated transversity and Sivers PDFs from the SIDIS asymmetries, the asymmetries on identified π and K are needed. The K asymmetry is fundamental to investigate the strange quark contribution to the nucleon structure.

The charged hadron sample selected for the transversity analysis is mainly composed of pions ($\sim 80\%$) and kaons ($\sim 15\%$). In COMPASS particle identification (PID) is possible thanks to a Ring Imaging Cherenkov detector (RICH), called RICH-1 (Sec. 2.6). In this Chapter the procedure adopted to select the π and K samples from the charged hadron sample will be explained. At the end the Collins and Sivers asymmetries extracted on identified π s and K s will be presented.

All the work presented in this chapter is original, and was first presented by the author at the SPIN-2010 conference.

5.1 The detector stability in 2007

Hadron identification is applied on top of all the data cleaning and selection described in Chap. 3. The stability of the RICH detector is monitored by looking at the fraction of identified pions. A first check on a *spill-by-spill* basis does not highlight any instability.

A more detailed check is done on a *run-by-run* basis, to spot out detector problems. The detector is divided in four concentric regions (Fig. 5.1), defined by the track angle θ_{RICH} :

- the very central region, close to the beam pipe (particles with $\theta_{RICH} < 30 \text{ mrad}$)
- a region in which the photons of the *ring* are detected by MAPMT only ($30 < \theta_{RICH} < 110 \text{ mrad}$)
- a region in which the photons of the *ring* are detected both by MAPMT and by MWPC ($110 < \theta_{RICH} < 200 \text{ mrad}$)
- the outer region in which the photons of the *ring* are detected by MWPC only ($\theta_{RICH} > 200 \text{ mrad}$)

A drop in the fraction of pions is visible in the more central region around run 59000 (W27). No specific explanation has been found in the experiment logbook. In the third zone ($110 < \theta_{RICH} < 200 \text{ mrad}$) the fraction of pions in the first *period* (*weeks* W25 and W26) is different than in the others. The effect is even clearer looking at the projections in Fig.5.2.

Investigating in the logbook it is found that in $W25 - W26$ there have been frequent trips of

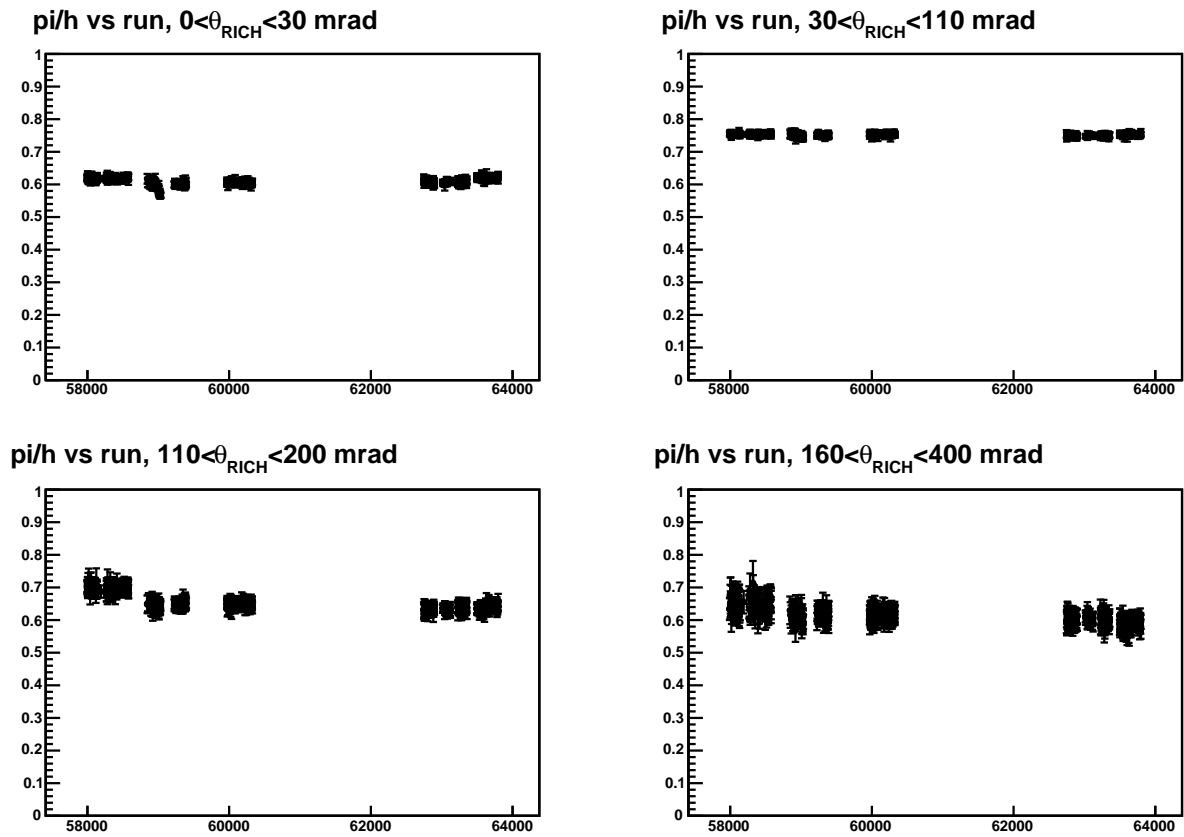


Figure 5.1: Fraction of identified pions per *run* as a function of the *run* number in four different detector zones.

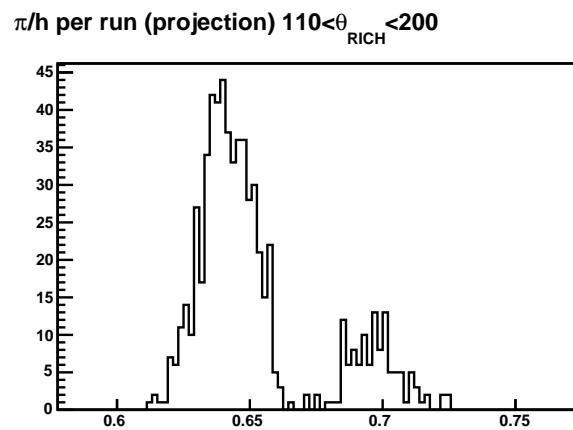


Figure 5.2: Fraction of identified π per *run*. The region $110 < \theta_{RICH} < 200$ mrad is selected. The smaller peak corresponds to W25-W26.

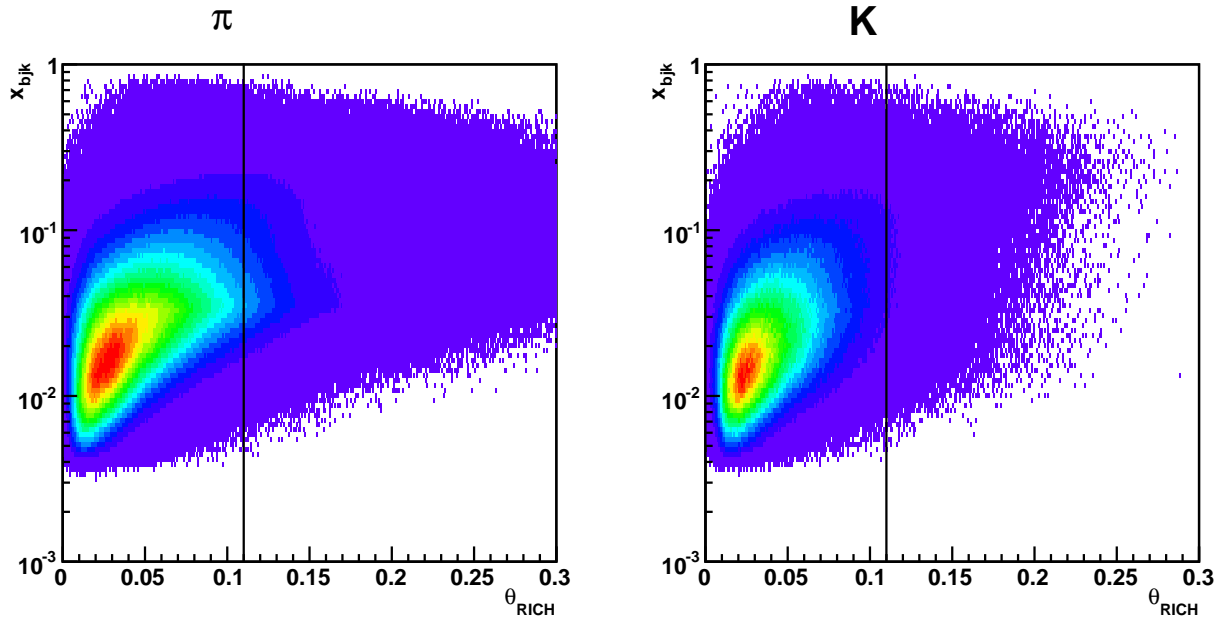


Figure 5.3: Correlation between the particle polar angle θ_{RICH} and x of the event

two MWPC (numbers 2 and 7 in Fig. 2.16) which play an important role in the reconstruction of mixed MAPMT-MWPC rings, and during the same week the voltage was lowered to stabilize the chambers. Since in this *period* the MWPC part of the RICH was unstable, it is decided not to use all the events with $\theta_{RICH} > 0.11$ rad for the analysis. Even if the problem affected two chambers only, it is not possible to use the remaining ones for the analysis for two different reasons: there are many rings that are reconstructed across different chambers and the inefficiency of one chamber influences the extracted value of the refractive index, and thus the identification capabilities of the detector. Due to the correlation between the track polar angle and x of the event, the cut at $\theta_{RICH} > 0.11$ mainly affects particles in the valence region (Fig. 5.3)

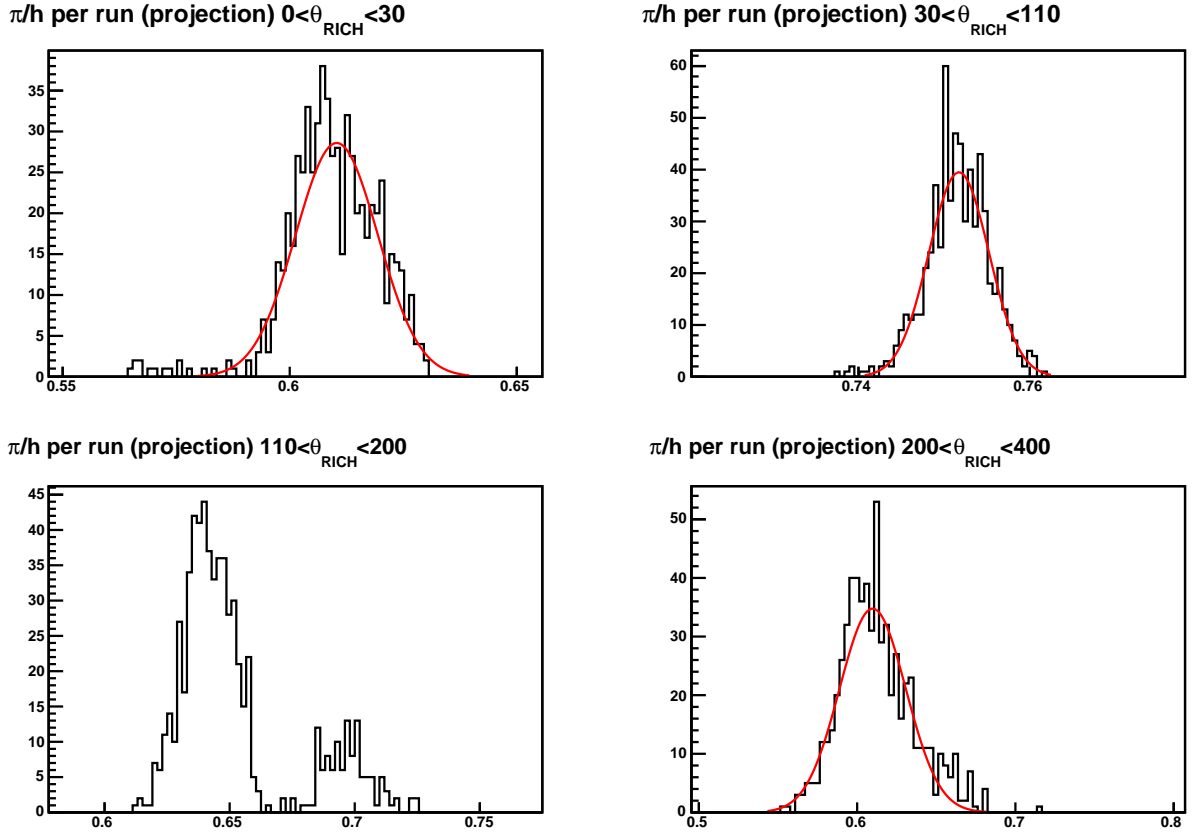
The fraction of pions per run has a Gaussian distribution (red line in Fig.5.4). The runs in which the fraction of pions is outside the 3σ confidence interval are marked for deletion. It is decided to drop the following events:

- for $57913 < run < 58600$ (W25-W26) events with $\theta_{RICH} > 0.11$ rad
- for $58982 < run < 59034$ (W27) all events
- for $run = 6284$ (W39) all events

The data on which the asymmetries on identified π s and K s will be extracted are only a sub sample of the set used to extract the charged hadron asymmetries: in part because of the acceptance in momentum of the RICH detector, in part due its instabilities, concentrated during the first two *periods* of the data-taking.

5.2 The PID efficiency and purity

The identification efficiency of the RICH detector is determined using as a test sample the kaons from the decay channel $\phi_{1020} \rightarrow K^+K^-$ and the pions from the decay $K^0 \rightarrow \pi^+\pi^-$. In both cases, the test sample is built selecting the pairs of hadrons with opposite charge which

Figure 5.4: Fraction of identified π over the number of charged hadrons per run.

| | |
|------------------------|--|
| p (GeV/ c) | 2.8, 9.6, 13, 18, 25, 35, 45, 60 |
| p (GeV/ c) | 2.8, 9.6, 13, 18, 25, 35, 50 |
| θ_{RICH} (mrad) | 0, 0.01, 0.02, 0.03, 0.04, 0.06, 0.11, 0.3 |

Table 5.1: Binning used to extract the efficiency-misidentification probability matrices. The exercise is done with two different binning as a function of the momentum.

invariant mass is that of the parent particle. The identification efficiency is the fraction of particles of the sample that are correctly identified, and is determined separately for positive and negative particles. An example of the determination of the identification efficiencies for positive particles is shown in Fig. 5.5: the hadron sample (black line in the plots) is built with the requirement that the negative decay particle is properly identified by the RICH, to suppress possible background contributions. The sample of identified particles is built requiring that also the positive particle is correctly identified (red line). Analogously, the sample of misidentified particles is built (lower row in the plot).

The efficiencies and misidentification probabilities are extracted in two dimensional matrices in bins of the particle momentum p and the track angle θ_{RICH} . The binning in momentum accounts for the effects arising from the saturation, while the binning in the angle θ_{RICH} accounts for the effects strictly dependent on the detector, as the occupancy, the background and the different photon detector types. Due to the limited statistics, the binning as a function of θ_{RICH} is not uniform (Fig. 5.6). The bin limits are reported in Tab. 5.1.

Given the matrices, it is possible to determine the purity of a specific sample [41, 51]. The purity of the sample is defined as the number of particles correctly identified (*true*) N_{ID}^T over the total number of identified particles N^I of the same specie, that contains both *true* and misidentified particles. The number of correctly identified particles is $N_{ID}^T = \epsilon * N^I$, where ϵ

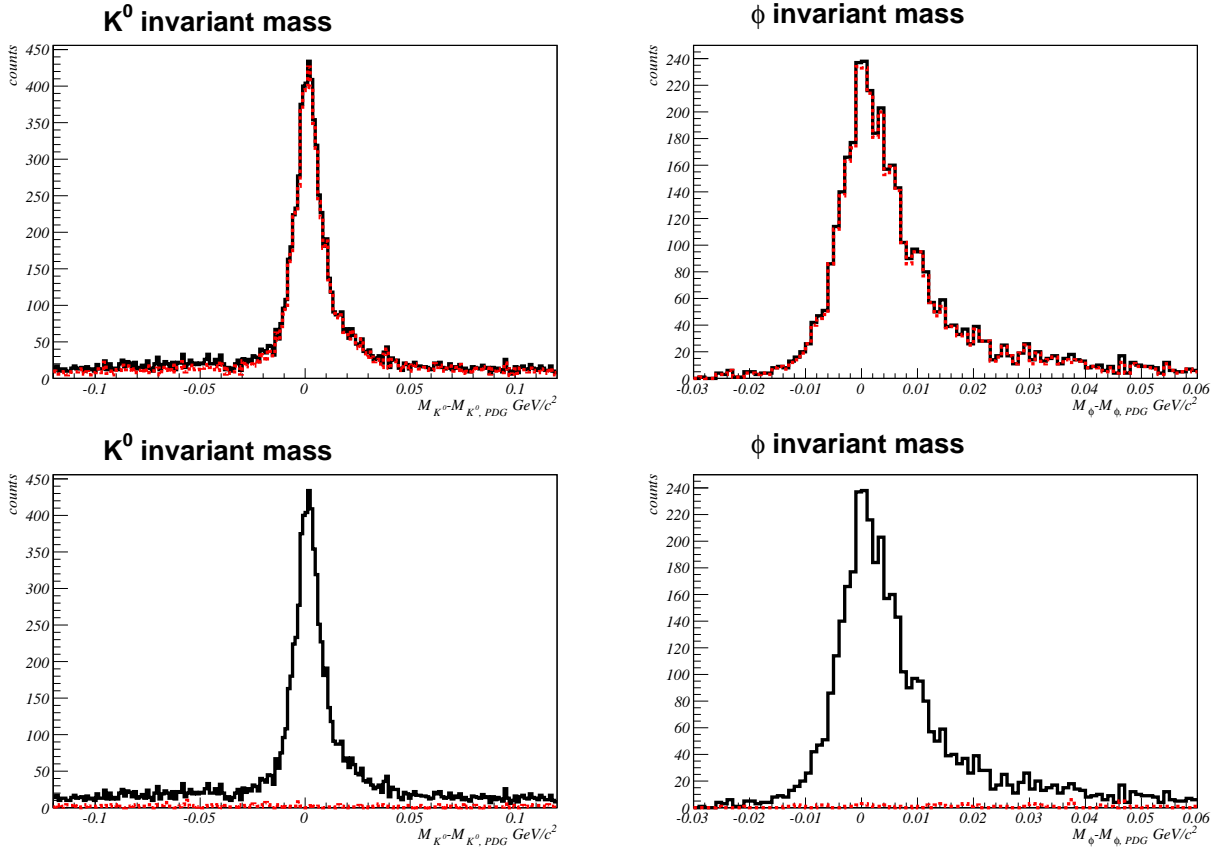


Figure 5.5: Example of the invariant mass spectra (black line) for $K^0 \rightarrow \pi^+\pi^-$ (left) and $\phi_{1020} \rightarrow K^+K^-$ (right) in one bin of the $\theta_{RICH} - p$ matrix. In red the corresponding spectrum for identified particles. Top row, examples of identification, bottom row: examples of misidentification ($\pi \rightarrow K$, left and $K \rightarrow \pi$ right).

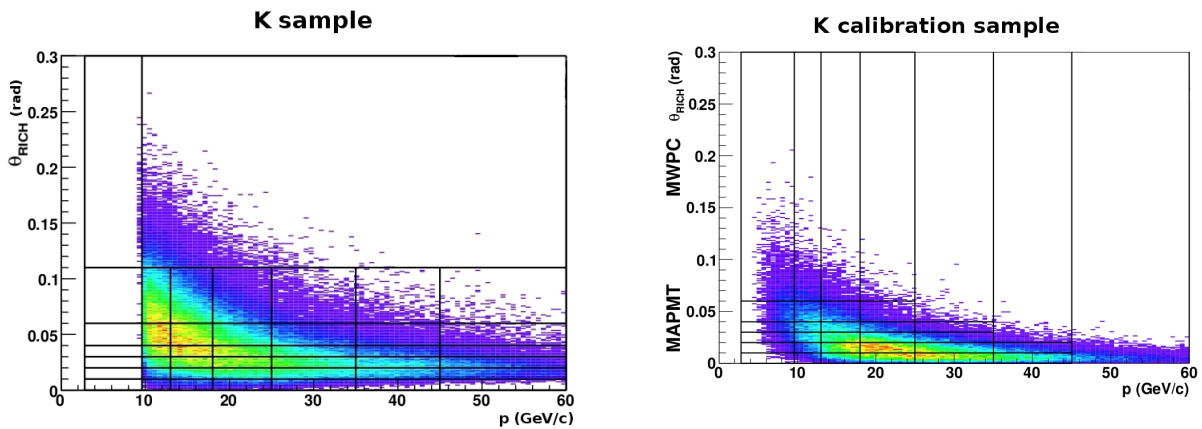


Figure 5.6: Phase space distributions of K s of the "transversity" sample (left) and of the calibration sample (right). The black lines in the figures are the limits of the bins.

is the identification efficiency. As an example, the purity of the kaon sample is:

$$Purity(K) = \frac{\epsilon_K \cdot N_K^T}{N_K^I}. \quad (5.1)$$

The number of *true* particles is not known, but it can be calculated knowing the number of identified particles and the identification-misidentification matrices. The misidentification of K or a π into a proton or of proton into a K or a π is negligible, thus the equation becomes:

$$\begin{pmatrix} N_\pi^I \\ N_K^I \end{pmatrix} = \begin{pmatrix} \epsilon_\pi & P(K \rightarrow \pi) \\ P(\pi \rightarrow K) & \epsilon_K \end{pmatrix} \cdot \begin{pmatrix} N_\pi^T \\ N_K^T \end{pmatrix} \quad (5.2)$$

The purity is not a property of the detector itself, as the efficiency and misidentification probabilities: it depends also on the specific sample that is considered. The event sample used in this analysis consists of $\sim 80\%$ pions and $\sim 15\%$ kaons. It is then clear from Eq. 5.1 that even a small value of the misidentification $\pi \rightarrow K$ causes a large contamination of the kaon sample, while the misidentification of a K into a π has much smaller effects.

To diminish the misidentification probability, it is possible to apply a cut (Fig. 5.7) requiring that the value of the maximum likelihood over the second one is larger than a threshold: the value of the ratio gives the quality of the separation of the two hypotheses, and, if it is close to one, the identification may be ambiguous. The drawback of this procedure is that not only the sample of misidentified particles is reduced, but also that of correctly identified ones.

5.2.1 Tuning of the likelihood

It is possible to tune the cut on the likelihood ratio, so as to privilege the physics channel that we want to measure. For this analysis, the tuning is such to enhance the purity of the K sample, while keeping its statistics as high as possible.

The algorithm is as follows: for each set of cuts the identification-misidentification matrices are extracted and the sample is selected. Then the purity is measured.

The Cherenkov effect saturates with the momentum, thus keeping constant the cut on the ratio of the likelihood the sample purities decreases with the momentum. The efficiency as a function of the momentum is extracted in bins, that are such as to contain an adequate statistics to perform the fit. Several likelihood cuts are tested for each value of the maximum momentum, that corresponds to the efficiency momentum bin limits: $35\text{GeV}/c$, $45\text{GeV}/c$ and $60\text{GeV}/c$. Fig. 5.7 shows that in the bin with $p_{max} = 35\text{GeV}/c$ the misidentification probability is negligible for all the chosen cuts on the likelihood ratio, that it increases in the bin with $p_{max} = 45\text{GeV}/c$, showing a lower value for higher likelihood cuts and that it is higher in the last momentum bin.

The tuning is done by looking at three quantities:

- the signal purity (Fig.5.8).
- FoM 1=purity*efficiency (Fig.5.9).
- FoM 2= purity * $\frac{N_K^{ID}}{N_{all}}$.(Fig.5.10).

The signal purity is the most important quantity: a high purity allows a clear interpretation of the measured K asymmetries. FoM2 gives the final number of true kaons present in the sample, and is used to maximize the final K statistics that will be used.

The selection with $p_{max} = 60\text{GeV}/c$ has a very low FoM1, even with strong cuts on the likelihood

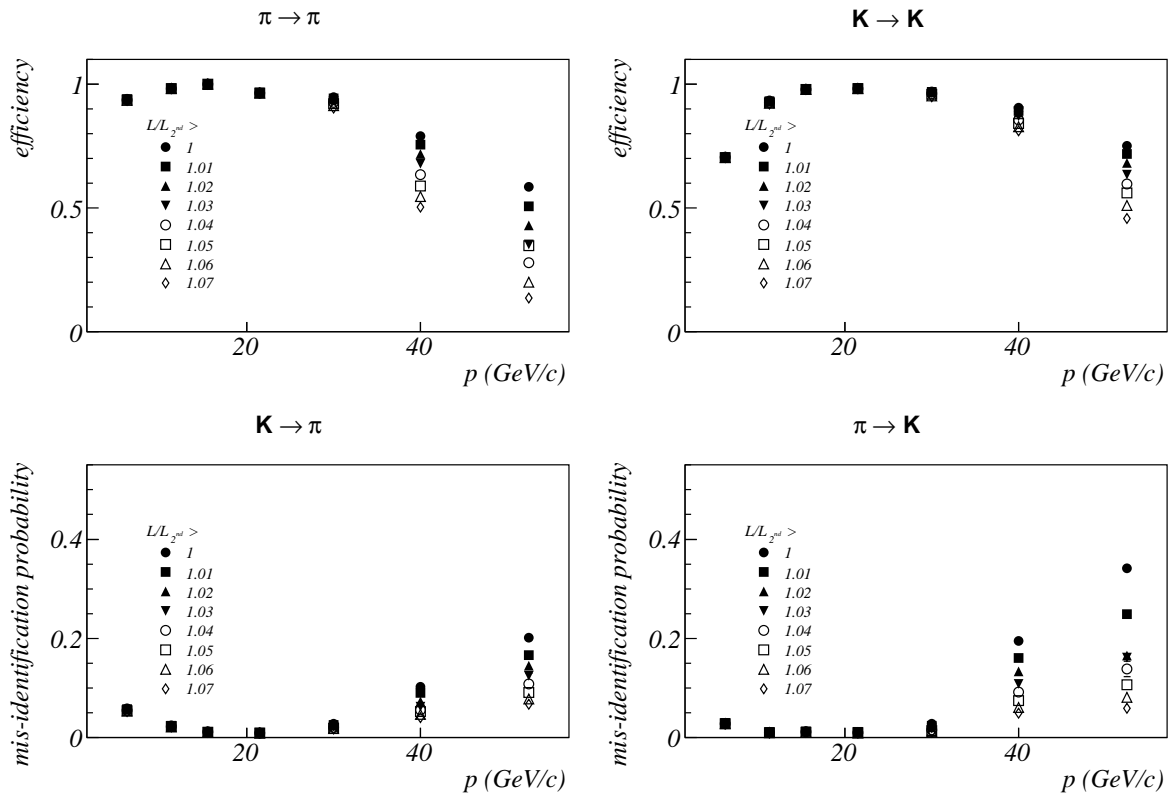


Figure 5.7: Top row: PID efficiency of π s (left) and K s (right), as a function of the particle momentum. Bottom row: misidentification probability of K s (left) and π s (right), as a function of the particle momentum. Different markers correspond to different cuts on the value of the maximum likelihood over the second one.

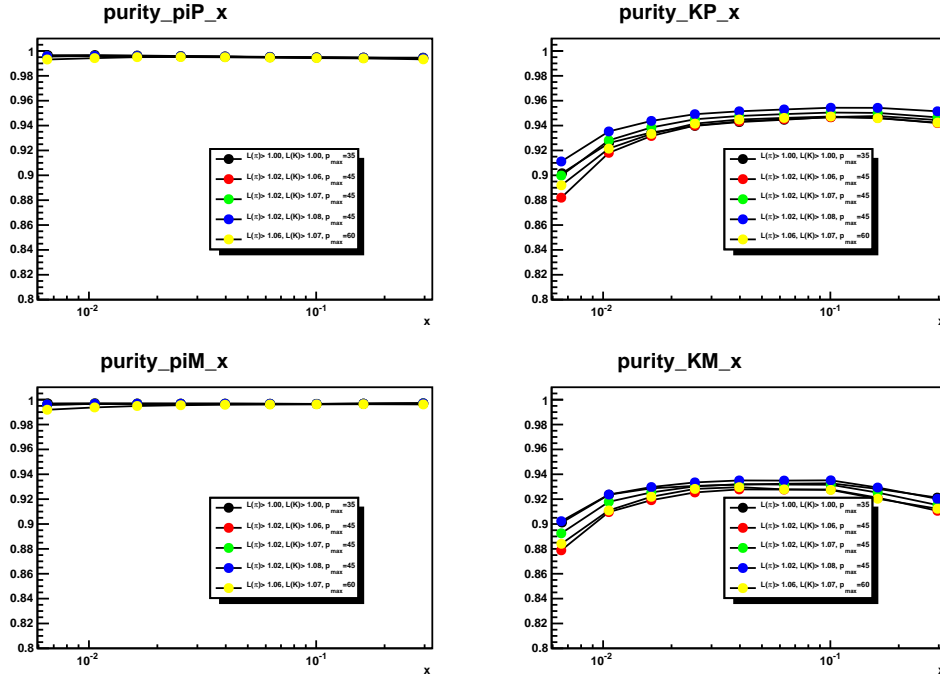


Figure 5.8: Purity of the sample as a function of x . The different colours correspond to different tuning of the cuts. Top row: positive π s and K s. Bottom row: negative π s and K s.

applied, and is not taken into account. A sample with $p_{max} = 35\text{GeV}/c$ and no cuts on the likelihood ratio and one with $p_{max} = 45\text{GeV}/c$ and several combinations of cuts are then compared. The values on the likelihood ratio cut are chosen in such a way that the $\pi \rightarrow K$ misidentification probability is below 10%, and then modified iteratively according to the test results.

The selection with $p_{max} = 35\text{GeV}/c$ shows a good purity and FoM1, but FoM2, i.e. the fraction of true kaons in the sample, is the lowest. On the contrary, the selection with $p_{max} = 45\text{GeV}/c$, $\mathcal{L}_\pi/\mathcal{L}_{2nd} > 1.02$ and $\mathcal{L}_K/\mathcal{L}_{2nd} > 1.06$ show a good FoM2, meaning that there is more statistics available. Moreover, it is possible to tune the likelihood cuts in such a way that the purity is the same as that of the sample with $p_{max} = 35\text{GeV}/c$, while keeping a higher FoM2. The values of the cuts are $\mathcal{L}_\pi/\mathcal{L}_{2nd} > 1.02$ and $\mathcal{L}_K/\mathcal{L}_{2nd} > 1.08$.

The same exercise has been repeated with a different definition of the momentum bins in the identification probabilities matrix (Tab. 5.1), to test the purity in a selection with maximum momentum $p_{max} = 50\text{GeV}/c$. No degradation of the measured purity or factor of merit was found, and thus the final tuning of the cuts is: $\mathcal{L}_\pi/\mathcal{L}_{2nd} > 1.02$ and $\mathcal{L}_K/\mathcal{L}_{2nd} > 1.08$, with $p_{max} = 50\text{GeV}/c$.

With the RICH it is also possible to identify electrons. From Fig. 2.17 it is clear that it is possible to separate electron from pions only at low values of momentum. The limit for electron identification is given by the ratio of the electron likelihood over the pion one. A fine tuning of this identification limit has been done monitoring the fraction of pions from the K^0 decay that are identified as electrons: it was found that it is possible to distinguish electrons from pions if $\mathcal{L}_e/\mathcal{L}_\pi > 1.8$. In the opposite case, the distinction is not possible and the electron hypothesis is not taken into account.

To summarize, the cuts for the hadron identification are as follows:

- if $\mathcal{L}(e) < 1.8 * \mathcal{L}(\pi)$ electron can be identified.

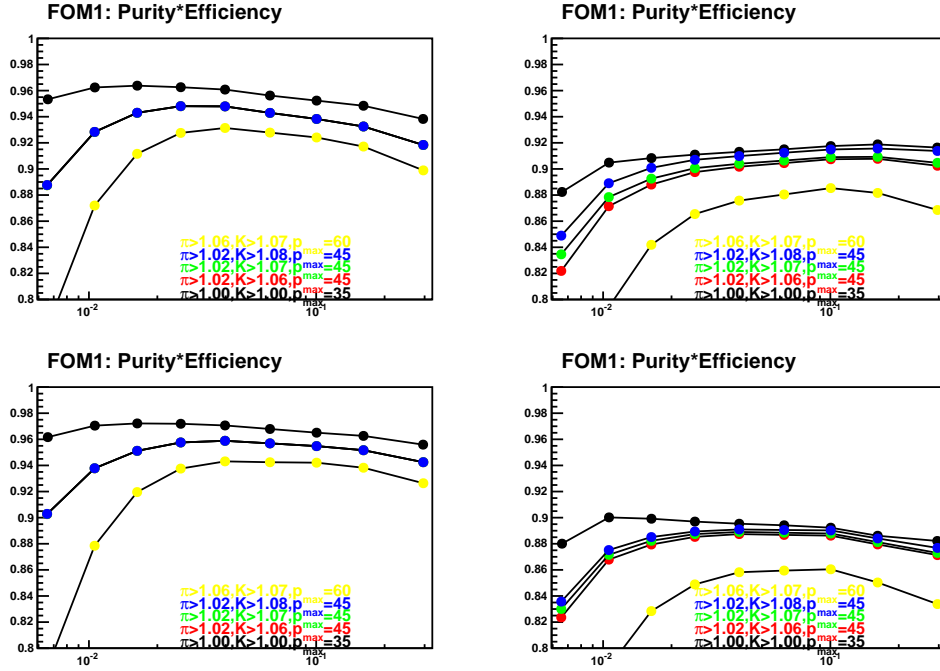


Figure 5.9: FoM 1=purity*efficiency of the sample as a function of x . The different colours correspond to different tuning of the cuts. Top row: positive π s and K s. Bottom row: negative π s and K s.

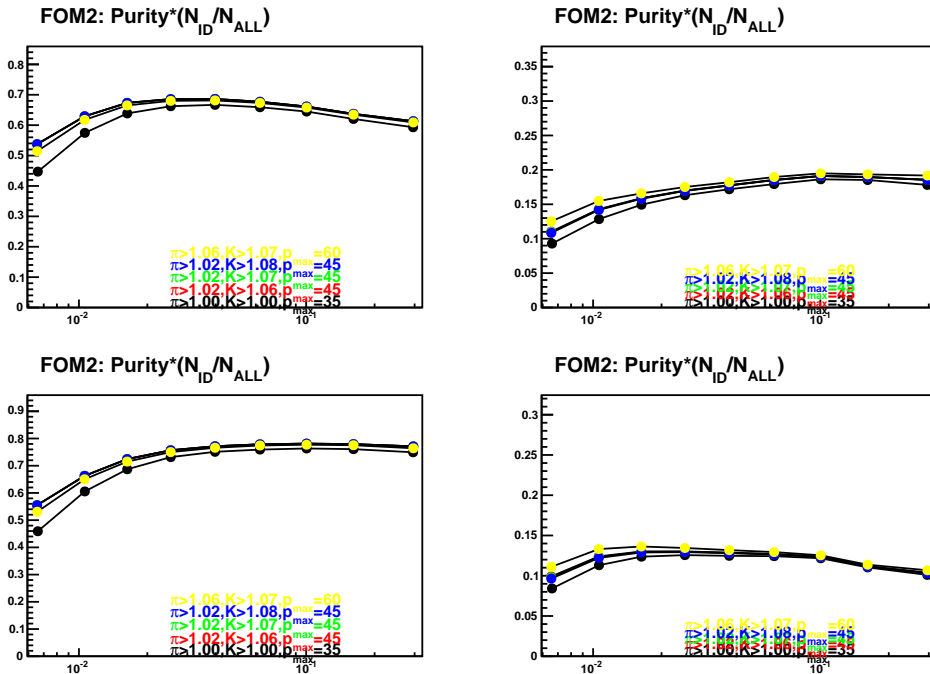


Figure 5.10: FoM 2= purity * $\frac{N_K^{ID}}{N_{all}}$ of the sample as a function of x . The different colours correspond to different tuning of the cuts. Top row: positive π s and K s. Bottom row: negative π s and K s.

| binning of the K sample | | |
|---------------------------|---|---|
| x | 6 | 0.003, 0.013, 0.020, 0.032, 0.050, 0.130, 1 |
| p_T | 6 | 0.10, 0.30, 0.50, 0.75, 0.90, 1.30, 100000 |
| z | 4 | 0.20, 0.30, 0.40, 0.65, 1 |
| W | 6 | 5, 6.7, 8.5, 9.5, 10.5, 12, 18 |

Table 5.2: Binning in x , p_T , z and W used to extract the Collins and Sivers asymmetries for identified kaons. This binning differs from that used to extract the asymmetries on the charged hadrons and pions sample (Tab. 3.8) due to the limited statistics.

- $p_{max} = 50 GeV/c$
- $\mathcal{L}_\pi / \mathcal{L}_{2nd} > 1.02$
- $\mathcal{L}_K / \mathcal{L}_{2nd} > 1.08$

5.3 Extraction of the Collins and Sivers asymmetries for identified particles

The procedure of the analysis to extract the asymmetries on identified π s and K s is the same used to extract the charged hadron asymmetries, described in Chap. 3 and 4.

Due to the limited statistics of the kaon sample (less than 15% of the full hadron sample), the binning to extract the kaon asymmetries (Tab. 5.2) has been reduced with respect to that used to extract the asymmetries for charged hadrons and identified pions (Tab. 4.1). The kinematic distributions of the charged hadrons, pions and kaons samples are shown in Figs. 5.11 and 5.12. Due to the high Cherenkov threshold of the kaons the shape of the distributions is different with respect to that of the charged pions. Moreover kaons are produced at higher p_T .

The final asymmetries for the identified pions and kaons samples, extracted with the unbinned maximum likelihood estimator, are shown in Figs. 5.13 to 5.16. The charged hadrons asymmetries (closed circles in the plots) are also shown for comparison.

The Collins asymmetry shows a strong signal in the valence region, both for pions and for kaons. In z and p_T the asymmetries of both kaons and pions show the same trend as the unidentified hadron asymmetries, with the only exception of the positive kaon asymmetry versus p_T where the kaons asymmetries show some trend to increase as p_T increases.

The Sivers asymmetry for positive hadrons shows a signal in the intermediate x region, both for kaons and for pions. In the valence region the strength of the pions asymmetry is less than that of the charged hadrons: this is in part due to the large kaon asymmetry and in part to fact that for W_{25} , where the measured asymmetry is big, a strong kinematic cut has been applied in the event selection due to the instabilities of the RICH detector. The Sivers asymmetry shows a clear signal at small values of W , both for positive pions and for positive kaons, while it is compatible with zero for negative kaons. In this region, that corresponds to the W range probed by the HERMES experiment, the strength of the signal is fully compatible with the last HERMES analysis for kaons, while it is smaller than but still compatible with their published charged pions asymmetry.

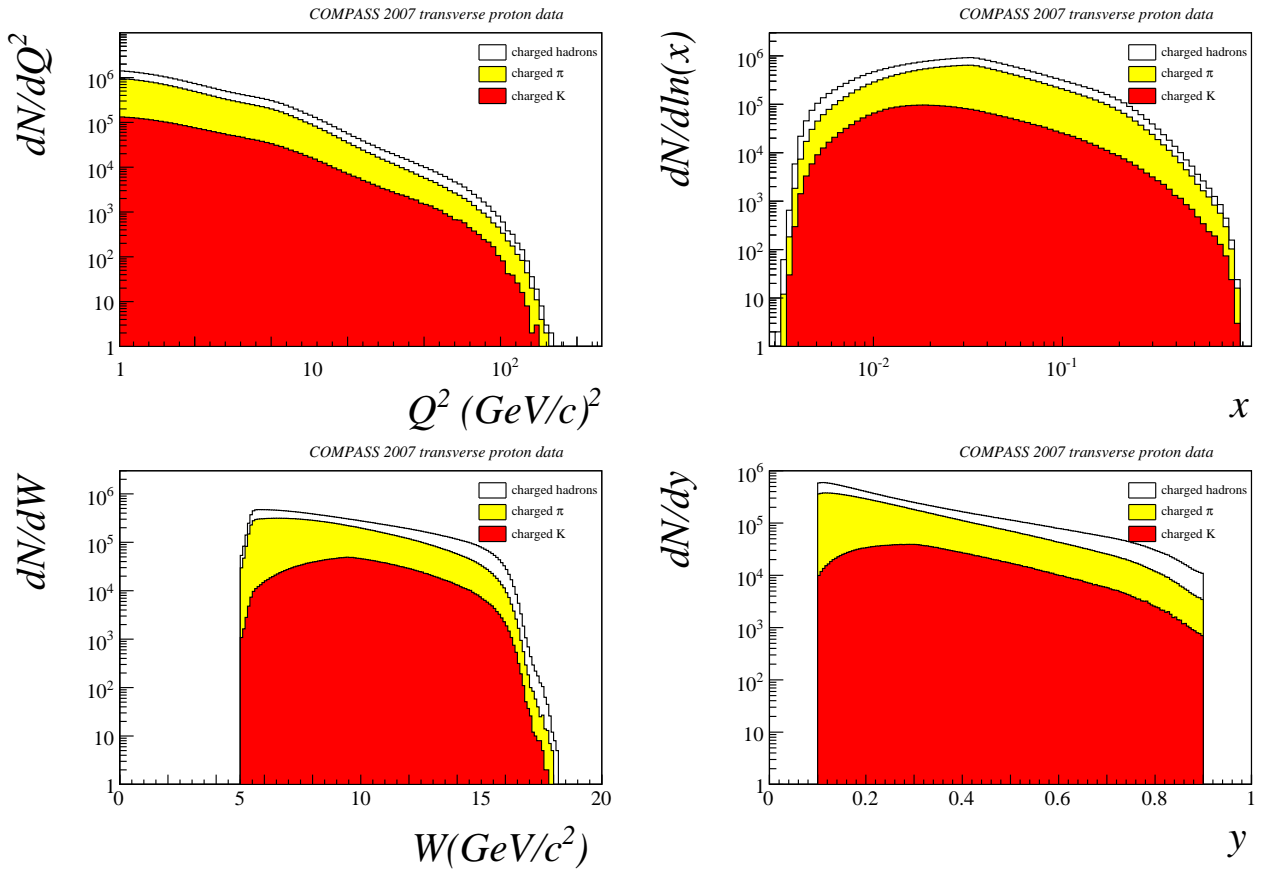


Figure 5.11: The event variables Q^2 , x , W and y distributions for charged hadrons (white), identified pions (yellow) or identified kaons (red). Full 2007 statistics. NB: one entry per hadron

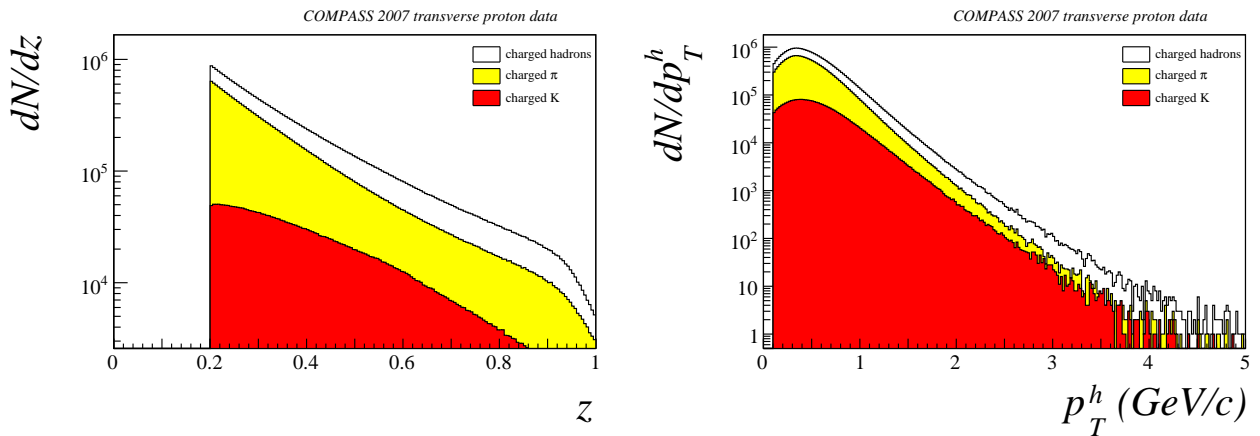


Figure 5.12: The hadron variables z and p_T distributions for charged hadrons (white), identified pions (yellow) and identified kaons (red). Full 2007 statistics.

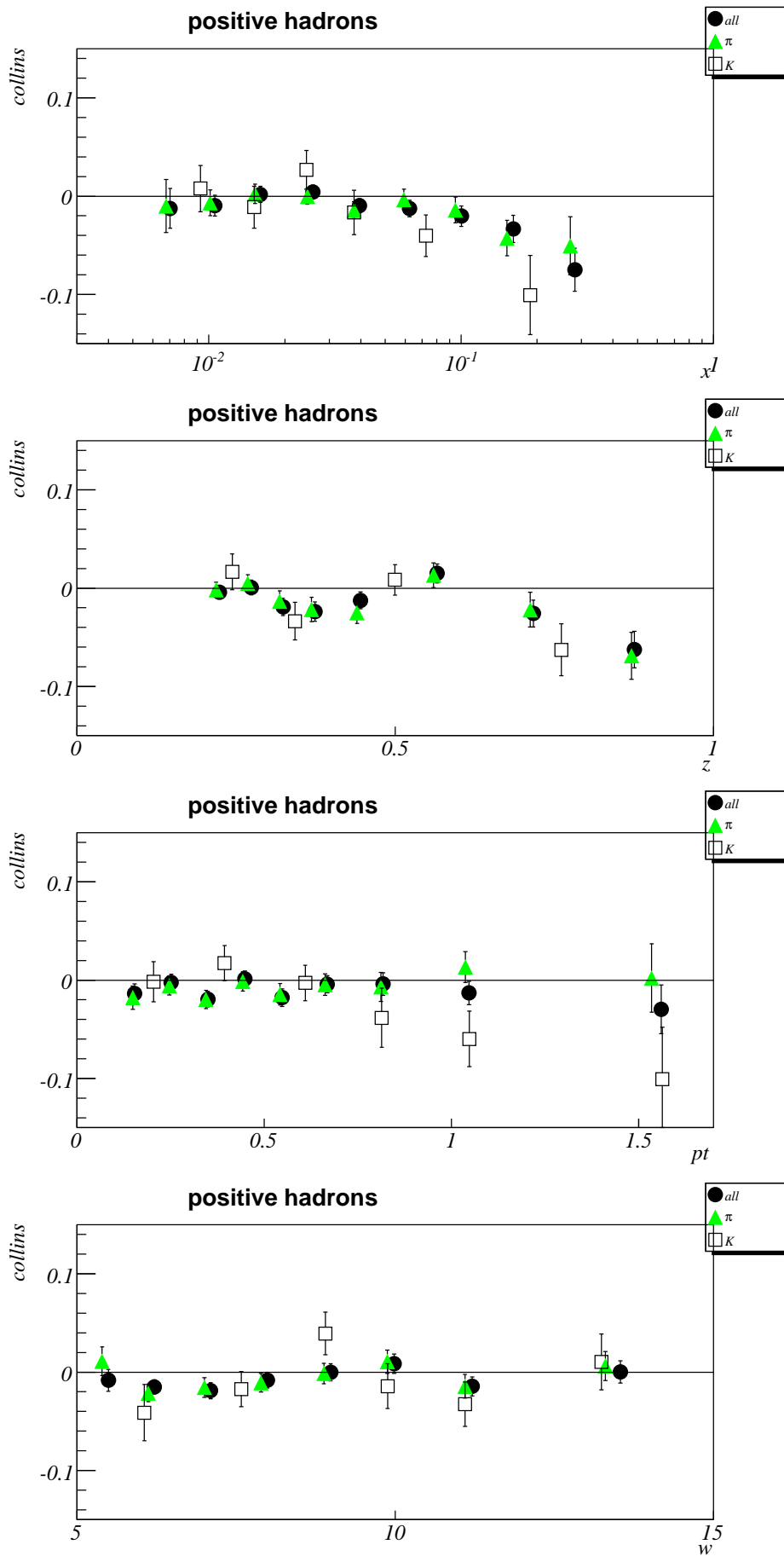


Figure 5.13: The Collins asymmetries for positive hadrons (full circles), pions (full triangles) and kaons (open squares) as a function of x, z, p_T and W .

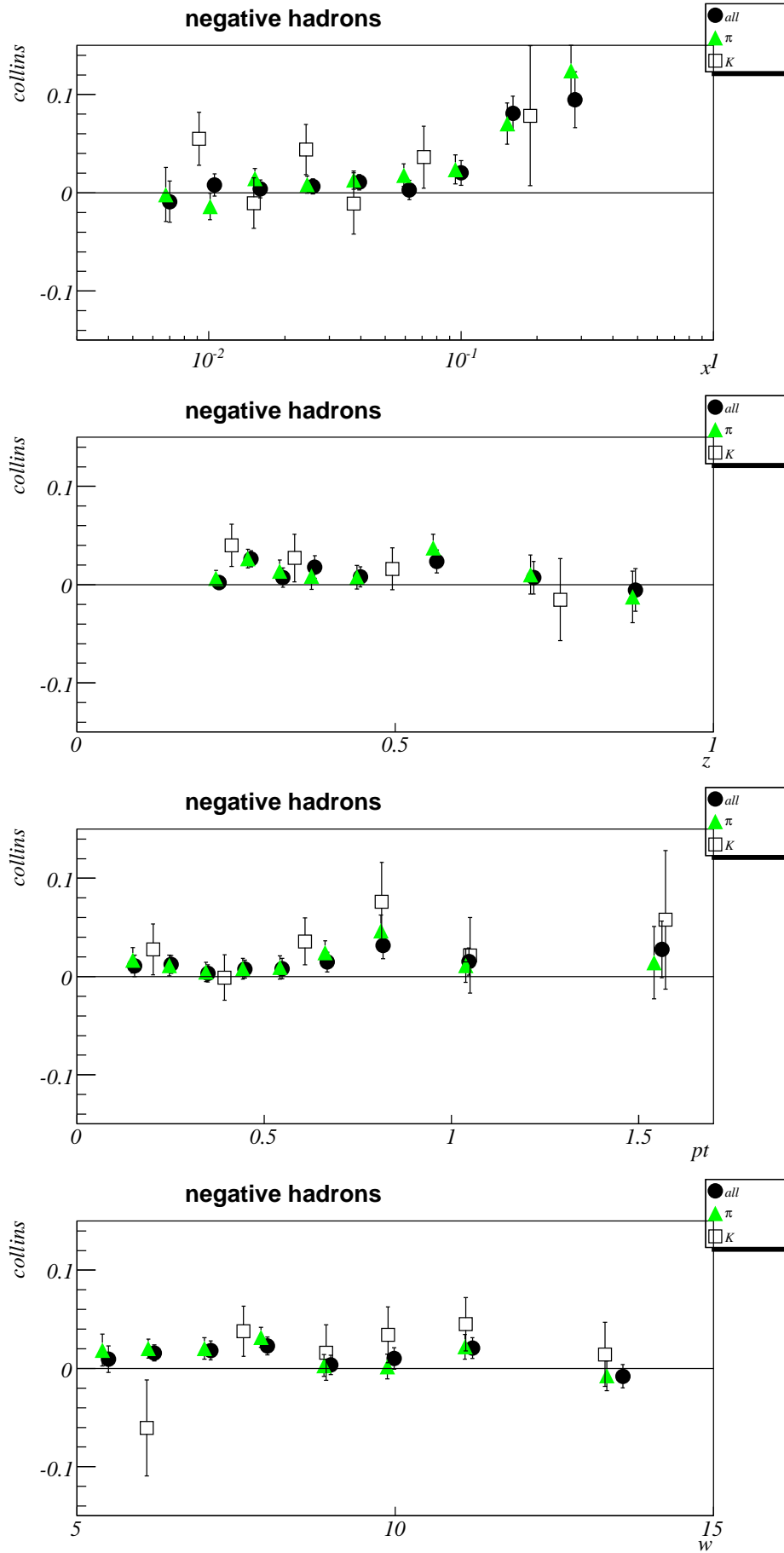


Figure 5.14: The Collins asymmetries for negative hadrons (full circles), pions (full triangles) and kaons (open squares) as a function of x, z, p_T and W .

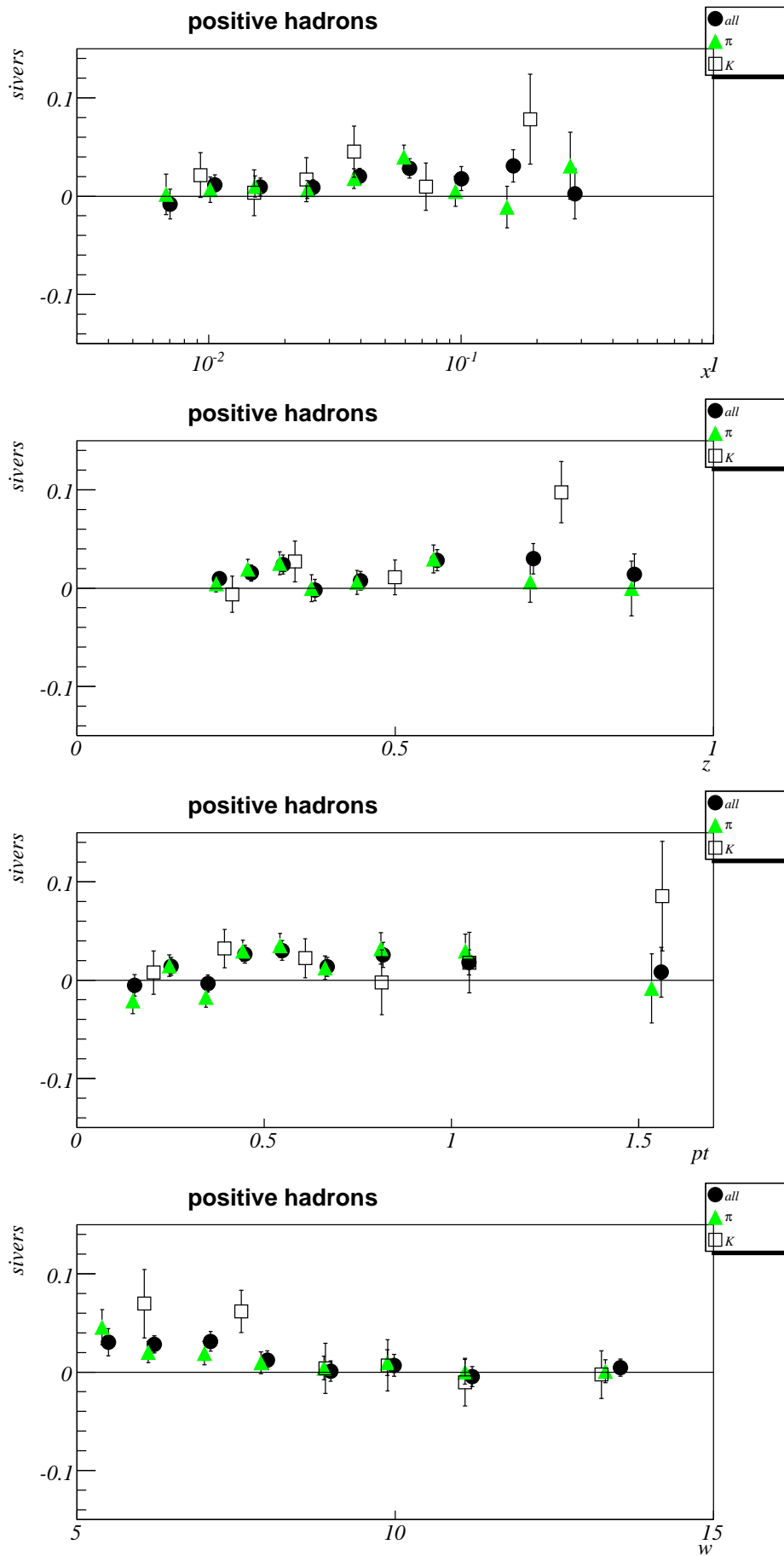


Figure 5.15: The Sivers asymmetries for positive hadrons (full circles), pions (full triangles) and kaons (open squares) as a function of x, z, p_T and W .

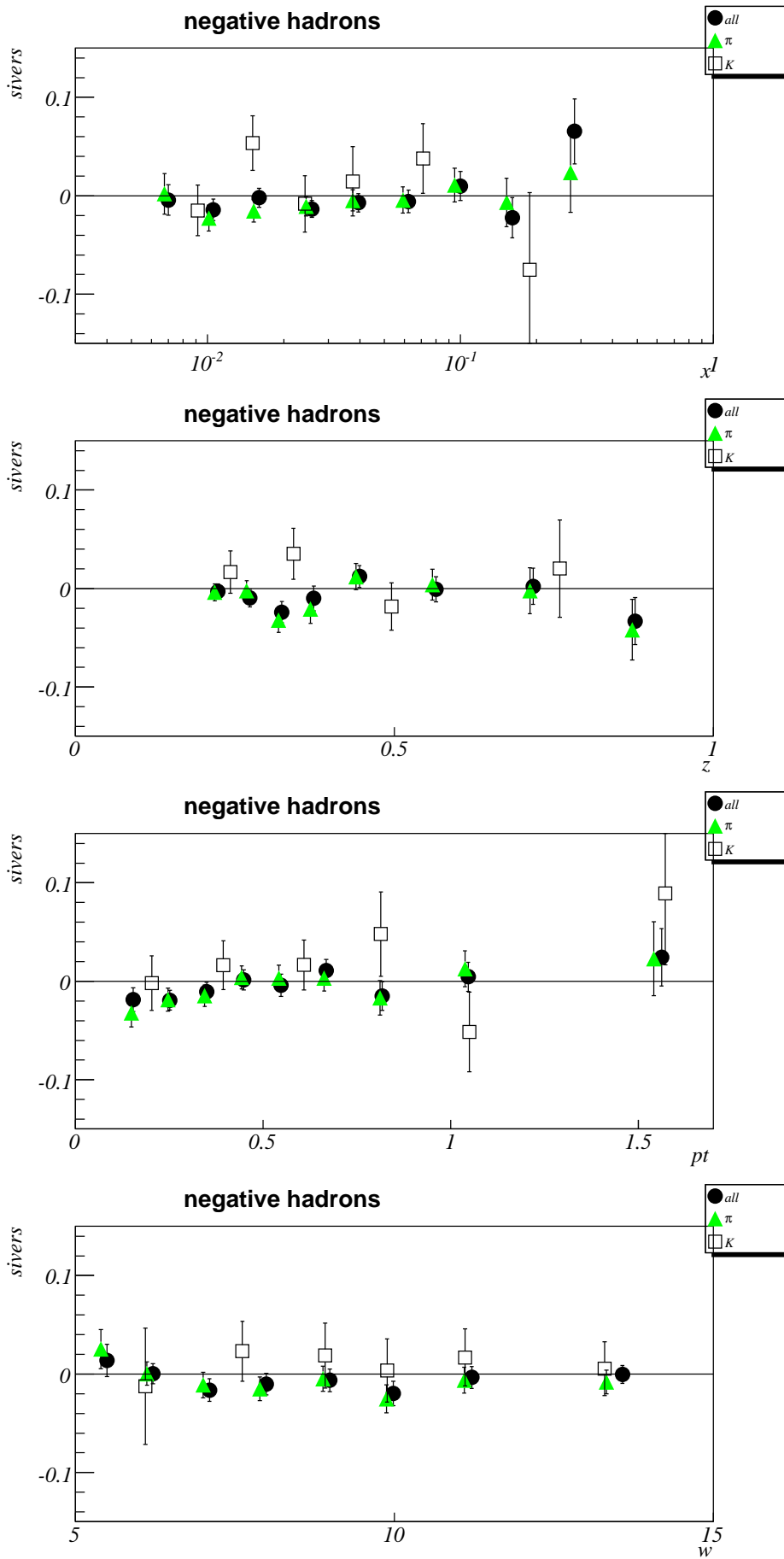


Figure 5.16: The Sivers asymmetries for negative hadrons (full circles), pions (full triangles) and kaons (open squares) as a function of x, z, p_T and W .

| Collins | | |
|--------------------|----------------------|----------------------|
| week | $\pi+$ | $K+$ |
| W25 | -0.0077 ± 0.0103 | -0.0127 ± 0.0238 |
| W28 | -0.0172 ± 0.0110 | 0.0056 ± 0.0265 |
| W30 | -0.0047 ± 0.0082 | 0.0001 ± 0.0200 |
| W39 | 0.0032 ± 0.0084 | -0.0377 ± 0.0205 |
| W41 | -0.0222 ± 0.0087 | -0.0134 ± 0.0208 |
| W42 | 0.0002 ± 0.0129 | 0.0069 ± 0.0312 |
| W25-28-30 | -0.0087 ± 0.0055 | -0.0025 ± 0.0133 |
| W39-41-42 | -0.0074 ± 0.0055 | -0.0198 ± 0.0132 |
| W25-28-30-39-41-42 | -0.0080 ± 0.0039 | -0.0112 ± 0.0094 |
| Collins | | |
| week | $\pi-$ | $K-$ |
| W25 | 0.0048 ± 0.0111 | -0.0101 ± 0.0306 |
| W28 | 0.0293 ± 0.0118 | 0.0692 ± 0.0347 |
| W30 | 0.0247 ± 0.0088 | 0.0275 ± 0.0262 |
| W39 | -0.0025 ± 0.0091 | 0.0219 ± 0.0272 |
| W41 | 0.0201 ± 0.0094 | 0.0245 ± 0.0274 |
| W42 | 0.0136 ± 0.0139 | 0.0310 ± 0.0410 |
| W25-28-30 | 0.0201 ± 0.0060 | 0.0259 ± 0.0173 |
| W39-41-42 | 0.0093 ± 0.0059 | 0.0246 ± 0.0175 |
| W25-28-30-39-41-42 | 0.0147 ± 0.0042 | 0.0252 ± 0.0123 |

Table 5.3: Mean value (over x) of the Collins asymmetries for positive and negative hadrons and identified π s and K s.

5.4 Determination of the systematic error

5.4.1 Compatibility among different periods

The mean values of the measured asymmetries in the different *periods* are shown in Tabs. 5.3 and 5.4. The Collins asymmetries measured in the first part of the data-taking are compatible with those measured in the second part of the data-taking, both for pions and for kaons (Fig. 5.17). The systematic difference found for the Sivers asymmetries between the first two and the second two *periods* (Sec. 4.2.4) is still visible on identified positive pions (Fig. 5.18), while the mean values of Sivers asymmetry for identified positive kaons are compatible within the large error bars. For the Sivers asymmetry for positive pions a scale error of 0.012 is taken. The size of this error is the semi-difference of the two mean values of the asymmetry in the two parts of the data-taking.

5.4.2 Other contributions

The systematic error is estimated summing in quadrature several contributions, introduced in Sec. 4.2. The main component of the error is the contribution due to the variation of the acceptance during the two coupled *periods*. The final value, that is averaged over the *periods*, is of the order of half of the statistical error; the numerical values are shown in Tab. 5.5 for the pion asymmetries and in Tab. 5.6 for the kaon asymmetries.

The second contribution comes from the compatibility of the results extracted with the different estimators, namely unbinned likelihood, 1D and 2D. The RMS of the distribution is 0.2

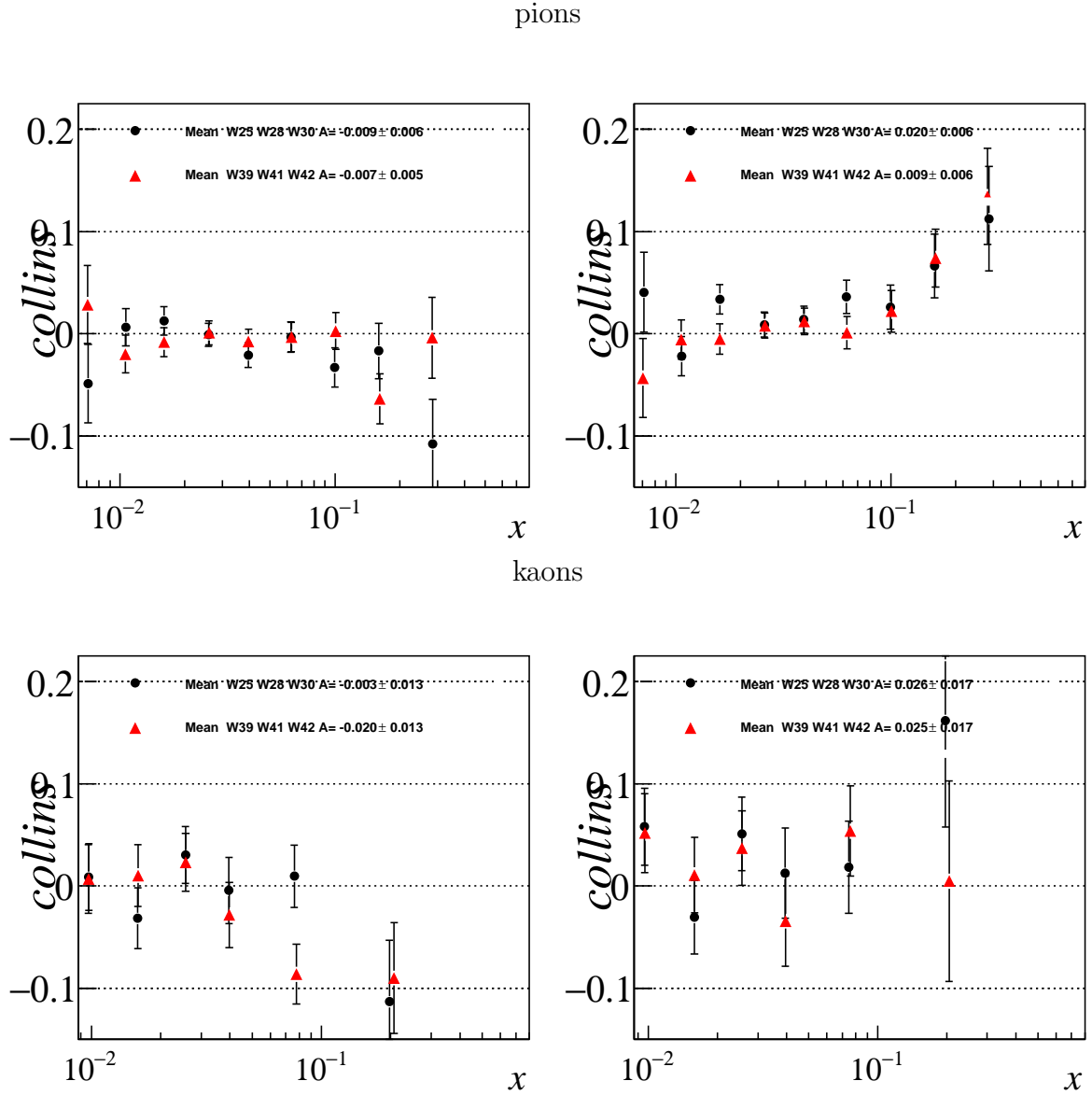


Figure 5.17: The Collins asymmetries for positive (left) and negative (right) identified pions and kaons as a function of x . Black squares are the first part of the run, the red triangles are the second part of the run.

| Sivers | | |
|--------------|----------------------|----------------------|
| week | $\pi+$ | $K+$ |
| W25 | 0.0186 ± 0.0094 | 0.0423 ± 0.0214 |
| W30 | 0.0265 ± 0.0075 | 0.0228 ± 0.0180 |
| W39 | -0.0016 ± 0.0077 | 0.0184 ± 0.0185 |
| W42 | 0.0057 ± 0.0118 | -0.0111 ± 0.0282 |
| W25-30 | 0.0235 ± 0.0059 | 0.0309 ± 0.0138 |
| W39-42 | 0.0006 ± 0.0064 | 0.0095 ± 0.0155 |
| W25-30-39-42 | 0.0131 ± 0.0043 | 0.0214 ± 0.0103 |

| Sivers | | |
|--------------|----------------------|----------------------|
| week | $\pi-$ | $K-$ |
| W25 | -0.0113 ± 0.0101 | 0.0101 ± 0.0269 |
| W30 | -0.0064 ± 0.0080 | 0.0096 ± 0.0230 |
| W39 | -0.0023 ± 0.0082 | 0.0279 ± 0.0238 |
| W42 | -0.0218 ± 0.0126 | -0.0191 ± 0.0362 |
| W25-30 | -0.0083 ± 0.0063 | 0.0098 ± 0.0175 |
| W39-42 | -0.0081 ± 0.0069 | 0.0137 ± 0.0199 |
| W25-30-39-42 | -0.0082 ± 0.0046 | 0.0115 ± 0.0131 |

Table 5.4: Mean value (over x) of the Sivers asymmetries for positive and negative hadrons and identified π s and K s.

| Collins | | | Sivers | | |
|---------|--------|--------|---------|--------|--------|
| week | $\pi+$ | $\pi-$ | week | $\pi+$ | $\pi-$ |
| W25 | 0.3 | 0.6 | W25 | 1.0 | 0.6 |
| W28 | 0.4 | 0.5 | W30 | 0.7 | 0.4 |
| W30 | 0.4 | 0.9 | W39 | 0.4 | 0.5 |
| W39 | 0.7 | 0.3 | W42 | 0.5 | 0.3 |
| W41 | 0.4 | 0.8 | Average | 0.6 | 0.5 |
| W42 | 0.4 | 0.9 | | | |
| Average | 0.4 | 0.7 | | | |

Table 5.5: Systematic error due to acceptance variation for identified π

| Collins | | | Sivers | | |
|---------|------|------|---------|------|------|
| week | $K+$ | $K-$ | week | $K+$ | $K-$ |
| W25 | 0.5 | 0.6 | W25 | 0.6 | 0.4 |
| W28 | 0.6 | 0.6 | W30 | 0.4 | 0.9 |
| W30 | 0.4 | 0.5 | W39 | 0.4 | 0.1 |
| W39 | 0.3 | 0.5 | W42 | 0.5 | 0.6 |
| W41 | 0.3 | 0.9 | Average | 0.5 | 0.5 |
| W42 | 0.3 | 0.7 | | | |
| Average | 0.4 | 0.6 | | | |

Table 5.6: Systematic error due to acceptance variation for identified K

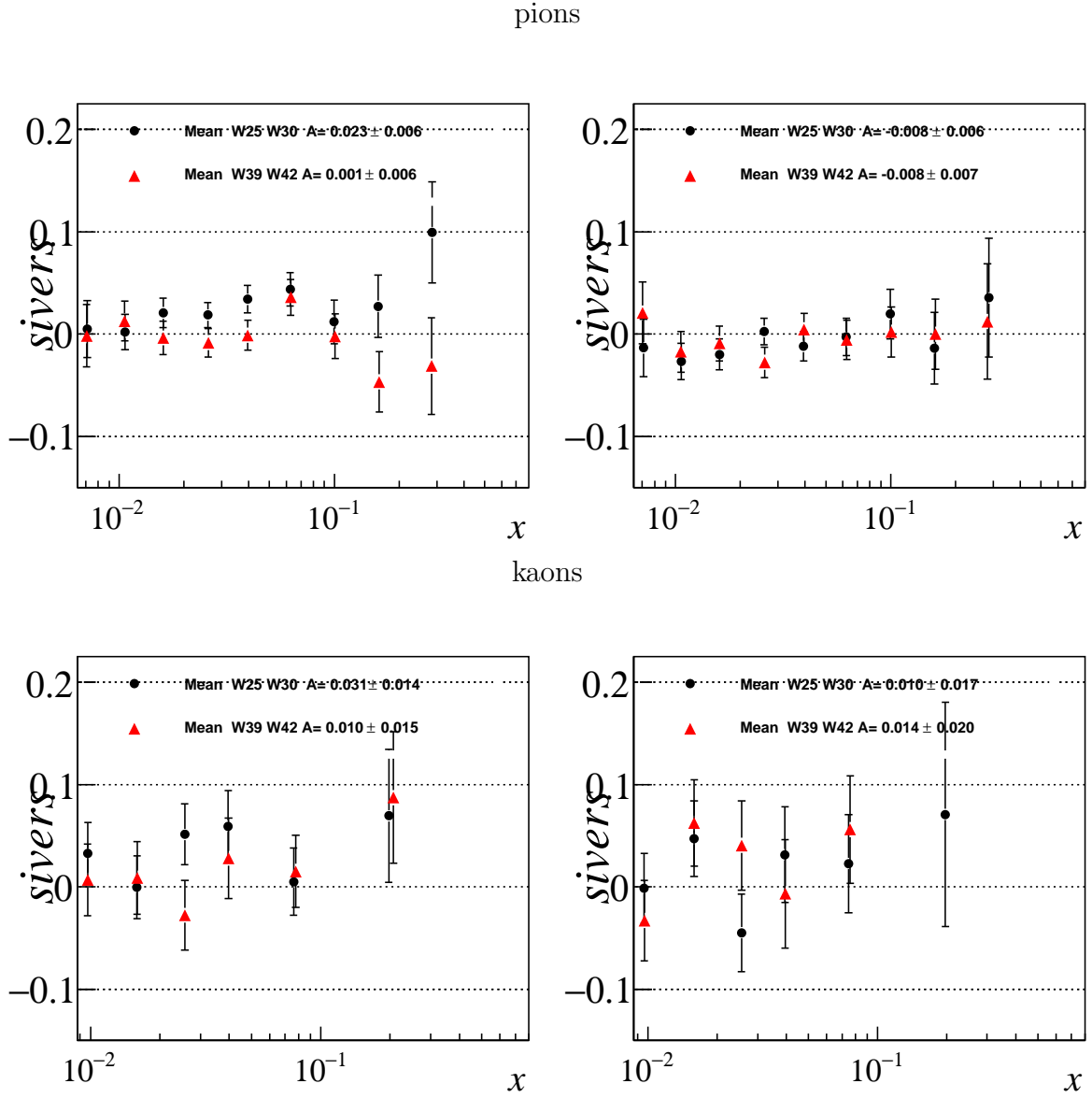


Figure 5.18: The Siverts asymmetries for positive (left) and negative (right) identified pions and kaons as a function of x . Black squares are the first part of the run, the red triangles are the second part of the run.

for the pull 1D-UL, both for pions and for kaons. The RMS of the pull distribution between 2D and UL is larger, of the order of 0.45 for pions and 0.6 for kaons. The 2D algorithm is expected to be less efficient and can show biases for the extraction of the kaon asymmetry: due to the small statistics there are bins in the ϕ_h, ϕ_s space that have less than 10 events and are not used for the fit. In agreement with the analysis of the charged hadrons asymmetries, a contributions of 0.2σ will be added to the systematic error.

Finally, adding all the contributions, the systematic error for the Collins asymmetry (Tab. 5.7) is $0.47 \sigma_{stat}$ for the positive pions and kaons, as well as for negative kaons. The systematic error for negative pions is $0.73 \sigma_{stat}$. The systematic error for the Sivers asymmetry (Tab. 5.8) is $0.54 \sigma_{stat}$ for positive and negative kaons and for negative pions. For positive pions the error is $0.63 \sigma_{stat}$, to which an absolute scale uncertainty of 0.012 has to be added.

| Collins | $\pi+$ | $\pi-$ | K+ | K- |
|---|---------------------|---------------------|---------------------|---------------------|
| Point to point systematic error | | | | |
| estimator for extraction of asymmetries | $0.2\sigma_{stat}$ | $0.2\sigma_{stat}$ | $0.2\sigma_{stat}$ | $0.2\sigma_{stat}$ |
| acceptance variations | $0.4\sigma_{stat}$ | $0.7\sigma_{stat}$ | $0.4\sigma_{stat}$ | $0.6\sigma_{stat}$ |
| total | $0.46\sigma_{stat}$ | $0.73\sigma_{stat}$ | $0.46\sigma_{stat}$ | $0.63\sigma_{stat}$ |
| Scale factors | | | | |
| target polarization | $0.05A$ | $0.05A$ | $0.05A$ | $0.05A$ |

Table 5.7: Contributions to the systematic error for Collins asymmetries, charged π and K. A is the measured value of the asymmetry.

| Sivers | $\pi+$ | $\pi-$ | K+ | K- |
|--|---------------------|---------------------|---------------------|---------------------|
| Point to point systematic error | | | | |
| estimator for extraction of asymmetries | $0.2\sigma_{stat}$ | $0.2\sigma_{stat}$ | $0.2\sigma_{stat}$ | $0.2\sigma_{stat}$ |
| acceptance variations | $0.6\sigma_{stat}$ | $0.5\sigma_{stat}$ | $0.5\sigma_{stat}$ | $0.5\sigma_{stat}$ |
| total | $0.63\sigma_{stat}$ | $0.54\sigma_{stat}$ | $0.54\sigma_{stat}$ | $0.54\sigma_{stat}$ |
| Scale factors | | | | |
| period compatibility (unit of final asymmetry) | 0.012 | 0 | 0 | 0 |
| target polarization | $0.05A$ | $0.05A$ | $0.05A$ | $0.05A$ |

Table 5.8: Contributions to the systematic error for Sivers asymmetries, charged π and K. A is the measured value of the asymmetry.

5.4.3 Contamination of the kaon sample

The kaon sample selected for this analysis is pure at the 90% level. This means that the remaining 10% of the events are pions misidentified as kaons. Thus, the asymmetry measured on the data (A_K, A_π) is not the "true" asymmetry on K and π (a_K and a_π), but a combination

of the two [9]. The exact calculation can be made using the definition of the purity P given in Sec. 5.2:

$$\begin{aligned} A_K &= \frac{a_K * N_K^T + a_\pi * N_\pi^T}{N^{ID}} &= a_K * P_K + a_\pi * (1 - P_K) \\ A_\pi &= &= a_K * (1 - P_\pi) + a_\pi * P_\pi \end{aligned}$$

Inverting these relation, it is possible to extract the "true" kaon and pion asymmetries. The kaon asymmetry is thus:

$$a_K = \frac{1}{P_K * P_\pi - [(1 - P_K) * (1 - P_\pi)]} * [P_\pi A_K - (1 - P_K) A_\pi].$$

From the formula it is clear that a large correction is to be applied to the measured asymmetry if the difference between the measured asymmetries for K and π is large: the absolute size of the correction is $A_K - a_k = 0.1(A_K - A_\pi)$. Making the hypothesis that $A_\pi = 0$, with the condition than $P_K \sim 0.9$ and $P_\pi \sim 1$, the maximum relative correction to the measured kaon asymmetry is of the 10% level, that has to be compared with a statistical error $\gtrsim 50\%$ of the kaon asymmetry size, thus negligible in the current analysis.

5.5 Conclusions

The Collins and Sivers asymmetries, for positive and negative pions, confirms the results extracted on the charge hadrons samples.

The Collins asymmetry (Fig. 5.19) is negative for positive kaons and it is positive for negative kaons and its size is larger than that of charged hadrons. The result is in good agreement with that of the HERMES experiment. The signal is strong also for the kaon sample, as a function of x . For positive kaons the asymmetry shows a trend as a function of p_T .

The Sivers asymmetry for pions is smaller than that measured for the charged hadrons sample. This result depends partly on the sizeable asymmetry measured on the kaon sample and partly is due to the fact that some of the events of *period* $W25$ were not used in this analysis due to the RICH detector instabilities. As discussed in Sec. 4.1.2, the asymmetry measured in $W25$ and $W30$ is large, while that measured in $W39$ and $W42$ is compatible with zero, and the final value is the average of the two. The rejection of part of the data of $W25$ only changes the relative weight of the different weeks. It is on the other side not possible to apply the same cut applied to $W25$ also to the other *periods*, since it would reject most of the statistics in the valence region.

The Sivers asymmetry for kaons shows a signal for positive kaons in the intermediate x region. This measurement confirms that, as measured by the HERMES experiment, the Sivers asymmetry for kaons is larger than for pions. Moreover, the asymmetry as a function of W shows clearly that the Sivers asymmetry is different from zero in the small W region, where the kinematic of the two experiments overlaps. The size of the measured asymmetries are fully compatible.

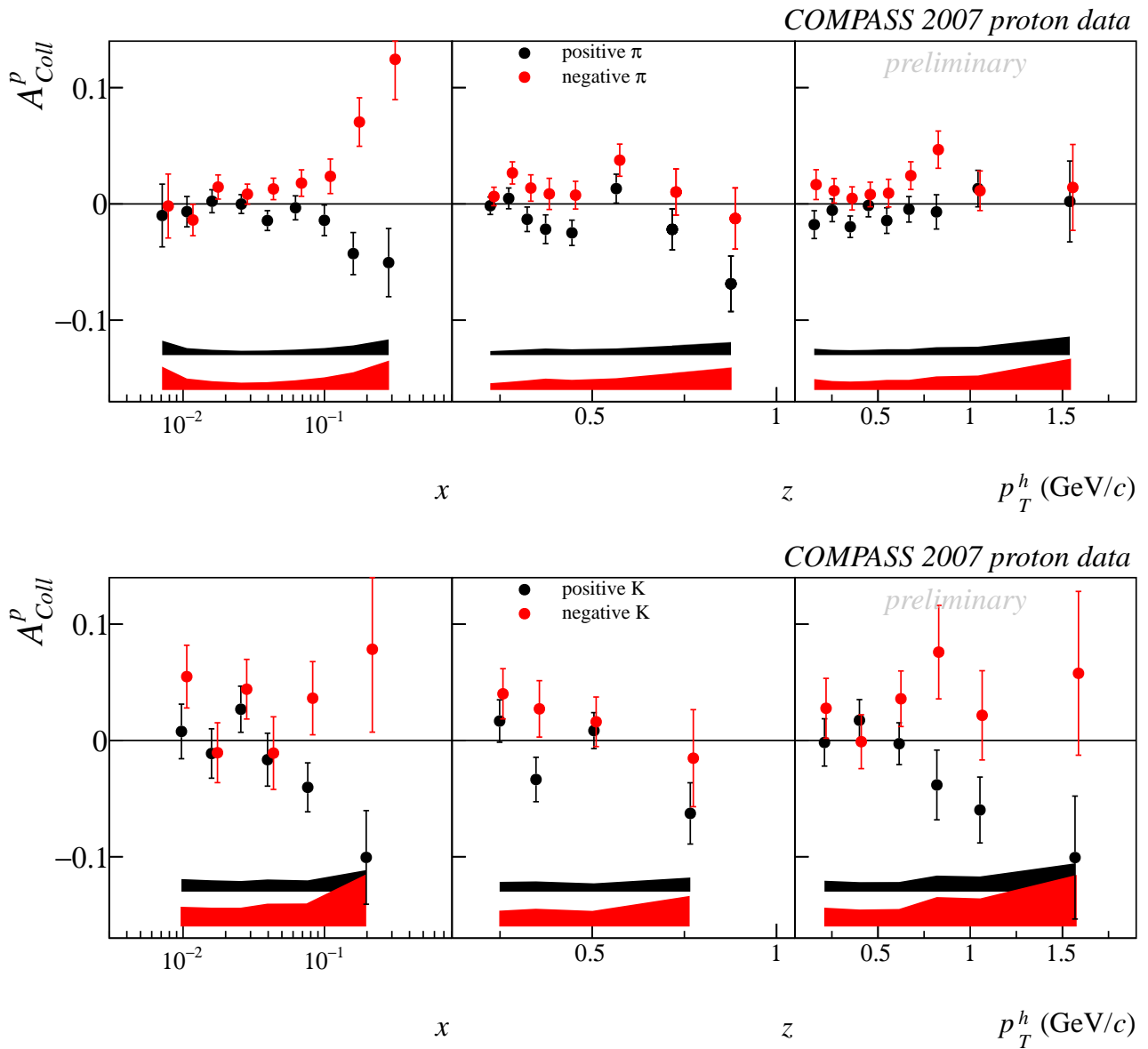


Figure 5.19: The Collins asymmetry for positive (black) and negative (red) pions (top) and kaons (bottom) as a function of x , z , p_T . The bands in the plots represent the systematic error for positive (black, upper band) and negative (red, lower band) hadrons. Note that the systematic scale errors are not included.

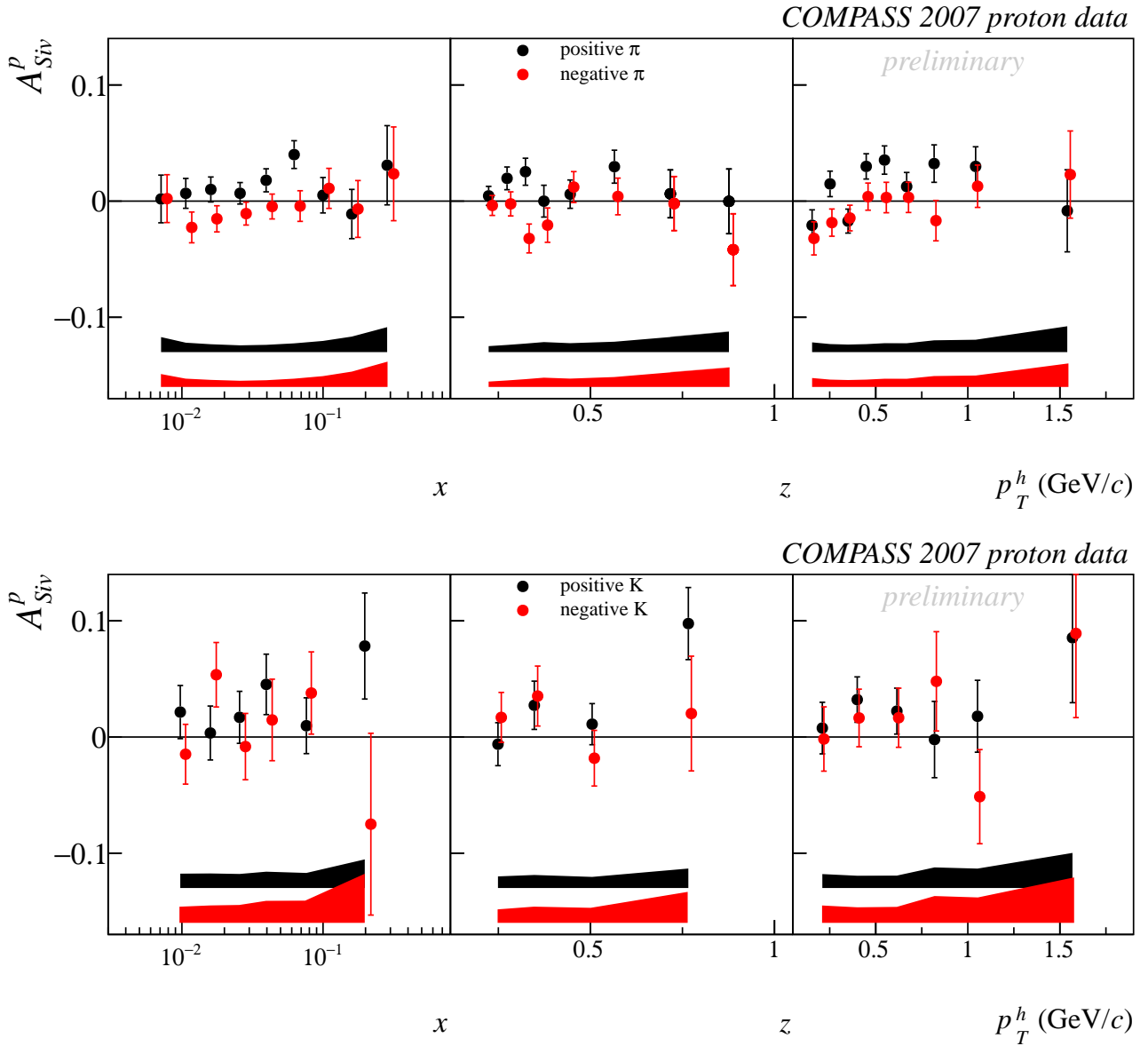


Figure 5.20: The Sivers asymmetry for positive (black) and negative (red) pions (top) and kaons (bottom) as a function of x , z , p_T . The bands in the plots represent the systematic error for positive (black, upper band) and negative (red, lower band) hadrons. Note that the systematic scale errors are not included.

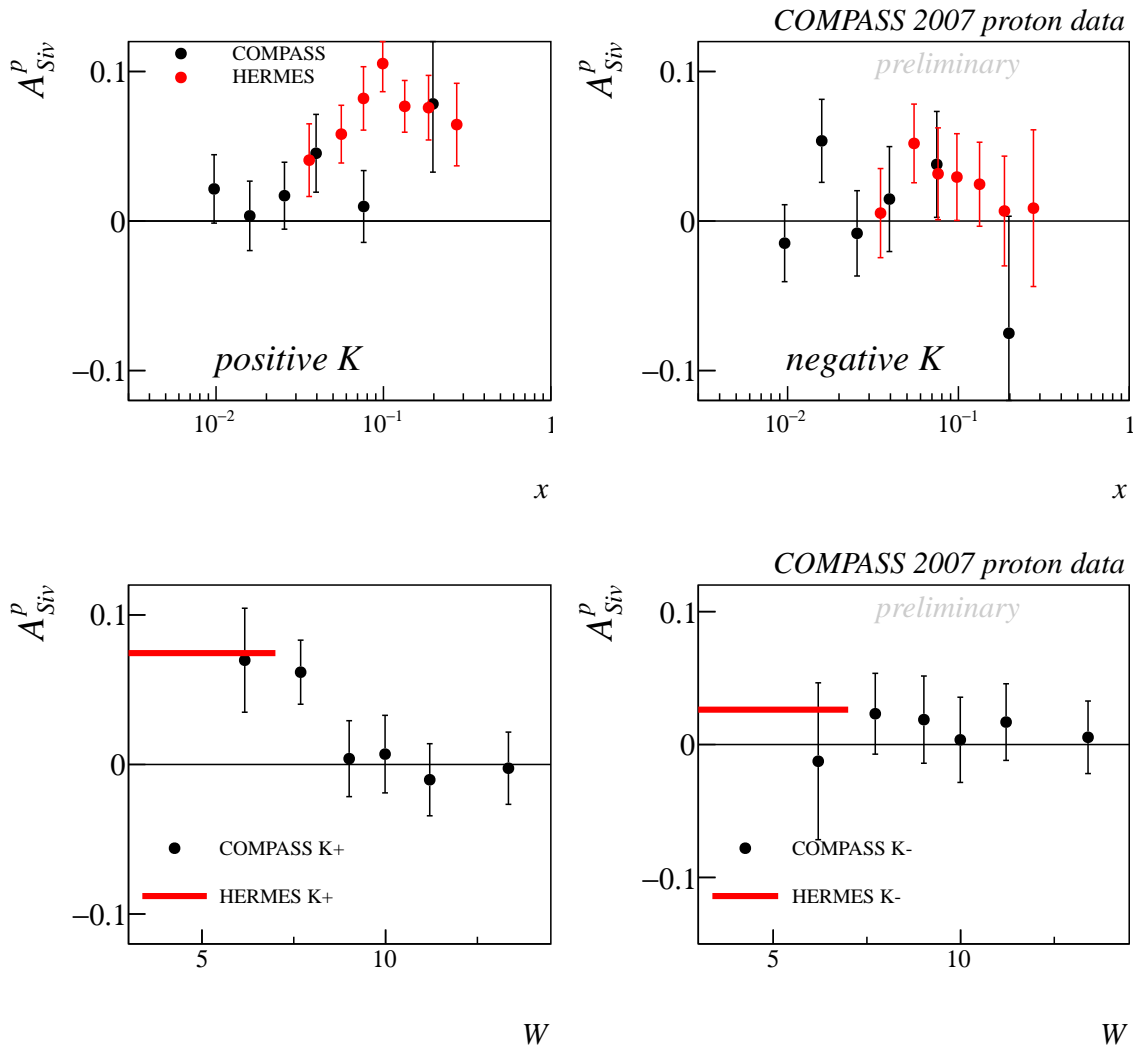


Figure 5.21: The Sivers asymmetry for positive (left) and negative (right) kaons as a function of x and W . The red points are the HERMES results, the red line is the average Sivers asymmetry as measured by HERMES; the length of the line corresponds to the approximate W range of the experiment.

Chapter 6

The extraction of the Sivers and transversity PDF

The extraction of the Sivers asymmetry for a charged pion sample on the COMPASS proton target has been described in Chap. 5 of this Thesis. The charged pions Sivers asymmetries had also been extracted on the COMPASS deuteron target [9], in the same kinematic range and with the same definition of the bins used. Combining the information of the two targets, it is possible to extract the flavour separated Sivers PDF. This analysis has already been done, using the HERMES proton data and the COMPASS deuteron data in a unique global fit [35, 51]. In this Section the flavour separated Sivers PDF will be extracted using the COMPASS data only, in the x bins of the measured asymmetry. The advantage of this approach is two-folded: on one side no assumptions are made on the shape of the Sivers PDF and on the other side the data do not need a Q^2 rescaling.

The same approach is then used to extract the transversity PDF. In this case the COMPASS Collins asymmetries (Chap. 5 and [9]) are not sufficient to extract the transversity PDF from the data, since the Collins FF is not known. In the analysis a parametrisation of the Collins FF extracted from the BELLE data only [51] will be used.

In the following, we will assume that the sea-quark contribution is negligible, and only the valence quarks play a role. We will also assume that the the fragmentation function $D_{u \rightarrow \pi^+}$ describing the fragmentation of a u quark into a π^+ is the same as $D_{d \rightarrow \pi^-}$ and their common value is called D_{fav} . Analogously, for the unfavoured FF: $D_{d \rightarrow \pi^+} = D_{u \rightarrow \pi^-} \equiv D_{unf}$. The Sivers asymmetries are then:

$$\begin{aligned} A_p^{\pi^+} &= -\frac{4f_{uT}^\perp \otimes D_{fav} + f_{dT}^\perp \otimes D_{unf}}{4u \otimes D_{fav} + d \otimes D_{unf}} \\ A_p^{\pi^-} &= -\frac{4f_{uT}^\perp \otimes D_{unf} + f_{dT}^\perp \otimes D_{fav}}{4u \otimes D_{unf} + d \otimes D_{fav}} \\ A_d^{\pi^+} &= -\frac{(f_{uT}^\perp + f_{dT}^\perp) \otimes (4D_{fav} + D_{unf})}{(u + d) \otimes (4D_{fav} + D_{unf})} \\ A_d^{\pi^-} &= -\frac{(f_{uT}^\perp + f_{dT}^\perp) \otimes (D_{fav} + 4D_{unf})}{(u + d) \otimes (D_{fav} + 4D_{unf})} \end{aligned}$$

where f_{uT}^\perp and f_{dT}^\perp are the Sivers PDF for the u and the d quarks and u and d are the unpolarized

PDFs and the Collins asymmetries are:

$$\begin{aligned}
A_p^{\pi^+} &= -\frac{4h_{uT} \otimes H_{fav} + h_{dT} \otimes H_{unf}}{4u \otimes D_{fav} + d \otimes D_{unf}} \\
A_p^{\pi^-} &= -\frac{4h_{uT} \otimes H_{unf} + h_{dT} \otimes H_{fav}}{4u \otimes D_{unf} + d \otimes D_{fav}} \\
A_d^{\pi^+} &= -\frac{(h_{uT} + h_{dT}) \otimes (4H_{fav} + H_{unf})}{(u + d) \otimes (4D_{fav} + D_{unf})} \\
A_d^{\pi^-} &= -\frac{(h_{uT} + h_{dT}) \otimes (H_{fav} + 4H_{unf})}{(u + d) \otimes (D_{fav} + 4D_{unf})}
\end{aligned}$$

where h_{uT} and h_{dT} are the transversity PDF for the u and the d quarks and H_{fav} and H_{unf} are the Collins FF. For the definition of the convolution we refer to Tab. 1.2.

6.1 The fit of the Sivers asymmetries

As a first step in the analysis, we assume that the transverse momentum of the hadron in the gamma-nucleon system is entirely given by the transverse momentum dependence in the Sivers PDF, as in [52], where the authors say that the transverse momentum contributed by the other factors will give some smearing effects which may be viewed as "sub-dominant". The general case will be treated in Sec. 6.2. In this approximation, in which the FF have no transverse momentum dependence, the convolutions in the formulae of the asymmetries are simple products for the unpolarised case while, for the numerator, we have that:

$$\int d^2 p_T \frac{|p_T|}{M} f_T^\perp(x, p_T^2) D(z) = f_T^{\perp(1/2)}(x) D(z)$$

where we have introduced the half-moment of the Sivers PDF. The measured asymmetries are parametrized as a function two unknowns (the Sivers u and d PDFs half-moments) and of the unpolarised PDF and FF, that are known. According to the definitions given in Chap. 3, the experimentally measured asymmetry, in each x bin, is integrated over the z and P_T^h range. Since the COMPASS acceptance is flat as a function of z and P_T^h [53]:

$$\begin{aligned}
A_{p,exp}^{\pi^+}(x) &= -\frac{\int dP_T^h \int dz (4f_{uT}^{\perp(1/2)} D_{fav} + f_{dT}^{\perp(1/2)} D_{unf})}{\int dP_T^h \int dz (4u D_{fav} + d D_{unf})} = \\
&\frac{4f_{uT}^{\perp(1/2)}(x) (\int dz D_{fav}(z)) + f_{dT}^{\perp(1/2)}(x) (\int dz D_{unf}(z))}{4u(x) (\int dz D_{fav}(z)) + d(x) (\int dz D_{unf}(z))}
\end{aligned} \tag{6.1}$$

Defining the integral of the FF over the COMPASS z range (from 0.2 to 1) as \tilde{D} :

$$\begin{aligned}
A_{p,exp}^{\pi^+}(x) &= -\frac{4f_{uT}^{\perp(1/2)} \tilde{D}_{fav} + f_{dT}^{\perp(1/2)} \tilde{D}_{unf}}{4u \tilde{D}_{fav} + d \tilde{D}_{unf}} \\
A_{p,exp}^{\pi^-}(x) &= -\frac{4f_{uT}^{\perp(1/2)} \tilde{D}_{unf} + f_{dT}^{\perp(1/2)} \tilde{D}_{fav}}{4u \tilde{D}_{unf} + d \tilde{D}_{fav}} \\
A_{d,exp}^{\pi^+}(x) &= -\frac{(f_{uT}^{\perp(1/2)} + f_{dT}^{\perp(1/2)}) (4\tilde{D}_{fav} + \tilde{D}_{unf})}{(u + d) (4\tilde{D}_{fav} + \tilde{D}_{unf})} \\
A_{d,exp}^{\pi^-}(x) &= -\frac{(f_{uT}^{\perp(1/2)} + f_{dT}^{\perp(1/2)}) (\tilde{D}_{fav} + 4\tilde{D}_{unf})}{(u + d) (\tilde{D}_{fav} + 4\tilde{D}_{unf})}
\end{aligned} \tag{6.2}$$

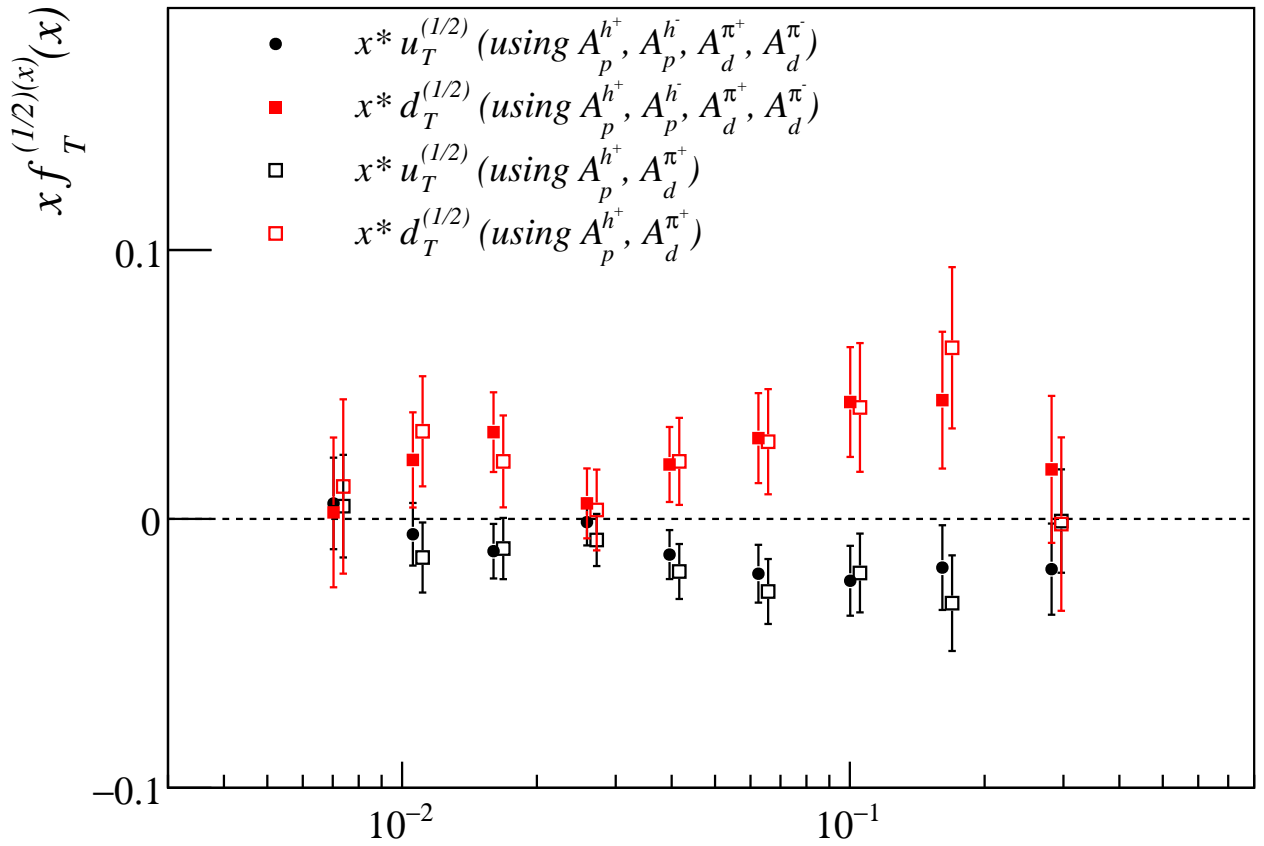


Figure 6.1: The Sivers PDFs $f_{uT}^{\perp(1/2)}$ (dots) and $f_{dT}^{\perp(1/2)}$ (squares), multiplied by x , extracted from the data. The open markers are obtained from the solution of the equation system $A_{p,exp}^{\pi^+}(x), A_{d,exp}^{\pi^+}(x)$, the closed markers are extracted from the fit of the four measured asymmetries.

The experimental asymmetries are associated to a statistical and a systematic error. The systematic error on the measured asymmetries is $0.46\sigma_{stat}$ for $A_p^{\pi^+}$ and $0.73\sigma_{stat}$ for $A_p^{\pi^-}$ (Sec. 5.4) and smaller than the statistical one for $A_d^{\pi^+}$ and $A_d^{\pi^-}$. In this analysis the two contributions are summed in quadrature.

In each x bin, the four asymmetries are measured at the same Q^2 average value: it is then possible to solve Eq. 6.2 as a function of $f_{uT}^{\perp(1/2)}(x)$ and $f_{dT}^{\perp(1/2)}(x)$ in each bin, without defining a parametrisation of the Sivers PDFs. The Sivers PDFs are extracted using the Kretzer FF [54] and the GRV98[55] unpolarised PDFs, with two different methods: using only $A_{p,exp}^{\pi^+}(x)$ and $A_{d,exp}^{\pi^+}(x)$ and analytically solving the system of equations, or using all the information in one fit to determine the best solution. In Fig. 6.1 the comparison between $f_{uT}^{\perp(1/2)}$ and $f_{dT}^{\perp(1/2)}$ extracted with the two methods is shown; as it is expected, the error is smaller when the four asymmetries are used, and the results obtained are well compatible. To test the quality of the fit, the expected values of the Sivers asymmetries can be computed using the extracted $f_{uT}^{\perp(1/2)}$ and $f_{dT}^{\perp(1/2)}$ (Fig. 6.2). When only two asymmetries are used ($A_p^{\pi^+}(x)$ and $A_d^{\pi^+}(x)$), the other two asymmetries ($A_p^{\pi^-}(x)$ and $A_d^{\pi^-}(x)$) are well reproduced, confirming the goodness of the hypotheses. On the other side, the results are more sensitive to the statistical fluctuations. In the following, only the fit of the four measured asymmetries will be used.

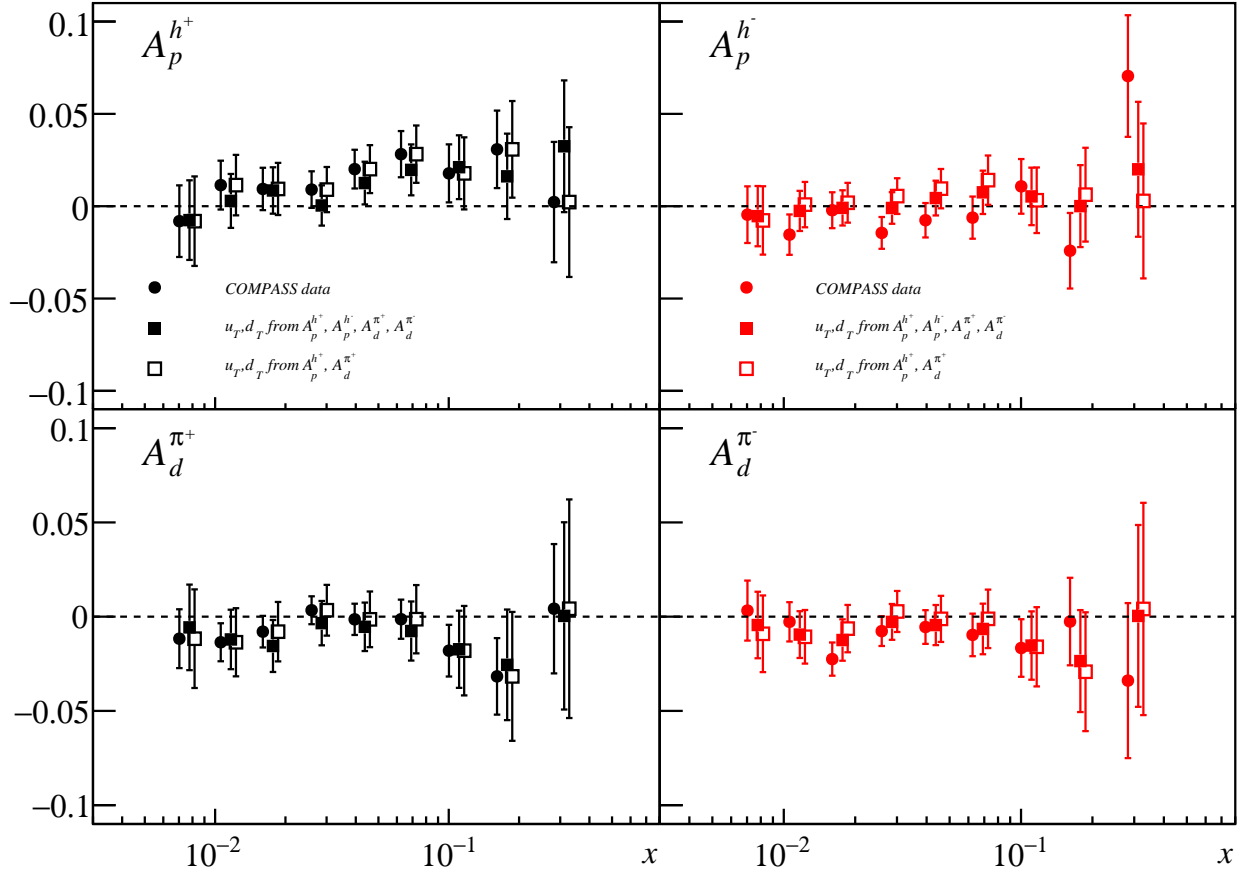


Figure 6.2: The Sivers asymmetries on the proton target (top row) and on the deuteron target (bottom row). The full dots are the measured asymmetries, the squares the asymmetries calculated with Eq. 6.2 using the extracted values of $f_{uT}^{\perp(1/2)}$ and $f_{dT}^{\perp(1/2)}$. Note that the errors on calculated value of the asymmetries include also the systematic error.

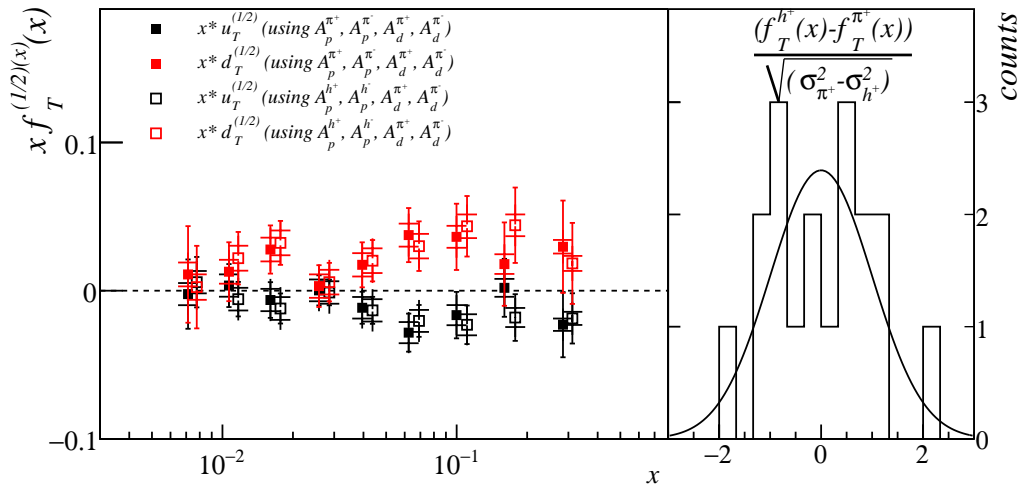


Figure 6.3: $x f_{uT}^{\perp(1/2)}$ and $x f_{dT}^{\perp(1/2)}$ in the nine x bins. The PDF extracted using $A_{p,exp}^{\pi^+}(x)$ and $A_{p,exp}^{\pi^-}(x)$ are compared with the same PDFs extracted using $A_{p,exp}^{h^+}(x)$ and $A_{p,exp}^{h^-}(x)$. In both cases the pion asymmetries on the deuteron are used. The error bar with larger edges represents the systematic uncertainty, the other the statistical one. The open squares are artificially shifted. On the right panel the distribution of the difference of the two extractions, normalised to the statistical error is compared to the expected distribution.

The systematic uncertainty

The measurement of $A_p^{\pi^+}$ is affected by a scale uncertainty of ± 0.01 (units of the final asymmetry, Sec. 5.4), that reflects in a systematic uncertainty in the Sivers PDF. The bin-by-bin approach, as well as the linear dependence of the PDFs from the measured asymmetries, allow to determine this scale uncertainty on the PDFs in a very natural way: the PDFs are extracted for the two boundaries conditions $A_p^{\prime\pi^+} = A_p^{\pi^+} + 0.01$ and $A_p^{\prime\pi^+} = A_p^{\pi^+} - 0.01$, and the two results define the systematic error band.

The asymmetries extracted using the h^+ or the π^+ samples show also a difference (Sec. 5.3): the Sivers PDF are thus extracted also using the charged hadron asymmetries for the proton. It is then investigated if this difference on the measured asymmetries is due to a statistical fluctuation of the result, or it is due some systematics. In fact the sample used to extract the Sivers PDF using the π^+ asymmetries on the proton ($f_T^{\pi^+}$) is a sub sample of that used to extract the Sivers PDF using the h^+ asymmetries on the proton ($f_T^{h^+}$), and the covariance is evaluated as $cov(f_T^{\pi^+}, f_T^{h^+}) = \sigma_{h^+}^2$. The compatibility of the two results is checked using the difference of the measured PDFs ($d = f_T^{h^+} - f_T^{\pi^+}$) normalised to its error ($\sigma_d = \sqrt{\sigma_{h^+}^2 + \sigma_{\pi^+}^2 - 2cov(f_T^{\pi^+}, f_T^{h^+})}$).

The PDFs extracted using the KRE FF and the GRV98 PDF are shown in Fig. 6.3. The closed squares are the u and d quark Sivers PDFs extracted using the pion Sivers asymmetries. The error bar with larger edges represents the systematic uncertainty, the other the statistical one: the systematic error is smaller than the statistical error, thus the scale uncertainty associated to the measurement does not prevent the extraction of the Sivers PDF from the data. The open squares are the u and d quark Sivers PDFs extracted using the pion Sivers asymmetries on the deuteron and the charged hadrons Sivers asymmetries on the proton. On the right panel, the distribution of the normalised difference between the two measured PDFs is shown. The distribution is compatible with the solid line, that is the expected Gaussian distribution that represents the expected statistical fluctuation of the result, thus no contribution to the systematic error is added.

The PDFs are extracted using different unpolarised PDF sets (MRST 2001 [56] and CTEQ 61

[57]), but no effect is found on the extracted PDFs.

In the following, the asymmetries extracted using the charged hadron asymmetries on the proton, the pion asymmetries on the deuteron, the Kretzer FF and the GRV98 PDF will be used.

6.2 The Gaussian factorisation of the quark transverse momentum

The second step in the analysis is to include the transverse momentum dependence of the PDF and the FF, that is assumed to be Gaussian: the generic function $a(x, k_T)$ is factorised as

$$a(x) \frac{1}{\pi\sigma^2} e^{-\frac{k_T^2}{\sigma^2}}.$$

In the literature, the Sivers PDF with the Gaussian hypothesis for the transverse momentum dependence is defined by different authors [23, 58, 59], each using a different notation. In App.C the convolution integrals over the quark transverse momentum p_T and the transverse momentum in the fragmentation process k_T are solved using the Amsterdam notation, used also in [23] and in Chap. 1. Their correspondence with the notation used in [58], where p_T and k_T have a different meaning, is also given. The notation used in [59] is as that used by [58], inverting p_T with k_T . For convenience, this analysis will use the notation of [59].

In the following it is assumed that the width of the Gaussian is the same in the Sivers and in the unpolarised case:

$$\begin{aligned} f_q^\perp(x, p_T) &= f_q^\perp(x) \frac{1}{\pi \langle p_T^2 \rangle} e^{-\frac{p_T^2}{\langle p_T^2 \rangle}} \\ f_q(x, p_T) &= f_q(x) \frac{1}{\pi \langle p_T^2 \rangle} e^{-\frac{p_T^2}{\langle p_T^2 \rangle}} \\ D_{h/q}(z, k_T) &= D_{h/q}(z) \frac{1}{\pi \langle k_T^2 \rangle} e^{-\frac{k_T^2}{\langle k_T^2 \rangle}} \end{aligned} \quad (6.3)$$

In this notation p_T is the transverse momentum of the quark in the nucleon, k_T is the transverse momentum in the fragmentation process and they are related to the measured transverse momentum of the hadron by the relation $\vec{P}_T^h = \vec{k}_T + z\vec{p}_T$. The average value of $\langle p_T^2 \rangle$ and $\langle k_T^2 \rangle$ can be taken from [58] (simply inverting p_T with k_T with respect to the article notation) and thus having: $\langle k_T^2 \rangle = 0.35 \text{ (GeV}/c)^2$ and $\langle p_T^2 \rangle = 0.20 \text{ (GeV}/c)^2$.

The measured Sivers asymmetry is:

$$\begin{aligned} A_{exp}(x) &= - \frac{\int_{0.2}^1 dz \int_{0.1}^\infty dP_T^h \frac{P_T^h z}{M} e^{-\frac{P_T^{h2}}{\langle P_T^{h2} \rangle}} \frac{\langle p_T^2 \rangle}{\langle P_T^{h2} \rangle^2} \sum_q e_q^2 f_T^\perp(x) D(z)}{\int_{0.2}^1 dz \int_{0.1}^\infty dP_T^h e^{-\frac{P_T^{h2}}{\langle P_T^{h2} \rangle}} \frac{1}{\langle P_T^{h2} \rangle} \sum_q e_q^2 f(x) D(z)} \\ &= - \frac{1}{M\sqrt{\pi}} \frac{\langle p_T^2 \rangle}{\sqrt{\langle P_T^{h2} \rangle}} \frac{e^{\frac{0.1^2}{\langle P_T^{h2} \rangle}}}{\left[1 - erf\left(\frac{0.1^2}{\langle P_T^{h2} \rangle}\right)\right]} \frac{\sum_q e_q^2 f_T^\perp(x) \int_{0.2}^1 dz z D(z)}{\sum_q e_q^2 f(x) \int_{0.2}^1 dz D(z)} \end{aligned}$$

where the integration over the COMPASS P_T^h range, $P_T^h > 0.1$ has been performed and $erf(x)$ is the error function, i.e. $erf(x) = \frac{1}{2\sqrt{\pi}} \int_0^x e^{-x^2} dx$.

Also in this case we use the half-moment of the Siverts function:

$$f_T^{(1/2)}(x) = \int dp_T^2 \frac{|p_T|}{M} f_q^\perp(x) \frac{1}{\pi \langle p_T^2 \rangle} e^{\frac{-p_T^2}{\langle p_T^2 \rangle}} = \frac{1}{2\pi M} f_q^\perp(x)$$

To simplify the notation, the integrals of the FF over z are redefined as \tilde{D}^{num} (numerator) and \tilde{D}^{den} (denominator) and thus we find:

$$\begin{aligned} A_{p,exp}^{\pi^+}(x) &= -2\sqrt{\pi} \frac{\langle p_T^2 \rangle}{\langle P_T^{h^2} \rangle} \frac{e^{\frac{0.1^2}{\langle P_T^{h^2} \rangle}}}{\left[1 - \text{erf}\left(\frac{0.1^2}{\langle P_T^{h^2} \rangle}\right)\right]} \frac{4f_{uT}^{\perp(1/2)} \tilde{D}_{fav}^{num} + f_{dT}^{\perp(1/2)} \tilde{D}_{unf}^{num}}{4u\tilde{D}_{fav}^{den} + d\tilde{D}_{unf}^{den}} \\ A_{p,exp}^{\pi^-}(x) &= -2\sqrt{\pi} \frac{\langle p_T^2 \rangle}{\langle P_T^{h^2} \rangle} \frac{e^{\frac{0.1^2}{\langle P_T^{h^2} \rangle}}}{\left[1 - \text{erf}\left(\frac{0.1^2}{\langle P_T^{h^2} \rangle}\right)\right]} \frac{4f_{uT}^{\perp(1/2)} \tilde{D}_{unf}^{num} + f_{dT}^{\perp(1/2)} \tilde{D}_{fav}^{num}}{4u\tilde{D}_{unf}^{den} + d\tilde{D}_{fav}^{den}} \\ A_{p,exp}^{\pi^+}(x) &= -2\sqrt{\pi} \frac{\langle p_T^2 \rangle}{\langle P_T^{h^2} \rangle} \frac{e^{\frac{0.1^2}{\langle P_T^{h^2} \rangle}}}{\left[1 - \text{erf}\left(\frac{0.1^2}{\langle P_T^{h^2} \rangle}\right)\right]} \frac{(f_{uT}^{\perp(1/2)} + f_{dT}^{\perp(1/2)})(4\tilde{D}_{fav}^{num} + \tilde{D}_{unf}^{num})}{(u+d)(4\tilde{D}_{fav}^{den} + \tilde{D}_{unf}^{den})} \\ A_{p,exp}^{\pi^-}(x) &= -2\sqrt{\pi} \frac{\langle p_T^2 \rangle}{\langle P_T^{h^2} \rangle} \frac{e^{\frac{0.1^2}{\langle P_T^{h^2} \rangle}}}{\left[1 - \text{erf}\left(\frac{0.1^2}{\langle P_T^{h^2} \rangle}\right)\right]} \frac{(f_{uT}^{\perp(1/2)} + f_{dT}^{\perp(1/2)})(\tilde{D}_{fav}^{num} + 4\tilde{D}_{unf}^{num})}{(u+d)(\tilde{D}_{fav}^{den} + 4\tilde{D}_{unf}^{den})} \end{aligned} \quad (6.4)$$

The half moments of the Siverts function extracted with the Gaussian factorisation of the transverse momentum is shown in Fig. 6.4, where they are compared with the same PDF extracted in the previous section. As expected, the two extractions are in good agreement, and the PDF extracted with the Gaussian p_T and k_T factorisation hypothesis are systematically larger in size. In the following discussion we have regarded the difference between the PDFs extracted with the two methods as a systematic error due to the theoretical uncertainties.

6.3 Conclusions and comparison with the theoretical models

From the previous analysis we can conclude that the Siverts PDF is different from zero. It is positive and large for the u-quark and negative and smaller for the d-quark. The numerical values of the measured PDF, in the different x bins are reported in Tab. 6.1, where also the final systematic errors are reported. Despite the rather large systematic error in the measurement of the h^+ Siverts asymmetry on the proton, the largest contribution to the systematic error on the PDF at large x is due to the theoretical uncertainty on the dependence of the PDF from the quark transverse momentum. The final systematic error is the sum in quadrature of the contributions coming from the data and from the theory.

It has to be noted (Fig. 6.5) that the Siverts PDF is significantly different from zero in the second and the third x bins. In this analysis the sea-quark contribution has been neglected, because it would be under-constrained in the fit. It is then not clear if the effect is due to this simplified hypothesis or if it is due to some fluctuations of the data. To answer also this question the more precise COMPASS data expected from the 2010 run will be very important.

The Siverts PDF extracted in this Chapter, without the Gaussian factorisation of the transverse momentum can be compared with the extraction via a global fit done by different authors.

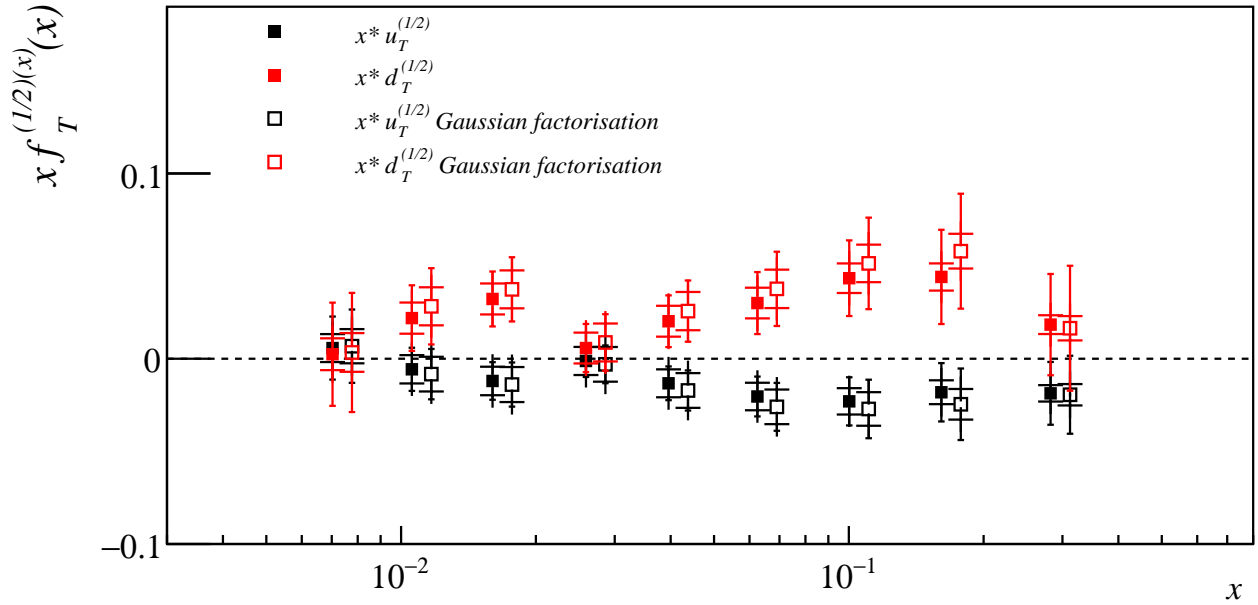


Figure 6.4: The half moment of the Sivers PDF multiplied by x , in black for the u -quark and in red for the d -quark. The open squares represent the PDF extracted assuming the Gaussian factorisation of the transverse momentum. The error bars with the larger edges represents the experimental systematic uncertainty.

| u quark | | systematics | | | |
|---------|------------------|-------------|--------|-------|-------|
| x | $f_T^{(1/2)}(x)$ | σ_f | theory | data | total |
| 0.0070 | 0.82 | 0.02 | -0.14 | 1.22 | 1.23 |
| 0.0106 | -0.54 | 0.01 | 0.25 | 0.48 | 0.54 |
| 0.0160 | -0.75 | 0.01 | 0.12 | 0.36 | 0.38 |
| 0.0259 | -0.05 | 0.01 | 0.07 | 0.22 | 0.23 |
| 0.0396 | -0.34 | 0.01 | 0.10 | 0.09 | 0.13 |
| 0.0625 | -0.33 | 0.01 | 0.09 | 0.03 | 0.09 |
| 0.1002 | -0.23 | 0.01 | 0.04 | 0.03 | 0.05 |
| 0.1609 | -0.11 | 0.02 | 0.04 | -0.00 | 0.04 |
| 0.2822 | -0.07 | 0.02 | 0.00 | 0.01 | 0.01 |
| d quark | | systematics | | | |
| x | $f_T^{(1/2)}(x)$ | σ_f | theory | data | total |
| 0.0070 | 0.34 | 0.03 | -0.14 | -1.09 | 1.09 |
| 0.0106 | 2.08 | 0.02 | -0.60 | -0.19 | 0.63 |
| 0.0160 | 2.02 | 0.01 | -0.32 | -0.20 | 0.38 |
| 0.0259 | 0.22 | 0.01 | -0.12 | -0.21 | 0.24 |
| 0.0396 | 0.51 | 0.01 | -0.14 | -0.07 | 0.16 |
| 0.0625 | 0.48 | 0.02 | -0.12 | -0.01 | 0.12 |
| 0.1002 | 0.43 | 0.02 | -0.08 | 0.00 | 0.08 |
| 0.1609 | 0.27 | 0.03 | -0.09 | 0.04 | 0.10 |
| 0.2822 | 0.07 | 0.03 | 0.01 | -0.02 | 0.03 |

Table 6.1: The measured Sivers PDFs of the u and d quarks, and the associated statistical and systematic errors

In this preliminary work, the Q^2 evolution of the PDF is not taken into account, but it is expected to have a larger impact only in the last x bins, in which the average Q^2 is higher.

In [35], the Siverts PDF half moment is given by:

$$f_T^{\perp(1/2)} = 2 N x^a (1-x)^{\frac{b(a+b)^{a+b}}{a^a b^b}} \sqrt{2 \cdot 2.7183} \frac{0.25}{M + 0.25} \frac{1}{-4 \cdot 0.981}$$

(note the the authors use the opposite sign convention) with the parameters $N_u = 0.35 \pm 0.08$, $N_d = -0.90_{-0.10}^{+0.43}$, $a_u = 0.73_{-0.58}^{+0.72}$, $a_d = 1.08_{-0.65}^{+0.82}$, $b = 3.46_{-2.90}^{+4.87}$, and is extracted using the COMPASS deuteron data and the HERMES proton data, at the scale $Q^2 = 2.4$ (GeV/c)² and assuming that the Siverts PDFs evolve as the unpolarised ones. This extraction well represents the shape of the measured PDFs, but is systematically larger. This is due in part to the fact that the authors use the Gaussian approximation of the transverse momentum and in part to the fact that the HERMES proton Siverts asymmetries are larger than the COMPASS ones. In [52] the Siverts PDF is extracted from the first HERMES data, at the average $Q^2 = 2.41$ (GeV/c)². The Siverts functions are:

$$\begin{aligned} f_{uT}^{\perp(1/2)}(x) &= -0.81x(x-1)u(x) \\ f_{dT}^{\perp(1/2)}(x) &= -1.86x(x-1)u(x) \end{aligned}$$

where $\sigma_u = 0.07$ and $\sigma_d = 0.28$. The values extracted largely overshoot the data, specially at high x .

In [59], the Siverts PDF is also extracted from the HERMES data only, at a scale $Q^2 = 2.5$ GeV/c. The parametrisation is:

$$x f_T^{\perp(1/2)} = -A x^{0.66} (1-x)^5$$

where $A^u = 0.17$ and $A^d = -0.17$. This fit shows a good compatibility with the measured PDFs.

The author of [51] uses the same parametrisation as [59]:

$$f_T^{\perp(1/2)} = S x^a (1-x)^b$$

but with different coefficients coming from the fit of the most recent HERMES proton and COMPASS deuteron data. The coefficients are $S_u = -0.29 \pm 0.09$, $a_u = -0.27 \pm 0.10$, $b_u = 2.65 \pm 0.81$ and $S_d = 0.59 \pm 0.31$, $a_d = -0.19 \pm 0.17$, $b_d = 2.93 \pm 1.03$. The functional form well represents the data, but the size of the asymmetry is overestimated, again because of the use of the HERMES proton asymmetries.

6.4 The extraction of the transversity PDF

The situation is more complicated if we want to extract the transversity PDF from the data. In fact, the amplitude of the Collins PDF gives the convolution of transversity with the Collins FF, that is also unknown. Due to the definition of the convolution integral in the $\sin(\phi_h - \phi_s)$ structure function (Tab. 1.2), it is convenient to introduce the half-moment of the Collins FF,

$$H^{(1/2)}(z) = \int d^2 \vec{k}_T \frac{-|k_T|}{2z m_\pi} H(z, \vec{k}_T) \quad (6.5)$$

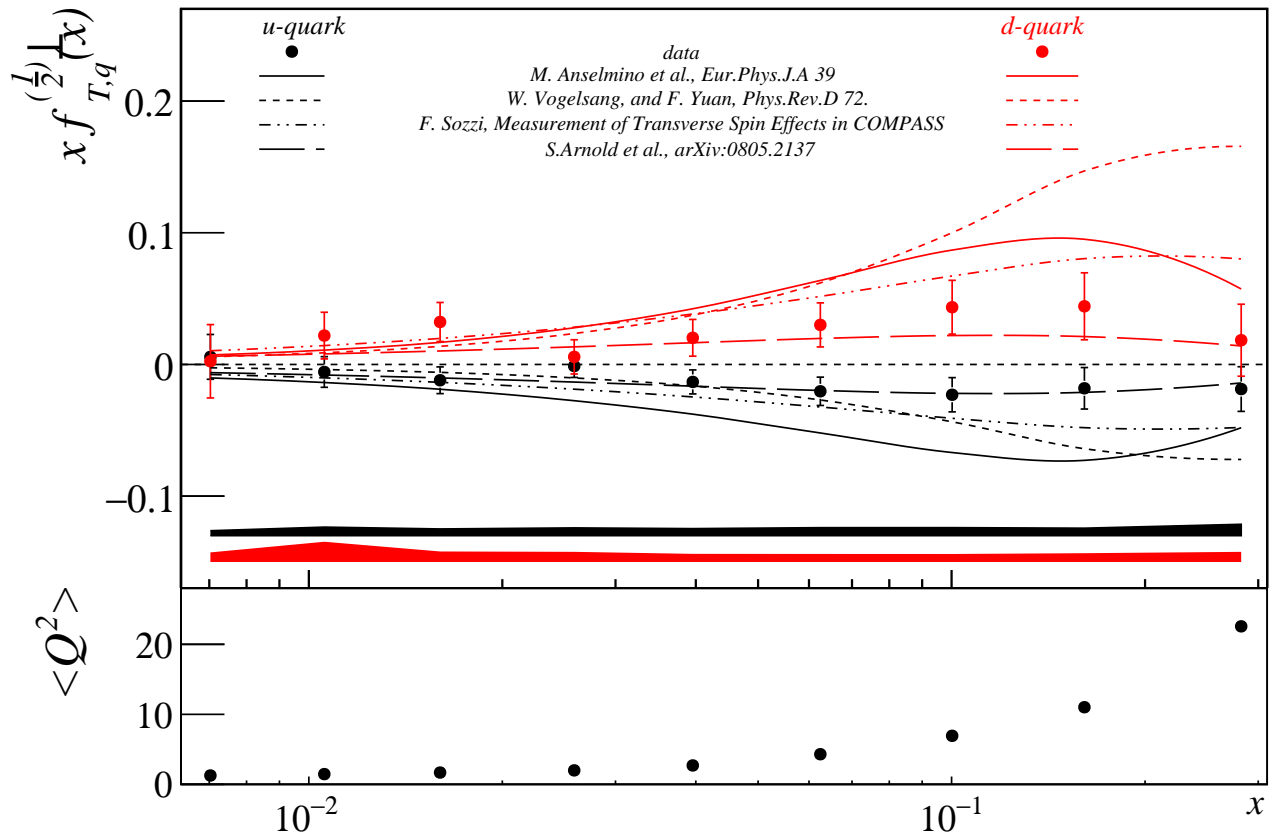


Figure 6.5: The half moment of the Sivers PDF extracted from the COMPASS proton and deuteron data for the u (black) and the d-quark (red). The bands in the plot represent the corresponding systematic error. The curves (without their uncertainty) represent the extraction of the Sivers PDF by various authors (details in the text), at a fixed Q^2 value. The Q^2 value of the measured PDF is shown in the bottom line.

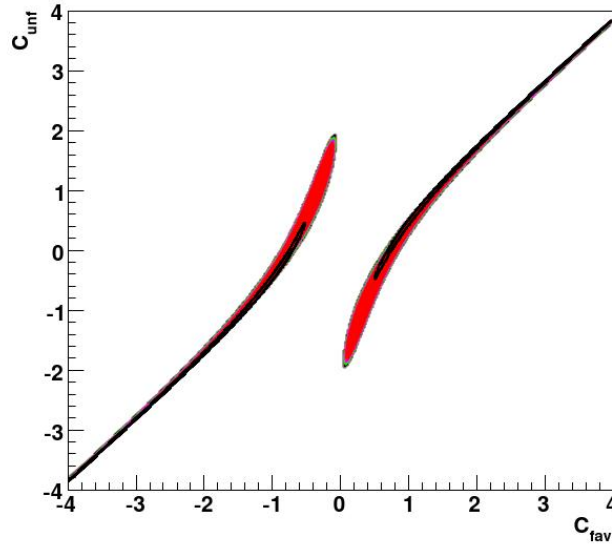


Figure 6.6: The 2σ confidence region of the C_{fav} , C_{unf} parameters from [51].

and its integral over the z range, $\tilde{H}^{(1/2)}$.

In a first approximation, we will neglect the p_T dependence of the transversity PDF. Neglecting the sea contributions, the measured Collins asymmetries are parametrised as:

$$\begin{aligned}
 A_{p,exp}^{\pi^+}(x) &= -\frac{4h_{uT}\tilde{H}_{fav}^{(1/2)} + h_{dT}\tilde{H}_{unf}^{(1/2)}}{4u\tilde{D}_{fav} + d\tilde{D}_{unf}} \\
 A_{p,exp}^{\pi^-}(x) &= -\frac{4h_{uT}\tilde{H}_{unf}^{(1/2)} + h_{dT}\tilde{H}_{fav}^{(1/2)}}{4u\tilde{D}_{unf} + d\tilde{D}_{fav}} \\
 A_{d,exp}^{\pi^+}(x) &= -\frac{(h_{uT} + h_{dT})(4\tilde{H}_{fav}^{(1/2)} + \tilde{H}_{unf}^{(1/2)})}{(u + d)(4\tilde{D}_{fav} + \tilde{D}_{unf})} \\
 A_{d,exp}^{\pi^-}(x) &= -\frac{(h_{uT} + h_{dT})(\tilde{H}_{fav}^{(1/2)} + 4\tilde{H}_{unf}^{(1/2)})}{(u + d)(\tilde{D}_{fav} + 4\tilde{D}_{unf})}.
 \end{aligned} \tag{6.6}$$

It is clear from Eq. 6.6 that it is not possible to extract from the data the transversity PDF and the integral of the Collins FF separately, but only the four products: $h_{uT}\tilde{H}_{fav}^{(1/2)}$, $h_{dT}\tilde{H}_{fav}^{(1/2)}$, $h_{uT}\tilde{H}_{unf}^{(1/2)}$ and $h_{dT}\tilde{H}_{unf}^{(1/2)}$.

To extract transversity, a constraint on Collins FF coming from the analysis of the BELLE data is then needed. In [51], the author uses only the BELLE data to determine the favoured and unfavoured Collins FF using the parametrisation:

$$H_a(z) = C_a z D_a(z) \tag{6.7}$$

where $a = fav, unf$ (note that $\Delta_T^0 D_q^h(z)_{[51]} = H_{\text{here}}^{(1/2)}$ and that there is a factor of 2 in the definition with respect to [60]). The author has extracted the values of the parameters C_{fav} and C_{unf} , but has found that the minimum is not well defined. The allowed range of the parameters is large but there is a strong correlation between the two, which can be described by the relation

$$C_{unf} = -2.7 + 3.2\sqrt{C_{fav}} \tag{6.8}$$

As a first exercise, Eq. 6.7 with the constraint of Eq. 6.8 is used as parametrisation of the Collins FF in the fit of the data. It is moreover assumed that the integral of the Collins FF over

the z range is the same in all the measured x bins, since the z distribution essentially does not depend on x . To improve the quality of the fit, the negative sign of the d -quark transversity PDFs is fixed according to the convention used in [30]. In total 19 parameters are used: 9 for the u -quark PDF, 9 for the d -quark PDF and the parameter C_{fav} of the Collins FF. As for the Sivers case, the Kretzer parametrisation of the unpolarised FFs and the GRV98 parametrisation of the unpolarised PDFs are used. The experimental asymmetries are well described, but the precision on the extracted PDFs is lower with respect to the Sivers case due to the correlations introduced by the fit of the Collins function. The extracted value of the u and d PDFs is shown in Fig. 6.7; the PDFs are different from zero in the valence region only. Due to the constraint applied to the d -quark transversity PDF, the estimation of the error on the PDF itself is not reliable at small x , where the fitted parameter is at its limit. This fact is a known issue of the minimiser [61], and an alternative strategy to fit the data has to be found. From the fit the value of $C_{fav} = 0.28 \pm 0.09$ is found. Due to the very high number of parameters, it is not possible to visualize the confidence region of the fit. It is anyhow shown the χ^2 value as a function of C_{fav} , that shows that coupling the COMPASS and BELLE data, the minimum of C_f is well defined (Fig. 6.8). Note that the plot is a projection of the distribution, which is a function of 19 variables, thus the value of C_f at the minimum of the χ^2 does not coincide with the best fitted C_f value.

To compare the extracted values of the transversity PDF with the extraction from other authors [30, 60, 51] and from the lattice calculations [62], we use the tensor charge defined as:

$$\begin{aligned}\delta u &= \int_{0.003}^1 h_{uT}(x) dx = 0.71 \pm 0.19(\pm 0.34) \\ \delta d &= \int_{0.003}^1 h_{dT}(x) dx = -0.65 \pm 0.32(\pm 0.47)\end{aligned}\tag{6.9}$$

where the error is calculated assuming that the error on the PDFs measured in each x bin are independent. Since the fit of the Collins FF introduces a strong correlation between the other parameters, the error is also calculated assuming the 100% correlation between the measured data, and its value is reported in the brackets. It has to be noted that no evolution in Q^2 is assumed for the transversity PDF. The authors of [30], from the global fit of the COMPASS deuteron data, the HERMES proton data and the latest BELLE data obtain the values of $\delta u = 0.54_{-0.22}^{+0.09}$ and $\delta d = -0.23_{-0.16}^{+0.09}$, at a reference Q^2 of $0.8 \text{ (GeV}/c)^2$, in good agreement with this analysis.

The author of [51] finds $\delta u = 0.39_{-0.13}^{+0.14}$ and $\delta d = -0.11_{-0.06}^{+0.11}$. The good compatibility with these results is expected, since the same data for the deuteron asymmetries and the same parametrisation of the Collins FF are used. The lattice calculation in [62] gives $\delta u = 0.857 \pm 0.013$ and $\delta d = -0.212 \pm 0.005$.

All the extractions show that the tensor charge of the u -quark is larger in size and opposite in sign than that of the d -quark. Our measured values for the u - and d -quark tensor charges are essentially equal, but it has to be considered that uncertainty on the d quark PDF is larger than that on the u quark.

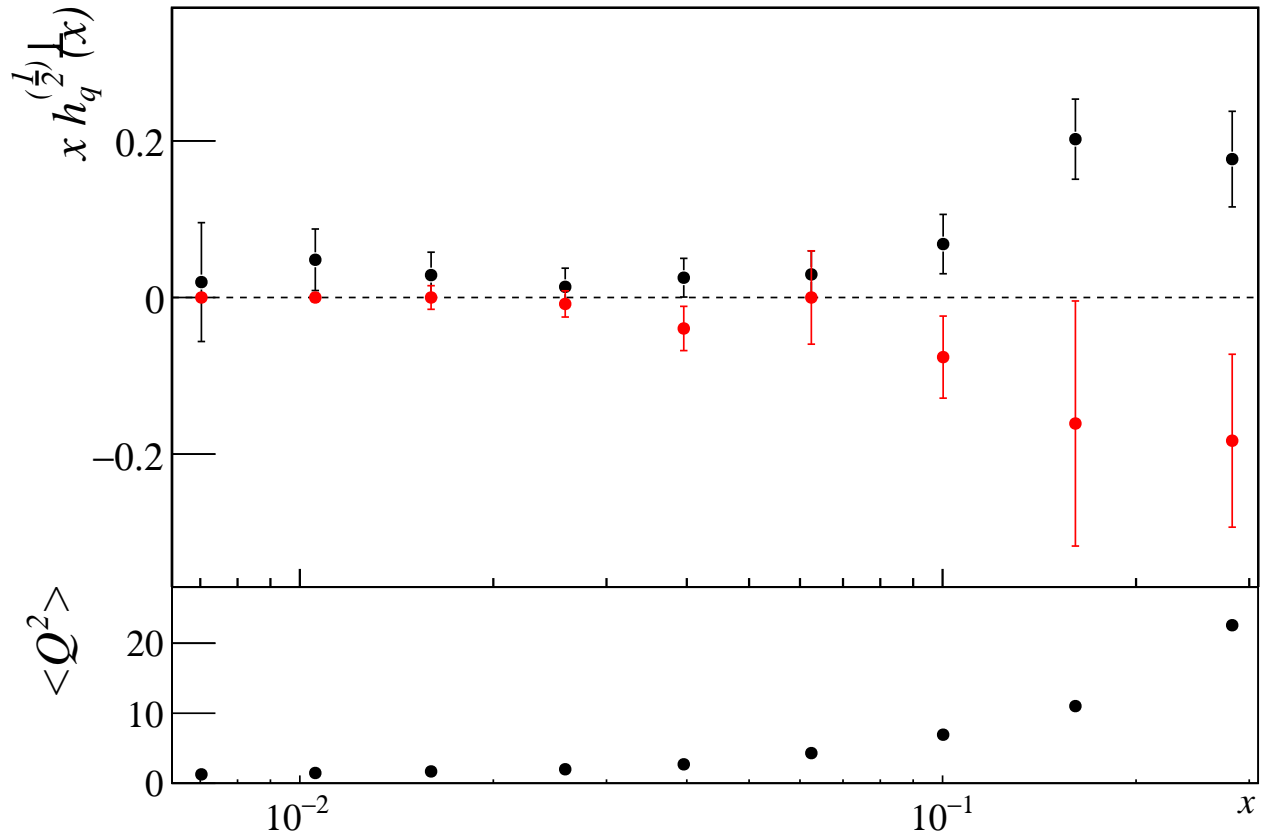


Figure 6.7: The transversity PDF extracted from the COMPASS proton and deuteron data for the u (black) and the d-quark (red). The Q^2 value of the measured PDF is shown in the bottom line.

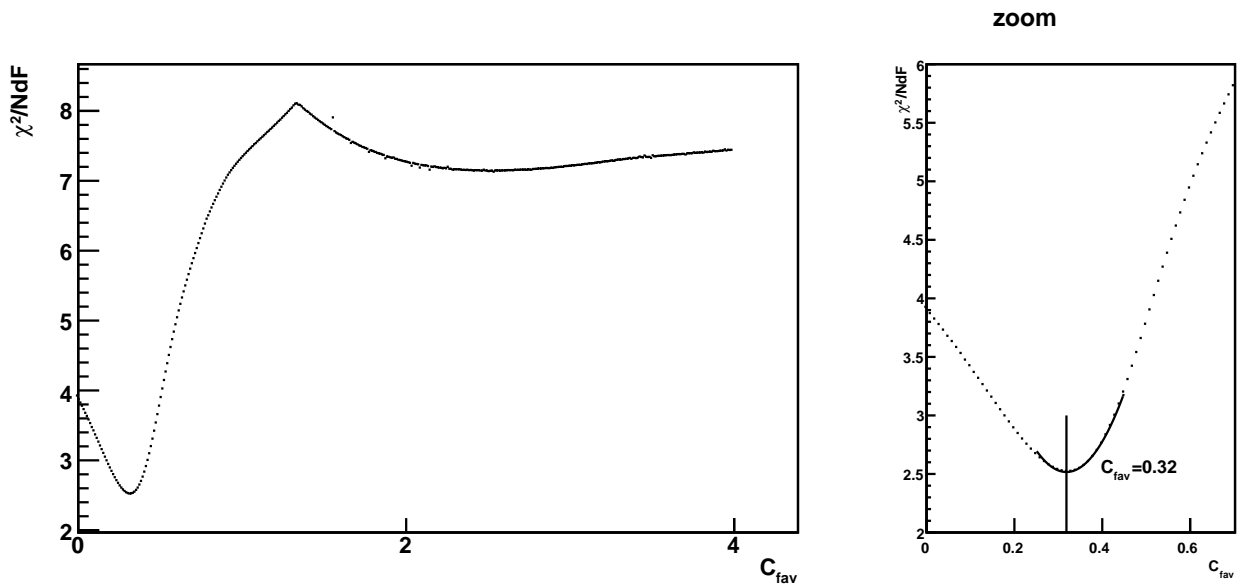


Figure 6.8: χ^2 value of the fit of the Collins asymmetries as a function of the value of C_{fav} . The minimum is well defined and it is found at the value of $C_{fav} = 0.32$

Conclusions

The COMPASS experiment plays a central role in the investigation of the transverse momentum and the transverse spin effects in SIDIS. In the years 2002-2004, COMPASS scattered a 160 GeV/c longitudinally polarised muon beam off a transversely polarised ${}^6\text{LiD}$ target, and measured for the first time the transverse-spin-target dependent cross-section asymmetries on the deuteron. For long time, these results could only be compared with the results of the HERMES experiment, that scattered 27 GeV/c electrons off a transversely polarised hydrogen target, accessing part of the transverse-spin-target dependent cross-section asymmetries on the proton, at a different average Q^2 .

In 2007 COMPASS took data with a transversely polarised NH_3 target. The first preliminary analysis of the data was presented at Transversity 2008, where it was first shown that the Collins asymmetry on the proton for the charged hadron is different from zero in the valence region and of opposite sign for positive and negative hadrons, in agreement with the HERMES results, obtained at a substantially lower energy. From that first analysis the Sivers asymmetry turned out to be smaller than that measured by HERMES, and even compatible with zero.

In this Thesis the long analysis process that brought to the finalisation of the results for the publication of the charged hadron asymmetries is described. The spectrometer in 2007 suffered from instabilities, that affected the measurement of the Sivers asymmetry more than the Collins asymmetry. Several algorithm were developed to determine the quality of the data, and great care was devoted to properly account in the systematic error for the known spectrometer instabilities. As a result it turned out that it is possible to use all the collected statistics to measure the Collins asymmetry, and the systematic error is of the order of half of the statistical one. On the other side, only four out of six periods are suitable to extract the Sivers asymmetry, and the average asymmetry measured in the first two and the second two periods are not statistically compatible. It has been necessary to add an extra scale factor to the systematics to account for this difference.

The Collins asymmetry shows a clear signal in the valence region, of opposite sign for positive and negative hadrons, of the same size of that measured by the HERMES experiment, a result that suggest that the Q^2 dependence is weak. No strong dependence of the Collins asymmetry is found as a function of the other variables.

The Sivers asymmetry is positive in the whole x range for positive hadrons, smaller than but still compatible with the asymmetry measured by the HERMES experiment. For negative hadrons the Sivers asymmetry is compatible with zero. A further study brought the unexpected indication that the Sivers asymmetry for positive hadrons is larger at small values of W , the invariant mass of the hadronic state, and compatible with zero at higher value of W and this trend is visible in all the different periods. It has to be noted that, due to the different kinematics of the two experiments, the HERMES range in W corresponds to the lower values of W measured by the COMPASS experiment.

The analysis of the 2007 proton data is then extended to the full transverse-target dependent cross-section. Thanks to the longitudinally polarised beam present at COMPASS, it is not only possible to measure the further three modulations depending only on the transverse

polarisation of the target, but it is also possible to measure for the first time on the proton the three modulations that depend also on the longitudinal polarisation of the beam. All these asymmetries are found to be compatible with zero.

To conclude the analysis of the 2007 proton data, the Collins and Sivers asymmetries are extracted on the identified hadron sample. Hadron identification is performed thanks to a large size Ring Imaging Cherenkov detector (RICH), that is carefully tuned to identify the particles with the best compromise possible between the efficiency and the purity of the sample. The Collins asymmetries on the pion sample is compatible with that on the charged hadron sample ($\sim 70\%$ of the hadron are identified as pions), and the Collins asymmetries on the positive kaons is negative in average, while the result is not clear for the negative kaons. For what concerns the Sivers asymmetry, the asymmetry on π^+ is somewhat smaller than that measured for the positive hadrons because of the different selection of the periods of data-taking. The Sivers asymmetry for positive kaons is different from zero on the whole x range and is larger at small values of W ; moreover it is larger than the asymmetry for the h^+ .

The Sivers asymmetries on the proton for positive and negative hadrons are then coupled with the corresponding measurement on the deuteron target, performed in the same kinematical range and with the same binning, and the first extraction of the Sivers PDF is performed in each of the nine x bins used for the analysis, without defining the functional form of the PDF. The Sivers PDF for the d -quark is positive, while it is negative for the u -quark and smaller in size.

From the measurement of the Collins asymmetries, again coupling the results extracted in this Thesis with the COMPASS results on the deuteron data, it is possible to measure in the nine x bins also the transversity PDF. In this case, since transversity is coupled with the unknown Collins FF, a parametrisation of the Collins FF itself coming from the fit of the BELLE data has to be introduced as an outer constraint to the fit. The transversity PDF are of opposite sign for the u and the d quark, and is different from zero at high x .

The next step in the understanding of the spin structure of the nucleon will come with the analysis of the 2010 COMPASS data, that will decrease the statistical as well as the systematic error of this analysis. In the next future, new experiment will come: COMPASS will measure a Drell-Yan process in polarised $\pi^- p^\uparrow$ scattering, JLAB will complete its 12 GeV program, and projects are being finalized to investigate Drell-Yan in polarised antiproton-polarised proton scattering (PAX at FAIR) and in polarised proton scattering off polarised protons (JPARC and NICA). In a more distant future, a new generation of polarised-electron polarised-proton collides is also expected (BNL and JLab).

Appendix A

The light-cone reference frame

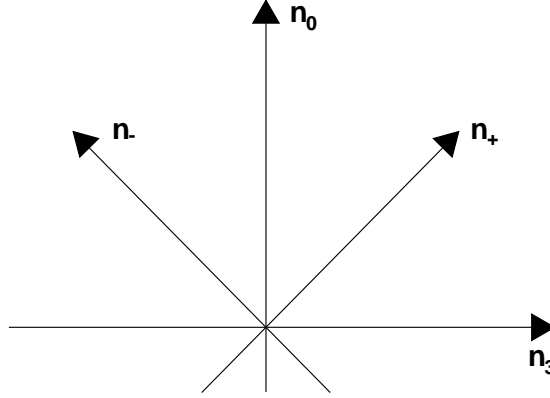


Figure A.1: The light-cone axes.

A four-vector a can be decomposed in its light cone coordinates $a^\pm = \frac{1}{\sqrt{2}}(a_0 \pm a_3)$ and $\vec{a}_T = (a_1, a_2)$.

With this notation:

$$a^2 = a_\mu a^\mu = 2a_+ a_- - \vec{a}_T^2 \quad (\text{A.1})$$

$$a \cdot b = a_+ b_- + a_- b_+ - \vec{a}_T \cdot \vec{b}_T \quad (\text{A.2})$$

Introducing the two Sudakov vectors $n_+ = [1, 0, \vec{0}_T]$ and $n_- = [0, 1, \vec{0}_T]$ (Fig. A.1), with the properties $n_+^2 = n_-^2 = 0$ and $n_+ \cdot n_- = 0$, it is possible to parametrize the generic four-vector a as:

$$a^\mu = a^+ n_+^\mu + a^- n_-^\mu + a_T^\mu \quad (\text{A.3})$$

The advantage of this reference system for the study of a DIS reaction is the following: if we work in the collinear reference frame, i.e. the frame in which P had no transverse momentum with respect to the incident γ , then

$$P^\mu = P^+ n_+^\mu + \frac{M^2}{2p^+} n_-^\mu \simeq P^+ n_+^\mu \quad (\text{A.4})$$

where the latter equal holds in the Bjorken limit. Analogously the vector q is:

$$q^\mu = \frac{Q^2}{2xp^+}n_+^\mu - xp^+n_-^\mu \simeq -xp^+n_-^\mu \quad (\text{A.5})$$

In the Bjorken limit and in the collinear frame P has only the "plus" component, q has only the "minus" component.

Appendix B

Fourier analysis of the COMPASS acceptance

In this appendix the details of the Fourier analysis of the COMPASS acceptance presented in Sec. 3.7.2 are shown [COMPASS note 2007-2].

l, m, n are integer and $l \geq 1, n \geq 1$ and $m \geq 0$

$$\int_{-\pi}^{\pi} d\phi_h \cos(m\phi_h \pm \Phi) = 2\pi\delta_{m0} \cos \Phi \quad (\text{B.1})$$

$$\int_{-\pi}^{\pi} d\phi_h \sin(m\phi_h \pm \Phi) = \pm 2\pi\delta_{m0} \sin \Phi \quad (\text{B.2})$$

$$\int_{-\pi}^{\pi} d\phi_h \cos(m\phi_h \pm \Phi) \cos(n\phi_h - l\Phi) = \pi\delta_{mn} \cos(l\Phi_s \pm \Phi_s) \quad (\text{B.3})$$

$$\int_{-\pi}^{\pi} d\phi_h \cos(m\phi_h \pm \Phi) \sin(n\phi_h - l\Phi) = -\pi\delta_{mn} \sin(l\Phi_s \pm \Phi_s) \quad (\text{B.4})$$

$$\int_{-\pi}^{\pi} d\phi_h \sin(m\phi_h \pm \Phi) \cos(n\phi_h - l\Phi) = \pi\delta_{mn} \sin(l\Phi_s \pm \Phi_s) \quad (\text{B.5})$$

$$\int_{-\pi}^{\pi} d\phi_h \sin(m\phi_h \pm \Phi) \sin(n\phi_h - l\Phi) = \pi\delta_{mn} \cos(l\Phi_s \pm \Phi_s) \quad (\text{B.6})$$

B.1 Example: 1D correlation between the Collins and Sivers asymmetries

The cross section has eight azimuthal modulations:

$$\sigma_{\pm}(\phi_h, \phi_s) \propto 1 \pm \left[a_c \sin(\phi_h + \phi_s) + a_s \sin(\phi_h - \phi_s) + a_2 \sin(3\phi_h - \phi_s) + a_4 \cos(\phi_h - \phi_s) \right. \\ \left. + a_5 \sin(\phi_s) + a_6 \sin(2\phi_h - \phi_s) + a_7 \cos(\phi_s) + a_8 \cos(2\phi_h - \phi_s) \right]$$

and the acceptance is parametrized as:

$$A(\phi_s) = c_0 \left(1 + 2s_1 \sin(\phi_s) + 2c_1 \cos(\phi_s) + 2s_2 \sin(2\phi_s) + 2c_2 \cos(2\phi_s) + 2s_3 \sin(3\phi_s) + \right. \\ \left. + 2c_3 \sin(3\phi_s) + 2s_4 \sin(4\phi_s) + 2c_4 \cos(4\phi_s) + 2s_5 \sin(5\phi_s) + 2c_5 \sin(5\phi_s) \right)$$

The asymmetries are extracted from the fit of:

$$F^{QR}(\Phi) = \frac{\prod_{i=1}^4 \int_{-\pi}^{\pi} N_i^{\uparrow}(\phi_h, \Phi) d\phi_h}{\prod_{i=1}^4 \int_{-\pi}^{\pi} N_i^{\downarrow}(\phi_h, \Phi) d\phi_h}$$

with the function $p_0[1 + A \sin(\phi)]$. Now the number of events $N(\Phi) = \int_{-\pi}^{\pi} N_i(\phi_h, \Phi) d\phi_h$ will be calculated.

Let's assume that $\Phi = \phi_h - \phi_s$, i.e. it is the Siverts angle. Then:

$$\begin{aligned} N(\Phi) \propto \int_{-\pi}^{\pi} \left(1 \pm \left[a_c \sin(2\phi_h + \Phi) + a_s \sin(\Phi) + a_2 \sin(2\phi_h - \Phi) + a_4 \cos(\Phi) + a_5 \sin(\phi_h - \phi) + \right. \right. \\ \left. \left. + a_6 \sin(\phi_h + \Phi) + a_7 \cos(\phi_h - \Phi) + a_8 \cos(\phi_h + \Phi) \right] \right) \left(1 + 2s_1 \sin(\phi_s) + 2c_1 \cos(\phi_s) + \right. \\ \left. + 2s_2 \sin(2\phi_s) + 2c_2 \cos(2\phi_s) + 2s_3 \sin(3\phi_s) + 2c_3 \cos(3\phi_s) + 2s_4 \sin(4\phi_s) + \right. \\ \left. + 2c_4 \cos(4\phi_s) + 2s_5 \sin(5\phi_s) + 2c_5 \cos(5\phi_s) \right) d\phi_h \end{aligned}$$

Now:

$$\begin{aligned} \int_{-\pi}^{\pi} \sigma(\phi_h, \Phi) d\phi_h &= 2\pi(1 + a_s \sin(\Phi) + a_4 \cos(\Phi)) \\ \int_{-\pi}^{\pi} A(\phi_h, \Phi) d\phi_h &= 0; \end{aligned}$$

What is still to evaluate is:

$$\begin{aligned} \int_{-\pi}^{\pi} d\phi_h \left[a_c \sin(2\phi_h + \Phi) + a_s \sin(\Phi) + a_2 \sin(2\phi_h - \Phi) + a_4 \cos(\Phi) + a_5 \sin(\phi_h - \phi) + a_6 \sin(\phi_h + \right. \\ \left. \Phi) + a_7 \cos(\phi_h - \Phi) + a_8 \cos(\phi_h + \Phi) \right] \left[2s_1 \sin(\phi_h - \Phi) + 2c_1 \cos(\phi_h - \Phi) + 2s_2 \sin(2\phi_h - 2\Phi) + \right. \\ \left. 2c_2 \cos(2\phi_h - 2\Phi) + 2s_3 \sin(3\phi_h - 3\Phi) + 2c_3 \cos(3\phi_h - 3\Phi) + 2s_4 \sin(4\phi_h - 4\Phi) + 2c_4 \cos(4\phi_h - \right. \\ \left. 4\Phi) + 2s_5 \sin(5\phi_h - 5\Phi) + 2c_5 \cos(5\phi_h - 5\Phi) \right]. \end{aligned}$$

To do this we make use of the formulae (B.1-B.6). Most of the product integrals give zero due to the δ . Only few of them are different from zero:

$$\begin{aligned} \int_{-\pi}^{\pi} d\phi_h a_6 \sin(\phi_h + \Phi) \cdot s_1 \sin(\phi_h - \Phi) &= 2\pi a_6 s_1 \cos(2\Phi) \\ \int_{-\pi}^{\pi} d\phi_h a_8 \cos(\phi_h + \Phi) \cdot s_1 \sin(\phi_h - \Phi) &= -2\pi a_8 s_1 \sin(2\Phi) \\ \int_{-\pi}^{\pi} d\phi_h a_6 \sin(\phi_h + \Phi) \cdot c_1 \cos(\phi_h - \Phi) &= 2\pi a_6 c_1 \sin(2\Phi) \\ \int_{-\pi}^{\pi} d\phi_h a_8 \cos(\phi_h + \Phi) \cdot c_1 \cos(\phi_h - \Phi) &= 2\pi a_8 c_1 \cos(2\Phi) \\ \int_{-\pi}^{\pi} d\phi_h a_c \sin(2\phi_h - \Phi) \cdot c_2 \cos(2\phi_h - 2\Phi) &= 2\pi a_c c_2 \sin(\Phi) \\ \int_{-\pi}^{\pi} d\phi_h a_2 \sin(2\phi_h + \Phi) \cdot c_2 \cos(2\phi_h - 2\Phi) &= 2\pi a_2 c_2 \sin(3\Phi) \end{aligned}$$

Thus:

$$N(\Phi) \propto 2\pi(1 \pm [a_s \sin(\Phi) + a_4 \cos(\Phi) + a_c c_2 \sin(\Phi) + a_2 c_2 \sin(3\Phi) + a_6 s_1 \cos(2\Phi) + a_8 c_1 \cos(2\Phi) + a_6 c_1 \sin(2\Phi) - a_8 s_1 \sin(2\Phi)])$$

and, at first order, assuming $a_i \ll 1$ and neglecting all the modulations apart from $\sin(\Phi)$:
 $F^{QR}(\Phi) \simeq (1 + 4(a_s + a_c c_2) \sin(\Phi)).$

We have than that $A_s^{fit} = a_s + a_c c_2.$

Appendix C

The determination of the convolution integrals

The Siverts asymmetries is (Sec. 1.4):

$$A_{Siv} = \frac{F_{UT}^{\sin(\phi_h - \phi_s)}}{F_{UU}} = \frac{\sum_q e_q^2 f_{1T}^{\perp q}(x, p_T) \otimes D_{h/q}(z, k_T)}{\sum_q e_q^2 f_q(x, p_T) \otimes D_{h/q}(z, k_T)} \quad (\text{C.1})$$

where the convolution is means that the product is integrated over p_T and k_T . Similarly, the Collins asymmetry is:

$$A_{Coll} = \frac{F_{UT}^{\sin(\phi_h + \phi_s)}}{F_{UU}} = \frac{\sum_q e_q^2 h_{1q}(x, p_T) \otimes H_{1h/q}^{\perp}(z, k_T)}{\sum_q e_q^2 f_q(x, p_T) \otimes D_{h/q}(z, k_T)} \quad (\text{C.2})$$

In the following Sections, the convolution integrals will be analytically solved, assuming the Gaussian factorisation of the transverse momentum and the notation used in Chap. 1 and in [23].

C.1 The evaluation of F_{UU}

It is usual to assume the Gaussian factorisation for the unpolarised parton distribution functions and the fragmentation functions:

$$f_q(x, p_T) = f_q(x) \frac{1}{\pi \langle p_T^2 \rangle} e^{-\frac{p_T^2}{\langle p_T^2 \rangle}} \quad (\text{C.3})$$

and

$$D_{h/q}(z, k_T) = D_{h/q}(z) \frac{1}{\pi \langle k_T^2 \rangle} e^{-\frac{k_T^2}{\langle k_T^2 \rangle}} \quad (\text{C.4})$$

The unpolarised term is, writing explicitly the convolution (Tab.1.2):

$$\begin{aligned} F_{UU} &= \sum_q e_q^2 \int d\vec{p}_T d\vec{k}_T \delta^{(2)}\left(\vec{p}_T - \vec{k}_T - \frac{\vec{P}_T^h}{z}\right) f_q(x, p_T) D_{h/q}(z, k_T) \\ &= \sum_q e_q^2 f_q(x) \frac{1}{\pi \langle p_T^2 \rangle} D_{h/q}(z) \frac{1}{\pi \langle k_T^2 \rangle} \int d\vec{p}_T d\vec{k}_T \delta^{(2)}\left(\vec{p}_T - \vec{k}_T - \frac{\vec{P}_T^h}{z}\right) e^{-\frac{p_T^2}{\langle p_T^2 \rangle}} e^{-\frac{k_T^2}{\langle k_T^2 \rangle}} \end{aligned}$$

The first integration in \vec{k}_T using the δ function is trivial. The integral reads then:

$$\int d\vec{p}_T e^{-\frac{p_T^2}{\langle p_T^2 \rangle}} e^{-\frac{p_T^2 + \frac{P_T^{h2}}{z^2} - 2p_T \cdot \frac{P_T^h}{z}}{\langle k_T^2 \rangle}}$$

with the substitution $\frac{\vec{P}_T^h}{z} = -\vec{q}$ we can rearrange the previous expression as:

$$\int d\vec{p}_T e^{-\left[\frac{\langle p_T^2 \rangle + \langle k_T^2 \rangle}{\langle p_T^2 \rangle \langle k_T^2 \rangle} \left(p_T + \frac{\langle p_T^2 \rangle}{\langle p_T^2 \rangle + \langle k_T^2 \rangle} \vec{q} \right)^2\right]} e^{-\frac{q^2}{\langle p_T^2 \rangle + \langle k_T^2 \rangle}}$$

The integral is a function of the vector \vec{p}_T , that has two components. We recognise the Gaussian in two dimensions, thus the integral reads:

$$\int d\vec{p}_T e^{-\left[\frac{\langle p_T^2 \rangle + \langle k_T^2 \rangle}{\langle p_T^2 \rangle \langle k_T^2 \rangle} \left(p_T + \frac{\langle p_T^2 \rangle}{\langle p_T^2 \rangle + \langle k_T^2 \rangle} \vec{q} \right)^2\right]} = \pi \frac{\langle p_T^2 \rangle \langle k_T^2 \rangle}{\langle p_T^2 \rangle + \langle k_T^2 \rangle}$$

Thus:

$$F_{UU} = \sum_q e_q^2 f_q(x) D_{h/q}(z) \frac{e^{-\frac{P_T^{h2}}{z^2(\langle p_T^2 \rangle + \langle k_T^2 \rangle)}}}{\pi(\langle p_T^2 \rangle + \langle k_T^2 \rangle)} \quad (\text{C.5})$$

It is convenient to express the same result using the notation of Anselmino et al. [58], where k_T and p_T have a different meaning:

$$\begin{aligned} (\vec{p}_T)_{\text{here}} &= (\vec{k}_T)_{[58]} \\ (\vec{k}_T)_{\text{here}} &= -(\vec{p}_T)_{[58]}/z \end{aligned} \quad (\text{C.6})$$

and the Gaussian factorisation of the transverse momentum reads:

$$\begin{aligned} f_q(x, k_T) &= f_q(x) \frac{1}{\pi \langle k_T^2 \rangle} e^{-\frac{k_T^2}{\langle k_T^2 \rangle}} \\ D_{h/q}(z, p_T) &= D_{h/q}(z) \frac{1}{\pi \langle p_T^2 \rangle} e^{-\frac{p_T^2}{\langle p_T^2 \rangle}} \end{aligned} \quad (\text{C.7})$$

and the average hadron transverse momentum is defined as $\langle P_T^{h2} \rangle = \langle p_T^2 \rangle + z^2 \langle k_T^2 \rangle$ thus:

$$F_{UU}^{\text{Anselmino et al.}} = \sum_q e_q^2 f_q(x) D_{h/q}(z) \frac{e^{-\frac{P_T^{h2}}{\langle P_T^{h2} \rangle}}}{\pi \langle P_T^{h2} \rangle} \quad (\text{C.8})$$

C.2 The evaluation of $F_{UT}^{\sin(\phi_h - \phi_s)}$

Let's assume for the Siverson PDF the same Gaussian factorisation as for the unpolarised PDF :

$$f_{1T}(x, p_T) = f_{1T}(x) \frac{1}{\pi \langle p_T^2 \rangle} e^{-\frac{p_T^2}{\langle p_T^2 \rangle}} \quad (\text{C.9})$$

Then, the corresponding structure function (Tab.1.2) is:

$$F_{UT}^{\sin(\phi_h - \phi_s)} = \sum_q e_q^2 \int d\vec{p}_T d\vec{z}_T \delta^{(2)}\left(\vec{p}_T - \vec{k}_T - \frac{\vec{P}_T^h}{z}\right) \left(-\frac{\hat{h} \cdot \vec{p}_T}{M}\right) f_{1T}(x) \frac{1}{\pi \langle p_T^2 \rangle} e^{-\frac{p_T^2}{\langle p_T^2 \rangle}} D_{h/q}(z) \frac{1}{\pi \langle k_T^2 \rangle} e^{-\frac{k_T^2}{\langle k_T^2 \rangle}}$$

where $\hat{h} = \frac{\vec{P}_T^h}{|\vec{P}_T^h|}$. The integral is solved as for the unpolarised case, the only difference being that now we have:

$$\int d\vec{p}_T \left(-\frac{\hat{h} \cdot \vec{p}_T}{M} \right) e^{-\left[\frac{\langle p_T^2 \rangle + \langle k_T^2 \rangle}{\langle p_T^2 \rangle \langle k_T^2 \rangle} \left(p_T + \frac{\langle p_T^2 \rangle}{\langle p_T^2 \rangle + \langle k_T^2 \rangle} \vec{q} \right)^2 \right]}$$

With the variable change $\vec{p}' = p_T + \frac{\langle p_T^2 \rangle}{\langle p_T^2 \rangle + \langle k_T^2 \rangle} \vec{q}$ the integral above becomes the sum of two parts: one that is proportional to $\int d\vec{p}' \vec{p}' e^{-p'^2}$, that is zero since $\vec{p}' e^{-p'^2}$ is odd, and the other is:

$$-\frac{\vec{q}^2}{|q|M} \frac{\langle p_T^2 \rangle}{\langle p_T^2 \rangle + \langle k_T^2 \rangle} \int d\vec{p}' e^{-\frac{\langle p_T^2 \rangle + \langle k_T^2 \rangle}{\langle p_T^2 \rangle \langle k_T^2 \rangle} p'^2} = -\frac{q}{M} \frac{\langle p_T^2 \rangle}{\langle p_T^2 \rangle + \langle k_T^2 \rangle} \pi \frac{\langle p_T^2 \rangle \langle k_T^2 \rangle}{\langle p_T^2 \rangle + \langle k_T^2 \rangle}$$

where we have integrated the Gaussian in two dimensions.

Finally:

$$F_{UT}^{sin(\phi_h-\phi_s)} = e^{-\frac{P_T^h}{z^2(\langle p_T^2 \rangle + \langle k_T^2 \rangle)}} \frac{P_T^h}{Mz\pi} \frac{\langle p_T^2 \rangle}{(\langle p_T^2 \rangle + \langle k_T^2 \rangle)^2} \sum_q e_q^2 f_{1T}(x) D_{h/q}(z) \quad (C.10)$$

We can express this structure function using the notation of [58], as for the unpolarised case:

$$F_{UT}^{sin(\phi_h-\phi_s)} \text{ Anselmino et al.} = e^{-\frac{P_T^h}{\langle P_T^2 \rangle}} \frac{P_T^h}{M\pi} \frac{z \langle k_T^2 \rangle}{\langle P_T^2 \rangle^2} \sum_q e_q^2 f_{1T}(x) D_{h/q}(z) \quad (C.11)$$

but with a word of caution: in fact, in [58] the authors use a different parametrisation of the Siverson PDF, $f_{1T}(x, k_T) = f_{1T}(x) \sqrt{2e} e^{-\frac{k_T^2}{M^2}} e^{-\frac{k_T^2}{\langle k_T^2 \rangle}} / (\pi \langle k_T^2 \rangle)$. In this case, defining $\langle k_T^2 \rangle_{siv}^2 = \frac{\langle k_T^2 \rangle M^2}{\langle k_T^2 \rangle + M^2}$, the structure function reads:

$$F_{UT}^{sin(\phi_h-\phi_s)} \text{ Anselmino et al.} = P_T^h z e^{-\frac{P_T^h}{\langle P_T^2 \rangle}} \frac{\sqrt{e}}{M\pi\sqrt{2}} \frac{\langle k_T^2 \rangle_{siv}^2}{\langle P_T^2 \rangle^2 \langle k_T^2 \rangle} \sum_q e_q^2 f_{1T}(x) D_{h/q}(z) \quad (C.12)$$

C.3 The evaluation of $F_{UT}^{sin(\phi_h+\phi_s)}$

The Collins structure function (Tab.1.2) is:

$$F_{UT}^{sin(\phi_h+\phi_s)} = \mathcal{C} \left[-\frac{\hat{h} \cdot k_T}{M_h} h_1 H_1^\perp \right]$$

We assume for transversity and the Collins FF the same Gaussian factorisation as for the unpolarised case. This integral solved as for the Siverson case, with the change of variables:

$$\begin{cases} \vec{p}_T \rightarrow \vec{k}_T \\ \vec{k}_T \rightarrow \vec{p}_T \\ \delta^{(2)} \left(\vec{p}_T - \vec{k}_T - \frac{\vec{P}_T^h}{z} \right) \rightarrow \delta^{(2)} \left(\vec{p}_T - \vec{k}_T + \frac{\vec{P}_T^h}{z} \right) \end{cases} \quad (C.13)$$

and thus

$$F_{UT}^{sin(\phi_h+\phi_s)} = -e^{-\frac{P_T^h}{z^2(\langle p_T^2 \rangle + \langle k_T^2 \rangle)}} \frac{P_T^h}{M_h z \pi} \frac{\langle p_T^2 \rangle}{(\langle p_T^2 \rangle + \langle k_T^2 \rangle)^2} \sum_q e_q^2 h_1(x) H_{1h/q}(z) \quad (C.14)$$

Bibliography

- [1] V. W. Hughes, Nucl.Phys A 518 (1990) 371.
- [2] J. Bjorken, Phys. Rev. 148 (1966) 1467.
- [3] J. Ellis, J. Jaffe, Phys. Rev. D 9 (1974) 1444.
- [4] L. Dick et al, Phys. Lett. B 57.
- [5] K. Heller et al, Phys. Rev. Lett. 41.
- [6] J. Ralston, D. Soffer, Nucl. Phys. B. 152.
- [7] V. Y. Alexakhin et al. [COMPASS Collaboration], Phys. Rev. Lett. 94 (2005) 202.
- [8] E. S. Ageev et al. [COMPASS Collaboration], Nucl. Phys. B 756 (2007) 31.
- [9] M. Alekseev et al. [COMPASS Collaboration], Phys.Lett. B 673 (2009) 127.
- [10] H. Wollny, Measuring azimuthal asymmetries in semi-inclusive deep-inelastic scattering off transversely polarized protons, Ph.D. thesis, Physikalisches Institut Albert-Ludwigs-Universität Freiburg (2010).
- [11] T.Negrini, Transverse λ polarization from a transversely polarized proton target at the compass experiment, Ph.D. thesis, Mathematisch-Naturwissenschaftliche Fakultät der Rheinischen Friedrich-Wilhelms-Universität Bonn (2009).
- [12] C. Amsler et al. [Particle Data Group], Phys. Rev. B 667 (2008) 1.
- [13] V. Barone, F. Bradamante, A. Martin, Transverse-spin and transverse-momentum effects in high-energy processes, Progress in Particle and Nuclear Physics 65 (2010) 267.
- [14] D. Boer, P. Mulders, F. Pijlman, Nucl.Phys. B 667 (2003) 201.
- [15] V. Barone, Introduction to pdf's and tmd's, in: Ferrara International School Niccolò Cabeo, 2010.
- [16] R. Jaffe, Lecture Notes in Physics 496 (1996) 178.
- [17] E. Leader, E. Pedrazzi, An introduction to gauge theories and modern particle physics, John Wiley and Sons, 1984.
- [18] R. Jaffe, AIP Conf.Proc. 588 (2001) 54.
- [19] M. Burkardt, C. Miller, W.-D. Nowak, Spin-polarized high-energy scattering of charged leptons on nucleons, Rep. Prog. Phys. 73 (2010) 016201.
- [20] E. Leader, Spin in Particle Physics, Cambridge University Press, 2001.

- [21] A. Bacchetta, U. D'Alesio, M. Diehl, C. Miller, Phys. Rev. D 70.
- [22] A. Bacchetta, M. Diehl, K. Goeke, A. Metz, P. J. Mulders, M. Schlegel, JHEP 0702 (2007) 93.
- [23] M. Radici, Phenomenology of tmd's, in: Ferrara International School Niccoló Cabeo, 2010.
- [24] X. Artru, III Workshop on High Energy Spin Physics, DSPIN 2009.
- [25] A. Airapetian et al. [HERMES Collaboration], Phys. Lett. B 693 (2010) 11.
- [26] M. Alekseev et al. [COMPASS Collaboration], Phys. Lett. B 692 (2010) 240.
- [27] X. Jiang, neutron transversity experiment at jlab, in: TMD 2010 - Workshop on Transverse Momentum Distributions, 2010.
- [28] L. Levorato on behalf of the COMPASS collaboration, Transversity 2008 conference proceedings.
- [29] R. Seidl, et al., Measurement of azimuthal asymmetries in inclusive production of hadron pairs in e^+e^- annihilation at $\sqrt{s} = 10.58$ *gev*, Phys. Rev. D 78 (3) (2008) 032011.
- [30] M. Anselmino, et al., Nucl. Phys. Proc. Suppl. 191 (2009) 98.
- [31] M. Burkardt, Gpd's and ssa's, in: Transversity 2005, 2005.
- [32] M. Burkardt, Phys.Rev. D 72 (2005) 094020.
- [33] A. Airapetian et al. [HERMES Collaboration], Phys Rev. Lett. 103 (2009) 152002.
- [34] M. Anselmino, et. al., Sivers function: Sidis data, fits and predictions, in: Transversity 2005, 2005.
- [35] M. Anselmino et al., Eur.Phys.J.A 39 (2009) 89.
- [36] P. Schweizer, et al., Pretzelosity distribution function h_{1T}^\perp , in: Transversity 2008, 2008.
- [37] B. Parsamyan, Analysis and interpretation of transverse spin dependent azimuthal asymmetries in sidis at the compass experiment, Ph.D. thesis, Università di Torino (November 2007).
- [38] A. Rostomyan, Tmds at hermes, in: TMD2010 - Workshop on Transverse Momentum Distributions, 2010.
- [39] A. Kotzinian, Sidis asymmetries in quark-diquark model, in: Transversity 2008, 2008.
- [40] P. Abbon et al. [COMPASS Collaboration], Nucl. Instrum. Meth. A 577 (2007) 455.
- [41] A. Abbon et al., Particle identification with compass rich-1, Nucl. Instrum. Meth. A 631 (2011) 26.
- [42] V. Kolosov, O. O. Kouznetsov, A. Magnon, F. Nerling, Present performances of compass electromagnetic calorimetry from data analysis, Tech. Rep. COMPASS-2008-5 (2008).
- [43] A. Albrecht et al., Compass rich-1, Nucl. Instrum. Meth. A 502 (2003) 112.
- [44] A. Albrecht et al., The radiator gas and the gas system of compass rich-1, Nucl. Instrum. Meth. A 502 (2003) 266.

- [45] A. Albrecht et al., The mirror system of compass rich-1, Nucl. Instrum. Meth. A 502 (2003) 236.
- [46] T. Ypsilantis, J. Seguinot, Nucl. Instr. Meth. A 343 (1994) 30.
- [47] R. Barlow, Extended maximum likelihood, Nucl. Instrum. Meth. A 297 (1990) 496.
- [48] A. Kotzinian, Remarks on acceptance effects in asymmetry extraction, Tech. Rep. COMPASS-2007-2 (2007).
- [49] A. Martin, G. Pesaro, P. Schiavon, F. Sozzi, H. Wollny, On the role of the acceptance in the unbinned maximum likelihood method, Tech. Rep. COMPASS-2009-13 (2009).
- [50] B. Parsamyan on behalf of the COMPASS collaboration, SPIN 2010- 19th International Spin Physics Symposium.
- [51] F. Sozzi, Measurement of transverse spin effects in compass, Ph.D. thesis, Università degli studi di Trieste (2007).
- [52] W. Vogelsang, F. Yuan, Phys.Rev.D 72 054028.
- [53] G. Sbrizzai, Measurements of azimuthal asymmetries in sidis at compass, Ph.D. thesis, Università degli studi di Trieste (2010).
- [54] S. Kretzer, Phys.Rev.D 62 (2000) 054001.
- [55] M. Glück, E. Reya, A. Vogt, Eur.Phys.J. C 5 (1998) 461.
- [56] A. Martin, R. Roberts, W. Stirling, R. Thorne, Phys.Lett.B 531 (2002) 216.
- [57] D. Stump, J. Huston, J. Pumplin, W. Tung, H. Lai, S. Kuhlmann, J. Owens, JHEP 0310.
- [58] M. Anselmino et al., Phys.Rev. D 71 (2005) 074006.
- [59] S. Arnold, A. Efremov, K. V. Goeke, M. Schlegel, P. Schweizer, arXiv:0805.2137[hep-ph].
- [60] A. Efremov, K. V. Goeke, P. Schweizer, Phys.Rev.D 73 (2006) 094025.
- [61] F. James, MINUIT, Function Minimization and Error Analysis Reference Manual.
- [62] M. Gockeler, et al., Phys. Lett. B 627 113.

Acknowledgements

"So long, and thanks for all the fish!"

D. Adams.

I would like to thank prof. Paolo Schiavon, a Tutor more than my Ph.D. tutor, my supervisor prof. Anna Martin for coordinating this analysis work and indicating always the best direction to take.

I would like to thank our group leader Franco Bradamante; Andrea Bressan, for all his suggestions; Silvia dalla Torre and Fulvio Tessarotto, for all of what I have learnt about the RICH detector.

I would like to thank my colleagues , with whom I shared the office, the journeys and the doubts (sometimes also the solutions): Federica Sozzi, Vinicio Duic, Giulio Sbrizzai, Stefano Levorato and Carmine Elia; and Elena Rocco for believing. I would like to thank them all for being now friends more than colleagues.

Thanks to all the COMPASS members, to B.Gobbo and R.Birsa.

A special mention is due to M.E. Boglione and A. Bacchetta who came in Trieste to give us lessons, and for the fruitful discussions, and of course to Delia Hash for being the referee of this Thesis.

Last but not least, thank to my husband Andrea, for pretending to be interested in the Collins and Sivers asymmetries, and for patiently waiting me at home (and also for bringing me to the airport at dawn).